Improving Stall Model Accuracy through Optimal Data Slicing by Analyzing Kirchhoff Stall Parameter Estimate Behaviour

Master of Science Thesis

P.A.R. Brill

3 February 2023

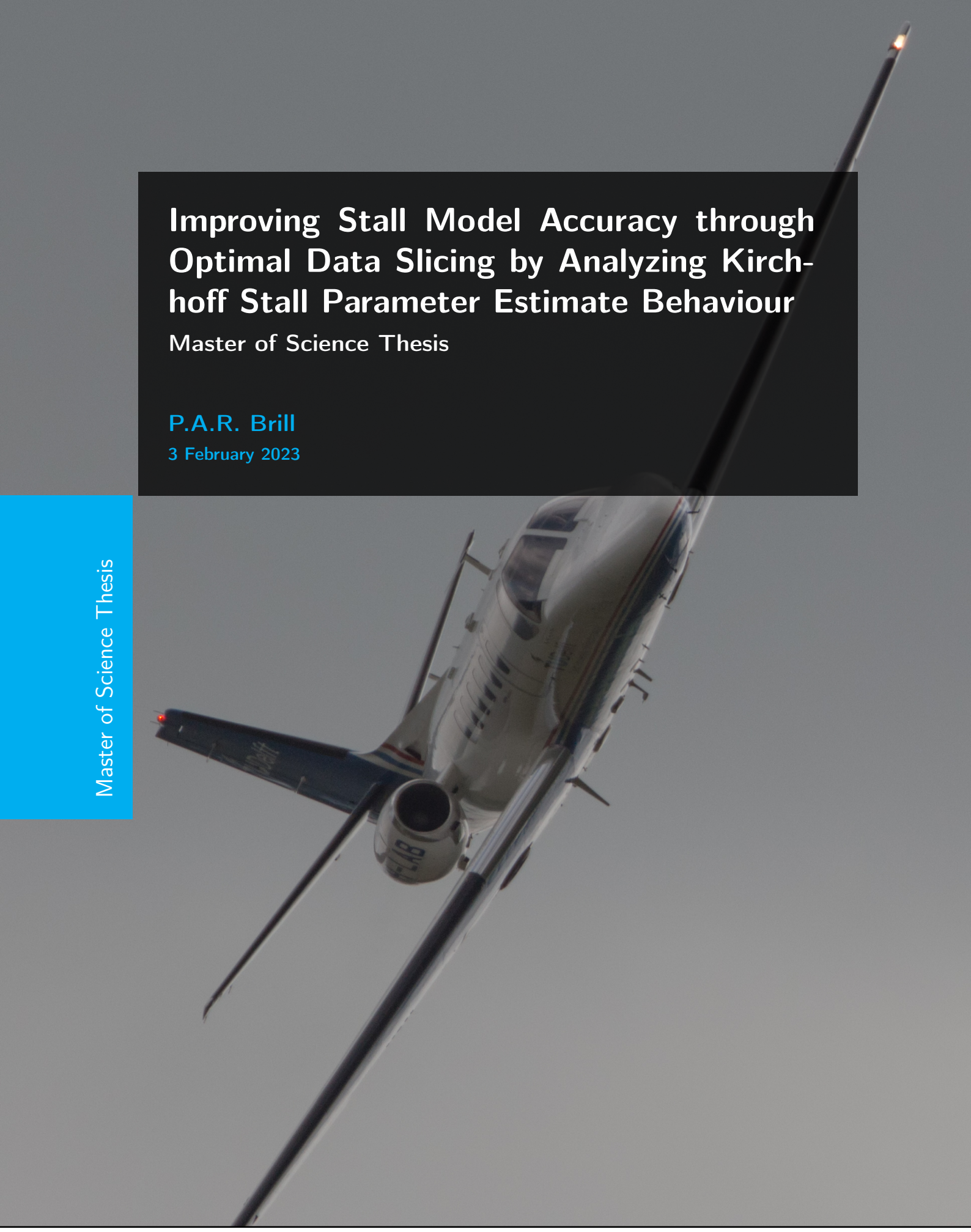

Master of Science Thesis

TU Delft Delft University of Technology

CITATION STALL MODELING TU Delft C&S

Faculty of Aerospace Engineering
Department of Control and Simulation

Improving Stall Model Accuracy through Optimal Data Slicing by Analyzing Kirchhoff Stall Parameter Estimate Behaviour

Master of Science Thesis

Master of Science Thesis

For the degree of Master of Science in Aerospace Engineering at Delft University of Technology

P.A.R. Brill

3 February 2023

Faculty of Aerospace Engineering · Delft University of Technology

Delft University of Technology
Department of
Control and Simulation

The undersigned hereby certify that they have read and recommend to the Faculty of Aerospace Engineering for acceptance a thesis entitled

Improving Stall Model Accuracy through Optimal Data Slicing by Analyzing Kirchhoff Stall Parameter Estimate Behaviour

by

P.A.R. Brill

in partial fulfillment of the requirements for the degree of

Master of Science Aerospace Engineering

Dated: 3 February 2023

Committee chair:

dr.ir. C.C. de Visser
Associate Professor
Control & Simulation

Responsible thesis supervisor:

dr.ir. D.M. Pool
Assistant Professor
Control & Simulation

External examiner:

dr.ir. M.F.M. Hoogreef
Assistant Professor
Flight Performance & Propulsion

Preface

Delft, 9 January 2023

Dear reader,

Before you lies the the product of one-and-a-half years of research. However, as many have experienced and said before me, it is even more so the product of hard work, perseverance, patience, but also of being adventurous and diving into everything you find in the process.

The thesis is a result of hard work because of the sheer amount of time and effort that are needed to finish the project. It is a result of perseverance because your code will never do what you expect it to do, as at least once per day you will see your efforts of the day before go up into nothing as you find that it will only result in an additional error to the ones you already had. Then, you have no choice but to take a deep breath, once in a while scream at your computer, and get back into it. It is also a result of patience as you find that you lack the skill of efficient programming, and to get your full results your code needs to run 24/7 for at least three weeks on 14 CPUs (thank you Harold, mom and dad, and solar power). But it is also the result of being adventurous, as you not only venture into a previously unknown field, but also have to take in and dive into all the unknown things you find in the meter-deep rabbit holes. Only to find yourself stuck in a tight passage and having to get your supervisors to pull you back up to the above-ground. In some way I guess you also need to be somewhat courageous -or is it naive?- to graduate at Aerospace Engineering.

Talking about my supervisors, I would like to thank Daan en Coen for their help and expertise throughout the entire project. As mentioned, I could sometimes be prone to getting lost in the vast amount of features that may warrant at least some investigation. Luckily, both Daan and Coen could help me to re-focus on the bigger picture and to guide me towards what were in their eyes the more valuable findings. I am happy to say that I also learned from this, as I think this initiative slowly but steadily moved more towards myself. Next for this guidance, I am also thankful for their enthusiasm about my research. I like the fact that they seem to be genuinely interested in what I found and did, and that is a great motivator. I think the drive of Daan to get us flying in the PH-LAB is a great example of this. Last, I want to thank

them for their humour, lightheartedness and availability through their open-door policy. This made working with them not only useful, but also fun.

Also my fellow thesis students in NB2.56 made graduating more fun. Having a place where everyone is in the same (sometimes it seems, sinking) boat creates a feeling of camaraderie. Or, it could also be that what binds us is a common enemy: MATLAB and Python errors. The more errors we encountered the more we had fun. It made the choice to persevere and continue with your work all the more possible. Free coffee also helps. The rat race for a nice desk and computer screen does not.

But I also want to thank my parents, Jan and Thea, for their unconditional support through this entire process and my studies as a whole. Not everything during this time, and I think this applies to the rest of life, too, was straightforward, nor was it easy. Sometimes life manages to throw a curveball at you and it hits you in the face. It is then that you really learn to value the people supporting you, the people that keep helping you to see clearly what you do it all for. To keep working on your dreams and your goals, and to -eventually- be given the title of "ingenieur", which to carry for the rest of your life to work in the cockpit (but, as I have also learned throughout my studies: don't hope). Maybe once I will be trained on a simulator model whose development was partly based on my own analyses. A stepping stone towards my childhood dreams.

This thesis consists of four main parts. First, you will find the final scientific paper describing the most important findings of my research. This is followed by a more elaborate description of all background research performed in order to make possible the writing of the scientific paper. This preliminary thesis report includes both a literature review and an investigation into four different research topics that were an option for this thesis. The third part contains an appendix to the preliminary report, an overview of all flight test data gathered in the PH-LAB research aircraft for stall model identification. The last part are the two appendices to the scientific paper, containing all compared and individual parameter behaviour plots that were analysed to come to the final conclusions in the scientific paper.

I am inexplicably proud that it all has resulted in what you are reading now, the crown on my 7.5 years of study, my MSc thesis. I wish you a lot of pleasure in reading it.

Yours faithfully,

Patrick Brill

Table of Contents

List of Figures

List of Tables

Nomenclature

Roman symbols

A	Aircraft specific acceleration
A	Amplitude
A	Aspect ratio
A	Regression matrix
a	Regressor
a_1	Parameter related to the abruptness of the flow separation
B	Orthogonal regressor matrix
B	Spline basis function
b	Aircraft spanwidth
b	Orthogonalized regressor
b	Barycentric coordinate
BEW	Basic Empty Weight
C	Coefficient
c	B-coefficient
$\bar{c}$	Aircraft mean aerodynamic chord length
$CRLB$	Cramér-Rao Lower Bound
D	Drag
D	Dispersion matrix
F	Reference frame
f	Frequency
$F()$	Probability distribution function
$f()$	System/kinematic equations
$f()$	Probability density function
G	Orthogonal regressor conversion matrix
$h()$	Measurement/observation equations
I	Aircraft moment of inertia
I	General Fisher information matrix
J	Cost function
K	Kalman gain

L	Lift
L	Number of states
ℓ	Moment around X_b axis
M	Model dependent Fisher information matrix
m	Moment around Y_b axis
m	Aircraft mass
m	Pdf moment
MSE	Mean Squared Error
N	Number of measurements
n	Number of states
n	Moment around Z_b axis
n	OLS model order
$N1$	Engine fan speed
$\mathcal{O}$	Observability matrix
P	State estimate covariance matrix
p	Roll rate
$p()$	Polynomial of simplex splines
Q	System noise covariance matrix
q	Pitch rate
R	Sensor noise covariance matrix
r	Yaw rate
R^2	Coefficient of determination
RMS	Root Mean Square
$RRMS$	Relative Root Mean Square
S	Power spectral density
S	Aircraft wing surface
S	Spline space
$S()$	Output sensitivity matrix
T	Thrust
T	Total time
T	Triangulation
t	Time
t	Simplex
u	Input
u	Aircraft velocity along F_b x-axis
V	Velocity
V	Set of non-degenerate points
v	Sensor/measurement noise
v	Aircraft velocity along F_b y-axis
W	Sigma point vector weight
W	Wind state estimate
w	System/process noise
w	Aircraft velocity along F_b z-axis
$\mathcal{X}$	Sigma points matrix
X	Position of flow separation point along chord ($X \in [0, 1]$)
X	Force in X_b direction
x	State

x	Aircraft position along F_E x-axis
x	x-location along aircraft fuselage length (from datum)
$\mathcal{Y}$	UT transformed sigma points matrix
Y	Force in Y_b direction
y	UT transformed state
y	Aircraft position along F_E y-axis
y	y-location along aircraft fuselage width (from datum)
y	Output
$\mathcal{Z}$	UT transformed measurement sigma points matrix
Z	Force in Z_b direction
z	Measurement
z	Aircraft position along F_E z-axis
z	z-location along aircraft fuselage height (from datum)

Greek symbols

α	Angle of attack
α	UKF scaling parameter related to sigma point spread
α^*	Angle of attack for which $X_0 = 0.5$
β	Angle of sideslip
β	UKF scaling parameter related to distribution of the state
Γ	Signal coherence
γ	Polynomial coefficient
δ	Control deflection
ε	Residual/error
θ	Pitch angle
θ	Parameter
κ	UKF secondary scaling parameter
κ	Multi-index
λ	UKF scaling parameter
λ	Bias
μ	Mean
τ_1	Time constant related to the relaxation of the flow separation point (transient effects)
τ_2	Time constant related to the time delay of the flow separation and reattachment (hysteresis)
σ	Standard deviation
σ^2	Variance
τ	Time constant
ϕ	Phase
φ	Roll angle
φ	Orthogonal parameter
ψ	Yaw angle
ω	Angular frequency

Subscripts

0	Steady state conditions/trim point
a	Aileron
b	Aircraft body-fixed reference frame
b	Boom vane

$c.g.$	Center of gravity
D	Drag coefficient
d	Spline space degree
E	Vehicle carried normal Earth reference frame
e	Elevator
k	Timestamp
L	Lift coefficient
ℓ	Roll moment coefficient
m	Measured
m	Pitch moment coefficient
n	Yaw moment coefficient
r	Rudder
T	Thrust coefficient
t	Thrust
TAS	True airspeed
v	AOA vane
x	In X_{F_b} direction
Y	Lateral force coefficient
y	In Y_{F_b} direction
z	In Z_{F_b} direction
κ	Spline basis function multi-index

Superscripts

$'$	Pdf central moment
$\dot{}$	Derivative
$\hat{}$	Estimate/mean
$\vec{}$	Vector
a	Augmented
(c)	Sigma point weight for covariance
d	Spline basis function degree
(m)	Sigma point weight for mean
nl	Nonlinear function
r	Spline space order
st	Stationary flight

Abbreviations

AHRS	Attitude & Heading Reference System
AOA	Angle of Attack
CCD	Central Composite Design
DADC	Digital Air Data Computer
DASMAT	Delft University Aircraft Simulation Model and Analysis Tool
DOE	Design of Experiments
EKF	Extended Kalman Filter
FFD	Full Factorial Design
FPR	Flight Path Reconstruction
FSTD	Flight Simulation Training Device
FTIS	Flight Test Instrumentation System

GPS	Global Positioning System
ICAO	International Civil Aviation Organisation
ICATEE	International Committee for Aviation Training in Extended Envelopes
IEKF	Iterated Extended Kalman Filter
JND	Just Noticable Difference
KF	Kalman Filter
LOC-I	Loss of Control In-Flight
OFM	Orthogonal Function Modeling
OLS	Ordinary Least Squares
pdf	probability density function
PSD	Power Spectral Density
PSE	Predicted Square Error
UKF	Unscented Kalman Filter
UPRT	Upset Prevention and Recovery Training
UT	Unscented Transform

Part I

Scientific Paper

Improving Stall Model Accuracy through Optimal Data Slicing by Analyzing Kirchhoff Stall Parameter Estimate Behaviour

Pieter A.R. (Patrick) Brill*
Faculty of Aerospace Engineering, Delft University of Technology, Delft, Zuid-Holland, 2629HS, the Netherlands

To improve the safety of commercial air transport, pilots are required to train on simulators to recognize the characteristics of an impeding stall and subsequently correctly recover from it. To prevent negative training, it is important that the accuracy of the used simulation models is high. A manner to model the nonlinear, unsteady aerodynamic effects during the stall is by using Kirchhoff's theory of flow separation. However, widespread difficulties exist in correctly estimating the stall-related parameters in these models. It is not always possible to simply gather more flight data to solve this problem. Therefore, the research in this paper aims to increase model accuracy by making optimal use of already existing flight data via introduction of the slice-based modeling method. This is done by analyzing the change in the parameter estimate values when applying the system identification procedure to sliced partitions of simulated flight data. These partitions incrementally increase in size with time from the stall. The simulation data is generated to be representative of the available flight test data. The change in parameter estimates was analyzed for both the pre-stall and post-stall phase. The estimated value for each partition was compared to the actual parameter value setting in the simulation model used to create the data. Manually, an optimal window was found for each parameter for which the estimated value and actual value were equal. For the stall-related parameters this window is often not more than 10 s **wider than the stall. For the linear stability and control derivatives it is found that using more data generally results in a better estimate. These window sizes were used in the estimation for each separate parameter on the real flight test data. Even though this method represents a prototype, in more than half of the validation cases a decrease in** MSE **of** 10 % **to** 35 % **could be achieved. This shows that the new slice-based modeling method is able to improve the accuracy of nonlinear stall models without the need to gather more flight data. Additionally, the parameter estimate behaviour analysis technique and slice-based modeling method may have applications that reach beyond the realm of stall modeling.**

Nomenclature

Roman symbols

a_1	=	stall abruptness parameter
A_x	=	longitudinal acceleration
A_z	=	vertical acceleration
c	=	chord length
C_D	=	drag coefficient
C_L	=	lift coefficient
C_L^{nl}	=	nonlinear unsteady C_L at high angles of attack
C_X	=	longitudinal force coefficient
C_Z	=	vertical force coefficient
D	=	dispersion matrix
J	=	nonlinear estimation objective function
k	=	timestamp
M	=	Fisher information matrix
m	=	aircraft mass
MSE	=	mean squared error
N_o	=	total number of outputs
N_p	=	total number of parameters
Q	=	quartile
R	=	noise covariance matrix
$RRMS$	=	relative root mean squared error
S	=	wing surface area
$S(k)$	=	output sensitivity matrix
V_{TAS}	=	true airspeed
t	=	time
X	=	airfoil flow separation point
x	=	nonlinear regressor
y	=	measurement signal
$\hat{y}$	=	model output

Greek symbols

α	=	angle of attack

*MSc Student, Department of Control & Simulation, patrickbrill@outlook.com.

α^*	=	angle of attack for which $X = 0.5$	ρ	=	air density
δ_a	=	aileron deflection	σ	=	standard deviation
δ_e	=	elevator deflection	σ^2	=	variance
δ_r	=	rudder deflection	τ_1	=	angle of attack rate effect time constant
θ	=	parameter	τ_2	=	stall hysteresis time constant
$\hat{\theta}$	=	estimated parameter			

I. Introduction

The most significant cause of fatal accidents in commercial air transport is loss of control in-flight [1]. Loss of control in-flight occurs when the pilots of an aircraft cannot recover the aircraft from an adverse flight condition outside its normal operational envelope [2]. An example of this is aerodynamic stall, which is defined as "an aerodynamic loss of lift caused by exceeding the critical angle of attack" [3]. To train pilots to handle these situations properly, the International Civil Aviation Organisation has urged member states to implement upset prevention and recovery training in their regulations [3]. In response to this, the European Aviation Safety Agency has updated its legislation on flight simulation training devices [4], stating that these must accurately model the aircraft behaviour in the stall to train pilots effectively in recognizing and handling the aircraft stall characteristics [5, 6].

Aerodynamic models valid in nominal flight phases are not immediately valid near the stall, where nonlinear and unsteady effects are present [7]. Therefore, the model needs to be extended with nonlinear terms, but this is not trivial. Often, the conventional stability and control derivatives are then estimated separately for the nominal flight phases and for near the stall and scheduling is required, e.g. as in [8, 9].

An elegant yet powerful method to model some of the characteristic behaviours of an aircraft in the stall without the need for scheduling is via Kirchhoff's theory of flow separation [10]. This can be used to identify aircraft stall models from flight data for both the longitudinal and lateral motions of the aircraft [11–13]. However, in practice, difficulties still arise in estimating and validating some of the stall model parameters with significant reliability [14, 15]. This issue is usually accounted to a lack of dynamic excitation present in the available flight data in combination with the short duration of the stall event.

Kirchhoff's theory is also used in stall modeling research at the Faculty of Aerospace Engineering of the Delft University of Technology. This research is centered around the Delft University Aircraft Simulation Model and analysis Tool (DASMAT) [16] which models the faculty-owned Cessna Citation II aircraft PH-LAB. Multiple research efforts have improved and extended this model from the normal flight envelope to the stall [17–20]. It has been shown that this model, in combination with the incorporated buffet model [21], provides aircraft stall behaviour in a full flight simulator which is strongly comparable to that of the stall in the actual aircraft [21, 22]. However, here too, difficulties exist in correctly estimating the parameters describing the nonlinear and unsteady effects. Again, additional flight testing is recommended.

Sufficient dynamic excitations in flight testing is important as this increases the amount of information that is present in the data for the to-be-estimated parameters. This is usually achieved by applying specific control inputs throughout flight test runs. These may be conventional inputs applied by the pilots of the aircraft [23, 24] or may be optimal inputs that are specifically tailored to increase the amount of information for a certain model parameter [25–27]. But this approach is only possible if a priori information about that parameter is available. The optimal-input approach is based on the concept of Fisher information [23, 28]. However, introducing this approach also requires additional flight testing. However, a drawback is that simply gathering more flight test data is often not an option due to high costs, lack of time, or both.

The research in [8, 9] makes use of a second, distinctively different method with the same goal of increasing stall model accuracy, but without the need for additional flight tests. This is the practice of partitioning data, introduced in [29]. This can result in an improved stall model, but requires scheduling according to the associated angle of attack of the partition on which the estimation was applied. Apart form the model accuracy increase, this research also showed that different partitions associated with different angles of attack will deliver different estimates for the same parameter. However, it is has never been demonstrated whether the slicing of data also has a positive effect on any model that also involves nonlinear parameters.

Summarized, on one hand there is a problem: often, research efforts have difficulties identifying the nonlinear parameters with the limited data available. E.g. as is the case for models using Kirchhoff's theory of flow separation. In these efforts, as much data as is available is used in the estimation procedure. No attention is paid towards which parts of the data may be valuable to the nonlinear Kirchhoff stall parameters and which parts may be valuable to the

linear stability and control derivatives. This may cause nonlinear stall parameters to model parts of the linear nominal behaviour in the data and vice versa, which is not in line with their intrinsic purpose. On the other hand, there is proof that different parts of already available flight test data deliver different estimates, as seen in [29]. This raises the question: can model accuracy be improved by choosing specific parts of data to which to apply the estimation of a specific parameter, in contrary to the usual practice of simply using all data for all parameters regardless of the circumstances under which the data were gathered?

The main contribution of this paper is to improve stall model accuracy through optimal data slicing by analyzing Kirchhoff stall parameter estimate behaviour. A new slice-based modeling method is introduced. Simulation data is generated from a simulation with the model structure of [19] with known parameter values set. The simulated flight trajectory is designed to closely resemble the available real flight data and given inputs. Via data slicing, partitioning and Fisher information analysis, it is for the first time possible to directly observe which part of the simulated data causes a change in the value of a parameter estimate. This is named "parameter estimate behaviour" for the remainder of this paper. However not part of the modeling method, this analysis can also be performed on flight test data for more insights that can validate the method. By comparing the parameter estimate behaviour of the simulation data to the actual simulation model value, an optimal time window can be found for all input types given during the stall, for the pre-stall and post-stall phases, and for every separate parameter. The optimal window sizes are subsequently applied to the estimation of every parameter using the flight test data. The accuracy achieved with the slice-based method is compared to that achieved when the normal modeling method is applied where simply all available data is used.

This paper is structured as follows. In section II, the research methodology is explained extensively. In section III, the results of this method are presented, after which they are analyzed and discussed in section IV. This paper concludes with section V.

II. Methodology

A. Aerodynamic Stall Model

Before discussing the full slice-based modeling method, the assumed aerodynamic stall model must be introduced. In order to capture the unsteady and nonlinear behaviour in the stall, Kirchhoff's theory of flow separation is used [10, 11]. It states that the nonlinear and unsteady behaviour of the lift coefficient at high angles of attack C_L^{nl} is a function of angle of attack α and flow separation point X:

$$C_L^{nl}(\alpha, X) = C_{L_\alpha}\left(\frac{1+\sqrt{X}}{2}\right)^2 \alpha \tag{1}$$

The movement of flow separation point X along the chord of the wing is itself also a function of the angle of attack α and the angle of attack rate $\dot{\alpha}$, such that $X = X(\alpha, \dot{\alpha})$. It can be described by an ordinary differential equation [11]:

$$\tau_1 \frac{dX}{dt} - X = \frac{1}{2}\{1 - \tanh\left[a_1(\alpha - \tau_2\dot{\alpha} - \alpha^*)\right]\} \tag{2}$$

The value of X is 1 when the flow is fully attached (separation point at trailing edge) and 0 when it is fully separated (separation point at leading edge). The parameters a_1, α^*, τ_1 and τ_2 are the nonlinear stall parameters. Parameter a_1 controls the abruptness of the stall, α^* is the angle of attack where $X = 0.5$, τ_1 influences the relaxation of the flow separation and τ_2 models the hysteresis effect. The value of these parameters depend on aircraft type and are ultimately the parameters that need to be estimated correctly to result in highest stall model accuracy.

The stall model investigated in this paper is the model as defined in [19]. The equation for the lift coefficient C_L of this model is given in Eq. (3). It was identified from flight test data by use of orthogonal function modeling [30]. Only the C_L model is considered in this paper as it was found in preliminary research that this contains most information on the stall parameters.

$$C_L = C_{L_0} + C_{L_\alpha}\left(\frac{1+\sqrt{X}}{2}\right)^2 \alpha + C_{L_{\alpha^2}}(\alpha - 6^\circ)_+^2 \tag{3}$$

In which $(\alpha - 6^\circ)_+^2$ is a spline function active only when $\alpha \geq 6^\circ$. The stability and control derivatives C_{L_0}, C_{L_α} and $C_{L_{\alpha^2}}$ are the linear parameters of the model. The parameter values estimated by [19] and the absolute lower and upper

bounds of the search space applied during estimation for these parameters are given in Table 1. These settings are used as main reference in this paper.

Table 1 Estimated parameter values and used search space bounds for estimation of the parameters, as in [19].

		Bounds	
θ_i	Value	Lower	Upper
a_1, −	27.6711	15	40
α^*, rad	0.2084	0.1	0.35
τ_1, s	0.2547	0.001	0.8
τ_2, s	0.0176	0	0.5
C_{L_0}, −	0.1758	0.1	0.4
C_{L_α}, −	4.6605	2	6
$C_{L_{\alpha^2}}$, −	10.7753	0	20

B. Overview of the Slice-based Modeling Method

The sliced-based modeling method introduced in this paper is a further development of the method introduced in [19]. The modeling method used there, in the remainder of this paper called the "normal modeling method", is depicted in Figure 1. In the normal method, the gathered flight data is directly passed to the flight path reconstruction. From the reconstructed states, the lift coefficient C_L is calculated. This C_L is passed to the model structure selection containing the orthogonal function modeling, together with any other reconstructed state that may be needed as a regressor x. In this paper, the model structure selection is not performed, but the final model structure of Eq. (3) is always used. This makes it possible to perform an analysis on a distinct set of known parameters, including calculation of the Fisher information. A nonlinear and linear estimation are performed, resulting in the final parameter estimate vector $\hat{\hat{\theta}}$. This finalizes the stall model.

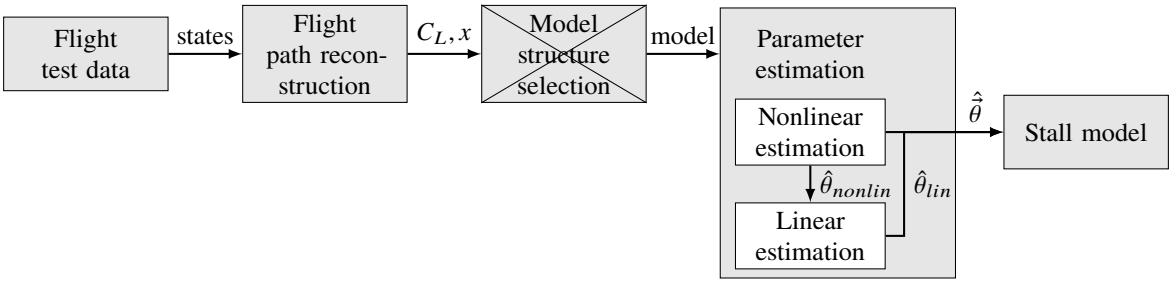

Fig. 1 Overview of the normal modeling method, as in [19]. The model structure selection that takes place in [19] has not been incorporated in the research described in this paper.

The slice-based modeling method is an extended version of the normal method described above. It is depicted in Figure 2. The slice-based method contains all but one of steps from the normal estimation procedure, represented by the boxes "Flight test data", "Flight path reconstruction", a slightly different parameter estimation called "Slice-based parameter estimation", and finally the estimated "Stall model". As mentioned, the model structure selection is not included, as the model structure is set a priori. The main addition of the new slice-based method is that the parameter estimation now uses an optimal time window for each separate parameter, indicated by the optimal slice number $n_{slice_{opt}}$. Finding this optimal window starts with generating a simulation data set. The parameter estimate behaviour that results from this simulation data is used as a substitute for the expected, but unknown, parameter estimate behaviour that may result from flight test data. The simulated data is also passed through flight path reconstruction. This data is then sliced and partitioned in three different manners. The nonlinear parameters $\hat{\theta}_{nonlin}$ and the linear parameters $\hat{\theta}_{lin}$ in the model are then estimated for all three slicing types and every partition within these types. This makes it possible to analyze the behaviour of the parameter estimates in time by use of the median of the parameter estimates $\tilde{\hat{\theta}}$, the quartiles Q of

their distribution and the associated Fisher information content M. From this behaviour, the sought-after optimal slice number $n_{slice_{opt}}$ can be selected for each separate parameter for each type of stall present in the flight test data, both for pre-stall and post-stall phases. In the following subsections, all of the above steps are discussed more extensively.

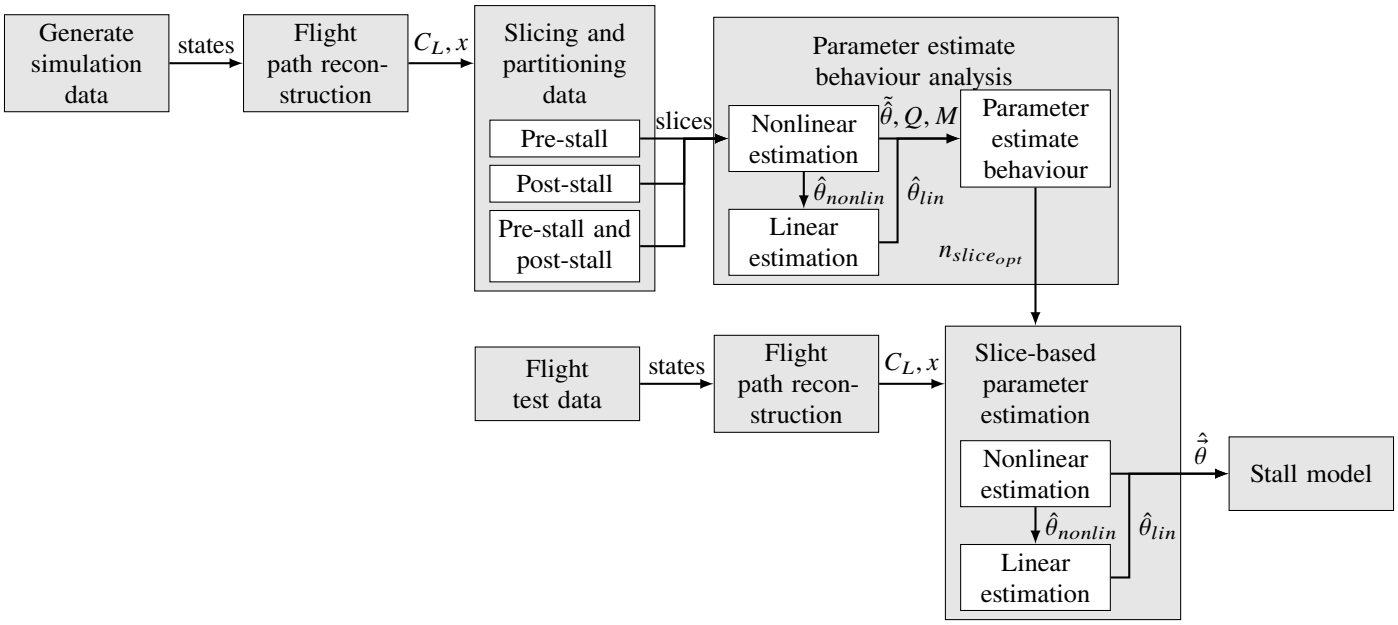

Fig. 2 Overview of the slice-based modeling method, as introduced in this paper.

C. Data Sets

In the research described in this paper two types of data are used: simulated flight data and real test flight data. This is different from existing stall modelling research, in which only real flight data is used. The use of simulated flight data creates the possibility to directly compare the estimated parameters with their actual, known values, rather than only model output validation. This can deliver direct insight into the performance of the parameter estimation procedure. Especially, because the simulation data is generated to mimic the available real flight test data. After the analysis of the simulated data, the real flight data can then be used for final parameter estimation and validation. The two types of data sets in this paper are discussed below.

1. Flight Test Data

Real flight data was gathered in two stall test flights by the TU Delft Cessna Citation II research aircraft in 2018 [19] and 2019 (not connected to a specific research paper). Three different types of stalls are chosen that differ from each other by the control input given within the stall. These are the following

- *No inputs.* To provide a baseline for this research, the most straightforward type of stall was chosen: the symmetric stall with no inputs. There are three such stalls in the data of 2018.
- *Inputs $-\delta_a$ 3-2-1-1 and $-\delta_e$ 3-2-1-1.* The 3-2-1-1 stalls were chosen to investigate the usability of this widely-applied input in stall modeling. The combination of the two surfaces was chosen as there are no stalls in the data with solely a δ_e input. There are thirteen such stalls in the data of 2019.
- *Inputs $-\delta_a$ wiggle and $-\delta_e$ wiggle.* The wiggle input was specifically developed in [24] and used in [19] as a pilot-applied input for use in stall flight modeling, to apply large deflections without leaving the desired stall state of the aircraft. This type with two control surfaces is chosen to be able to compare the parameter estimate behaviour in this stall type to the behaviour of the 3-2-1-1 stall type. There are six such stalls in the data of 2018.

To make the terminology for the real flight data consistent with the simulated flight data, for a certain stall run of a certain input type the term "realization" is used. Thus, there are three, thirteen and six realizations per the different input types in the flight test data. The aim of the simulation data is to mimic the data gathered in the real flight tests, with the three input types present therein, but within a controlled environment.

2. Simulation Data

The simulated flight data was created by use of DASMAT [16], containing the model of the PH-LAB Cessna Citation II research aircraft. The aerodynamic model is as developed by [19] and also contains the buffet model as developed by [18]. Stall runs are simulated using the "stall autopilot" as developed in [21, 22].

The simulated flight data starts with the aircraft trimmed in steady, straight, symmetric flight. To improve the unscented Kalman filter's convergence in the flight path reconstruction, successive excitations are introduced. A 3-2-1-1 input followed by return to symmetric flight is given successively for the aileron, elevator and rudder. This introduces excitations in all six degrees of freedom.

After this begins the "stall run", which is used in the parameter estimation procedure. First, steady straight symmetric flight is maintained for 120 s. A wings-level hold controller is active during this time to prevent the aircraft form entering its unstable spiral eigenmode. Hereafter, the stall autopilot is engaged to perform a symmetric stall. The stall entry and recovery procedure are discussed in detail in [21]. The stall autopilot is turned off when the original altitude is almost reacquired. Then, the aircraft is steered back to steady straight symmetric flight, which is retained for 120 s by use of an altitude hold and a roll attitude hold controller.

An overview of the simulated flight and the definition of the different phases contained therein is given in Table 2 and this is visualized in Figure 3. Phase 7 to phase 12 and their importance are discussed further in subsection II.E.

Table 2 Phases in the simulated flight data.

Phase	t_{begin}, s	t_{end}, s	Description
0	0	30	steady straight symmetric flight
1	30	50	$-\delta_a$ 3-2-1-1 (t_{input} = 40 s)
2	50	90	$-\delta_a$ 3-2-1-1 recovery
3	90	110	$-\delta_e$ 3-2-1-1 (t_{input} = 100 s)
4	110	150	$-\delta_e$ 3-2-1-1 recovery
5	150	170	$+\delta_r$ 3-2-1-1 (t_{input} = 160 s)
6	170	210	$+\delta_r$ 3-2-1-1 recovery
7	210	330	steady straight symmetric flight
8	330	369	stall entry
9	369	382	stall (buffet activated)
10	382	440	stall recovery
11	440	500	return to trimmed flight
12	500	560	steady straight symmetric flight

Three different stall types were simulated to mimic the real flight data. These three input types in the simulation data are shown in Figure 4. The first stall type has no distinct inputs and is the standard stall as flown by the stall autopilot. This is the baseline to which the other types can be compared. The second type has a 3-2-1-1 input on both the elevator and the aileron. To achieve the desired high angles of attack, a constant δ_e input of -0.11 rad was set at the start of the stall, and to it was applied a 0.02 rad 3-2-1-1 input. For the δ_a, a 0.04 rad 3-2-1-1 input was applied to the trim deflection. The last type is the wiggle input, also on the elevator and aileron. A MATLAB `sawtooth()`-signal was used to manually tweak the inputs to imitate the inputs from the test flight data as closely as possible. Important to note is the different "frequency" for the δ_a and δ_e inputs.

Last, a random noise signal with the same standard deviation as in the unscented Kalman filter noise and measurements covariance matrices in the flight path reconstruction is added to all states and measurements. Also, a known bias is added to the input signals (linear accelerations and angular velocities). In reality, the α and β are measured by the air data boom installed on the nose of the aircraft. Therefore, the α and β signals are passed through the formula for the air data boom corrections [31], such that the final signals behave as if they were measured by the vanes on the air data boom. The simulation run is performed 30 times to acquire 30 differently seeded realizations in order to reach the central limit theorem's minimum sample size.

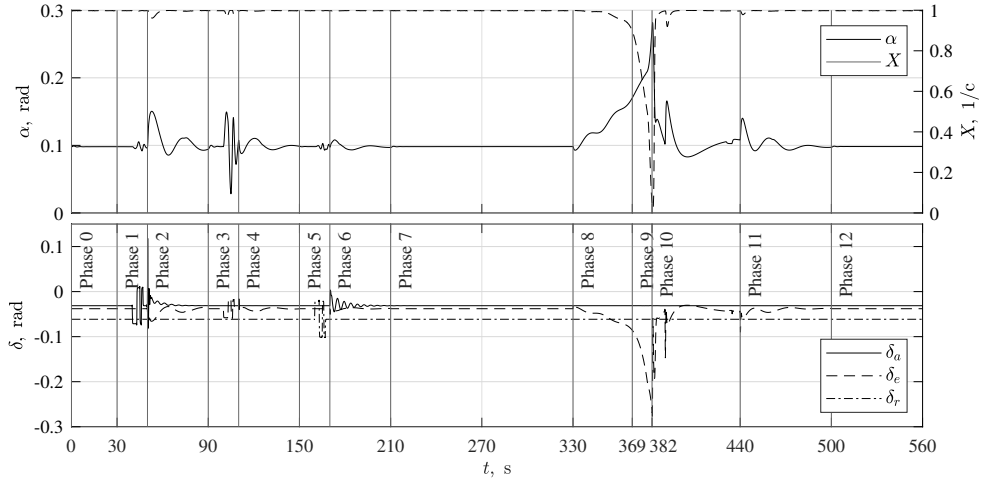

Fig. 3 Overview of the phases from Table 2 in the simulated data.

D. Flight Path Reconstruction

The flight path reconstruction is performed to filter out noise and bias from the measured aircraft states and measurements such that reliable data is available for the parameter estimation. It is needed for both the simulation data as well as the flight test data. Flight path reconstruction is performed by use of the unscented Kalman filter (UKF) [32, 33]. It has been shown that the UKF achieves higher reliability in estimation of the states of nonlinear systems when compared to the extended Kalman filter, although at the cost of higher computational cost [34–36]. As the Kalman filter procedure only has to be performed once per dataset of a flight, the higher expected reliability is chosen over the computational cost, as in earlier TU Delft stall modeling research [17–19]. It is shown in [36] that the UKF is also usable when applying sensor fusion techniques, which is also required in this research. The kinematic and measurement model applied in the UKF are taken directly from [19].

Then, using the reconstructed states, the longitudinal force coefficient C_X and vertical force coefficient C_Z in the aircraft reference frame are calculated via:

$$C_X = \frac{mA_x}{\frac{1}{2}\rho V_{TAS}^2 S} \tag{4}$$

$$C_Z = \frac{mA_z}{\frac{1}{2}\rho V_{TAS}^2 S} \tag{5}$$

In which m is the aircraft mass calculated from the available mass model. A_x and A_z are the reconstructed accelerations of the aircraft center of gravity in longitudinal and vertical direction, respectively. The calculated air density at the reconstructed altitude is denoted by ρ and the reconstructed true airspeed by V_{TAS}. S is the aircraft wing surface. Thereafter, the lift coefficient C_L is calculated via:

$$C_L = C_X \sin\alpha - C_Z \cos\alpha \tag{6}$$

This C_L can then be used in the nonlinear and linear parameter estimation, in combination with the reconstructed states for the angle-of-attack α and its derivative in time $\dot{\alpha}$ as regressors x. However, in the case of the simulated data, slicing and partitioning takes place first.

E. Slicing and Partitioning Data

With data slicing, the simulation data is partitioned in time into partitions of different widths. For this, phase 7 to phase 12 from Table 2 are of importance as they are the basis of the different slicing types considered in this paper. Phase 7 is the start of the steady straight symmetric flight foregoing the stall. Phase 8 is the start of the deceleration into the stall. Phase 9 is the stall, whose entry is defined by the beginning of the stall buffet. The start of phase 10, the stall

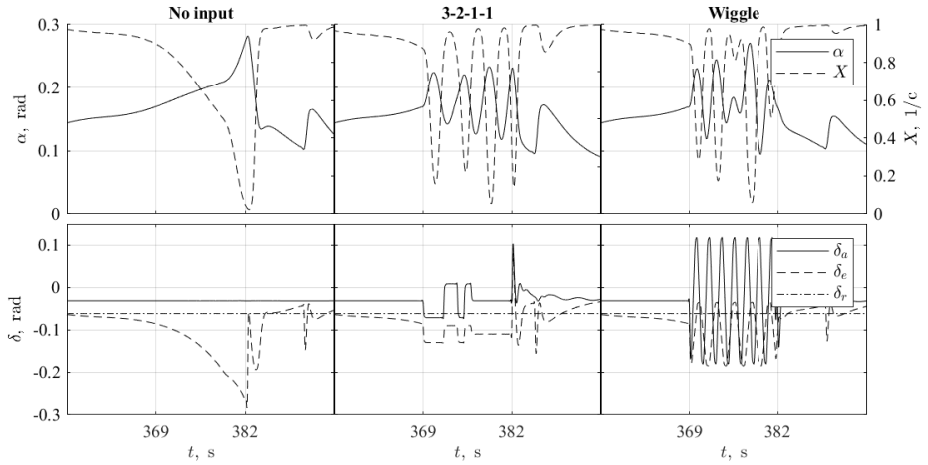

Fig. 4 Overview of the three simulated input types within the stall (phase 9), showing the angle of attack α and flow separation X, as well as the inputs δ_a, δ_e and δ_r. Note the non-zero aileron and rudder deflections in trimmed flight, caused by the non-zero C_{ℓ_0} and C_{n_0} coefficients as found by [19] present in the simulation model.

recovery, is when the angle of attack has reached its maximum value and airspeed begins to increase again. The stall buffet may still be active at that point. The recovery ends and phase 11 starts when the original altitude is reacquired. Phase 11 and 12 together contain 120 s of (quasi) steady straight symmetric flight. All phases 7 ti 12 together contain 350 s of data.

These 350 s of data are divided into 350 "slices", each containing 1 s of data. Combinations of multiple slices are called a "partition", which in this paper are constructed from the slices in three different manners. These three manners are called the "slicing types". In a later step, the parameters can be estimated for every partition which is the core of the parameter estimate behaviour analysis. Whenever from this analysis an optimal pre-stall and post-stall partition are chosen with a starting time and end time expressed in a corresponding slice number n_{slice}, they comprise a "window".

The three different slicing types considered in this research are indicated in Figure 5. This figure indicates the direction and numbering of the slices n_{slice} and the respective times t they are located at. The vertical lines in the figure indicated by "Window Ref. [18, 19]" correspond approximately to the data window used in [18, 19] to perform the estimation procedure of each stall. In these research efforts, the cutoff points were usually arbitrarily chosen to be around the beginning of the stall entry and somewhere during stall recovery. It is worthwhile to investigate later if this may have influenced the estimated stall parameters, which is discussed in section III.

Slicing type 1 contains partitions that start with the last second of data in the stall and that increase in size towards the pre-stall phases. Slicing type 2 contains partitions that start with the first second of data in the stall and that increase in size towards the post-stall phases. For slice types 1 and 2, the first partition contains 1 s of data and the last 172 s and 191 s, respectively. The first partition of slicing type 3 contains all slices that make up the stall and the partitions increase in size towards both sides of the stall (each increment adds 2 slices of 1 s). For slice type 3, the first partition contains 13 s of data and the last 331 s.

In the slice-based modeling method, the parameter estimate behaviour analysis is not performed for the real flight test data. This has no added value as there is no actual parameter value that the estimates can be compared with, in contrast to the simulation data where the values in the model are set to a known value. However, as part of the proof of concept, the parameter estimate behaviour of the real flight data is discussed in the results of section III. It is discussed to what extent the simulation data is representative of the real flight test data. In the case of the flight test data, the phases as in Table 2 can also be identified by closely examining the behaviour of the aircraft in time and assigning parts around the stall to a certain stall phase. Note that some phases before stall entry and after stall recovery may be of variable length or may not be present at all.

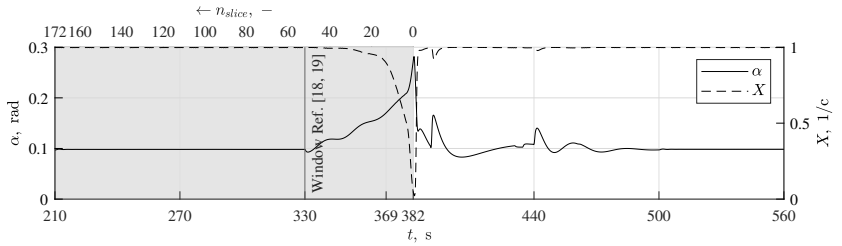

(a) Slicing type 1, pre-stall.

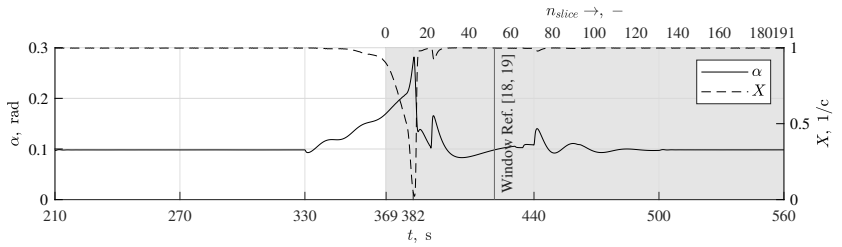

(b) Slicing type 2, post-stall.

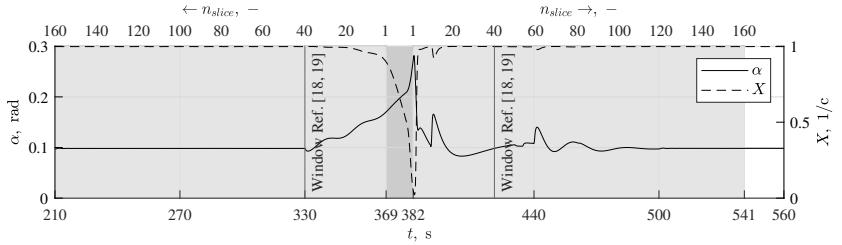

(c) Slicing type 3, pre-stall and post-stall.

Fig. 5 Overview of the three slicing types.

F. Parameter Estimate Behaviour Analysis

The parameter estimate behaviour analysis of the simulation data consists of two main parts. The first part is the parameter estimation for all partitions of the three slicing types. The second part is visualizing the parameter estimate behaviour by use of metrics $\tilde{\hat{\theta}}$ and Q describing the median and distribution of the parameter estimates of the 30 realizations and by calculating the Fisher information M.

1. Nonlinear and Linear Estimation

The parameter estimation procedure is based on that presented in [19] and consists of a nonlinear estimation of the stall parameters, followed by a linear estimation of the stability and control derivatives.

The nonlinear estimation is performed by use of the `fmincon()` function of MATLAB. The parameter estimates are found by minimizing the objective function $J(\vec{\theta}, x)$, which is the mean squared error MSE of the lift coefficient. Mathematically given as:

$$\hat{\vec{\theta}} = \arg\min_{\vec{\theta}} J(\vec{\theta}, x), \quad \text{with } J(\vec{\theta}, x) = \frac{1}{n}\left(\hat{C}_L(\vec{\theta}, x) - C_L\right)^T \left(\hat{C}_L(\vec{\theta}, x) - C_L\right) \tag{7}$$

With x the nonlinear regressors α and $\dot{\alpha}$ and with C_L the lift coefficient, all calculated from the flight path reconstruction. The total number of data points is denoted by n. The parameter vector $\vec{\theta}$ is defined as:

$$\vec{\theta} = \begin{bmatrix} a_1 & \alpha^* & \tau_1 & \tau_2 & C_{L_0} & C_{L_\alpha} & C_{L_{\alpha^2}} \end{bmatrix}^T \tag{8}$$

Last, $\hat{C}_L(\vec{\theta}, x)$ is the model output for the lift coefficient, calculated with the parameter estimates currently regarded in the optimization routine. It is calculated by numerically solving Eq. (2) with the currently regarded parameter estimates, resulting in X. This is then used in Eq. (3) to calculate $\hat{C}_L$.

The nonlinear optimization routine of `fmincon()` makes use of the gradient $\frac{\partial J(\vec{\theta},x)}{\partial \vec{\theta}}$ of the cost function surface $J(\vec{\theta},x)$. Calculating this is not trivial, as is discussed in [19]. This calculation is related to that of the Fisher information matrix, as discussed in Appendix A.

The optimization is performed for 500 initial conditions, with each initial condition consisting of seven parameter estimates randomly generated from a uniform distribution with upper and lower bounds as given in Table 1. The global optimum is regarded as the median of all optima found that come within 5 % of the lowest found final cost function value. The stall parameters following from the nonlinear optimization are set constant for the following linear estimation.

The linear estimation is a straightforward ordinary least squares estimation with $\left[\left(\frac{1+\sqrt{X}}{2}\right)^2 \alpha\right]$ regarded as an extra regressor. It is calculated by numerically solving Eq. (2) with the found nonlinear parameter estimates. From the linear estimation the final estimates of C_{L_0}, C_{L_α} and $C_{L_{\alpha^2}}$ are found.

2. Parameter Estimate Behaviour: Optima Distribution Metrics

The optima distribution metrics can be calculated for any individual parameter, or they can be compared by their normalized metrics.

The individual parameter behaviour of any set of realizations can be visualised in boxplots. This shows the median $\tilde{\hat{\theta}}$, the inter-quartile range $Q_{2,3}$ (consisting of quartiles 2 and 3) and the full range of optima excluding outliers Q_{1-4} (consisting of all quartiles 1 to 4). Outliers are defined as being more than 1.5 times the inter-quartile range away from the inter-quartile range. These three metrics are calculated for every partition of the three slicing types, such that a boxplot can be drawn at every slice number n_{slice}. This individual behaviour can be analyzed for both the simulation data and the test flight data.

In order to be able to compare the behaviour of the parameter estimates to each other, these metrics can also be normalised with respect to the actual parameter value. This can only be done for the simulated flight data where the actual value is known. The normalised bias of the parameter estimates can be calculated by:

$$\frac{\tilde{\hat{\theta}}_i - \theta_i}{\theta_i} \times 100\% \tag{9}$$

In which $\tilde{\hat{\theta}}_i$ is the median of the sample of all estimated parameters of the 30 realizations and θ_i is the actual value setting in the simulation from Table 1.

Also the behaviour of the mean squared error MSE can be plotted, in the same manner as for the parameters. The median of the MSE of all realizations is denoted by $\tilde{MSE}$. The same quartile ranges $Q_{2,3}$ and Q_{1-4} exist for the MSE.

3. Parameter Estimate Behaviour: Fisher Information

Information content in a signal can be quantified via a description of the sensitivity of a model's output y to changes in a parameter θ_i. This is given by the (partial) derivative $\frac{\partial y}{\partial \theta}$. For multiple-input-multiple-output models with N_p number of parameters gathered in a parameter vector $\vec{\theta}$, and N_o the number of system outputs, the information content is given by the $N_p \times N_p$ Fisher information matrix M, defined as [23]:

$$M = \sum_{k=1}^{N} S(k)^T R^{-1} S(k) \tag{10}$$

With $k = 1, 2, \ldots, N$ the discrete sample number of the data signal. R is a $N_o \times N_o$ diagonal matrix of which the elements introduce a scaling to the output sensitivities according to the measurement noise related to that output, i.e. the noise covariance. For this research, R is set to 1 as there is only one output. The output sensitivities themselves are captured in the $N_o \times N_p$ output sensitivity matrix $S(k)$, which is given by [23]:

$$S(k) = \begin{bmatrix} \frac{\partial y_1(k)}{\partial \theta_1} & \frac{\partial y_1(k)}{\partial \theta_2} & \cdots & \frac{\partial y_1(k)}{\partial \theta_{N_p}} \\ \frac{\partial y_2(k)}{\partial \theta_1} & \frac{\partial y_2(k)}{\partial \theta_2} & \cdots & \frac{\partial y_2(k)}{\partial \theta_{N_p}} \\ \vdots & \vdots & \ddots & \vdots \\ \frac{\partial y_{N_o}(k)}{\partial \theta_1} & \frac{\partial y_{N_o}(k)}{\partial \theta_2} & \cdots & \frac{\partial y_{N_o}(k)}{\partial \theta_{N_p}} \end{bmatrix} \tag{11}$$

The sensitivity matrix $S(k)$ can usually be calculated analytically, derived from the dynamic equations of the to-be-estimated model [23]. E.g. for linear systems with one output, the matrix $S(k)$ is equal to the kth row of the regression matrix of this system.

The inverse of the Fisher information M is the dispersion matrix D. The diagonal entries of the matrix D are the theoretical lower limit for the estimated covariances of the parameters, i.e. the Cramér-Rao Lower Bound:

$$D = M^{-1} \leq \mathrm{Cov}[\vec{\theta}] \tag{12}$$

And thus, the Cramér-Rao Lower Bound for the parameter standard deviations σ_{θ_i} are the square-root of the diagonal elements of D, i.e.:

$$\sigma_{\theta_i} = \sqrt{D_{ij}}, \quad \text{with } i = j = 1, 2, \ldots, N_p \tag{13}$$

An advantage of the use of the Fisher Information when analyzing signals is that it is related to the *theoretical* lower limit of the parameter covariances. Therefore, it is unrelated to the algorithm used in the actual estimation of the parameters. It purely describes the added value of the signal to estimate a certain parameter.

The Fisher information is parametric, which means that it differs for different given model structures. The derivation of the analytical definition of the Fisher information for the model given by Eq. (3) is described in Appendix A. This definition is used to calculate the information content of the C_L signal from flight path reconstruction.

More interesting than the total Fisher information in a signal is the derivative of the Fisher information in time. This can say something about the value of a certain part of a data signal to a certain parameter. This is compared directly to the parameter estimates' median $\tilde{\hat{\theta}}$ and distribution shape $Q_{2,3}$ and Q_{1-4}. For every 1 s slice, the Fisher information can be calculated for a specific parameter via:

$$\frac{\Delta M_{\theta_i}}{\Delta n_{slice}} = \sum_{k=k_{n_{slice_{begin}}}}^{k_{n_{slice_{end}}}} S_{i_{\theta_i} j_{\theta_i}}(k)^T R^{-1} S_{i_{\theta_i} j_{\theta_i}}(k), \quad \text{with } i_{\theta_i} = j_{\theta_i} = 1, 2, \ldots, 7 \tag{14}$$

As the total Fisher information is a sum via Eq. (10), the Fisher information of one slice $\frac{\Delta M_{\theta_i}}{\Delta n_{slice}}$ is in fact the derivative per second. In this equation, $k_{n_{slice_{begin}}}$ and $k_{n_{slice_{end}}}$ are the indices of the beginning and ending of a slice and i_{θ_i} and j_{θ_i} are the row and column number, respectively, for parameter θ_i in the matrix $S(k)$.

G. Slice-based Parameter Estimation

The final goal of this paper is to prove that using different time windows of data for estimation of a certain parameter can increase model accuracy. This concept is applied in the slice-based parameter estimation step.

The input to the slice-based parameter estimation is an optimal time window, found by analyzing the parameter estimate behaviour in the simulation data as explained above. The begin and end of this time window are identified by the optimal pre-stall and post-stall slice number $n_{slice_{opt}}$, for every individual parameter, for every of the three stall input types. This $n_{slice_{opt}}$ is found manually and is the point in time where the median of the parameter optima of the 30 realizations is equal to the actual parameter value used in the simulation.How this works in practice is explained in the results of section III.

The actual parameter estimation consists of a new manner of estimating the parameters on the real flight test data. The realizations of the flight test data are randomly divided into fifteen training realizations and seven validation realizations. This is from a ratio of roughly 2-to-1 within each stall input type (i.e. 2-to-1 for no input, 9-to-4 for 3-2-1-1, 4-to-2 for wiggle). First, the nonlinear estimation is performed on the optimal window for the first parameter, a_1. This value is then saved. Then, the optimal window for α^* is chosen and the estimation is performed again. During this, the parameter a_1 can be varied again to give full freedom to the nonlinear optimization algorithm. This is then also performed for τ_1, τ_2 and the stability and control derivatives. At this point, X is calculated for the full data such that it can be used as a regressor in the linear estimation, in which the final values for C_{L_0}, C_{L_α} and $C_{L_{\alpha^2}}$ are calculated. Apart from using optimal windows, the optimization routine is the same as explained for the parameter estimate behaviour analysis in subsubsection II.F.1.

To compare the increase in accuracy of the slice-based modeling method to the normal modeling method, both procedures as depicted in Figure 1 and Figure 2 are applied to the flight test training data. This results in two different final parameter estimate vectors $\hat{\tilde{\theta}}$. For both, the model outputs $\hat{y}_{C_L}$ are calculated based on the reconstructed states from the validation flight test data and these are compared to the measured y_{C_L} by means of the MSE and $RRMS$ metrics.

III. Results

A. Parameter Estimate Behaviour Analysis

The parameter estimate behaviour analysis is performed by use of the three introduced metrics. The first are the medians $\tilde{\hat{\theta}}$ and $\tilde{MSE}$ of the parameter optima and MSE, respectively. Second is the associated distribution of these optima and MSE, which can be described by visualizing the inter-quartile range $Q_{2,3}$ (quartiles 2 and 3) and the full range of optima excluding outliers Q_{1-4} (all quartiles 1 to 4). Last is the derivative of the Fisher information per slice $\frac{\Delta M}{\Delta n_{slice}}$.

These metrics can be visualized in a comparative and individual manner. Both types appear below. These types of graphs were constructed for all stall input types, slicing types and different parameters. For conciseness, only a selected number of these graphs are shown. They represent parameter estimate behavioural characteristics that are present throughout all these different graphs.

Important to note is that the plots for α and X when regarding simulated data are those of realization 1. With the naked eye, these are not distinguishable between the realizations. For real data, α for all different realizations is shown and for X and $\frac{\Delta M}{\Delta n_{slice}}$ the average of all realizations is depicted. Note that for flight test data this is purely indicative as the actual X and $\frac{\Delta M}{\Delta n_{slice}}$ are not known, due to the actual parameter values being unknown. Therefore, they are calculated with the a priori known values in Table 1.

For slicing type 1, the steady, straight, symmetric flight part before and after the stall was 120 s long. No significant findings could be made in the first and last 60 s of this data. To decrease computational time for slicing type 2 and 3, these first and last 60 s of data were removed from the analysis. This means that for these slicing types the graphs are shorter than for slicing type 1.

1. Behaviour of the Mean Squared Error and Interaction between Parameter Estimates

In Figure 6 the behaviour of the MSE is shown for a wiggle input in flight test data. Throughout the stall, the MSE increases and thereafter it decreases. This behaviour exists in all stall types, both in simulation data as in flight test data. The only difference between the simulated data and the flight test data is that in the simulated data the distribution of MSEs is very narrow.

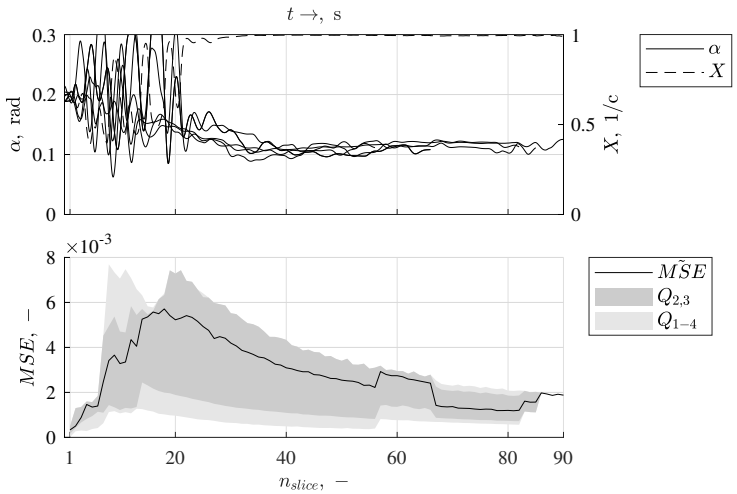

Fig. 6 Behaviour of the MSE. Flight test data, wiggle input, post-stall. The upper plot shows the angle of attack α and average flow separation point X. In the lower plot, $\tilde{MSE}$ is the median of all six realizations, $Q_{2,3}$ is the inter-quartile range, Q_{1-4} is the full range excluding outliers. As the plots show the post-stall, the time runs same to the slicing numbers, i.e. from left to right.

The normalized biases of the parameter estimates in Figure 7 are a clear example of the suspected cause of the increase and then decrease in the MSE. The interaction between the X-parameter estimates and the normal stability and control derivatives can be observed. This interaction is present in all different stall types. Changes in the X-parameter

estimates are present only immediately before and after the stall. All X-parameters have moved to their final estimate before $n_{slice} = 10$. This is different for the stability and control derivatives. They differ significantly from their actual values right before and after the stall, with the estimates of C_{L_0} and $C_{L_{\alpha^2}}$ being even more than 100 % lower than their actual values. Erratic changes in all stability and control derivative estimates can be observed as changes occur in the X-parameters close to the stall. Only after $n_{slice} = 10$ is it that the stability and control derivatives start to move steadily to their final values, which are all within 50 % of the actual values.

The described behaviour of the parameter estimates can explain the changes in MSE in Figure 6. In the stall, unsteady flight conditions exist and the X parameter estimates are adjusted by the optimization routine to keep the rise in MSE as small as possible. The changes in X parameter estimates are accommodated by changes in the stability and control derivatives, evident by the large differences C_{L_0} and $C_{L_{\alpha^2}}$ attain from their actual value before $n_{slice} = 10$. After the stall this effect occurs too, but with the parameters switched. Here, changes of the X-parameters accommodate the changes in stability and control parameter estimates. As the stability and control derivatives get close to their actual values, the model becomes better at describing the steady flight conditions that become a larger part of each partition. This causes the decrease in MSE after the stall. An adverse effect of this is that the model becomes worse at modeling the aircraft in the stall. This is evident by the large differences of the estimates of τ_1 and τ_2 to their actual value in Figure 7 after $n_{slice} = 5$. These differences become more than 200 %.

It is for this reason that many of the X parameter optimal slice numbers in Table 3 contain no more than 5 s of data before or after the stall. On the contrary, for the stability and control derivatives it is observed that the more data is used the better their estimates become.

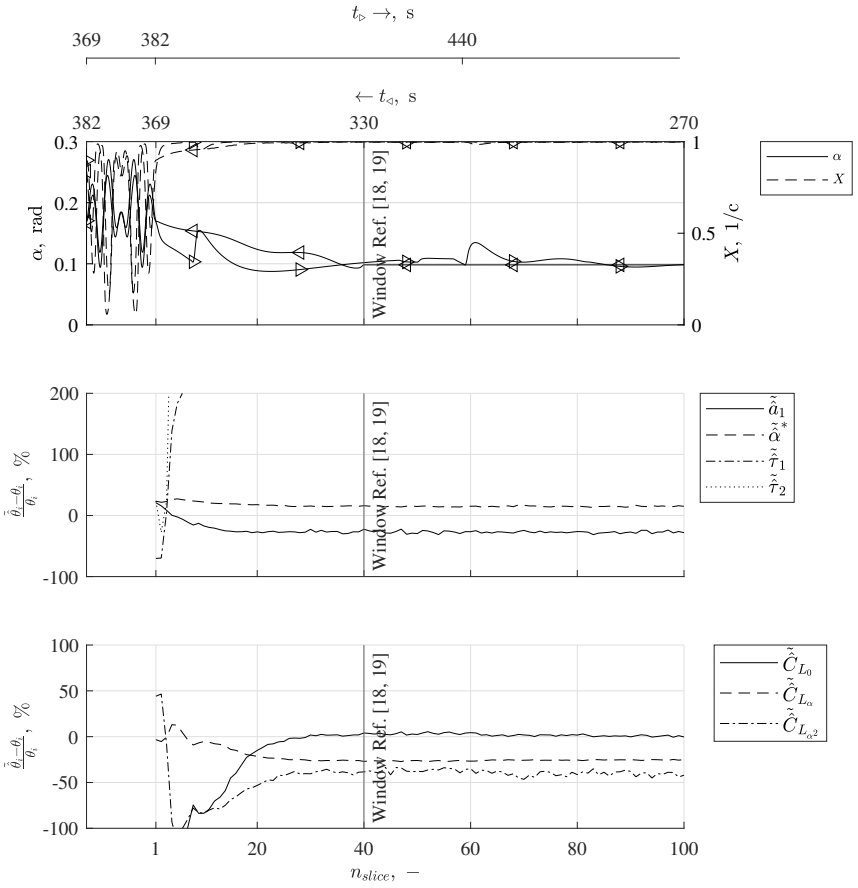

Fig. 7 Compared behaviour of all parameters. Simulation data, wiggle input, both pre-stall and post-stall (slicing type 3). The upper plot shows the angle of attack α and the flow separation point X. In the two lower plots, each line is the normalized bias $\frac{\tilde{\tilde{\theta}}_i - \theta_i}{\theta_i}$ for each parameter. The left triangle $\triangleleft$ indicates the pre-stall data, where times runs from right to left and the right triangle $\triangleright$ indicates the post-stall data where times runs from left to right. Each slice n_{slice} contains 1 s of the pre-stall and 1 s of the post-stall data.

2. Behaviour of α^* in Different Stall Input Types

The behaviour of a parameter estimate is strongly influenced by the type of input given during the stall. In Figure 8 an example of this is shown, in this case for the parameter α^*. The subfigures show the parameter estimate behaviour for simulation data with a no-input stall and a stall with 3-2-1-1 inputs.

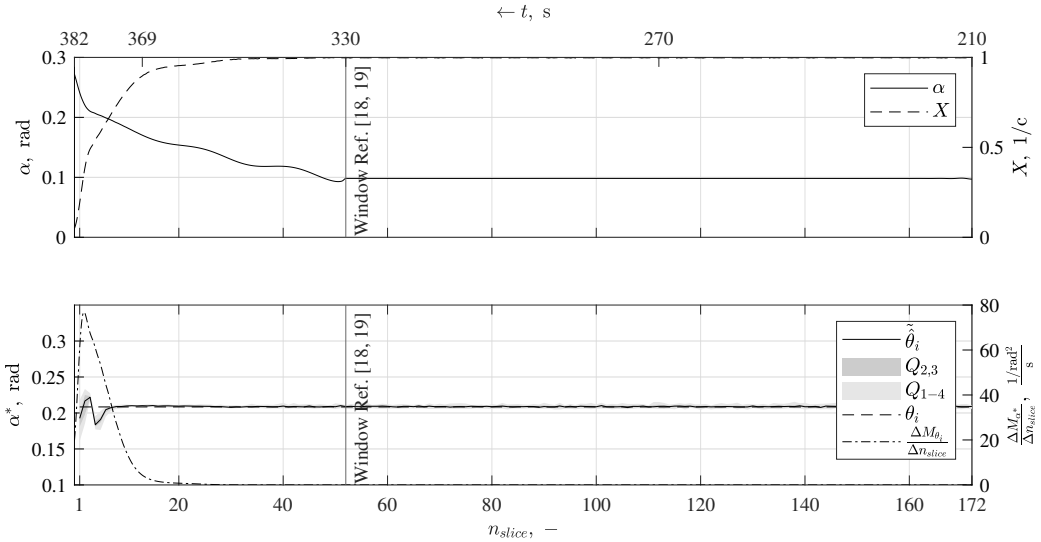

(a) Simulation data, no input, pre-stall.

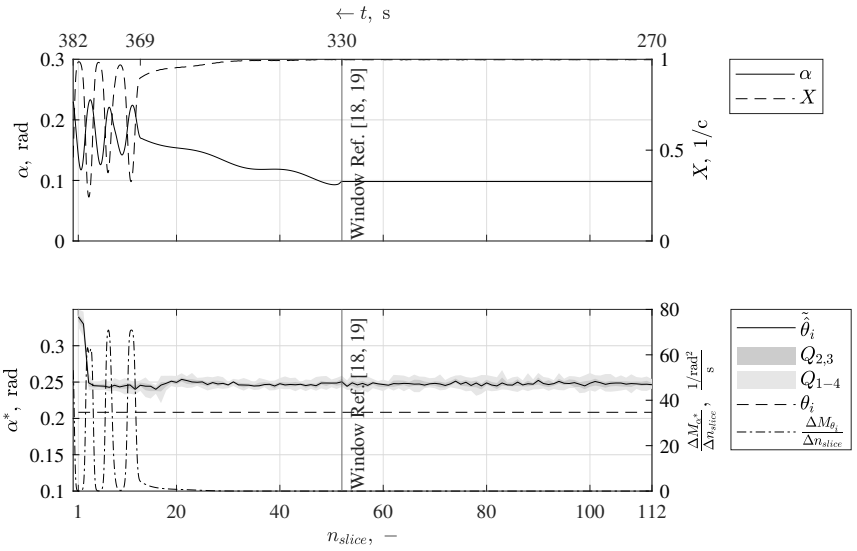

(b) Simulation data, 3-2-1-1 input, pre-stall.

Fig. 8 Individual behaviour of parameter α^*. The upper plot of each subfigure shows the angle of attack α and flow separation point X. In the lower plots, $\hat{\tilde{\theta}}_i$ is the median of the parameter optima of all 30 realizations, $Q_{2,3}$ is the inter-quartile range, Q_{1-4} is the full range excluding outliers. θ_i is the actual parameter value in the simulation and $\frac{\Delta M_{\theta_i}}{\Delta n_{slice}}$ is the Fisher information derivative related to the parameter. As the plots show the pre-stall, the time runs opposite to the slicing numbers, i.e. from right to left.

Two main features can be observed. First, the 3-2-1-1 inputs induce a constant error in the estimate of the α^* parameter, where this error is near zero for the no-input stall. Second, the Fisher information related to α^* is higher for the no-input stall. These observations are affiliated. The 3-2-1-1 input causes a very sudden stall entry and subsequent periodic motion in the angle of attack, resulting in four separate peaks in the Fisher information. The no-input stall is

more gradual. Because of this, the total Fisher information is higher for the gradual stall, i.e. the area under the shown Fisher derivative is larger. This means that a no-input stall generates more information for the α^* parameter, which can in part explain the smaller error.

Why the Fisher information is higher for the no-input stall can physically be explained as follows. For this stall type, the angle of attack is slowly increased through the point where $X = 0.5$. This is also the point where the derivative of the Fisher information is highest. This is logical, as the parameter α^* dictates this point. It can therefore be estimated more accurately. For a stall where inputs are given resulting in a rapidly changing angle of attack, such as the 3-2-1-1 or wiggle, the angle of attack where $X = 0.5$ cannot be estimated accurately due to significant transient effects being present. Also, the amount of time in which the separation point is in the vicinity of 0.5 is only brief. For this reason, it was chosen that only the no-input stall is used for estimation of the α^* parameter, as indicated in Table 3.

3. Behaviour of τ_2 in Different Stall Input Types

Next to the α^* parameter, the τ_2 parameter is also sensitive to different input types. In Figure 9, the parameter estimate behaviour of τ_2 is shown for both the no-input stall and the stall with wiggle inputs in simulation data.

For the no-input stall, a strong tendency of the τ_2 estimate exists to go to the lower bound and only moves away from the bound after $n_{slice} = 80$. This tendency is also observed for the stall with the wiggle input, however the τ_2 estimate does not remain at the lower bound as long as for the no-input stall and attains its final value of roughly 0.3 s between $n_{slice} = 15$ and $n_{slice} = 25$. This "lower-bound tendency" is also present in the flight test data in varying severity, but may also not be present at all. This means that parameter estimate behaviour of simulation data shows resemblance with the flight test data, although sometimes they can also differ.

Analogous to the case of parameter α^*, the Fisher information related to parameter τ_2 can also explain the behaviour of the estimate of τ_2. For the no-input case, the Fisher information is zero everywhere, except for the stall recovery. This is also when the lower-bound tendency begins. All the information that is available for estimation of parameter τ_2 is thus concentrated in only a narrow timeframe of roughly $12 \leq n_{slice} \leq 14$. For the wiggle inputs, the Fisher information contains multiple peaks distributed over the timespan of the entire stall, summing to a higher total information content in the signal. Physically, this makes sense. Parameter τ_2 describes the hysteresis effect, which only occurs if large and quick changes in the angle of attack, and thus movement of the flow separation point, are present. In the no-input stall this is only the case during stall recovery, but the wiggle inputs induce more of these movements throughout the stall.

Nevertheless, in both cases it is clear that the τ_2 parameter estimate benefits from data that is only very close to the stall. Otherwise, it may be estimated to the lower bound as in the no-input case or it may be wrongly estimated as for the wiggle inputs after $n_{slice} = 15$. This confirms the importance of the research in this paper: simply slicing in the manner of [18, 19] would in both cases result in different parameter estimates than the actual parameter value. This is indicated by the vertical line in the graph, which is approximately the cutoff point for data in the research of [18, 19].

4. Behaviour of τ_1 in Simulation Data versus Flight Test Data

In the slice-based modeling method, parameter estimate behaviour that results from simulation data is used as a substitute for the expected, but unknown, parameter estimate behaviour resulting from flight test data. Therefore, the similarity of the parameter behaviour resulting from both data types must be compared. In Figure 10, the behaviour of the estimate τ_1 is shown, following from a stall with 3-2-1-1 inputs in both simulation data and flight test data.

From the simulation data it becomes clear that the τ_1 estimate also has the lower-bound tendency that was observed for τ_2, although in lesser extent. As soon as the Fisher information derivative shows has the first peak, the estimate moves to the lower bound. The lower-bound tendency in this case is interesting, as the actual parameter value of 0.2547 s is not near the lower bound. This may be the reason that the estimate of τ_1 moves away from this bound very suddenly around $n_{slice} = 18$, in contrary to τ_2 in Figure 9b where this movement is more gradual, in the range $15 \leq n_{slice} \leq 25$.

In the flight test data, the lower-bound tendency can also be observed. Until $n_{slice} = 8$, the estimate for τ_1 moves to the lower bound, before very suddenly moving to the upper bound after this. Thus, it seems that analyzing the parameter estimate behaviour of simulation data is representative of the parameter estimate behaviour that follows from the flight test data. However, for the test flight data, the distribution of the optima is significantly broader. The same is generally observed for all input and slicing types. Thus, parameter estimate behaviour is less predictable for test flight data than for simulation data, even though significant trends in the behaviour in flight test data can generally be predicted by use of simulation data.

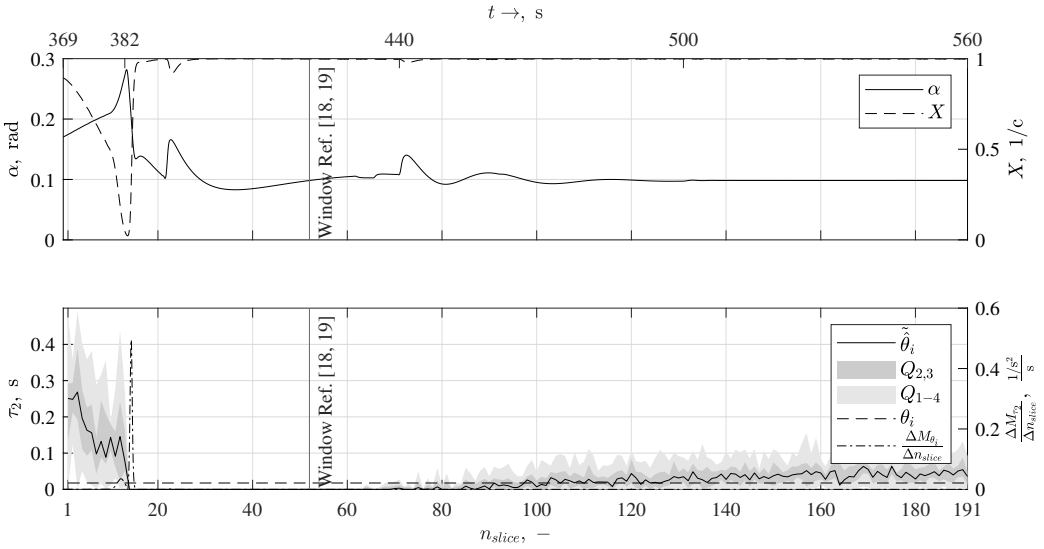

(a) Simulation data, no input, post-stall.

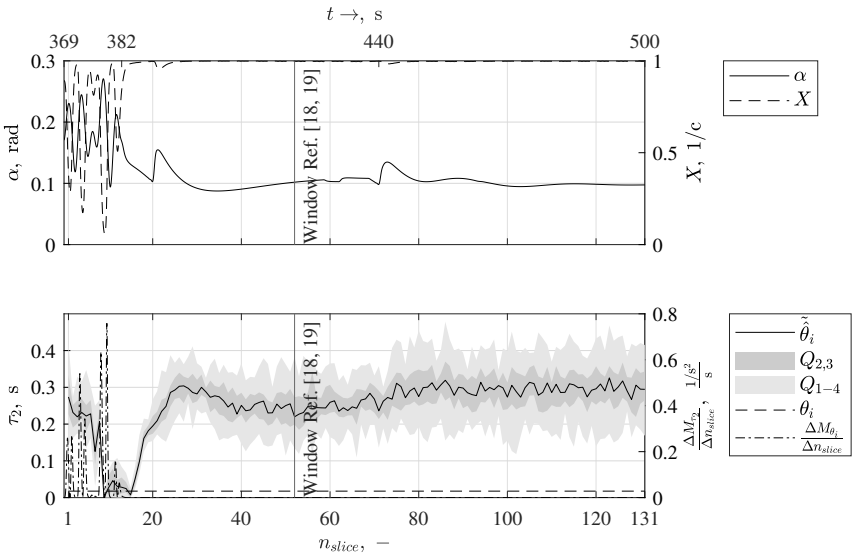

(b) Simulation data, wiggle input, post-stall.

Fig. 9 Individual behaviour of parameter τ_2. The upper plot of each subfigure shows the angle of attack α and flow separation point X. In the lower plots, $\hat{\tilde{\theta}}_i$ is the median of the parameter optima of all 30 realizations, $Q_{2,3}$ is the inter-quartile range, Q_{1-4} is the full range excluding outliers. θ_i is the actual parameter value in the simulation and $\frac{\Delta M_{\theta_i}}{\Delta n_{slice}}$ is the Fisher information derivative related to the parameter. As the plots show the post-stall, the time runs same to the slicing numbers, i.e. from left to right.

From the parameter estimate behaviour in the simulation data, another observation can be made. A moment in time where the distribution of optima is narrow, i.e. where the optima seem to be more certain, does not necessarily represent a timespan where that estimate is correct. In Figure 10a, the reliability is highest around $n_{slice} = 35$, but this does not deliver a correct estimate. However, in other cases this similarity does seem present, for example in Figure 9b in the range $8 \leq n_{slice} \leq 15$. The same contrary evidence can be found for multiple input and slicing types and also other parameters than τ_1 and τ_2.

Finally, Figure 10a again shows the important finding also made earlier for τ_2: just choosing all available data, as in the research of [18, 19], can result in incorrect estimates for a certain parameter. In this case made evident for parameter τ_1. Using the window of [18, 19] would result in an estimate value of roughly 0.8 s, instead of the correct 0.2547 s.

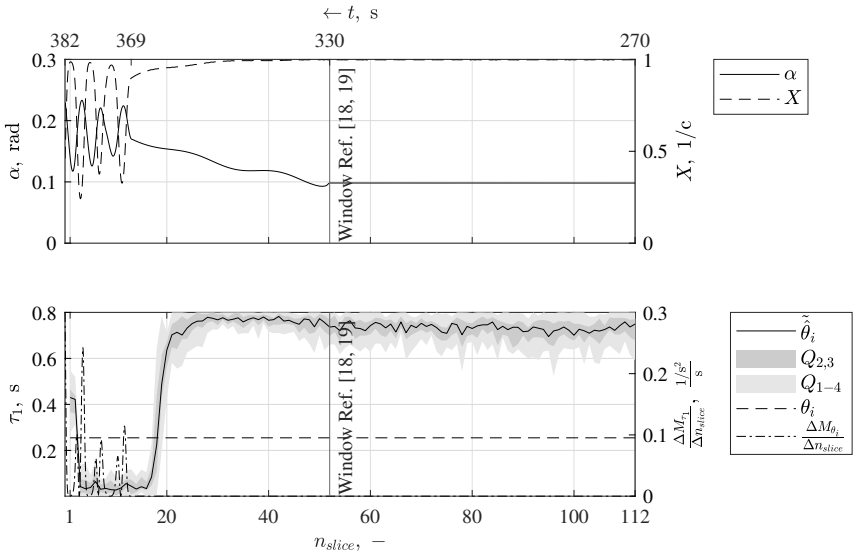

(a) Simulation data, 3-2-1-1 input, pre-stall.

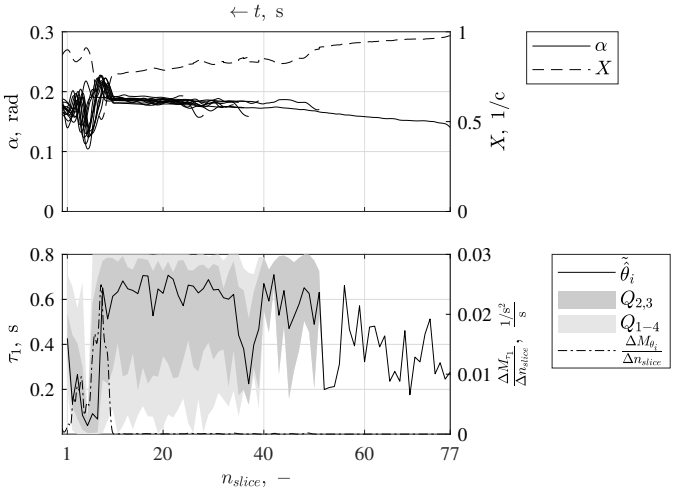

(b) Flight test data, 3-2-1-1 input, pre-stall.

Fig. 10 Individual behaviour of parameter τ_1. The upper plot of each subfigure shows the angle of attack α and flow separation point X (X is the average of all realizations for flight test data). In the lower plots, $\tilde{\hat{\theta}}_i$ is the median of the parameter optima of all realizations, $Q_{2,3}$ is the inter-quartile range, Q_{1-4} is the full range excluding outliers. θ_i is the actual parameter value in the simulation and $\frac{\Delta M_{\theta_i}}{\Delta n_{slice}}$ is the Fisher information derivative related to the parameter ($\frac{\Delta M_{\theta_i}}{\Delta n_{slice}}$ is the average of all realizations for flight test data). As the plots shows the pre-stall, the time runs opposite to the slicing numbers, i.e. from right to left.

B. Slice-based Estimation Procedure

The slice-based estimation procedure is based on performing the parameter estimation on an optimal time window for each parameter. In the parameter estimate behaviour analysis, the pre-stall and post-stall slice number $n_{slice_{opt}}$ for each optimal time window is chosen manually. This is done by comparing the parameter estimates with the actual parameter value in the simulation. The optimal slice number is chosen as the point where the parameter estimate and the actual parameter value are equal, also taking into account any behavioural features that have been observed as discussed in the foregoing subsection III.A. The selected optimal slice numbers $n_{slice_{opt}}$ are presented in Table 3. An entry with "n/a" means not applicable, because data from that stall type is not used for estimation of that parameter. E.g. the

parameter estimate of α^* is only based on training data from the flight test data where no additional inputs were given by the pilots. When an "all" is indicated for a parameter, it means that for that stall type all available data should be used in the estimation.

Important to note is that the values in Table 3 are the numbers n_{slice} associated with the slicing types 1 and 2. However, to select the window of the flight test data used in the slice-based parameter estimation, it is easier to convert the slice numbers to time in seconds before stall entry and after stall recovery, respectively. E.g. for parameter a_1, the no input, pre-stall optimal slice number $n_{slice_{opt}} = 30$. This means that the partition for the training flight test data is begun at $30 - 13 = 17$ s before the stall, as the stall in the simulation data is 13 s long. This time is indicated in parentheses in Table 3.

Table 3 Optimal slicing numbers $n_{slice_{opt}}$ as found for the simulated stall runs. The depicted slice number for the pre-stall is the slice number corresponding to slicing type 1 and the slice number for the post-stall is the slice number corresponding to slicing type 2. The corresponding time before stall entry (in pre-stall columns) and after stall recovery (in post-stall columns) used to slice the training flight test data is indicated in parentheses.

	$n_{slice_{opt}}$, −					
	No input		3-2-1-1		Wiggle	
θ_i	Pre	Post	Pre	Post	Pre	Post
a_1, −	30 (17 s)	all	13 (0 s)	70 (57 s)	19 (6 s)	20 (7 s)
α^*, rad	all	all	n/a	n/a	n/a	n/a
τ_1, s	30 (17 s)	17 (4 s)	18 (5 s)	13 (0 s)	16 (3 s)	16 (3 s)
τ_2, s	30 (17 s)	14 (1 s)	15 (2 s)	14 (1 s)	18 (5 s)	14 (1 s)
$\in \{C_{L_0}, C_{L_\alpha}, C_{L_{\alpha^2}}\}$, −	all	all	all	all	all	all

C. Accuracy of the Slice-based Modeling Method

To evaluate the increase in accuracy of the slice-based modeling method as depicted in Figure 2 it is compared to the normal modeling method as depicted in Figure 1 (excluding model structure selection). Both methods were applied to the same flight test data set for direct comparison. The normal modeling method is applied to the training flight test data by simply performing the full estimation on the entire realization. The slice-based modeling method uses the selected optimal time window from Table 3 for each parameter. The resulting parameter estimates for both methods are given in Table 4.

Table 4 Parameter estimate comparison of the normal modeling method and slice-based modeling method applied to flight test data.

θ_i	Normal modeling method	Slice-based modeling method
a_1, −	31.8630	34.1856
α^*, rad	0.2289	0.2202
τ_1, s	0.3541	0.4595
τ_2, s	0.1297	0.2182
C_{L_0}, −	0.1944	0.2065
C_{L_α}, −	4.5172	4.4192
$C_{L_{\alpha^2}}$, −	5.3935	5.1026

All parameters except τ_1 and τ_2 are roughly equal to each other, which are both significantly higher with the slice-based modeling method than with the normal modeling method. This is expected, as for the parameter estimate behaviour of τ_1 and τ_2 in subsection III.A it was found that specifically these are most inclined to change when using data outside of the stall region. This incline was also found for a_1, however less severe, also resulting is a slightly

different estimate in Table 4. For the other parameters, the parameters only slightly differ: α^* can in both cases be estimated accurately and for C_{L_0}, C_{L_α} and $C_{L_{\alpha^2}}$ the same amount of data is used.

To investigate the effect that these differences in parameter estimates have on model accuracy, the parameter estimates from both methods are applied in Eq. (3) to calculate output y_{C_L} for seven validation data sets. Table 5 shows the MSE and $RRMS$ values for both methods for the seven validation data sets. The MSE and $RRMS$ are in the same order of magnitude for both methods, but differences are present nonetheless. In four of the seven validation cases, the new method achieves better accuracy in the range of roughly $\Delta MSE = -10$ % to $\Delta MSE = -35$ %. However, in three cases a worse accuracy is achieved. On average the new method shows an increase in performance with $\Delta MSE = -6.24$ %.

Table 5 MSE and RRMS values for the validation datasets.

		Normal modeling method		Slice-based modeling method		
Input	Realization	MSE, –	$RRMS$, %	MSE, –	$RRMS$, %	ΔMSE, %
No input	3	$9.4366 \cdot 10^{-4}$	3.8914	$6.0021 \cdot 10^{-4}$	3.1035	−36.4
3-2-1-1	1	$1.4391 \cdot 10^{-4}$	1.9242	$1.9270 \cdot 10^{-4}$	2.2266	+33.9
3-2-1-1	2	$1.4938 \cdot 10^{-4}$	1.9654	$3.2383 \cdot 10^{-4}$	2.8937	+116
3-2-1-1	7	$3.1524 \cdot 10^{-4}$	3.1063	$2.8571 \cdot 10^{-4}$	2.9572	−9.37
3-2-1-1	10	$7.0719 \cdot 10^{-4}$	3.6531	$6.0736 \cdot 10^{-4}$	3.3854	−14.1
Wiggle	1	$8.2055 \cdot 10^{-4}$	4.1256	$5.2208 \cdot 10^{-4}$	2.4903	−36.4
Wiggle	6	$2.2765 \cdot 10^{-3}$	5.3092	$2.4903 \cdot 10^{-3}$	5.5528	+9.39
Mean		$7.6522 \cdot 10^{-4}$	3.4250	$7.1746 \cdot 10^{-4}$	3.2299	−6.24

The outputs of the models estimated with the normal modeling method and the slice-based modeling method can also be compared visually. In Figure 11a, for each stall input type the validation case with the best increase of the slice-based method relative to the normal method is shown. It shows both the model outputs $\hat{y}_{C_L}$ and the validation measurement y_{C_L}. In the figure, two main improvements with the slice-based modeling method relative to the normal modeling method can be observed. One is visible before the stall and one is visible within the stall. Before the stall, the normal modeling method shows a constant error in C_L of roughly +0.04. In the new modeling method this error is significantly smaller, between 0 and +0.025. The second improvement exists in the stall, where the slice-based method is better at modeling the nonlinear effects. The normal method shows less sudden changes in C_L during the stall, which are more pronounced with the slice-based method. This is visible in Figure 11b, showing both model outputs $\hat{y}_{C_{L_{normal}}}$ and $\hat{y}_{C_{L_{slice-based}}}$ and the validation measurement y_{C_L} from Figure 11a, but focused on the stall. The above two findings show that the slice-based modeling method is able to improve model fit not only in the stall, but also outside of the stall.

IV. Discussion

A. Interpretation of the Results

This paper has introduced a new slice-based modeling method. It is shown that this new method can improve stall model accuracy through optimal data slicing by analyzing Kirchhoff stall parameter estimate behaviour. A simulation data set representative of available flight test data was created and then sliced and partitioned. By applying a nonlinear and linear estimation to each partition, the parameter estimate behaviour of the Kirchhoff stall model parameters and stability and control derivatives could be analyzed. This resulted in an optimal slice number and corresponding optimal window size of data on which to perform the final slice-based parameter estimation. A number of important findings can be made from the results. These are discussed below.

First of all, applying the new slice-based modeling method results in a stall model which has increased accuracy over the model found via the normal estimation method. A decrease in MSE of about 10 % to 35 % can be achieved for the largest share of the validation datasets, as summarized in Table 5. This is significant, as the slice-based estimation method uses the exact same data as the normal estimation method. This answers the primary question of the research discussed by this paper: model accuracy can be improved by choosing specific parts of data to which to apply the estimation of a specific parameter.

The application of this new modeling method is made possible by the novel analysis introduced in this paper, i.e. by

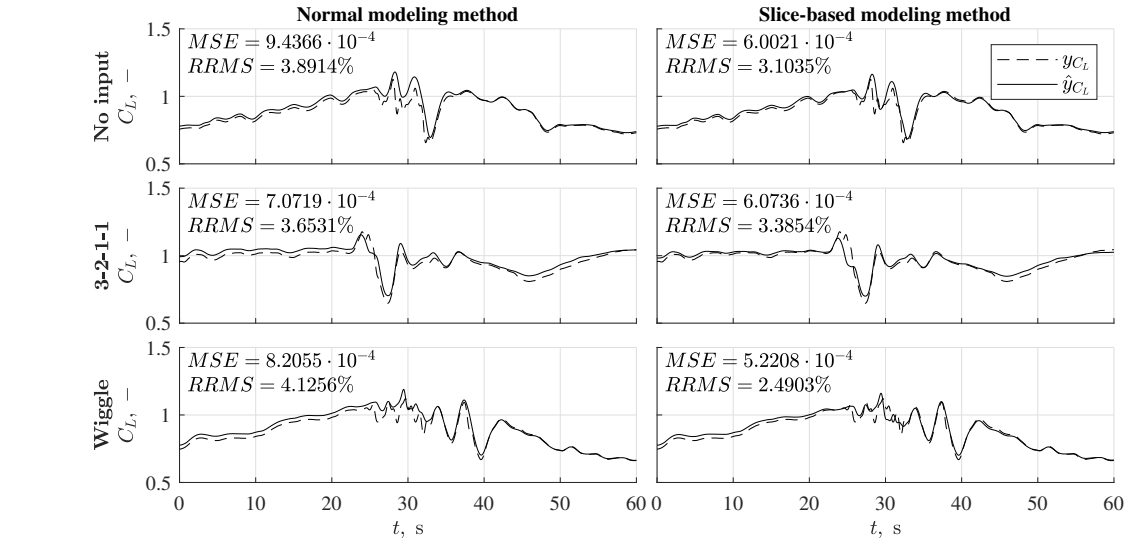

(a) Overview of all three best-improvement validation cases.

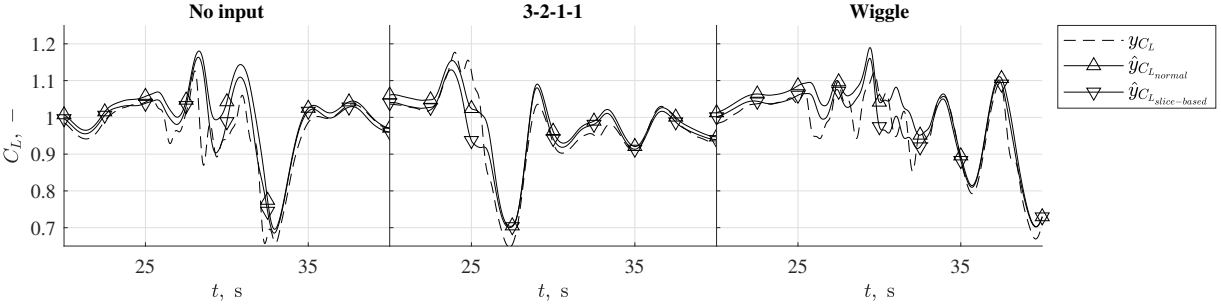

(b) Comparison within the stall.

Fig. 11 Comparison of the normal modeling method and the slice-based modeling method, showing the validation stall runs where the best improvement is achieved (no input realization 3, 3-2-1-1 realization 10, wiggle realization 1). The model outputs are denoted $\hat{y}_{C_L}$ and the validation data measurement is denoted y_{C_L}.

explicitly considering parameter estimate behaviour through data slicing and partitioning. Through this method it is for the first time possible to identify directly the effect of certain windows of data on the estimate of a parameter. Formerly, only the Fisher information could be used for this purpose. From the results it becomes clear that the Fisher information is especially useful to quickly identify which type of input given during the stall may result in more useful data for estimation of a specific parameter. An example of this was discussed for the parameter α^*, based on findings in Figure 8. Here, the parameter was estimated with no error relative to the actual parameter value for the simulation that contained the no-input stall. This type of stall contained a higher Fisher information than the stall with the 3-2-1-1 inputs. The latter resulted in an erroneous estimate for α^*. However, the results show that there is not always a direct link between the Fisher information and the correctness of a certain parameter. The Fisher information can thus not be used as a sole indicator to find the optimal slice number $n_{slice_{opt}}$. A high Fisher information derivative often coincides with large changes in the parameter estimate, as for the movement toward the lower bound before $n_{slice} = 13$ in Figure 9. However, it does not explain all movements, as for example in Figure 10a for the sudden movement at $n_{slice} = 18$. Therefore, it is suggested to use the Fisher information in combination with the introduced method of parameter estimate behaviour analysis.

Using these two concepts in conjunction provides a reliable basis to manually select optimal time windows for each parameter, as summarized in Table 3. Mainly, it becomes clear that better model accuracy is achieved when only data close to the stall is used for estimation of the stall parameters, and as much data as is available is used for the stability and control derivatives. Here, "close to the stall" generally means a window that roughly starts no more than 5 s before stall entry and ends no more than 5 s after stall recovery.

Depending on the type of stall, differences to this general rule can exist. For example, for a_1 the optimal time before and after the stall may vary from 0 s of data before the stall to using all available data after stall recovery. For estimation of α^*, it is recommended to only use data that contains very gradual stall entries without any control inputs and use all data available within these data sets. This is substantiated by analysis of the Fisher information related to α^* in these stall types. The estimates of parameters τ_1 and τ_2 are the most sensitive to the used data window. Very sudden changes in parameter estimates occur for slice numbers soon before or after the stall that may decrease their power in modeling the behaviour of the aircraft in the stall. The optimization algorithm primarily changes the estimates to lower the MSE in the regions before and after the stall. This is expected, as τ_1 and τ_2 describe nonlinear effects that only take place when dynamic excitations exist around the stall angle of attack. Therefore, the recommended time to include before or after the stall for estimation of these parameters is never more than 17 s and usually even less than 5 s. Next to this, it is found that no-input stalls are not effective for estimating τ_1 and τ_2. These stall types were used in the slice-based parameter estimation in this paper, but it may be an option to not use these stall types at all. Lastly, this paper recommends to use as much data as available for the estimation of the stability and control derivatives C_{L_0}, C_{L_α} and $C_{L_{\alpha^2}}$.

An important feature of the slice-based modeling method is that simulation data is used as a substitute for real flight data. It is assumed that the parameter estimate behaviour for the simulation data can be used to predict the parameter estimate behaviour for flight test data. As a means of validation, the parameter estimate behaviour for both types of data were compared. From this, it becomes evident that simulation data does in part represent flight test data, although not fully. This is because for flight test data large differences exist between realizations of the same stall type. The realizations of the simulation data differ only through an artificially added white noise signal to the simulation output before applying flight path reconstruction. Some inputs or conditions that are present in the flight test data are simply too complex to recreate in a simulation. However, some distinct features in parameter estimate behaviour are consistent between both data types. These are for example the lower-bound tendencies of the τ_1 and τ_2 parameters, but also the very predictable behaviour of α^*. Both also contain the behaviour of the MSE to increase during the stall and decrease outside of it. Related to this, the general parameter estimate behaviour where in the stall the stability and control derivatives are changed by the optimization routine to accommodate for changes in the stall parameters and vice-versa outside of the stall is present in both simulation data as well as flight test data. Thus, despite some differences between simulation data and flight test data, the roughly comparable behaviour does provide a solid basis for the slice-based modeling method.

Examining the parameter estimate behaviour that results from test flight data can also shed new light on related research, as it may explain the reason why some estimate has been found for a certain parameter. An example of this is a conclusion drawn in [19] about parameter τ_2. There it is suggested that the estimate of τ_2 could simply be set to 0, because its estimate of 0.0176 s is very close to 0. Also, only a small difference in MSE to validation data was found when the estimate of τ_2 was actually set to 0. However, the parameter estimate behaviour analysis in this paper may give an explanation for this. First, in this paper it was found that there is a significant interaction between the estimates of the stall parameters and the estimates of the stability and control derivatives. The small change in MSE reported in [19] could come from the fact that the stability and control derivatives estimates reduce part of the MSE by compensating for the lack of τ_2. A second explanation is that for the research in [19], only flight test data containing wiggle inputs was used. It was found in this paper that the τ_2 parameter often has a lower-bound tendency when wiggle inputs are applied. This was not found for the 3-2-1-1 inputs in the parameter estimate behaviour analysis. Also including the data with 3-2-1-1 inputs may explain why a significantly higher estimates for τ_2 than that in [19] of 0.0176 s are found, namely 0.1297 s for the normal estimation method and 0.2182 s for the slice-based estimation method. Because also a higher model accuracy is achieved, it is argued that setting τ_2 to 0 should not be done and for every new data set a parameter estimation behaviour analysis is warranted to make a decision on whether such an assumption is valid.

The parameter estimate behaviour analysis is the main addition of the slice-based modeling method. However, this addition does add significant computational load relative to the normal estimation method. For the full analysis of data, for every slice, in every slicetype, for every realization of every stall input type from both simulation data and flight test data, a full nonlinear estimation of 500 initial conditions had to be performed. This results in a total of over 14.5 million optimizations and an accompanying calculation time of three weeks, for 24 hours per day*. Here it should be noted that the optimizations are independent, and therefore the problem can be readily partitioned and solved in parallel on large scale parallel computing hardware. For example, in this paper use was made of MATLAB's parallel programming toolbox. In future analyses computational load may also be decreased by varying the resolution of n_{slice} to larger than 1 s at moments in time where less activity in parameter estimate behaviour is expected.

*1x PC with 6x Intel Core i7-8700 @3.20GHz (16GB RAM) and 2x PC with 4x Intel Xeon E5-1620 v3 @3.50GHz (16GB RAM)

It is demonstrated in this paper that performing a parameter estimate behaviour analysis can deliver new fundamental insights into how parameter estimates change in reaction to specific parts of data that are available for estimation. It is shown that it is possible to increase the accuracy of nonlinear stall models without the need for gathering more flight data by introducing the slice-based modeling method including the parameter estimate behaviour analysis. Additionally, the possibilities of the method extend beyond the realm of stall modeling for fixed wing aircraft. In fact, any system identification procedure that contains a parameter estimation based on measurement data can benefit from the slice-based modeling method. In every parameter estimation problem, certain parts of data are more valuable to some parameters than to other parameters. Tailoring the optimal time window used in the parameter estimation to each individual parameter may increase the accuracy of any model found through system identification.

B. Recommendations

Even though the results show the applicability of the parameter estimate behaviour analysis method and its usefulness to improve model performance with the slice-based modeling method, it leaves room for improvement. Several recommendations can be made.

The current slicing method only makes use of three types of slicing in time, i.e. the pre-stall phase, post-stall phase and both the pre-stall and post-stall phases. These types were defined such that every additional slice adds to the size of a partition. A problem with this is that the resulting parameter estimate behaviour from adding that slice is less pronounced because the partitions contain increasingly more foregoing data. A solution to this could be to create a moving window of some sort, that analyzes each part more specifically. This window size could then also be varied. Another recommendation comparable to this is that the slicing and partitioning could be based not only on time, but on independent variables such as α and $\dot{\alpha}$. However, this would introduce problems with the estimation of the X parameter, as well as all partitions having variable sizes. This would make comparison between the partitions more difficult, unless a solution is found to retain the same amount of data points in each partition.

Also, the current method only adds a white noise signal to the simulation output causing very similar realizations. Therefore, a certain dependency on any initial setting is not fully made undone. This applies to the trimmed initial condition, the size and timing of the inputs given, but also to more integral features, such as the actual stall parameter setting in the simulation. For future research a method is recommended that may evaluate the sensitivity of the parameter behaviours to these settings. Also, this creates more differences between the realizations, which can resemble better the differences that exist between the realizations of the real flight data.

Related to this is the inclusion of orthogonal function modeling (OFM). As a starting point for this research, the model as found in [19] was used. However, this eliminated the effect of OFM in the estimation procedure. For a full evaluation of the slicing selection method as introduced in this paper, it is recommended that an analysis is performed as to what changes occur in the chosen regressors of the OFM as the slicing type progresses in time. This may add certain knowledge on "regressor behaviour analysis" to the parameter estimate behaviour analysis performed in this research.

The last recommendation applies to the new modeling method itself. The current method represents a prototype, as the optimal time windows were chosen manually by investigation of the parameter estimate behaviour plots. While this provides a strong argument for using data slicing and selection for stall parameter analysis in the first place, a more thorough optimization method, for example by changing the time windows of each parameter separately and assessing the model performance increase, may be desirable.

V. Conclusion

In this paper it is proven that the accuracy of aerodynamic stall models using Kirchhoff's theory of flow separation can be improved by use of the newly introduced slice-based modeling method. When applied to validation flight test data the new method can decrease the MSE in more than half of the validation cases by 10 % to 35 %. On average, a decrease of 6 % was achieved.

The slice-based modeling method is based on a parameter estimate behaviour analysis. In this analysis, simulation data is generated that represents real flight test data that is available. This simulation data is sliced and combined into different partitions that include different time windows of this data. By applying a parameter estimation procedure to these partitions, it can be identified which parts of the data cause a change in the estimate of a specific parameter. By identifying where the parameter estimates attain the same value as the actual parameter value in the simulation an optimal time window can be identified for every parameter, for every type of stall. This window is then applied in a final parameter estimation on flight test data, resulting in a model with increased accuracy relative to the normally used method. Similarities can be found between the parameter estimate behaviour in simulation data and the estimate

behaviour in flight test data that the simulation data is aimed to represent.

Every parameter in the Kirchhoff based stall model has a accompanying optimal time window. For the stall parameters a_1, α^*, τ_1 and τ_2 this window generally starts no more than roughly 5 s before the stall and no more than 5 s after the stall, even though differences exist between the parameters depending on which control inputs are given during the stall. For the stability and control derivatives C_{L_0}, C_{L_α} and $C_{L_{\alpha^2}}$ in the model applies that all available data should be used in the estimation for better model accuracy.

Next to the parameter estimate behaviour analysis, the Fisher information is a strong indicator which region of data is beneficial to use in the estimation of a certain parameter. A connection exists between the Fisher information and the parameter estimate behaviour. In parts of the data where the Fisher information is high also changes of the parameter estimate can be observed. However the Fisher information is not a direct indicator for finding optimal window size, it is very valuable in aiding to make a quick decision on whether a certain stall type or type of input in a flight test is beneficial to a certain parameter or not.

In conclusion, this paper shows that the slice-based modeling method can be used for improving stall models without the need for additional flight tests by making smarter use of data that is readily available. This not only makes it possible to improve existing models, but also creates the possibility to make future research flight test data even more efficient and valuable. Furthermore, the slice-based modeling method can be applied to any system identification problem that includes a parameter estimation. This means that the new method can also have a large impact outside the realm of stall modeling. All-in-all, it is clear that the slice-based modeling method can enable researchers to create more representative flight simulation models, resulting in better pilot training, contributing to safer commercial air transport.

Appendices

A. Analytical Definition of Fisher Information for the Aerodynamic Stall Model

Recall the C_L model as given by Eq. (3):

$$C_L = C_{L_0} + C_{L_\alpha}\left(\frac{1+\sqrt{X}}{2}\right)^2 \alpha + C_{L_{\alpha^2}}(\alpha - 6°)_+^2$$

The parameter vector of this model is given by Eq. (8):

$$\vec{\theta} = \begin{bmatrix} a_1 & \alpha^* & \tau_1 & \tau_2 & C_{L_0} & C_{L_\alpha} & C_{L_{\alpha^2}} \end{bmatrix}^T$$

There is only one output, the measurement y_{C_L}. The sensitivity matrix $S(k)$ then contains all derivatives of y_{C_L} relative to the parameters in $\vec{\theta}$. The resulting matrix $S(k)$ is the result of applying the chain rule via:

$$\begin{aligned} S(k) &= \begin{bmatrix} \frac{\partial y_{C_L}(k)}{\partial a_1} & \frac{\partial y_{C_L}(k)}{\partial \alpha^*} & \frac{\partial y_{C_L}(k)}{\partial \tau_1} & \frac{\partial y_{C_L}(k)}{\partial \tau_2} & \frac{\partial y_{C_L}(k)}{\partial C_{L_0}} & \frac{\partial y_{C_L}(k)}{\partial C_{L_\alpha}} & \frac{\partial y_{C_L}(k)}{\partial C_{L_{\alpha^2}}} \end{bmatrix} = \\ &= \begin{bmatrix} \frac{\partial y_{C_L}(k)}{\partial X}\frac{\partial X(k)}{\partial a_1} & \frac{\partial y_{C_L}(k)}{\partial X}\frac{\partial X(k)}{\partial \alpha^*} & \frac{\partial y_{C_L}(k)}{\partial X}\frac{\partial X(k)}{\partial \tau_1} & \frac{\partial y_{C_L}(k)}{\partial X}\frac{\partial X(k)}{\partial \tau_2} & \frac{\partial y_{C_L}(k)}{\partial C_{L_0}} & \frac{\partial y_{C_L}(k)}{\partial C_{L_\alpha}} & \frac{\partial y_{C_L}(k)}{\partial C_{L_{\alpha^2}}} \end{bmatrix} \end{aligned} \tag{15}$$

Finding the derivatives when $\theta_i \in \{C_{L_0}, C_{L_\alpha}, C_{L_{\alpha^2}}\}$ is straightforward. These are:

$$\frac{\partial y_{C_L}(k)}{\partial \theta_i} = \begin{cases} 1 & \text{when } \theta_i = C_{L_0} \\ \left(\frac{1+\sqrt{X(k)}}{2}\right)^2 \alpha(k) & \text{when } \theta_i = C_{L_\alpha} \\ \max(0, \alpha(k) - 6°)^2 & \text{when } \theta_i = C_{L_{\alpha^2}} \end{cases} \tag{16}$$

The value of $X(k)$ over the entire interval $k = 1, 2, \ldots, N$ can be found by numerically integrating Eq. (2).

The derivatives when $\theta_i \in \{a_1, \alpha^*, \tau_1, \tau_2\}$ are more difficult to find, but can be obtained via the procedure as explained for the nonlinear cost function derivatives associated with X in [19]. These are:

$$\frac{\partial y_{C_L}(k)}{\partial X} = \frac{1}{4} C_{L_\alpha} \alpha(k) \left(1 + \frac{1}{\sqrt{X(k)}}\right) \tag{17}$$

$$\frac{\partial G(k)}{\partial X} = -\frac{1}{\tau_1} \tag{18}$$

$$\frac{\partial G(k)}{\partial \theta_i} = \begin{cases} -\frac{\frac{1}{2}\{1-\tanh^2\left[a_1(\alpha(k)-\tau_2\dot{\alpha}(k)-\alpha^*)\right]\}\{\alpha(k)-\tau_2\dot{\alpha}(k)-\alpha^*\}}{\tau_1} & \text{when } \theta_i = a_1 \\ -\frac{\frac{1}{2}\{1-\tanh^2\left[a_1(\alpha(k)-\tau_2\dot{\alpha}(k)-\alpha^*)\right]\}\{-a_1\}}{\tau_1} & \text{when } \theta_i = \alpha^* \\ -\frac{\frac{1}{2}\{1-\tanh\left[a_1(\alpha(k)-\tau_2\dot{\alpha}(k)-\alpha^*)\right]\}-X(k)}{\tau_1^2} & \text{when } \theta_i = \tau_1 \\ -\frac{\frac{1}{2}\{1-\tanh^2\left[a_1(\alpha(k)-\tau_2\dot{\alpha}(k)-\alpha^*)\right]\}\{-a_1\dot{\alpha}(k)\}}{\tau_1} & \text{when } \theta_i = \tau_2 \end{cases} \tag{19}$$

Then, the result for $\frac{\partial X(k)}{\partial \theta_i} = S$ (do not confuse S with $S(k)$!) can be found by numerically integrating the ordinary differential equation $\frac{dS}{dt} = \frac{\partial G(k)}{\partial X} S + \frac{\partial G(k)}{\partial \theta_i}$ over the interval $k = 1, 2, \ldots, N$. Note that in this case it is thus not only important that the model structure is known, but also an a priori estimate of the parameters in $\vec{\theta}$ is needed as these are present in the derivative equations.

Acknowledgements

This paper was written as part of the MSc thesis project of author Patrick Brill. Sincere thanks go out to daily supervisors dr.ir. Daan Pool and dr.ir. Coen de Visser for their help and guidance.

References

[1] IATA, "Loss of Control In-Flight Accident Analysis Report," , 2019.

[2] Lambregts, A., Nesemeier, G., Wilborn, J., and Newman, R., "Airplane Upsets: Old Problem, New Issues," *AIAA Modeling and Simulation Technologies Conference and Exhibit*, American Institute of Aeronautics and Astronautics Inc, 2008.

[3] ICAO, "ICAO Doc 10011: MANUAL ON AEROPLANE UPSET PREVENTION AND RECOVERY TRAINING," , 2014.

[4] EASA, "Certification Specifications for Aeroplane Flight Simulation Training Devices 'CS-FSTD(A)'," , 2018.

[5] Gingras, D., and Ralston, J., "Aerodynamics modelling for training on the edge of the flight envelope," *The Aeronautical Journal*, Vol. 116, No. 1175, 2012, pp. 67–86.

[6] Gingras, D. R., Ralston, J. N., Oltman, R., Wilkening, C., Watts, R., and Desrochers, P., "Flight Simulator Augmentation for Stall and Upset Training," *AIAA Modeling and Simulation Technologies Conference*, American Institute of Aeronautics and Astronautics Inc, 2014.

[7] Murphy, P. C., Klein, V., and Frink, N. T., "Nonlinear Unsteady Aerodynamic Modeling Using Wind-Tunnel and Computational Data," *Journal of Aircraft*, Vol. 54, No. 2, 2017, pp. 659–683.

[8] Sri-Jayantha, M., and Strengel, R. F., "Determination of Nonlinear Aerodynamic Coefficients Using the Estimation-Before-Modeling Method," *Journal of Aircraft*, Vol. 25, No. 9, 1988, pp. 796–804.

[9] Grant, P. R., Liu, S., Luo, Z., and Moszczynski, G., "Development of Post-stall Flight Models from Certification Flight Test and Wind-tunnel Data," *AIAA SciTech Forum*, American Institute of Aeronautics and Astronautics Inc, 2017.

[10] Goman, M., and Khrabov, A., "State-Space Representation of Aerodynamic Characteristics of an Aircraft at High Angles of Attack," *Journal of Aircraft*, Vol. 31, No. 5, 1994, pp. 1109–1115.

[11] Fischenberg, D., "Identification of an Unsteady Aerodynamic Stall Model from Flight Test Data," *20th Atmospheric Flight Mechanics Conference*, American Institute of Aeronautics and Astronautics Inc, 1995, pp. 138–146.

[12] Singh, J., and Jategaonkar, R., "Identification of Lateral-Directional Behavior in Stall from Flight Data," *Journal of Aircraft*, Vol. 33, No. 3, 1996, pp. 627–630.

[13] Fischenberg, D., and Jategaonkar, R., "Identification of Aircraft Stall Behavior from Flight Test Data," *RTO SCI Symposium in System Identification for Integrated Aircraft Development and Flight Testing*, North Atlantic Treaty Organization Research and Technology Organization, 1999, pp. 17.1–17.8.

[14] Kumar, R., Ghosh, A., and Misra, A., "Parameter Estimation from Flight Data of Hansa-3 Aircraft Using Quasi-Steady Stall Modeling," *Journal of Aerospace Engineering*, Vol. 26, No. 3, 2013, pp. 544–554.

[15] Dias, J. N., "Unsteady and Post-Stall Model Identification Using Dynamic Stall Maneuvers," *AIAA Atmospheric Flight Mechanics Conference*, American Institute of Aeronautics and Astronautics Inc, 2015.

[16] van der Linden, C., *DASMAT-Delft University Aircraft Simulation Model and Analysis Tool, A Matlab/Simulink Environment for Flight Dynamics and Control Analysis*, Delft University of Technology, 1998.

[17] van den Hoek, M., de Visser, C., and Pool, D., "Identification of a Cessna Citation II Model Based on Flight Test Data," *Fourth CEAS Specialist Conference on Guidance, Navigation and Control*, Springer, 2017, pp. 259–277.

[18] van Horssen, L., de Visser, C., and Pool, D., "Aerodynamic Stall and Buffet Modeling for the Cessna Citation II Based on Flight Test Data," *2018 AIAA Modeling and Simulation Technologies Conference*, American Institute of Aeronautics and Astronautics Inc, 2018.

[19] van Ingen, J. B., de Visser, C. C., and Pool, D. M., "Stall Model Identification of a Cessna Citation II from Flight Test Data Using Orthogonal Model Structure Selection," *AIAA Scitech 2021 Forum*, American Institute of Aeronautics and Astronautics Inc, 2021.

[20] Delfosse, A., Pool, D. M., and de Visser, C., "Asymmetric Stall Modeling of the Cessna Citation II Aircraft," , 2022. Unpublished.

[21] Smets, S., de Visser, C., and Pool, D., "Subjective Noticeability of Variations in Quasi-Steady Aerodynamic Stall Dynamics," *AIAA Scitech 2019 Forum*, American Institute of Aeronautics and Astronautics Inc, 2019.

[22] Imbrechts, A., de Visser, C., and Pool, D., "Just Noticeable Differences for Variations in Quasi-Steady Stall Buffet Model Parameters," *AIAA SciTech 2022 Forum*, American Institute of Aeronautics and Astronautics Inc, 2022.

[23] Klein, V., and Morelli, E. A., *Aircraft System Identification, Theory and Practice*, American Institute of Aeronautics and Astronautics Inc, 2006.

[24] Morelli, E. A., Cunningham, K., and Hill, M. A., "Global Aerodynamic Modeling for Stall/Upset Recovery Training Using Efficient Piloted Flight Test Techniques," *AIAA Modeling and Simulation Technologies (MST) Conference*, American Institute of Aeronautics and Astronautics Inc, 2013.

[25] Mulder, J., *Design and evaluation of dynamic flight test manoeuvres*, Delft University of Technology, 1986.

[26] Morelli, E. A., "Flight Test of Optimal Inputs and Comparison with Conventional Inputs," *Journal of Aircraft*, Vol. 36, No. 2, 1999, pp. 389–397.

[27] Seren, C., Bommier, F., Verdier, L., Bucharles, A., and Alazard, D., "Optimal Experiment and Input Design for Flight Test Protocol Optimization," *AIAA Atmospheric Flight Mechanics Conference and Exhibit*, American Institute of Aeronautics and Astronautics Inc, 2006.

[28] Ly, A., Marsman, M., Verhagen, J., Grasman, R. P., and Wagenmakers, E.-J., "A Tutorial on Fisher information," *Journal of Mathematical Psychology*, Vol. 80, No. 1, 2017, pp. 40–55.

[29] Batterson, J. G., and Klein, V., "Partitioning of Flight Data for Aerodynamic Modeling of Aircraft at High Angles of Attack," *Journal of Aircraft*, Vol. 26, No. 4, 1989, pp. 334–339.

[30] Morelli, E. A., "Efficient Global Aerodynamic Modeling from Flight Data," *50th AIAA Aerospace Sciences Meeting including the New Horizons Forum and Aerospace Exposition*, American Institute of Aeronautics and Astronautics Inc, 2012.

[31] Laban, M., *On-Line Aircraft Aerodynamic Model Identification*, Delft University of Technology, 1994.

[32] Julier, S. J., and Uhlmann, J. K., "A New Extension of the Kalman Filter to Nonlinear Systems," *Signal Processing, Sensor Fusion, and Target Recognition VI*, SPIE, 1997, pp. 182–193.

[33] Wan, E. A., and van der Merwe, R., "The Unscented Kalman Filter for Nonlinear Estimation," *IEEE 2000 Adaptive Systems for Signal Processing, Communications, and Control Symposium*, Institute of Electrical and Electronics Engineers Inc, 2000, pp. 153–158.

[34] Chowdhary, G., and Jategaonkar, R., "Aerodynamic parameter estimation from flight data applying extended and unscented Kalman filter," *Aerospace Science and Technology*, Vol. 14, No. 2, 2010, pp. 106–117.

[35] Teixeira, B. O., Tôrres, L. A., Iscold, P., and Aguirre, L. A., "Flight path reconstruction - A comparison of nonlinear Kalman filter and smoother algorithms," *Aerospace Science and Technology*, Vol. 15, No. 1, 2011, pp. 60–71.

[36] Gross, J., Gu, Y., Gururajan, S., Seanor, B., and Napolitano, M. R., "A Comparison of Extended Kalman Filter, Sigma-Point Kalman Filter, and Particle Filter in GPS/INS Sensor Fusion," *AIAA Guidance, Navigation, and Control Conference*, American Institute of Aeronautics and Astronautics Inc, 2010.

Part II

Preliminary Thesis Report

Chapter 1

Introduction

An immense part of the operation of airlines is the licensing and training of flight crew. Not only is the training of flight crew heavily regulated, it is also an inherent driver for airlines to uphold proficiency of flight crews to increase their own safety standards. Nowadays, flight crews may and can be fully trained on Flight Simulation Training Devices. These simulators are built according to very specific requirements in order to increase the fidelity of the simulators such that pilots behave as if they are in an actual aircraft of that type. An important part of the fidelity of the simulators depends on the quality of the flight model of the aircraft. This determines the movements of the simulated aircraft which need to be mimicked as close to reality as possible. Usually this involves very complex and complicated models.

Additional complexity of these models has been introduced recently, since the European Aviation Safety Agency has required airlines to train their flight crew in Upset Prevention and Recovery on their simulators. Upsets of an aircraft occur when, due to whatever reason, the aircraft is placed outside its normal flight envelope. One of the most regularly occurring types of upsets is the stall, when the airflow over the wing of the aircraft has separated and lift is lost as a result. Normally this occurs because of too high angles of attack of the wing. The behaviour of the aircraft in this region is often highly nonlinear, which further increases the model complexity of flight simulators.

The Citation Stall Modeling Group of the Faculty of Aerospace Engineering at the Delft University of Technology aims to create an accurate, yet simpler, aircraft model for simulation purposes of the PH-LAB Cessna Citation II aircraft that captures the nonlinear behaviour of the aircraft in the stall. Already numerous research has been performed on different aspects of this model, such as its behaviour in the normal envelope, its longitudinal and lateral stall behaviour, its stall buffet, and the subjective experience that the model gives, which ultimately is the goal of this model.

The aim of this thesis is to further this research. In this preliminary part of the thesis a literature survey is performed to find the research gap of the state of the art in stall modeling of aeroplanes and to perform a preliminary research based on this literature. The final yield

of the preliminary research presented here is a research objective and research question based on literature and a proof of applicability of this objective through demonstration by some preliminary results.

In order to achieve this, the preliminary part of this thesis is structured as follows. In chapter 2 the background of this research is discussed and an introduction is given to the core of the Citation Stall Modeling Group's stall model: Kirchoff's Theory of Flow Separation. In chapter 3 an overview is given the PH-LAB aircraft and gathered data on its behaviour in the stall. Also a literature review is performed on the design of flight test experiments. Next, in chapter 4 flight path reconstruction is performed in order to filter the flight data and make it usable in the aerodynamic modeling of the aircraft. The actual modeling technique used is then discussed in chapter 5. A possible research direction is investigated in chapter 6. Penultimate, in chapter 7, some preliminary results are presented on the most promising possible research direction and the final research objective and research questioned are proposed. This preliminary thesis concludes with chapter 8.

Chapter 2

Background

In this chapter the an introduction is given into the aim of the stall modeling of aircraft. First, the regulatory background and direct need for stall modeling research is discussed. Then, Kirchoff's theory of flow separation is introduced which is a model that aims to accurately approximate the nonlinear and unsteady effects that exist for an aircraft in or close to stall. A literature review is performed on the application of this model in research of the TU Delft Citation Stall Modeling Group. Last, other stall modeling research that utilizes Kirchoff's theory is introduced and a conclusion is drawn with regard to the main recommendations done by the literature treated in this chapter.

2-1 Upset Prevention and Recovery Training

The most significant cause of fatal accidents in commercial air transport is Loss of Control In-Flight (LOC-I) [23]. LOC-I occurs when the aircraft deviates from the intended flight path or an adverse flight condition places the aircraft outside of its normal flight envelope. The main cause of these LOC-I accidents is often a failure to prevent or recover from a stall or upset during flight.

Because of the significance and high fatality rate of this type of accidents, in recent years increasingly more focus in airline pilot training has been put on Upset Prevention and Recovery Training (UPRT). For this reason, the International Civil Aviation Organisation (ICAO) has urged member states to implement UPRT in their regulations such that it becomes standard in pilot training [24]. This ICAO Doc 10011 provides a large number of recommendations on the implementation of UPRT in pilot training, such as an overview of the proposed training programmes, the contents of this training, instruction types, and required regulatory oversight. However, more significant for the research presented in this paper is that this document also provides fidelity requirements for Flight Simulation Training Devices (FSTDs). Effective and safe pilot training calls for a "good" fidelity of the FSTD. Because if the FSTD does not satisfactorily model the airplane's behaviour during a stall, the training beyond critical

angle of attack can introduce misperceptions about recognition of the upset and the recovery experience [19].

Therefore, [24] calls for an FSTD's simulation responses at or beyond the stall angle of attack to be similar to that of the actual aircraft in flight. The dynamics of the aircraft are, however, often different from the rest of the envelope. This can be trained in some aircraft, but a significant problem is that in current training pilots are often only limitedly exposed to aircraft-specific stall characteristics of their aircraft type -if they are at all- [19]. In order to provide pilots with effective training, flight models of certain types should thus be updated with stall characteristics specific to that aircraft.

The European Union has, in response to ICAO, updated its legislation and certification specification for FSTDs [14]. For stall model dynamics, AMC10 FSTD(A).300.d.3 prescribes a more profound set of stall characteristics that should be included in simulator models than already given as an example in [24] above. These are:

- degradation of the static/dynamic lateral-directional stability;
- degradation in control response (pitch, roll, and yaw);
- uncommanded roll acceleration or roll-off requiring significant control deflection to counter;
- apparent randomness or non-repeatability;
- changes in pitch stability;
- stall hysteresis;
- Mach effects;
- stall buffet; and
- angle of attack rate effects.

These are important stall characteristics as also defined by the International Committee for Aviation Training in Extended Envelopes (ICATEE) in [18]. This paper finds that the augmentation of a type-representative flight model by addition of these characteristics produces a significant subjective fidelity in the stall and post-stall regime. Overmore, apart from some pilots voicing personal preference, statistically the evaluating pilots could tell no difference between the type-representative model and the type-specific model as developed by the manufacturer. This confirms the importance of the above listed characteristics for stall modeling. Therefore, for the further investigation into aircraft stall behaviour, these characteristics will serve as a basis.

2-2 Kirchoff's Theory of Flow Separation

The stall itself is defined as the "an aerodynamic loss of lift caused by exceeding the critical angle of attack" [24], where the critical angle of attack is defined as the point where the aircraft lift coefficient reaches its maximum before decreasing with further increasing angle of attack. However this point is not trivial and also the characteristics as mentioned above are not universally applicable to every aircraft type or even flight condition. Therefore it can be very valuable to define a general description of the behaviour of an aircraft around the stall critical angle of attack. A mathematical description that incorporates a number of the characteristics above is known as Kirchoffs's theory of flow separation.

2-2-1 Mathematical Description of Kirchoff's Theory of Flow Separation

The application of Kirchoff's theory to the mathematical model of an aircraft has been described by [20]. It describes the lift coefficient's (C_L) nonlinear and unsteady behaviour (denoted by superscript nl) at high angles of attack by means of the following equation:

$$C_L^{nl}(\alpha, X) = \frac{\pi}{2}\alpha\left(1+\sqrt{X}\right)^2 \tag{2-1}$$

Where the theoretical steady behaviour (denoted by superscript st) can be described by:

$$C_L^{st}(\alpha) = C_L^{nl}(\alpha, X_0), \quad \text{with: } X_0 = X_0(\alpha) \tag{2-2}$$

With X_0 being a function of α describing the position of the separation point of the flow over the airfoil with the aircraft in stationary flight. However, when not in stationary flight condition, i.e. $\dot{\alpha} > 0$, the progression of the separation point is affected due to unsteady effects. To be precise, the separation is delayed until higher angles of attack. This behaviour can be described by means of an first order differential equation:

$$\tau_1\frac{dX}{dt} + X = X_0(\alpha - \tau_2\dot{\alpha}), \quad \text{s.t. } X = X(\alpha, \dot{\alpha}) \tag{2-3}$$

Where τ_1 is a time constant related to the relaxation of the flow separation point and τ_2 is a time constant related to the time delay of the separation or reattachment of the flow (hysteresis). These constants and the function X_0 may be found via experimental data. As X is a function of both α and $\dot{\alpha}$, it can be concluded that in non-stationary conditions the unsteady behaviour of the lift curve is a function of angle of attack and angle of attack rate and angle of attack prehistory via the flow separation behaviour, i.e.: $C_L^{nl}(\alpha, X(\alpha, \dot{\alpha}))$.

The application of the above theory to identify a stall model from flight test data has first been performed in [15], which rewrites Equation (2-1) in generic form:

$$C_L = C_{L_\alpha}\left(\frac{1+\sqrt{X}}{2}\right)^2\alpha \tag{2-4}$$

In which the aircraft-specific C_{L_α} has been inserted over the generic thin-airfoil theory's 2π/rad used in Equation (2-1). Also an alternative approximation of X_0 is used to make Equation (2-3) more suitable for identification from flight data. This is given by:

$$X_0 = \frac{1}{2}\{1 - \tanh\left[a_1(\alpha - \alpha^*)\right]\} \tag{2-5}$$

Implementing this result into Equation (2-3) results in:

$$\tau_1\frac{dX}{dt} + X = \frac{1}{2}\{1 - \tanh\left[a_1(\alpha - \tau_2\dot{\alpha} - \alpha^*)\right]\} \tag{2-6}$$

Where the additional parameter a_1 is related to the abruptness of the flow separation, and α^* is the angle of attack where the flow separation point is halfway down the chord (i.e. $X = 0.5$).

The four parameters a_1, α^*, τ_1 and τ_2 are at the core of the model for the separation point X and are called the "Kirchoff parameters" or simply the "X parameters". Their influence on the behaviour of the flow separation point around the stall angle of attack is given in Figure 2-1.

The effect of each of the parameters is shortly described below.

- *Stall abruptness parameter a_1 [-].* The parameter a_1 controls the abruptness of the stall as can be seen in Figure 2-1a. It controls the window in which the separation point X moves forward and as a result also has an effect on the maximum stall coefficient.
- *Separation delay parameter α^* [rad] or [deg].* The parameter α^* is the angle of attack where the flow separation point is halfway down the chord and has a direct effect on the stall angle of attack and maximum lift coefficient, as can be seen in Figure 2-1b. Note that α^* is higher than the critical angle of attack.
- *Transient effects parameter τ_1 [s].* Parameter τ_1 is a multiplication on the derivative $\frac{dX}{dt}$ and therefore directly influences the slope, and thus the relaxation, of the flow separation point and in turn the lift coefficient. See Figure 2-1c.
- *Stall hysteresis parameter τ_2 [s].* The last parameter is τ_2 which governs the hysteresis behaviour of the aircraft in stall as depicted in Figure 2-1d. It governs the separation and reattachment of the flow an the difference between the angles of attack at which these happen, i.e. how "inclined" the air is to separate and reattach to the airfoil.

In this manner the Kirchoff model directly models two important characteristics of the stall: angle of attack rate effects and the stall hysteresis. However it may affect more of the characteristics via the X parameter. For example, it might be the case that degradation in stability and control effectiveness [58] or the stall buffet [57] are related to the X parameter. What *is* certain is that the Kirchoff model models nonlinear behaviour and in unsteady flight conditions, which make it a very powerful tool in stall modeling.

2-2-2 Unsteady and Nonlinear Behaviour of an Aircraft around the Stall Angle of Attack

With the defined Kirchoff model, there are three methods to model the C_L-curve: 1) purely linearly, 2) nonlinearly, but in steady/stationary conditions ($\dot{\alpha} = 0$ deg/s) and 3) nonlinearly and in unsteady $\dot{\alpha} > 0$ [deg/s] flight conditions. To study the effect of Kirchoff's theory of flow separation and the increase in fidelity it can provide to a model of an aircraft in stall a simulation can be performed. The Figure 2-2 shows four cases with increasing fidelity of the C_L-calculation of Equation (2-4) based on the three mentioned methods. An overview of the cases has been given in Table 2-1. The time constants and parameters have been arbitrarily chosen.

Case 1 shows an arbitrary separation progression, where the point of flow separation starts at $\alpha = 10$ deg and progresses towards the leading edge linearly until $\alpha = 15$ deg. The

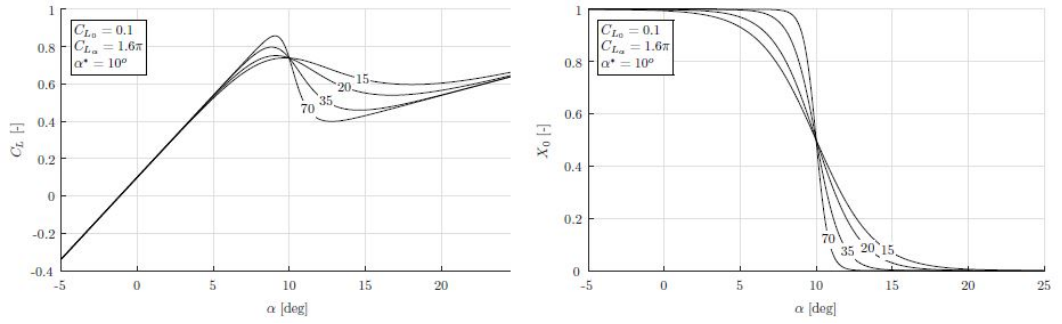

(a) Parameter a_1.

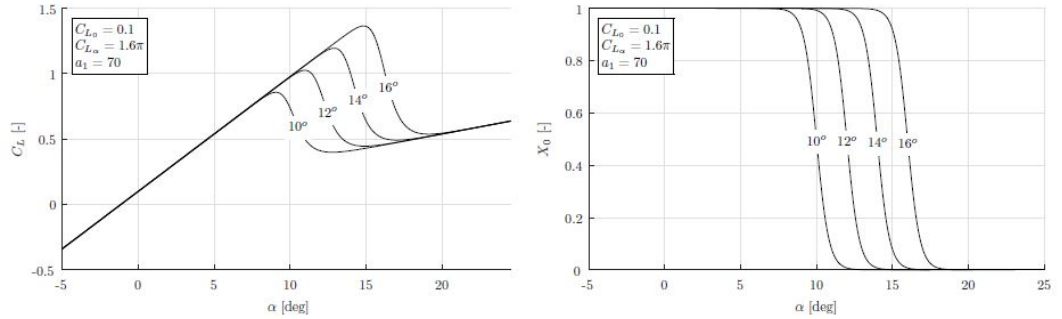

(b) Parameter α^*.

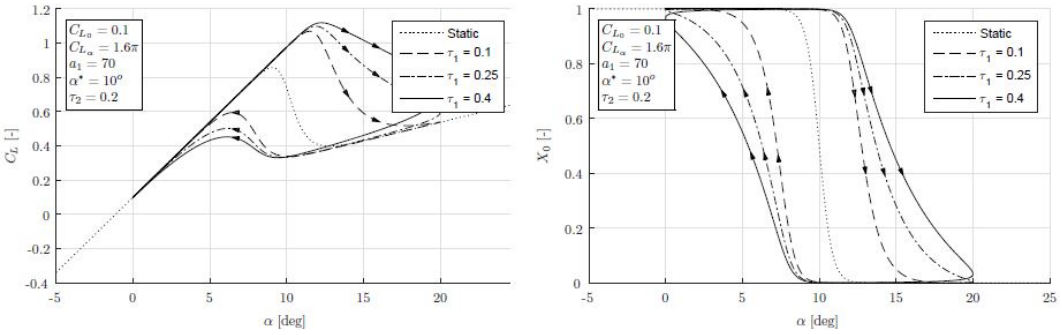

(c) Parameter τ_1.

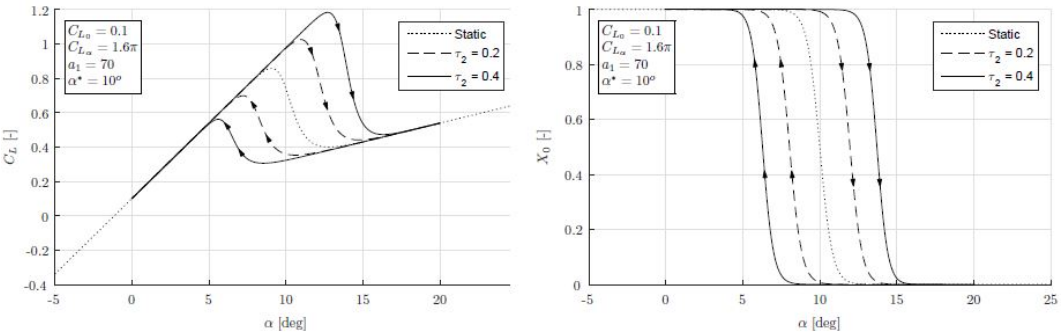

(d) Parameter τ_2.

Figure 2-1: Effect of the Kirchoff parameters on the lift coefficient C_L and separation point X [57].

Table 2-1: Overview of the Kirchoff cases.

#	Case	Equation	Added parameters	Description
1	Stationary flight, linear separation	Equation (2-2)	$C_{L_\alpha} = 2\pi$	X_0 manually defined, $\dot{\alpha} = 0$ deg/s
2	Stationary flight, tanh-approximation	Equation (2-5)	$a_1 = 50$, $\alpha^* = 12.5$ deg	X_0 calculated, $\dot{\alpha} = 0$ deg/s
3	Unsteady flight, full $X(\alpha, \dot{\alpha})$-ODE	Equation (2-6)	$\tau_1 = 0.5$ s, $\tau_2 = 0.01$ s	For $t = 0 - 20$ s: $\dot{\alpha} = +1$ deg/s
4	Unsteady flight, stall recovery	Equation (2-6)	-	For $t = 0 - 15$ s: $\dot{\alpha} = +1$ deg/s, for $t = 15 - 20$ s: $\dot{\alpha} = -1$ deg/s

dashed lines in the figure are, from top to bottom, the lines corresponding to $X = 1$, 0.8, 0.6, 0.4, 0.2 and 0. It can be observed that this results in an expected, but unnatural curve. The normal linear model (method "1)" above) is only valid until $\alpha = 10$ deg in such cases. Implementing the tanh-approximation for X_0 in case 2 results in a more continuous curve, describing nonlinear, but steady effects (method "2)"). When implementing the full ODE for X in case 3, it can indeed be seen that the angle of attack rate influences the curve. Not only can higher C_L-values be reached, the separation is also delayed until higher angles of attack. This captures the unsteady effects as a result of angle of attack rate as they exist in the high angle of attack region. The last case 4 is the same as case 3, but at $\alpha = 15$ deg the stall is recovered, showing that the recovery follows another "path" in the curve as stall entry, satisfying nonlinear, unsteady effects (method "3)").

From this it can be concluded that Kirchoff's theory correctly models the key characteristics of stall hysteresis (from case 4) and angle of attack rate effects (case 3). This behaviour is indeed also confirmed in [20]. This makes it possible to expand the linear models that can model the normal flight envelope to the edges of the envelope where high angles of attack introduce nonlinear effects.

2-2-3 Application of Kirchoff's Theory in Aircraft Stall Models

With the application of Kirchoff's theory being a viable option to model the nonlinear behaviour of the aircraft in the stall region, several papers attempted to incorporate this into the aircraft aerodynamic model for both the symmetric and asymmetric motions of the aircraft.

The initial longitudinal model was given in the same paper of [15], by use of a conventional 2-point model modeling both the wing and tail. This can be described by the equation:

$$C_L = C_{L,wb} + \frac{S_t}{S} C_{L,t} = \\ = C_{L_0} + C_{L_{\alpha,wb}} \left(\frac{1 + \sqrt{X}}{2} \right)^2 \alpha + C_{L_{q,wb}} \frac{qc}{V} + C_{L_{\dot{\alpha},wb}} \frac{\dot{\alpha} c}{V} + C_{L_{\alpha,t}} \alpha_t + \frac{\partial C_{L,t}}{\partial \delta_e} \delta_e \quad (2\text{-}7)$$

With:

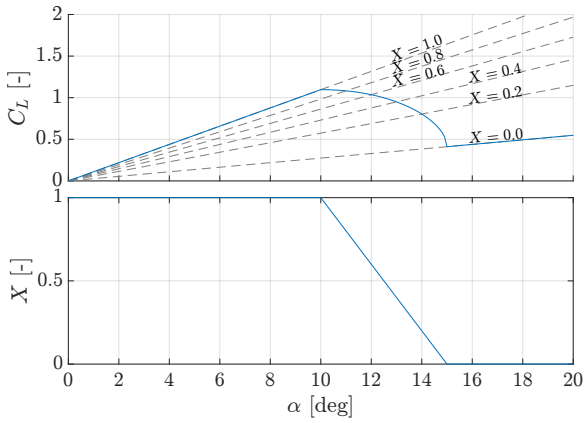

(a) Case 1: Linear X_0.

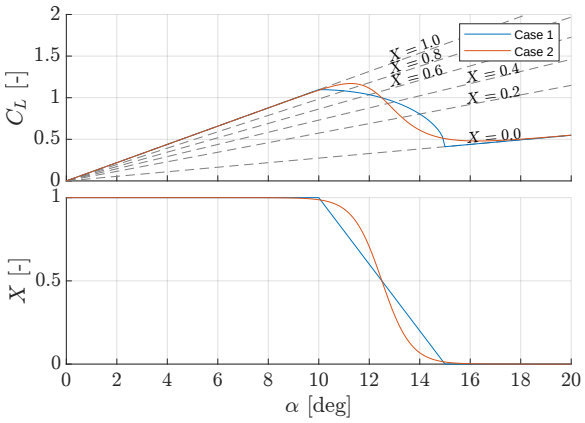

(b) Case 2: tanh-approximation X_0.

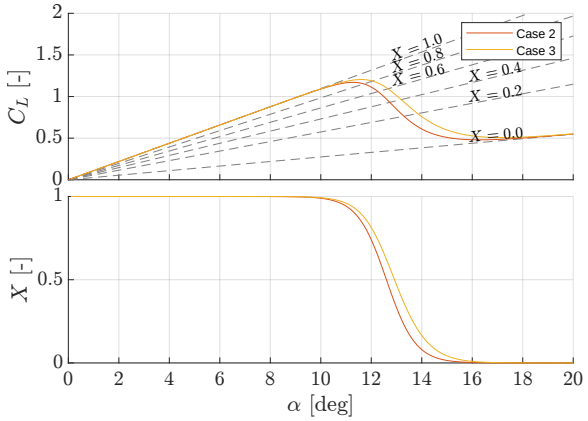

(c) Case 3: Full ODE X ($\dot{\alpha}_{t=0-20s} = +1$ deg/s).

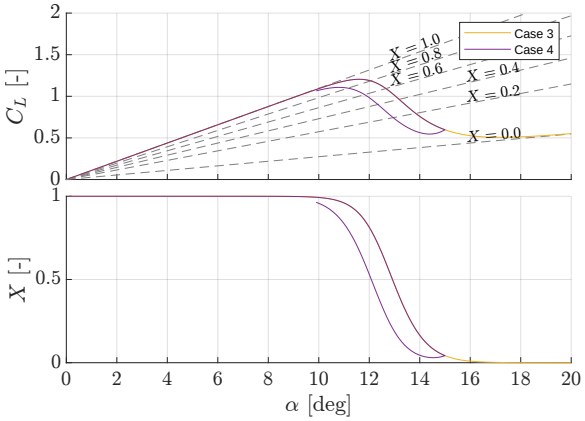

(d) Case 4: Full ODE X ($\dot{\alpha}_{t=0-15s} = +1$ deg/s, $\dot{\alpha}_{t=15-20s} = -1$ deg/s).

Figure 2-2: Overview of the behaviour of Kirchoff's theory of flow separation with increasing model fidelity.

$$\alpha_t = \alpha + i_t - \varepsilon_t + \alpha_{dyn} = \\ = \alpha + i_t - \left(\frac{\partial \varepsilon_t}{\partial \alpha} \alpha(t - \Delta t) + \frac{\partial \varepsilon_t}{\partial X} \{1 - X(t - \Delta t)\} \right) + \alpha_{dyn} \quad (2\text{-}8)$$

Where i_t is the tail trim angle, ε_t is the downwash angle at the tail, in which Δt is the lag of the downwash formulated as $\Delta t = \frac{r_t^*}{V}$ and α_{dyn} is the dynamic angle of attack formulated as $\tan^{-1}(\frac{qr_t}{V})$. Here r_t is the distance between aircraft c.g. and tail neutral point and r_t^* the distance between the wing and tail neutral points.

The drag force can be defined as:

$$C_D = C_{D_0} + \frac{1}{\pi A e} C_L^2 + \frac{\partial C_D}{\partial X}(1 - X) \quad (2\text{-}9)$$

Last, the pitching moment can be computed from the above equations around the c.g., resulting in (in simplified form):

$$C_m = C_{m_0} + C_{m_\alpha}\alpha + \frac{\partial C_m}{\partial X}(1 - X) \tag{2-10}$$

Applying the above model to simulations and validating this longitudinal model, [15] indeed found considerable improvements of this unsteady nonlinear model over the usual linear model or nonlinear steady modeling methods, especially for the region of $\alpha > 10$ deg. The related time constants and parameters could all be identified satisfactorily. Any stall model identification routine performed should thus include the identification of these parameters and inclusion of Kirchoff's flow theory in the model equations.

Where [15] was the first to implement Kirchoff's theory to an aircraft stall model, it only did so for the longitudinal motions. A method was coined in [47] to expand the same method to also the lateral-directional motions. The proposed model was defined with the equations for rolling and yawing moment:

$$C_\ell = C_{\ell_0} + C_{\ell_\beta}\beta + C_{\ell_p}p^* + C_{\ell_{\delta_a}}\delta_a + C_{\ell_{\delta_r}}\delta_r + \frac{b}{2}(C_{N,\text{left}} - C_{N,\text{right}})\Delta y \tag{2-11}$$

$$C_n = C_{n_0} + C_{n_\beta}\beta + C_{n_p}p^* + C_{n_{\delta_a}}\delta_a + C_{n_{\delta_r}}\delta_r + \frac{b}{2}(C_{c,\text{left}} - C_{c,\text{right}})\Delta y \tag{2-12}$$

With the normal force coefficient C_N and chord force coefficient C_c defined as:

$$\begin{aligned} C_{N,\text{left,right}} &= C_{L,\text{left,right}}\cos\alpha + C_{D,\text{left,right}}\sin\alpha \\ C_{c,\text{left,right}} &= C_{L_\alpha}\sqrt{X_{\text{left,right}}}\sin^2\alpha \end{aligned} \tag{2-13}$$

This model has a good ability to model also the aircraft asymmetric motions during a stall. It also provides in the significant asymmetric behaviour of aircraft in quasi-steady stall (uncommanded roll-off). Cross-coupling of derivatives may even further improve the model's behaviour. While it can also accurately describe dynamic stalls, not one parameter identification seems to be able to capture the behaviour in both types of stalls.

The complete model of both symmetric and asymmetric motions as described above is validated in [16] by use of wind tunnel data, and the effect of the model parameters for hysteresis and transient effects is investigated by use of flight data identification. The paper finds that for the longitudinal motions a distinction can be made between quasi-steady stalls and dynamic stalls, where it finds that quasi-steady stalls can be accurately modeled by only including the angle of attack rate and hysteresis effect, as defined by only the right side of Equation (2-3) with parameters a_1, α^* and τ_2. Dynamic stalls introduce strong transient effects into the stall behaviour and as such, this must be modeled by the full ODE of Equation (2-3) also including parameter τ_1. Also a review is done of the lateral motions. For these three cases the model accurately simulates the aircraft motion when compared to flight data.

2-3 TU Delft Citation Stall Modeling

The department of Control & Simulation of the Faculty of Aerospace Engineering of the Delft University of Technology makes use of the Delft University Aircraft Simulation Model and

Analysis Tool (DASMAT) for research into modeling and simulation of flight mechanics of the Faculty-owned Cessna Citation II aircraft [55]. The baseline model of the tool is the Citation 500 aircraft, but the tool is designed such that it can be made applicable to any type of aircraft or flight condition and over the course of time the model's fidelity was further increased to match that of the Citation II. Furthermore, the model allows further development of itself, for example extending the envelope of the model into the stall region. Together with the updated legislation by EASA as discussed above, this started the research of stall modeling from flight test data at the TU Delft.

The first research on this topic was performed in [54]. The goal of this research was to implement a new method to improve the fidelity of the normal-envelope DASMAT model for the Cessna Citation II aircraft, such that further research into the stall and post-stall region has a solid basis. This was done by using an Unscented Kalman Filter (UKF) for flight path reconstruction and using linear regression techniques in combination with a model structure selecting technique making use of Orthogonal Function Modeling (OFM). This structure selection procedure is further discussed in [37]. Results from [54] show that the UKF provides good reconstructions of flight data and the identified model structure and estimated parameters show significantly improved behaviour when compared to the original DASMAT model.

Building on the above research, the first research into the stall region was performed by [57]. This paper investigated how much of the stall model can be identified from only quasi-steady stall flight data. FPR was performed by UKF which showed reliable results. Unfortunately, due to the lack of an angle of sideslip-vane this could only be estimated via a "pseudo-beta" calculated from other states. Based on the flight data, nonlinear-parameter estimation methods were used to identify the longitudinal motion equations for lift, drag and pitching moment with inclusion of the Kirchoff coefficients and parameters as introduced above. All parameters could be estimated well, except for the transient τ_1 effect due to having no dynamic stalls in the dataset. For this, the paper also developed a stall buffet model not only for the sake of including this important behaviour, but is was also shown that this buffet model could be used to estimate the transient behaviour as well. This buffet model is based on a white noise signal passed through a second-order filter, activated based on the flow separation point from the Kirchoff model. Due to the lack of angle of sideslip-measurements no estimates could be made for the lateral motions. Also, no pitch rate coefficients could be estimated due to the data, again, only containing quasi-steady stall data and no excitations in the lower angle of attack region. Though, the model did prove reliable in the longitudinal motions in the stall region and could be implemented in the Citation II DASMAT stall model.

Based on the recommendations of [57], the stall model was further developed in [58]. This paper made use of orthogonal function modelling as was also performed by [54], but now applied to stall flight data and including Kirchoff's X parameter and variations thereof as possible regressors for the model structure selection. As the new flight data also included angle of sideslip-measurements the lateral motions could also be modeled. The identification methodology consisted of a nonlinear estimation for the X-parameters (α^*, a_1, τ_1, τ_2) from the calculated total lift coefficient C_L, after which X can be used as a possible regressor in the model structure selection. Iterating this process for all data sets and evaluating the frequency of selected regressors, a model structure was chosen whose parameters could then be estimated by making use of standard linear least-squares estimation. The paper found an effect of X for the lift and pitching moment models. The complete model showed high

correspondence with validation flight data compared to the existing models of [54] and [57]. Challenges that remain are that no pitch rate-related parameters were chosen in the structure selection, no effect of degraded rudder en aileron effectiveness or uncommanded roll-off could be incorporated in the model -even though these are important ICATEE stall characteristics, and also the yaw moment model showed lesser reliability. More flight test with more dynamic excitations before the stall could help improve the model further.

An attempt to improve on these shortcomings related to the lateral modeling of the Cessna Citation in stall was done in [11]. The model structure selection for the Cessna Citation was extended to make possible the choice of regressors for the left and right wing separately for the asymmetric model equations. The possible extension was of the $2X$-type, which included a separate X value for each wing, but one shared coefficient parameter associated with them. I.e. for the lift a $\left(\frac{1+\sqrt{X_{\text{left,right}}}}{2}\right)^2 \alpha_{\text{left,right}}$ term for both the left and right wing, but multiplied with the same constant C_{L_α}. This was compared to the "normal" $1X$ model with the original regressors with only one X for both wings. It was found that, even though the differences were moderate, the $2X$ model consistently scored better than the $1X$ model. Also an investigation was performed into the reduced control effectiveness and uncommanded roll acceleration as it was an important stall characteristic as defined by the regulator. However, no conclusive results could be found (yet) on this effect.

An important part of flight model development as performed in [57] and [58] is their applicability to actual use in flight simulators and flight training. Therefore not only the objective model behaviour is of importance, but also the subjective behaviour of the model as experienced in flight simulation by actual pilots. In [48], the model developed by [55], [57] and [58] has been used in the TU Delft Simona Research Simulator to determine Just Noticable Difference (JND) thresholds in aircraft behaviour as a result of varying key parameters in the model. This has been performed for the stall model with the Kirchoff parameters for τ_1 and a_1 based on the baseline values as found by [58]. It was found that the JND upper and lower thresholds for a_1 were +15% and -7% from the baseline value, respectively, and for τ_1 this was found to be as small as +31% and -25%, even while τ_1 has only limited objective effect on the model characteristics. This paper thus especially proves the importance of accurate and precise parameter estimation for stall models in order to provide a high-fidelity experience in the simulator.

Similar research has been performed by [25] in the Simona Research Simulator, but this time with the JND thresholds for the stall buffet model parameters as found by [57]. Both the stall buffet frequency and the threshold expressed in the separation point X_{thres} were investigated. Especially this last one does have a connection with stall modeling as a high-fidelity stall buffet model is thus dependent on a high-fidelity modeling of X. The JND threshold did not exceed 20% from the baseline value. Additionally, it was found that the differences in the X_{thres} for the buffet onset were even felt earlier than the ± 2 [deg] according to regulations. This puts even more emphasis on a good estimation of the X model parameters, as pilots are susceptible to even small differences and wrong estimates thus may easily induce mismatched feelings for pilots.

Remaining research of the TU Delft Citation Stall Modeling Group is performed on the Fokker 100 aircraft. In [31] a stall buffet model is developed for the aircraft and in [5] the Kirchoff model and Orthogonal Function Modeling is used to estimate an asymmetric stall

model. These papers were not further investigated, however the fact that the application of the methods used for the Citation are also used for modeling with the Fokker 100 reinforces the mandate of their use.

2-4 Conclusion on Stall Modeling Research using Kirchoff's Theory of Flow Separation

One of the main recommendations as provided in the research on the TU Delft's Cessna Citation II laboratory aircraft is the lack of dynamic excitations in the flight data before the stall. It is assumed the lack hereof plays a role in the unexpected lack of q-related regressors in the model as this is almost 0 during the stall, difficulties in modeling the expected -but not identified- degradation of control effectiveness towards the stall and the overall difficulty of identifying yawing behaviour.

In [12] an investigation has been performed into the effect of directly including dynamic manoeuvres before the stall. By making use of an elevator and rudder doublet in approach to the stall, the yawing effects on the longitudinal motions could be incorporated more pronounced in the model, as well as improvement of the pitch rate and angle of attack rate effects. However, correlation between the pitch rate and angle of attack rate remained present such that the new model does still not reproduce an exact quasi-steady stall manoeuvre for the longitudinal motions.

Whatever the conclusion or main focus of research papers into stall modeling using Kirchoff's theory of flow separation may be, very frequently a recurring recommendation is that more flight tests should be performed including different types of stalls, more excitations leading up to the stall in the different regressors, differently or more specifically designed control inputs, etc [54, 58, 11, 12]. However one could argue this may not be an efficient solution. Even in [5] the conclusion was drawn that the Fokker 100 database is not sufficient to estimate high performance stall models with the accuracy needed for pilot training. Even though the data base used here contained a incredible amount of stalls (already more than 200 stalls that also had to include notable bank angles in the data, of which 79 were usable), but lacked excitation in the control surfaces, creating unreliable estimates, yet again advocating for further flight testing. However, flight testing is an expensive practise and the many recommendations prove that performing yet more flight tests may still not yield the desired results. One could draw the conclusion that just the design of more flight test methods is thus not sustainable, and a more robust method, or as a start maybe just a better insight into it, must be found that aims to increase the value of already *existing* data in order to exploit it to its full potential. More discussion on flight testing and flight test data follows in chapter 3.

Chapter 3

Flight Test Data

In this chapter the test aircraft and its measurement system and the practice of gathering useful data by means of flight testing are discussed. First, a description is given of the Cessna Citation II test aircraft and its Flight Test Instrumentation System (FTIS) is given. Next, an overview of the flights and data that are used in this theses is given and the applicability throughout the flight envelope is investigated. Last, a literature review is done on flight test practices, input design and data information content, as this has may have an impact on the aerodynamic model estimation of the aircraft.

3-1 Test Aircraft and Flight Test Instrumentation System

The test aircraft used for the stall modeling at the TU Delft Citation Stall Modeling Group is a Cessna 550 Citation II aircraft with registration PH-LAB. It is a twin-engine turbofan aircraft built in 1993. A schematic overview of the aircraft is given in Figure 3-1 and a number of important dimensions and weights are given in Table 3-1.

Table 3-1: Properties of the PH-LAB Cessna Citation II aircraft.

Variable	Value	Unit
$\bar{c}$	2.09	m
b	15.9	m
S	30.0	m^2
m_{BEW}	4157.2	kg
$I_{xx_{BEW}}$	12392	kg·m^2
$I_{yy_{BEW}}$	31501	kg·m^2
$I_{zz_{BEW}}$	41908	kg·m^2
$I_{xy_{BEW}}$	2252.2	kg·m^2

The fuselage frame F_f is used to establish the location of aircraft equipment, payload and fuel aboard the aircraft and the location of the *c.g.*. The origin (or "datum") of the fuselage

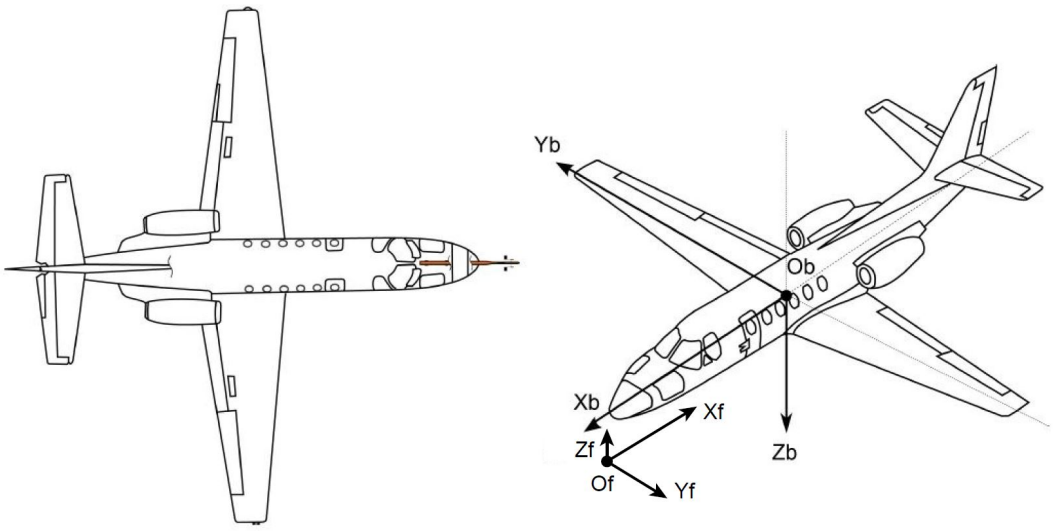

Figure 3-1: Schematic view of the Cessna Citation II PH-LAB, including the aircraft body frame F_b and fuselage frame F_f.

frame is fixed with respect to the airframe and is roughly 19 inch before and 91 inch below the nose of the aircraft.

The PH-LAB is equipped with a Flight Test Instrumentation System that is able to collect all data that is gathered during operation of the aircraft. An overview of the FTIS components aboard the aircraft is given in Figure 3-2. The FTIS gathers data on many different parameters, from aircraft orientation to activated autopilot modes. Not all data is relevant to this thesis. Details of all important sensors and data to this thesis that are incorporated in the FTIS are given in Table 3-2.

The different types of sources of measurements on board the FTIS are:

- *Analog:* Analog measurement data;
- *AHRS:* Attitude & Heading Reference System (Inertial Measurement Unit);
- *DADC:* Digital Air Data Computer;
- *GPS:* Global Positioning System;
- *Synchro:* Angle measurement data;
- *Interval:* Digital measurement data.

All different sensors have different sample rates and noise characteristics. The $N1$ measurements are variable in sample rate and variance, as the raw signal is a sinusoid of which the frequency changes with $N1$ and its value is calculated based on the period of the sinusoid at that moment. Thus its sample rate and variance vary as $N1$ varies. The different sample rates of all the different data sources may have an effect of the usability of the data when they are combined in analysis or modeling. Also the noise variance values say something about the reliability of the data. Both these factors need to be taken into account when performing the Flight Path Reconstruction in chapter 4.

A mass model has been developed of the PH-LAB which models all mass-related parameters of the aircraft and how these change during the flight like its mass, moments of inertia and

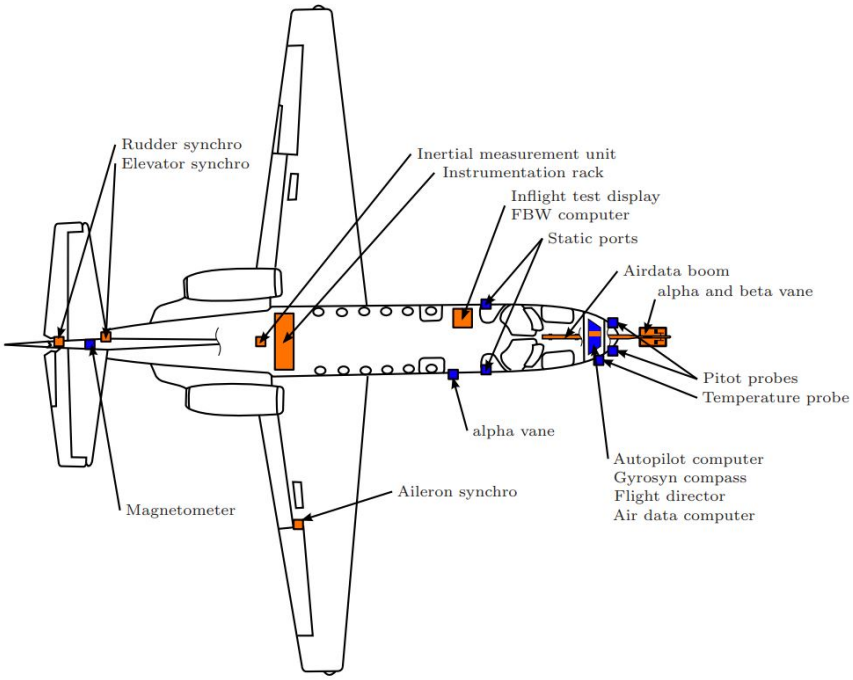

Figure 3-2: Overview of the FTIS components on board the PH-LAB.

center of gravity position. This is based on modeled components like taken fuel, payload and fuel flow during flight and their position and contribution to the total moment of inertia. It required an initialization based on specific start fuel and payload and passenger weights. If this is not available it assumes a standard initialization, which is very general. Therefore care should be taken to initialize the massmodel with the actual values that were present during the flight if this information is available.

3-2 Overview of Citation Flight Test Data

The PH-LAB is used extensively by the TU Delft and the Royal Netherlands Aerospace Centre NLR. Flights are performed for a large variety of different purposes in different parts of the flight envelope and with different types of (combinations of) measurement equipment. For example, the angle of attack and angle of sideslip vanes on the air data boom are not always installed on the aircraft. Also some flight may include manoeuvres that are not useful for the intended purpose of the modeling.

For the research in this thesis it is of importance that the data contains a significant number of stalls and sufficient excitation to be able to model the aerodynamic model accurately. It was decided that only flights are chosen that have available measurements from the air data boom and that were specifically flown for the purpose of stall modeling. There was also data available from other flights that included stalls, but the latter being not the main purpose of the flight. Also the air data boom is not available on some of these flights. To be able to model the lateral behaviour of the aircraft correctly air data boom measurements are critical [57, 58, 11] and thus only flights are chosen that include these measurements.

Table 3-2: Overview of measurement equipment available on the PH-LAB and relevant data variables with sample rates and measurement noise variances.

Source	Rate [Hz]	Variable	Description	Noise σ^2	Unit
Analog	1000	α_v	Angle-of-attack nose vane	$4.4 \cdot 10^{-8}$	rad
AHRS	52.1	φ	Roll angle	$2.8 \cdot 10^{-6}$	rad
		θ	Pitch angle	$4.5 \cdot 10^{-7}$	rad
		ψ	Yaw angle	$1.9 \cdot 10^{-6}$	rad
		p	Roll rate around X_B	$9.1 \cdot 10^{-4}$	rad/s
		q	Pitch rate around Y_B	$1.5 \cdot 10^{-4}$	rad/s
		r	Yaw rate around Z_B	$5.4 \cdot 10^{-5}$	rad/s
		A_x	Specific force along X_B	$3.9 \cdot 10^{-5}$	m/s^2
		A_y	Specific force along Y_B	$3.8 \cdot 10^{-4}$	m/s^2
		A_z	Specific force along Z_B	$2.7 \cdot 10^{-3}$	m/s^2
DADC	16.0	V_{TAS}	True airspeed	$2.5 \cdot 10^{-2}$	m/s
GPS	1.0	x	Position in X_E	$1.1 \cdot 10^{-1}$	m
		y	Position in Y_E	$1.1 \cdot 10^{-0}$	m
		z	Position in Z_E	$2.2 \cdot 10^{-2}$	m
		$\dot{x}$	Velocity along X_E	$2.3 \cdot 10^{-5}$	m/s
		$\dot{y}$	Velocity along Y_E	$2.4 \cdot 10^{-5}$	m/s
		$\dot{z}$	Velocity along Z_E	$1.0 \cdot 10^{-4}$	m/s
Synchro	100.0	δ_a	Aileron deflection	$1.4 \cdot 10^{-5}$	rad
		δ_e	Elevator deflection	$1.4 \cdot 10^{-4}$	rad
		δ_r	Rudder deflection	$4.0 \cdot 10^{-5}$	rad
		α_b	Angle-of-attack boom vane	$4.4 \cdot 10^{-4}$	rad
		β_b	Angle-of-sideslip boom vane	$2.1 \cdot 10^{-4}$	rad
Interval	variable	$N1_l$	Left engine (#1) fan speed	variable	%
		$N1_r$	Right engine (#2) fan speed	variable	%

Though, a general investigation of the effect of the lack of air data boom measurements on flight path reconstruction has been performed in chapter 4. Also, only flights were chosen that were purposefully performed for stall modeling as it is deemed that data from such a "quasi"-controlled environment provides the best basis to perform this research on.

The flights from which data is taken are listed in Table 3-3. The part of the flight envelope for which data is available from these flights is visualised in Figure 3-3. For an overview of all experiment runs in these flights and the plotted aircraft trajectory during these flights, see Appendix A.

In Figure 3-3 the three graphs contain all points in the Citation flight envelope where measurements are available from the four stall flights. The color of the data points show the associated angle of attack of that data point. Please note that this figure shows *all* data available from the flights, but that in practice usually only a specific selection is used in modelling that is most applicable to the intended model purpose and contains the most useful information.

In Figure 3-3a clearly the stall runs can be seen, with the increasing angle of attack as the Mach number decreases to the left. The main altitudes at which stall data has been collected

Table 3-3: List of stall flight tests.

Flight #	Date	From	Description
1	11-11-2016	[58]	Stall flights 2016 1 of 2
2	11-11-2016	[58]	Stall flights 2016 2 of 2
3	07-02-2018	-	Stall flight 2018
4	30-10-2019	-	Stall flight 2019

can easily be identified: at roughly 5700, 5000 and 4500 m for flight 1 and 2, at 2700 m for flight 3 and at 3200 m for flight 4. This delivers a dataset over a wide range of angle of attack and sideslip as is visible in Figure 3-3b, even for high angles of attack significant angles of sideslip could be achieved. The anomaly that is visible in this figure where the lowest α and β are achieved is the result of a significant wing dip during stall run 32.

Last, in Figure 3-3c the "load diagram" of the data is plotted but with the vibration in pitch rate instead of load factor (the steady state load factor cannot be calculated as the lift force is not known yet). But this figure also delivers important information: it can be observed that with decreasing equivalent air speed where the highest angles of attack are achieved, large variations and excitation in pitch rate begin to occur. The definition in [13] of a 'stall' is: "a loss of lift caused by exceeding the aeroplane's critical angle of attack, (...) which may be recognised by continuous stall warning activation accompanied by at least one of the following: a) buffeting (...)". However the critical angle of attack is not known as it based on the $C_{L_{max}}$, and there is no data on C_L for the flights as it is yet to be estimated. When investigating the time series of the flight data as in Appendix A, one of the clearest indications of the stall was thus not in the angle of attack, but more clearly the presence of the stall buffet which is -indeed- best visible in the pitch rate q. This is substantiated by Figure 3-3c where the high pitch rates are common at the low speeds. Because of this, in this thesis, the definition of the beginning of the stall is defined as the point where the stall buffet begins to occur in the data of q and the beginning of the stall recovery is when the buffet last occurs for that stall run.

3-3 Flight Data Information Content

As was concluded in chapter 2 the performed flight maneuvers present in the data signals are of high importance to acquire the desired usability of the data in regard to the correct estimation of the aerodynamic model. As found the most important requirement to the data seems to be that there exists sufficient dynamic excitation before the stall. The positive effect of this was for example proven in [12], even though for some model regressors there still remained difficulty in achieving the desired model quality. The findings in this case apply to the stall region modeling of aircraft, but the same requirement of sufficient excitation also applies to normal aircraft identification problems: there needs to be sufficient excitation in the data for the intended purpose of the desired model. A description of what the "amount of excitation" in data is, is given in this section.

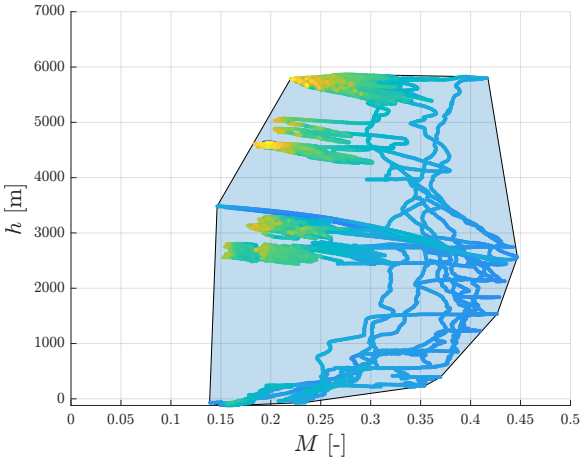

(a) Flight data within the flight envelope.

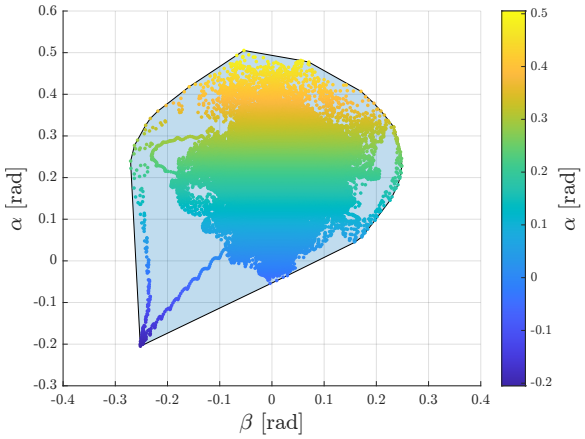

(b) Flight data for α and β.

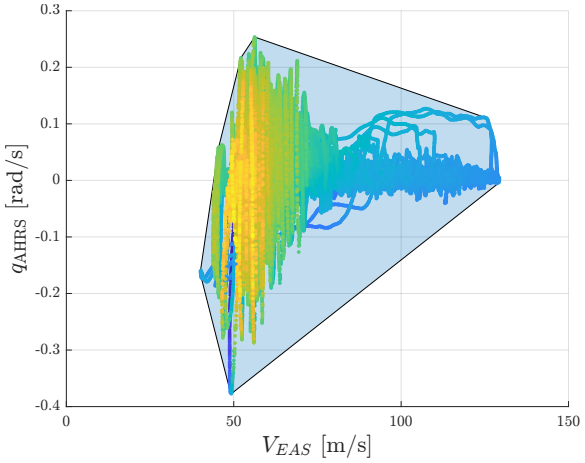

(c) Flight data for pitch rate q.

Figure 3-3: Overview of the gathered data within the flight envelope of the PH-LAB.

3-3-1 Information Content of Data

In [28] an introduction is given into flight test manoeuvre design. There are two main types of inputs: one are general inputs that excite the system over a broad frequency which is applicable to systems of which no or little a priori knowledge is known. Other are inputs that are designed with the system in mind because there is a priori knowledge, one of which are so-called "optimal inputs". Next to choosing the flight condition at which data is desired there are three main specifications that need to be defined for the input. These are the maneuver time length, which control surface to excite and the input form. These choices must be made with a common goal which is to maximize the information content in the data.

Nonparametric Descriptions of Information Content

The first general manner in which the information content can be quantified is via the signal-to-noise ratio. In fact, Flight Path Reconstruction as discussed in chapter 4 aims to achieve exactly this: an increase in signal to noise ratio of the data. A second quantification of

information content is in the frequency domain via the signal coherence Γ_{uy} between an input signal $u(t)$ and output signal $y(t)$, as defined in [41]:

$$\Gamma_{uy}(\omega) = \sqrt{\frac{S_{xx}(\omega)}{S_{yy}(\omega)}} = \sqrt{\frac{|S_{uy}(\omega)|^2}{S_{uu}(\omega)S_{yy}(\omega)}} \tag{3-1}$$

With S the power spectral density of the subscripted signal. The coherence is a measure of describing how much of a systems output y is contributed by the system response x under the influence of input u, as compared to the contribution of a noise signal n, the output is defined as:

$$y(t) = x(t) + n(t), \quad \text{with } x(t) = u(t) * h(t) \tag{3-2}$$

The coherence is 1 for full coherence (all output dictated by system response x) and 0 for no coherence. If u and y are uncorrelated, $S_{uy} = 0$ and thus so is their coherence. For two uncorrelated signals counts:

$$\mathrm{E}\{xy\} = \mathrm{E}\{x\} \cdot \mathrm{E}\{y\} \tag{3-3}$$

Two signals are not only uncorrelated but *also* orthogonal if:

$$\mathrm{E}\{xy\} = 0 \tag{3-4}$$

Both the signal-to-noise ratio and coherence are nonparametric and therefore apply to any model type.

Parametric Descriptions of Information Content

As aerodynamic models *are* parametric, other information content descriptions can be useful [28]. For a single-input-single-output model with one parameter, one can quantify information content by the sensitivity of the model output to changes in the parameter θ, which is given by the derivative $\frac{\partial y}{\partial \theta}$. The best input for such an experiment to estimate the parameter of that system maximizes the squared output sensitivity over the test time T. This is mathematically given by:

$$u^* = \max_{u \in U} \sum_{k=1}^{N} \left[\frac{\partial y(k)}{\partial \theta}\right]^2 = \min_{u \in U} \sum_{k=1}^{N} \left\{\left[\frac{\partial y(k)}{\partial \theta}\right]^2\right\}^{-1} \tag{3-5}$$

Where u^* is the scalar optimal input waveform over the specified test time $[0, T]$, U is the set of all admissible inputs and the summation over N time points approximates a time-integral where $T = N\Delta t$ with the sampling interval Δt. In practise the equation governs that the sensitivity of the output to changes in the model parameter (the derivative $\frac{\partial y}{\partial \theta}$) must be maximized with an optimal input. High output sensitivity thus means: a small change in the parameter θ results in a large change in output y, which enables an estimation routine to find

accurately the parameter value that results in the best fit between output y and the available measurement.

For multiple-input-multiple-output models with N_p number of parameters gathered in a parameter vector $\vec{\theta}$ and N_o the number of system outputs, the information content is given by the $N_p \times N_p$ information matrix M. Here the sensitivity is captured in the $N_o \times N_p$ output sensitivity matrix $S(k)$, which is given by:

$$S(k) = \begin{bmatrix} \frac{\partial y_1(k)}{\partial \theta_1} & \frac{\partial y_1(k)}{\partial \theta_2} & \dots & \frac{\partial y_1(k)}{\partial \theta_{N_p}} \\ \frac{\partial y_2(k)}{\partial \theta_1} & \frac{\partial y_2(k)}{\partial \theta_2} & \dots & \frac{\partial y_2(k)}{\partial \theta_{N_p}} \\ \vdots & \vdots & \ddots & \vdots \\ \frac{\partial y_{N_o}(k)}{\partial \theta_1} & \frac{\partial y_{N_o}(k)}{\partial \theta_2} & \dots & \frac{\partial y_{N_o}(k)}{\partial \theta_{N_p}} \end{bmatrix} \tag{3-6}$$

Then, the information matrix M is defined as:

$$M = \sum_{k=1}^{N} S(k)^T R^{-1} S(k) \tag{3-7}$$

Where R is a diagonal matrix of which the elements introduce a scaling to the output sensitivities according to the measurement noise related to that output, i.e. the noise covariance matrix. The information matrix M is also called the "Fisher Information". The Fisher Information is a very important concept in experiment design for model estimation as it is a measure of the information content of the data from an experiment. The sensitivity matrix $S(k)$ can be calculated by using finite differences on the dynamic equations of the to-be-estimated model, if this a priori knowledge of the model parameters is available.

- As an example the Fisher Information is calculated here for the C_L model of Equation (5-43). This equation consists of seven to-be-estimated parameters collected in vector $\vec{\theta}$, as given by Equation (5-58):

  $$\vec{\theta} = \begin{bmatrix} a_1 & \alpha^* & \tau_1 & \tau_2 & C_{L_0} & C_{L_\alpha} & C_{L_{\alpha^2}} \end{bmatrix}^T$$

  There is only one the one output measurement: y_{C_L}. The sensitivity matrix $S(k)$ then contains all derivatives of y_{C_L} relative to the parameters in $\vec{\theta}$. The resulting matrix $S(k)$ is the result of applying the chain rule via:

$$\begin{aligned} S(k) &= \begin{bmatrix} \frac{\partial y_{C_L}(k)}{\partial a_1} & \frac{\partial y_{C_L}(k)}{\partial \alpha^*} & \frac{\partial y_{C_L}(k)}{\partial \tau_1} & \frac{\partial y_{C_L}(k)}{\partial \tau_2} & \frac{\partial y_{C_L}(k)}{\partial C_{L_0}} & \frac{\partial y_{C_L}(k)}{\partial C_{L_\alpha}} & \frac{\partial y_{C_L}(k)}{\partial C_{L_{\alpha^2}}} \end{bmatrix} = \\ &= \begin{bmatrix} \frac{\partial y_{C_L}(k)}{\partial X(k)} \frac{\partial X(k)}{\partial a_1} & \frac{\partial y_{C_L}(k)}{\partial X(k)} \frac{\partial X(k)}{\partial \alpha^*} & \frac{\partial y_{C_L}(k)}{\partial X(k)} \frac{\partial X(k)}{\partial \tau_1} & \frac{\partial y_{C_L}(k)}{\partial X(k)} \frac{\partial X(k)}{\partial \tau_2} & \frac{\partial y_{C_L}(k)}{\partial C_{L_0}} & \frac{\partial y_{C_L}(k)}{\partial C_{L_\alpha}} & \frac{\partial y_{C_L}(k)}{\partial C_{L_{\alpha^2}}} \end{bmatrix} \end{aligned} \tag{3-8}$$

The derivatives in this matrix have been extensively discussed in chapter 5, resulting in the derivatives of Equation (5-66), Equation (5-68), Equation (5-69) and Equation (5-70). Altering these equations for use in the matrix $S(k)$ for the timestamp k, the derivatives when $\theta_i \in \{C_{L_0}, C_{L_\alpha}, C_{L_{\alpha^2}}\}$ become:

$$\frac{\partial y_{C_L}(k)}{\partial \theta_i} = \begin{cases} 1 & \text{when } \theta_i = C_{L_0} \\ \left(\frac{1+\sqrt{X(k)}}{2}\right)^2 \alpha(k) & \text{when } \theta_i = C_{L_\alpha} \\ \max(0, \alpha(k) - 6°)^2 & \text{when } \theta_i = C_{L_{\alpha^2}} \end{cases} \tag{3-9}$$

And the derivatives required when $\theta_i \in \{a_1, \alpha^*, \tau_1, \tau_2\}$ become:

$$\frac{\partial y_{C_L}(k)}{\partial X(k)} = \frac{1}{4} C_{L_\alpha} \alpha(k) \left(1 + \frac{1}{\sqrt{X(k)}}\right) \tag{3-10}$$

$$\frac{\partial G(k)}{\partial X(k)} = -\frac{1}{\tau_1} \tag{3-11}$$

$$\frac{\partial G(k)}{\partial \theta_i} = \begin{cases} -\frac{\frac{1}{2}\{1-\tanh^2[a_1(\alpha(k)-\tau_2\dot{\alpha}(k)-\alpha^*)]\}\{\alpha(k)-\tau_2\dot{\alpha}(k)-\alpha^*\}}{\tau_1} & \text{when } \theta_i = a_1 \\ -\frac{\frac{1}{2}\{1-\tanh^2[a_1(\alpha(k)-\tau_2\dot{\alpha}(k)-\alpha^*)]\}\{-a_1\}}{\tau_1} & \text{when } \theta_i = \alpha^* \\ -\frac{\frac{1}{2}\{1-\tanh[a_1(\alpha(k)-\tau_2\dot{\alpha}(k)-\alpha^*)]\}-X(k)}{\tau_1^2} & \text{when } \theta_i = \tau_1 \\ -\frac{\frac{1}{2}\{1-\tanh^2[a_1(\alpha(k)-\tau_2\dot{\alpha}(k)-\alpha^*)]\}\{-a_1\dot{\alpha}(k)\}}{\tau_1} & \text{when } \theta_i = \tau_2 \end{cases} \tag{3-12}$$

After which, just as in chapter 5, $\frac{\partial X(k)}{\partial \theta_i} = S$ (do not confuse S with $S(k)$!) is the value found when numerically integrating the ODE $\frac{dS}{dt} = \frac{\partial G(k)}{\partial X(k)} S + \frac{\partial G(k)}{\partial \theta_i}$.

Note that in this case it is thus not only important that the model structure is known, but also an a priori estimate of the parameters in $\vec{\theta}$ is needed as these are present in the derivative equations.

The inverse of the Fisher information M is the dispersion matrix D. The diagonal entries of the matrix D are shown in [28] to be the theoretical lower limit for the estimated parameters' covariances, i.e. the Cramér-Rao Lower Bound ($CRLB$). Mathematically:

$$D = M^{-1} \leq \text{Cov}[\vec{\theta}] \tag{3-13}$$

And thus, the Cramér-Rao Lower Bound for the parameter standard deviations σ_{θ_i} are the square-root of the diagonal elements of D, i.e.:

$$\sigma_{\theta_i} = \sqrt{D_{ij}}, \quad \text{with } i = j = 1, 2, \ldots, N_p \tag{3-14}$$

A significant advantage of the use of the Fisher Information in input design is that it gives the *theoretical* lower limit of the parameter covariances and is thus unrelated to the algorithm used in the actual estimation of the parameters. Therefore, the design of specific inputs or

the selection of what data to be used in the estimation of parameters can be performed *before* the estimation itself is done.

With the above knowledge, it can be concluded that the final goal of input design or data selection for aerodynamic estimation is to minimize the theoretical lower bound of parameter variances such that the certainty of the parameters that can be estimated is increased. And, as the contributions of each of the inputs (which are the regressors) to the information content are known via the derivatives in $S(k)$, it should be possible for one to *actively and directly* influence -or maybe even "tailor"- the certainty of the individual final estimated parameters by either using a specific control input or selecting specific data with a desired type of content.

3-3-2 A General Description of Stochastic Variables and Fisher Information

One peculiarity associated with the calculation of the Fisher Information above is that is is directly related to the model structure for which a priori knowledge is required. It may be worthwhile to also have a more general definition of the Fisher Information available that is more broadly applicable, even though its quality may be less.

Within the subject of the fundamentals of parameter estimation it is crucial to see the estimated parameter not as deterministic, but as a stochastic variable, i.e. its value depends on random circumstances. But within the randomness of all values possible for a stochastic variable, some values are more likely to occur than others. This behaviour can be expressed by the probability distribution function $F_{\bar{x}}$ for the stochastic variable $\bar{x}$ (the bar declaring the variable as stochastic) as a function of the deterministic quantity x. This is expressed as [41]:

$$F_{\bar{x}}(x) = \Pr\{\bar{x} \leq x\} \tag{3-15}$$

The probability of an event is always between 0 and 1 and is monotonously increasing, such that:

$$F_{\bar{x}}(a) \leq F_{\bar{x}}(b) \text{ if } a \leq b, \quad \text{s.t. } F_{\bar{x}}(-\infty) = 0 \text{ and } F_{\bar{x}}(+\infty) = 1 \tag{3-16}$$

The derivative of the probability distribution function $F_{\bar{x}}$ is the probability density function (pdf) $f_{\bar{x}}$, which is defined as [41]:

$$f_{\bar{x}}(x) = \frac{dF_{\bar{x}}(x)}{dx} = \lim_{\Delta x \to 0} \frac{\Pr\{\bar{x} \leq x + \Delta x\} - \Pr\{\bar{x} \leq x\}}{\Delta x} = \lim_{\Delta x \to 0} \frac{\Pr\{x < \bar{x} \leq x + \Delta x\}}{\Delta x}, \quad \text{where } f_{\bar{x}}(x) \geq 0 \tag{3-17}$$

Such that follows:

$$\begin{aligned} \int_{-\infty}^{+\infty} f_{\bar{x}}(x)dx &= F_{\bar{x}}(+\infty) - F_{\bar{x}}(-\infty) = 1 - 0 = 1 \\ \int_{-\infty}^{a} f_{\bar{x}}(x)dx &= F_{\bar{x}}(a) - F_{\bar{x}}(-\infty) = F_{\bar{x}}(a) \\ \int_{a}^{b} f_{\bar{x}}(x)dx &= F_{\bar{x}}(b) - F_{\bar{x}}(a) = \Pr\{a < \bar{x} \leq b\} \end{aligned} \tag{3-18}$$

Often the exact probability distribution or pdfs cannot be determined explicitly. Some other quantities can be introduced that still say something about these functions, even though they are itself unknown. For example, the expectancy of $\bar{x}$ is $\mathrm{E}\{\bar{x}\}$ which is the average value of the stochastic variable when infinite samples are taken. It is defined as the first order moment m_1 of the pdf [41]:

$$m_1 = \mathrm{E}\{\bar{x}\} = \int_{-\infty}^{+\infty} x f_{\bar{x}}(x) dx \tag{3-19}$$

Which is the called the mean value $\mu_{\bar{x}}$. Also a "central" moment can be taken which is the moment of the pdf relative to the mean. For example the first order central moment m_1' is defined as [41]:

$$\begin{aligned} m_1' &= \mathrm{E}\{(\bar{x} - \mu_{\bar{x}})\} = \int_{-\infty}^{+\infty} (x - \mu_{\bar{x}}) f_{\bar{x}}(x) dx \\ &= \int_{-\infty}^{+\infty} x f_{\bar{x}}(x) dx - \mu_{\bar{x}} \cdot \int_{-\infty}^{+\infty} f_{\bar{x}}(x) dx \\ &= \mu_{\bar{x}} - \mu_{\bar{x}} = 0 \end{aligned} \tag{3-20}$$

Saying basically that the expected deviation of $\bar{x}$ from the mean $\mu_{\bar{x}}$ is zero. The second order central moment is given as [41]:

$$m_2' = \mathrm{E}\{(\bar{x} - \mu_{\bar{x}})^2\} = \int_{-\infty}^{+\infty} (x - \mu_{\bar{x}})^2 f_{\bar{x}}(x) dx \tag{3-21}$$

Which is called the variance $\sigma_{\bar{x}}^2$ of the parameter x. Its square-root is then the standard deviation $\sigma_{\bar{x}}$.

The fundamental description of the stochastic variables above are needed for the general description of the Fisher Information in [30]. In a practical sense related to parameter estimation, a pdf can describe the probability that one observes a certain outcome x_i of a stochastic variable X_i given a *known* deterministic value of a parameter θ. The collection of all possible outcomes of X_i is denoted $\mathcal{X}$. The mathematical notation for this pdf is:

$$p_\theta(x_i) = f(x_i|\theta) \tag{3-22}$$

The Fisher Information $I_X(\theta)$ is then a measure to quantify the amount of information about the parameter θ embedded in the random variable X and is defined as [30]:

$$I_X(\theta) = \begin{cases} \int_{\mathcal{X}} \left(\frac{d}{d\theta} \log f(x|\theta) \right)^2 p_\theta(x) dx & \text{if } X \text{ is continuous} \\ \sum_{x \in \mathcal{X}} \left(\frac{d}{d\theta} \log f(x|\theta) \right)^2 p_\theta(x) & \text{if } X \text{ is discrete} \end{cases} \tag{3-23}$$

In this equation the derivative $\frac{d}{d\theta} \log f(x|\theta)$ is called the score function, which is a function of x describing how sensitive the model f is to changes in θ at a particular θ. Note the similarity of the Fisher Information definition to Equation (3-21). And indeed, the Fisher Information is actually the *variance* of the score function.

Also note that Equation (3-23) and Equation (3-7) are indeed the same. The term $S(k)^T S(k)$ of the sensitivity matrices is equivalent to the score function term $\left(\frac{d}{d\theta}\log f(x|\theta)\right)^2$ and the noise matrix R^{-1} is equivalent to the pdf $p_\theta(x)$ which fundamentally includes the "spread" of stochastic variable X which is included more explicitly in R. As Equation (3-7) is discrete rather than continuous it is a sum rather than an integral.

3-4 Flight Test Design

Where the last sections discussed how the amount of information in data can be quantified, it is also important to investigate how this information can be introduced into the data in practical terms. I.e. what types of manoeuvres are used in flight testing and how to select this data. There are multiple methods in which flight data can be gathered and stored. Even though the methods differ in approach, all aim to acquire the same goal: increasing the information content of the data about the to-be-estimated parameters in regions of interest.

3-4-1 Data Partitioning

As mentioned in chapter 2 the main challenge in the estimation of the stability and control derivatives at high angles of attack are the nonlinearities that exist in these regions. The Kirchoff Model is a method to incorporate these in a relatively simple model. However, when flight data is gathered over large variations of angle of attack or sideslip, it may be that the parameter estimates found are not "tailored" enough to the region of focus.

In [3] a method is discussed that aims to partition the available data by dividing a manoeuvre that covers a large range of some variable into several portions each of which spans a smaller range of that variable. Partitioning is then performed by eliminating the dependence of $y(t)$ on one of the variables $x_i(t)$ by redefining $y(t)$ on subsets of the variables $\{x_1, x_2, \ldots, x_3\}$. For example, for the yawing moment coefficient C_n it is expected that at high angles of attack (e.g. $20^\circ < \alpha < 30^\circ$) flow separation affects the yaw in a nonlinear manner. In that case the dependency of C_n on its variables, i.e.:

$$C_n = C_n(\alpha, \beta, p, r, \delta) \tag{3-24}$$

Can be partitioned into separate groups:

$$\begin{aligned} C_n(\alpha = 21^\circ) &= C_n(\beta, p, r, \delta), \quad \text{for } 20^\circ < \alpha < 22^\circ \\ C_n(\alpha = 23^\circ) &= C_n(\beta, p, r, \delta), \quad \text{for } 22^\circ < \alpha < 24^\circ \\ &\vdots \\ C_n(\alpha = 29^\circ) &= C_n(\beta, p, r, \delta), \quad \text{for } 28^\circ < \alpha < 30^\circ \end{aligned} \tag{3-25}$$

All available data of the outputs and inputs is then partitioned into the group where that certain angle of attack α was present. Every partition may in itself be partitioned further if necessary (i.e. the group $22^\circ < \alpha < 24^\circ$ may be further subdivided into $22^\circ < \alpha < 23^\circ$ and

$23° < \alpha < 24°$ or even smaller sections). Each partitions may have more or less data time present in it, depending on which manoeuvre was flown.

The paper of [3] also uses modified stepwise regression methods which can be used to find the best applicable model structure for each subdivision in the data. The final model will thus be more or less "scheduled" throughout all subdivisions not only in the parameter estimates, but may even differ for each subdivision in model structure itself.

The partitioning method delivered a richer set of points available to model nonlinearities at high angles of attack. However a drawback remains that as the subsets are partitioned, some may include no to little control surface deflections at all, which deteriorates the estimates of the control derivatives. A consideration should thus be made between the increase of quality of some some parameters due to partitioning as they capture nonlinearities better, while it may deteriorate for other derivatives as the data contains less information for those parameters.

3-4-2 Conventional Manoeuvres

Flight test manoeuvres can usually be divided into two groups: manoeuvres flown by conventional inputs and manoeuvres flown by optimal inputs. Conventional inputs are less tailored to the identification goal, but do not require any a priori information on the modeling or estimation technique, and are therefore still broadly applicable and widely used in flight testing (even though some can be tailored partly to some specific region of interest). They all have the aim to have some type of balanced perturbation around the trimming conditions, such that there *is* excitation, but the aircraft does not depart far from the desired flight condition.

A number of conventional inputs are listed below [28]. An overview of the time series and power spectrum of these inputs can be found in Figure 3-4. These are the *experimental* power spectra calculated from the signal via the Matlab `pspectrum()`-function. For square wave and pulse function the experimental spectra deliver incorrect results so also the analytical spectrum is plotted.

- *Impulse and double impulse.* The most rudimentary inputs are impulses. The double impulse consists of two impulse immediately following each other, which aims to keep the aircraft close to the initial condition. From the power spectrum it can be seen the impulse had a broad frequency range, but very low power. Because of the latter it is not very suitable for extensive aircraft identification purposes, but it can be used to excite some fundamental behaviour of the aircraft that make it useful in validation.

- *Frequency sweep.* The frequency sweep input is a sinusoid with changing frequency as the input is applied. It is performed to gain information on the aircraft responses over a broader frequency range. The application of the sinusoid's frequency can change over time in two manners, either linearly or logarithmicly. From the spectra it can be seen that for the linear case the information is more focused on the higher frequencies as the frequency is increased quicker than power can be accumulated for the lower-energy lower frequencies. A solution is to increase the frequency logarithmicly which gives more focus about the lower frequencies and therefore has a broader band in which the input accumulates power.

- *Multisine.* A multisine input is a sum of sinusoids with various frequencies and amplitudes superimposed on each other. The frequencies can be chosen such that information is gathered over a specific frequency band and the amplitudes can be chosen to accumulate a certain power over a specific frequency region. An often-used input are harmonically summed sinusoids, mathematically given by:

$$u(t) = \sum_{k \in K} A_k \cos\left(\frac{2\pi k t}{T} + \phi_k\right) \tag{3-26}$$

Where k is the k-th harmonic and is an integer in the set K of K_i frequencies of interest, whith which different combination can be made. A_k is the amplitude of sinusoid k, and T is the application time of the input. The same phase can be added to all harmonics to make sure that the input starts and ends at 0 input. The phase shifts ϕ_k can be optimized individually to reduce the crest factor of the signal. A common manner to do this is via:

$$\begin{aligned} A_k &= \sqrt{P/K_i} \\ \phi_0 &= 0 \\ \phi_k &= \phi_{k-1} - \frac{\pi k^2}{K_i} \end{aligned} \tag{3-27}$$

With P a chosen power level for that harmonic. In Figure 3-4e the power for increasing frequency is 1, 2 and then 3 for harmonics $k = 6$, $k = 12$ and $k = 24$ for $T = 18$ s. Note that the actual power are sole impulses on the three selected frequencies. This is the reason that sinusoisal inputs must always be a combination of multiple sinusoids as otherwise the bandwidth becomes too narrow.

More different and elaborate optimization techniques exist for making effective combinations of multisines and have for example been applied in [21], based on the same input type of Equation (3-26).

- *Pulse, doublet, 3-2-1-1 and 2-1-1.* Step-like input forms are very common conventional inputs, as they are very easy to apply manually, and by changing the time and amplitude of the inputs significant broadband excitation can be achieved. The basis of these inputs is the fundamental rectangular pulse function $\Pi(t)$. As the pulse function itself often causes significant departures from the desired flight condition, the most basic input is the doublet, as shown in Figure 3-4g.

The doublet analytical spectrum is centered around one dominant frequency, which can be changed by increasing or decreasing the application time of the two pulses. An application of the doublet is to be able to focus on a certain response at a certain frequency, but being more generally applicable than *one* sine wave input for which the *exact* frequency is needed to be known that excites the particular motion one is interested in. It can be especially interesting to use multiple doublets at different center frequencies to manually increase the broadband of the input.

The 3-2-1-1 input is the somewhat "manual" or rudimentary version of the frequency sweep. The long pulse followed by the shortened pulses imitates the increasing frequency

of the frequency sweep. Looking at the analytical spectrum the bandwidth of the 3-2-1-1 is rather wide and somewhat constant over that width. This relatively constant bandwidth over a wider range, combined with the ease at which this input can be flown (frequency sweep often requires more advanced automation) make it a very widely used input for identification purposes. The 3-2-1-1 manoeuvre is also extensively used in the flight of Table A-3.

The last conventional pulse-like manoeuvre used in aircraft identification is the 2-1-1, which is related to the 3-2-1-1 but with the added benefit the aircraft departs less from the intended flight condition, for example when very specific measurements at that condition are needed. However this comes at the cost of a lesser bandwidth.

- *Wiggle.* A last input type was introduced by [39] and was especially designed for pilot application, but where the 3-2-1-1 was not suitable. This is the "wiggle" which is a quasi-random noise introduced by manual inputs of the pilot. Especially during stall flight tests these can be useful as they do not make the aircraft deviate significantly from the desired stall entry trajectory and are simple for the pilot to apply. This input is modeled in Figure 3-4j as white noise passed trough lowpass filter with cutoff frequency of 5 Hz via Matlab's `lowpass()`-function. The resulting time series was also compared to the actual inputs given in the flights of Table A-1, Table A-2 and Table A-4 and they showed very similar behaviour. It can be seen that also the spectrum is rather wide and excites many different frequencies. A drawback is that on some control surfaces the quick movements may be hindered through control forces and the cutoff frequency decreases, such that the quasi-random signal approaches more and more that of a sine-wave, which was also observed in the mentioned flights for the δ_e deflections.

The advantage of conventional inputs is that they -depending on how much tailoring is required- can be applied by either the automation on board the aircraft or just manually by the pilot. Even manual inputs deliver reliable data with a good information content. This makes conventional inputs, despite their simplicity, still very applicable in aerodynamic model identification today.

3-4-3 Optimal Input Manoeuvres

Even though the conventional manoeuvres often deliver data that is already very useful, they remain *general*. As such, if some a priori knowledge about the to-be-modeled aircraft and to-be-modeled parameters is known, it should be possible to maximize the information content of the data by optimizing the inputs. These are called "optimal inputs". Optimal inputs consist of conventional inputs as the pulse-like inputs or multisines, but are optimized for their amplitude and application time or amplitude, frequency and phase, respectively. All input optimization techniques require maximization of the information in the data, and use some form of the information matrix as defined by Equation (3-7).

One of the earliest attempts at optimizing inputs for aerodynamic model identification was performed by [40], focusing on optimization of orthonormal sine functions by optimizing a cost function based on the trace of the inverse of the Fisher information, i.e. $J = \text{tr}[M^{-1}]$. The optimized orthonormal sine function (called the "DUT" method) inputs were compared to other input types, among which the conventional doublet and 3-2-1-1 inputs. In sample mean

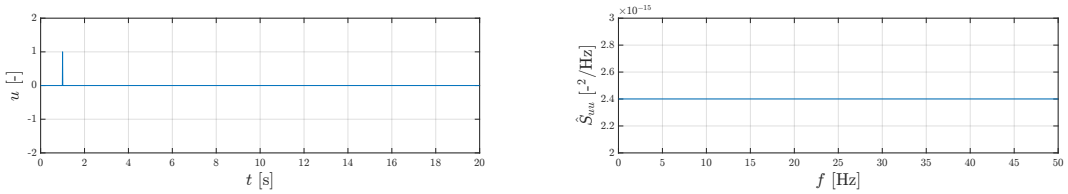

(a) Impulse.

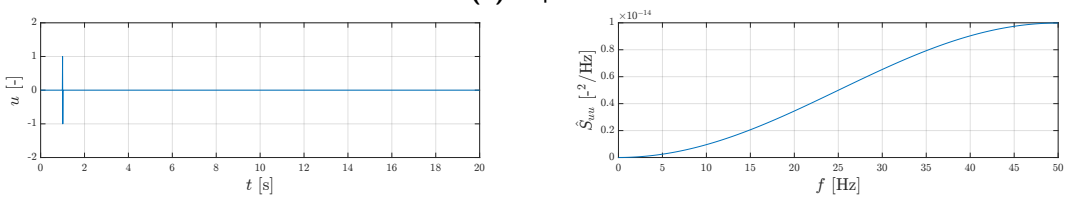

(b) Double impulse.

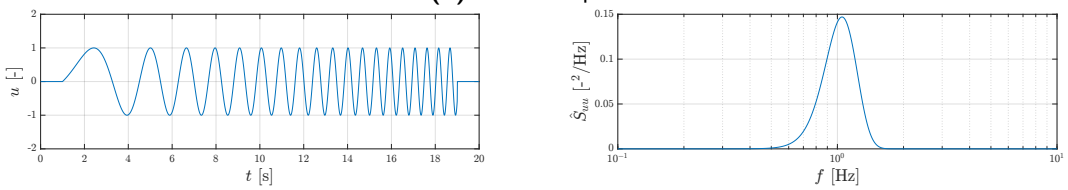

(c) Frequency sweep (linear).

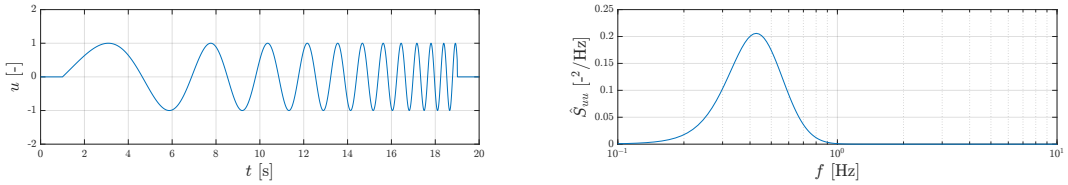

(d) Frequency sweep (logarithmic).

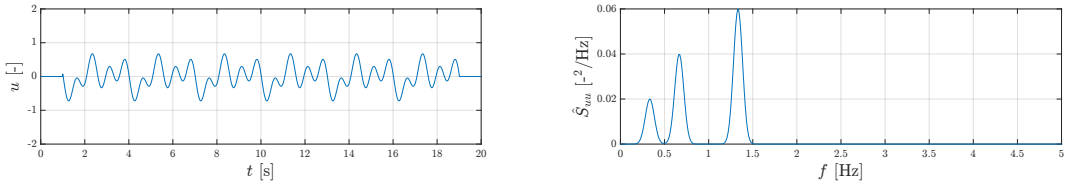

(e) Multisine.

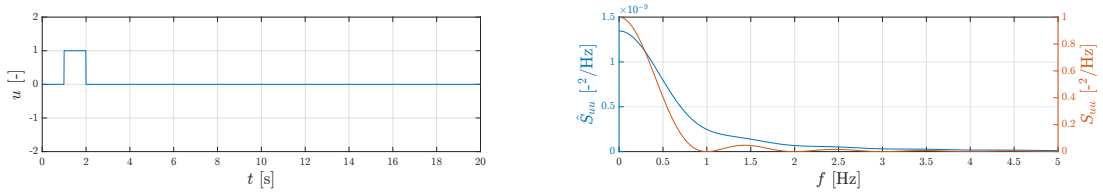

(f) Pulse. Blue is the experimental spectrum and red is the analytical spectrum.

Figure 3-4: (1/2) Timeseries and power spectra of conventional flight test inputs.

of the stability and control derivatives the DUT method had a bias better than the doublet input, but not better than the 3-2-1-1 manoeuvre. The mean itself generally was close to the 3-2-1-1 manoeuvre, but not always. The same conclusion holds for the standard deviations. It was concluded that the optimized inputs should be able to reach at least the same accuracy as the conventional methods, even though in the experiment itself the conventional 3-2-1-1

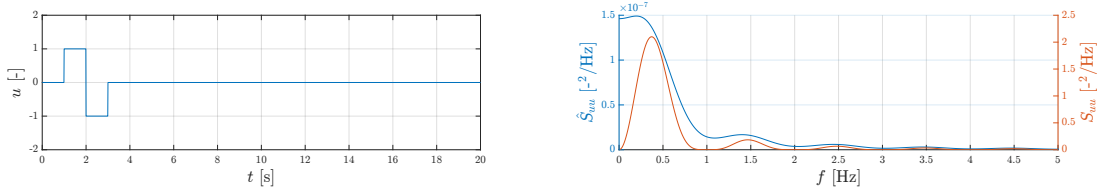

(g) Doublet. Blue is the experimental spectrum and red is the analytical spectrum.

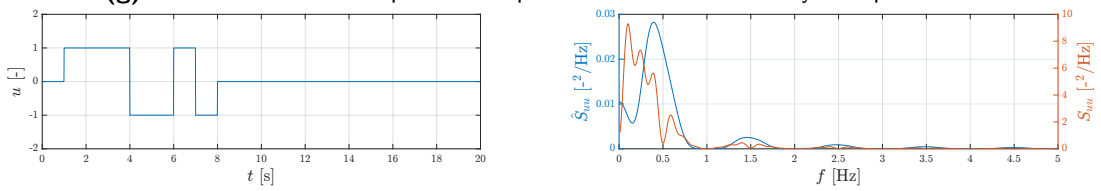

(h) 3-2-1-1. Blue is the experimental spectrum and red is the analytical spectrum.

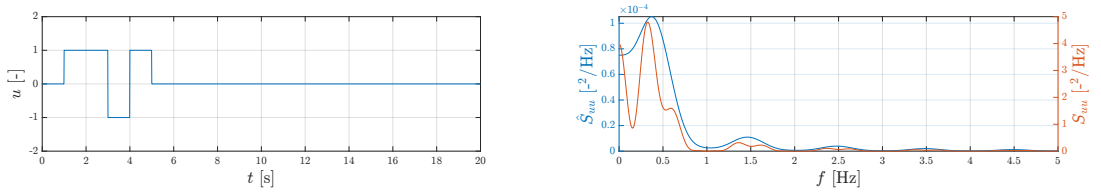

(i) 2-1-1. Blue is the experimental spectrum and red is the analytical spectrum.

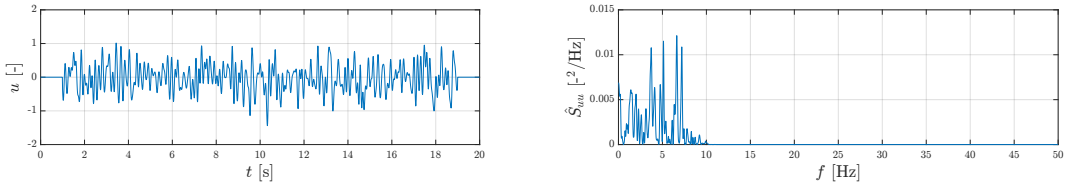

(j) Wiggle.

Figure 3-4: (continued, 2/2) Timeseries and power spectra of conventional flight test inputs.

manoeuvre had very good performance that the optimized signal could not yet match.

Just as [40] compared its own optimization technique to the conventional doublet and 3-2-1-1 manoeuvres, the same was done in [35]. The same choice was made on cost function for the optimal inputs, being the trace of the dispersion matrix D. Rather than using sine functions, the aim was to construct an optimal square-wave input signal based on pulses. Via dynamic programming including a number of constraints, optimal control inputs for the different control surfaces were found and applied to a F-18 aircraft. In the lateral case, the estimated parameter standard deviation were on average 20% smaller with the optimal inputs. For longitudinal motions this was as high as 72%. In the longitudinal case estimated standard deviation were also 64% better than the doublet estimates. This research in this paper showed what [40] could not yet achieve: surpassing the conventional inputs' estimation performance.

A comparable optimization was performed by [46], but extended the optimization of optimal input design via dynamic programming for a single flight test to that of an entire protocol: multiple flight tests with multiple experiments during testing of commercial airliners at Airbus. The paper proves the possible far-reaching impact that optimal input design can have on flight testing: entire protocols can, theoretically, be created that are the most efficient in information maximization of the data. This could save not only money and costs, but moreover removes the rather large heuristics that are present in flight test design. Unfortunately

the designed method was not further validated.

In [36] the optimal input design is applied to orthogonal multisines in the form of Equation (3-26), to optimize the inputs on all three control surfaces concurrently on a hypersonic vehicle. The goal of the multisine was optimization of the phase-shift ϕ_k for all harmonics with as a goal minimizing the crest factor. After each experiment run using the multisine inputs a conventional 2-1-1 manoeuvre was applied for validation and comparison. The multisine inputs delivered results that were comparable to that of the 2-1-1 data, proving the applicability of the multisines. The same optimization technique was applied to a scale model of a commercial airliner in [38]. Also here the results show the applicability of optimized multisines as inputs for flight model identification. However, the input signals are significantly complex, such that it was concluded that manually applying these inputs is not possible. It should thus be assessed if an aircraft has enough advanced automation capable of performing these manoeuvres when looking to apply this method to full-scale commercial flight testing.

3-5 Conclusion on Flight Test Manoeuvres and Flight Test Data Selection

From the above analysis, one thing has become clear: for aerodynamic model identification purposes not only the quantity, but also the quality of the gathered data is of great importance to be able to construct reliable models. The former could be seen as the amount of absolute information available, and the latter as the density of information within signals *that is applicable to a specific model structure*. But evidently from chapter 2 it remains clear that even when more and more data is gathered, the same problems seem to re-occur: the data does more than often appear to not be entirely suitable to find very reliable estimates for some of the parameters in the models. Often the recommendation is made for more data *quantity*: more flight tests should be performed. Quality of the data can then only be increased by increasing said quantity.

This thesis argues that there are more methods to increase the quality of the data, especially with regards to stall modeling, based on the findings in the current chapter. One starting point is that current research of the TU Delft Citation Stall Modeling Group already provides a robust and substantiated model structure via [58]: this means that a priori information is available about the model. The second starting point is that the method of partitioning learns that depending on how data is sliced, it can deliver different estimates for the model parameters than if it were not sliced: there exists a relationship between the data slicing and model performance.

Two methods to increase model quality via increase of data quality (i.e. the information content) are deemed possible because of these the above two prerequisites: 1) using optimal flight manoeuvre modeling techniques via the Fisher information to increase the data quality with respect to stall manoeuvres that cannot be attained via the conventional methods, or 2) using partitioning or specific timeseries slicing to increase the quality of the data to use data that is more applicable to the stall modeling and leave out data that may affect the estimates toward more neutral flight conditions, also via the Fisher information. The Fisher information may be a very powerful tool in this as the a priori known model structure gives an opportunity to recurrently assess the information content specific to this model.

Some advantages and disadvantages arise for both methods. For the first, it is another manner of creating more data quantity, which costs time and money. Also, a more practical concern is that it is not yet known if the PH-LAB is available in planning terms, or if any of the hardware and automation aboard the aircraft is sufficiently advanced to precisely execute optimal inputs correctly. Tough, no literature has been found that directly implements optimal input methods to a full-scale commercial aircraft.

For the second, significantly less resources are required. A disadvantage may be though that information content is defined by a *sum*: is more data not always better, even if it is sliced very specifically to increase quality with respect to a desired model structure? On the other hand, there is no literature on any slicing methods, both with respect to stall modeling nor any other aerodynamic modeling focus region. Already between [57] and [58] exist large differences: about 8 s per stall versus 50 s, respectively, but no specific reasoning has been given for the choice. Furthermore, if a method can be developed that relates slicing of data via the Fisher information and the quality of the estimated model exists, this is something that could be widely applied and creates a concrete protocol for *any* future research on stall modeling.

Chapter 4

Flight Path Reconstruction

The first step in processing the gathered data to to perform Flight Path Reconstruction (FPR). The data signals as described in chapter 3 contain an unknown noise and bias as the sensors are not perfect. Furthermore, there is a difference in sampling rate of the numerous signals. This causes the problem that the only available data is not only "wrong" (because of the noise and bias) but also that the data cannot be used for modeling "as is". For example, a signal with a 52.1 Hz sampling rate cannot be used to explain dynamics observed in a 1 Hz signal.

This means that, in order to be able to use the data for modeling, the noises and biases must be filtered as well as a estimation must be made of the signals that would have been measured if all variables were measured by the same sampling rate. This process is called FPR and can be performed by applying a Kalman Filter (KF).

For this thesis an Unscented KF (UKF) is used. As there are many types of Kalman Filters with each their own characteristics and applicability, the reasoning behind this choice is discussed first. Second, the mathematical workings of the UKF is discussed. Thereafter, the specific kinematic and measurement model which is applied to the data is explained, this includes the two different models for both data with measurements of the air data boom and without. Then, the required pre- and post-processing steps of the data are discussed. The chapter concludes with a tuning of the UKF and testing its performance on actual flight data.

4-1 Considerations on Kalman Filter Type

The original KF is an optimal filter with a guaranteed convergence, which makes it an incredibly powerful tool in state estimation procedures. However, it is only applicable to purely linear system dynamics. In order to deal with nonlinear systems -as is the problem of FPR in this thesis- the KF can be extended with a integration step to obtain the state prediction and linearization step to use the steps from the normal KF: the Extended Kalman Filter (EKF). Or, when including an iterative inner loop in the procedure, the Iterated Extended Kalman Filter (IEKF) for improved convergence behaviour. An even further extension is the UKF in

which linearization is not needed, aiming for further improved estimation for highly nonlinear models.

All previous TU Delft Citation models have been developed from flight data filtered by the UKF [54, 57, 58], which showed reliable results. In [57] an elaborate investigation has been performed into the performance of the IEKF, the Unscented Kalman Filter and different types of smoother algorithms. It was found that the IEKF and UKF had the best performance. They were comparable in their performance, even though the computational time of the IEKF was significantly shorter. However, as the filtering on the data only needs to be performed once and then can be saved for further use, computation time is not a dealbreaker. But additionally, it was also found that for the UKF the choice of noise covariances matrices was less crucial, and as it also omits linearization which theoretically should provide superior reliability.

In external research of [4] the use of the EKF has been compared to the UKF for an online, recursive FPR practise with real flight data. Even though the research of this thesis is not a recursive but rather an offline FPR problem, the main conclusions of this paper are still applicable as the fundamentals of the state estimation work the same. The paper finds that there is no significant improvement when using the UKF over the EKF. Both provide reliable results. Even though the UKF has a slightly higher reliability of the estimated parameters and faster convergence, it comes at a higher computational power. The EKF does still provide reliable results. In further research in [49] the performance of the EKF, IEKF and UKF are compared in relation to purely the FPR. It is found here that, even though all again provide reliable results, the UKF provides the highest reliability in relation to noise levels, tuning of the noise covariance matrix and estimation of IMU bias terms. The estimation of the IMU bias terms in combination with GPS measurements is a form of "sensor fusion" which is also incorporated in the FPR of [54, 57, 58]. A further analysis on the effect of KF choice in the case of sensor fusion has been researched in [22]. Comparable, reliable results are obtained from both the EKF as UKF when sensor fusion is incorporated in the FPR procedure. Further improvements may even be found for the EKF when some states are modeled not as a constant but as random walk (as also implemented for wind estimation in [57]).

Because the preferred method for the TU Delft Citation stall modeling group is the use of the UKF, external research confirms the reliability and applicability of the UKF, and computational time is not a stringent factor, the UKF was chosen to perform the FPR in this research.

There also exist different versions of the UKF. One that was considered for use in the FPR is the Square-Root UKF as presented by [56]. The aim of the Square-Root UKF to improve the numerical stability of the filter by making use of direct propagation of the sigma points via QR decomposition, Cholesky factor updating and efficient least-squares, instead of updating a new set of sigma points as in Step 1 described below. The paper finds that the square-root UKF has no lesser performance that the normal UKF, but has lower computational cost and the desired higher numerical stability. However the specific structure of the kinematic and measurement equations in the FPR problem of this thesis with the use of sensor fusion and noise within the input signal makes the Square-Root UKF unfeasible. Also, when testing the normal UKF desirable results were already obtained, thus the normal UKF was chosen.

4-2 The Unscented Kalman Filter

In this section a description is given of the UKF. Regard a system whose behaviour is described by a set of nonlinear ordinary differential equations as a function of states: $f(\vec{x})$. As often not all states are directly measurable, also regard a set of measurement equations relating the measurement signals to the states: $h(\vec{x})$. Next to being a function of the states, both equations can also be affected by a certain input $\vec{u}$ and noises $\vec{w}$ and $\vec{v}$. Of course, these variables may all be a function of time t, as well as the equations themselves. This results in a system of equations for state derivatives $\dot{\vec{x}}$ and measurements $\vec{z}$, defined as:

$$\begin{aligned} \dot{\vec{x}}(t) &= f(\vec{x}(t), \vec{u}(t), \vec{w}(t), t) \\ \vec{z}(t) &= h(\vec{x}(t), \vec{u}(t), \vec{v}(t), t) \end{aligned} \tag{4-1}$$

In practise for $\vec{z}$, the actual measured signal (denoted by subscript "$_m$") is not continuous, but discrete at times t_i. As discussed later in this chapter, for input $\vec{u}$ also a discrete, measured signal is used. This results in the system description:

$$\begin{aligned} \dot{\vec{x}}(t) &= f(\vec{x}(t), \vec{u}_m(t), \vec{w}(t), t) \\ \vec{z}_m(t_i) &= h(\vec{x}(t_i), \vec{u}_m(t_i), \vec{v}(t_i), t_i), \quad \text{for } i = 1, 2, \dots \end{aligned} \tag{4-2}$$

For the purposes of FPR, it is assumed that the process noises $\vec{w}$ are introduced into the system via noise present in the input signal and thus related to $\vec{u}_m$, while the sensor noise $\vec{v}$ is introduced via noise in the measurement signals due to imperfection of the sensors aboard the aircraft and thus related to $\vec{z}_m$. It is assumed all noises have a constant zero mean and a certain constant variance, but are mutually uncorrelated. Expressed in terms of matrices Q and R relating the variance to the input and measurement signals this is:

$$\begin{aligned} \mathrm{E}\{\vec{w}(t)\} &= 0 \\ \mathrm{E}\{\vec{w}(t)\vec{w}^T(\tau)\} &= Q = \begin{bmatrix} \sigma^2_{w_{u_1}} & 0 & \cdots & 0 \\ 0 & \sigma^2_{w_{u_2}} & \cdots & 0 \\ \vdots & \vdots & \ddots & \vdots \\ 0 & 0 & \cdots & \sigma^2_{w_{u_n}} \end{bmatrix} \\ \mathrm{E}\{\vec{v}(t_i)\} &= 0 \\ \mathrm{E}\{\vec{v}(t_i)\vec{v}^T(t_j)\} &= R = \begin{bmatrix} \sigma^2_{v_{z_1}} & 0 & \cdots & 0 \\ 0 & \sigma^2_{v_{z_2}} & \cdots & 0 \\ \vdots & \vdots & \ddots & \vdots \\ 0 & 0 & \cdots & \sigma^2_{v_{z_m}} \end{bmatrix} \\ \mathrm{E}\{\vec{w}(t)\vec{v}^T(t_i)\} &= 0 \end{aligned} \tag{4-3}$$

The variances in the Q and R matrices are usually known from the sensor characteristics as in Table 3-2. However, while testing the UKF it was found using these values directly do not result in the required UKF performance, thus the values as in Table 4-5 were used.

When using the UKF it is regarded that the states $\vec{x}$ are stochastic variables with a certain mean/expectancy and variance. When denoting the actual, correct, state as $\vec{x}$ and its mean as $\hat{\vec{x}}$, its mean and covariance matrix are given by:

$$\begin{aligned} E\{\vec{x}\} &= \hat{\vec{x}} \\ E\{(\hat{\vec{x}}-\vec{x})(\hat{\vec{x}}-\vec{x})^T\} = P &= \begin{bmatrix} \sigma_{x_1}^2 & 0 & \cdots & 0 \\ 0 & \sigma_{x_2}^2 & \cdots & 0 \\ \vdots & \vdots & \ddots & \vdots \\ 0 & 0 & \cdots & \sigma_{x_L}^2 \end{bmatrix} \end{aligned} \tag{4-4}$$

The fundamentals of the UKF were developed in [26] by introducing the Unscented Transform (UT). Practical application of the UKF for system identification purposes based on this UT has been introduced in [59]. The main advantage of the UKF, as has been mentioned, is that no linearization is needed for propagation of the state estimate statistics. This means that it is able to capture up to third order nonlinearities, compared to only the first order (due to linearization) in the EKF. This may improve convergence of the UKF in cases where the EKF may be sub-optimal or even divergent. The description of the UKF below is based on these two papers and the described algorithms.

Below, the fundamentals of the UKF and UT are described first. Thereafter, the UKF procedure is discussed step by step, as depicted in Figure 4-1. Last, the tuning of the Q and R matrices is discussed for use in the UKF.

4-2-1 Fundamentals of the UKF

Rather than using the linearized dynamics in form of the Jacobians to propagate the statistics of the state variables as with the IEKF, the UKF makes use of the Unscented Transform that directly propagates the statistics. To achieve this the UT propagates a set of "sigma points" $\mathcal{X}$ chosen such that their sample means and sample covariances are $\hat{\vec{x}} = E\{\vec{x}\}$ and $P^{xx} = E\{(\vec{x}-\hat{\vec{x}})(\vec{x}-\hat{\vec{x}})^T\}$, respectively, and propagates these through the nonlinear function of the system dynamics, yielding a cloud of transformed points with the statistics $\hat{\vec{y}}$ and P^{yy}.

The sigma points are grouped in a matrix that consists of $2L+1$ sigma vectors $\vec{\mathcal{X}}_i$, with L the number of state variables. These vectors are given by:

$$\begin{aligned} \vec{\mathcal{X}}_0 &= \hat{\vec{x}} \\ \vec{\mathcal{X}}_i &= \hat{\vec{x}} + \left(\sqrt{(L+\lambda)P^{xx}}\right)_i, \quad \text{for } i = 1,\ldots,L \\ \vec{\mathcal{X}}_i &= \hat{\vec{x}} - \left(\sqrt{(L+\lambda)P^{xx}}\right)_{i-L}, \quad \text{for } i = L+1,\ldots,2L \end{aligned} \tag{4-5}$$

Resulting in the complete L-rows-by-$(2L+1)$-columns sigma point matrix $\mathcal{X}$, given by:

$$\mathcal{X} = \begin{bmatrix} \vec{\mathcal{X}}_0 & \vec{\mathcal{X}}_1 & \cdots & \vec{\mathcal{X}}_L & \vec{\mathcal{X}}_{L+1} & \cdots & \vec{\mathcal{X}}_{2L} \end{bmatrix} \tag{4-6}$$

In which each vector has its respective weight:

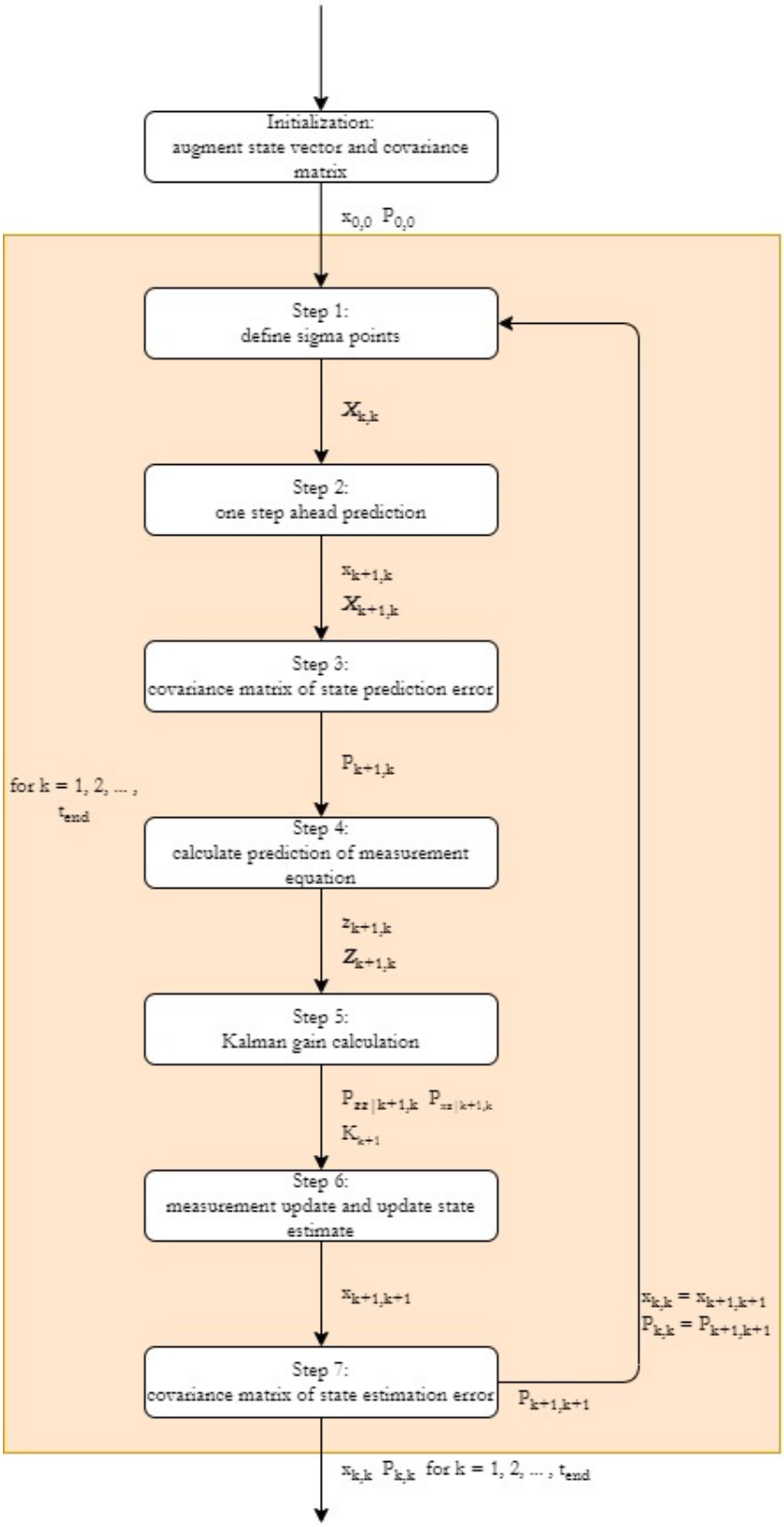

Figure 4-1: Overview of the Unscented Kalman Filter procedure.

$$\begin{aligned} W_0^{(m)} &= \lambda/(L+\lambda) \\ W_0^{(c)} &= \lambda/(L+\lambda) + (1-\alpha^2+\beta) \\ W_i^{(m)} &= W_i^{(c)} = 1/[2(L+\lambda)], \quad \text{for } i = 1,\ldots,2L \end{aligned} \tag{4-7}$$

In which λ is a scaling parameter defined as:

$$\lambda = \alpha^2(L+\kappa) - L \tag{4-8}$$

In which α is a constant determining the spread of the sigma points around $\hat{x}$ of a certain state and usually a small positive value (i.e. $1.0 \cdot 10^{-3}$), κ a secondary scaling parameter usually set to 0, and β is used to incorporate knowledge about the distribution of the state x, which for a Gaussian distribution $\beta = 2$ is optimal. These three parameters can be used to tune the UKF, performed later in this chapter. Last, $\left(\sqrt{(L+\lambda)P^{xx}}\right)_i$ is the ith column of the matrix square root of $(L+\lambda)P^{xx}$.

With the sigma points defined, the transformation procedure can be performed on the sigma point matrix, which is mathematically described by:

1. Propagate each point through the function to yield the set of transformed sigma points:

$$\vec{\mathcal{Y}}_i = f(\vec{\mathcal{X}}_i), \quad \text{for } i = 0,\ldots,2L \tag{4-9}$$

2. Calculate the mean of the transformed state vector:

$$\hat{\vec{y}} = \sum_{i=0}^{2L} W_i^{(m)} \vec{\mathcal{Y}}_i \tag{4-10}$$

3. Calculate the covariance of the transformed state vector:

$$P^{yy} = \sum_{i=0}^{2L} W_i^{(c)} (\vec{\mathcal{Y}}_i - \hat{\vec{y}})(\vec{\mathcal{Y}}_i - \hat{\vec{y}})^T \tag{4-11}$$

4-2-2 Mathematical Description of the UKF

The above steps comprise the UT, which is at the core of the UKF procedure as explained below. All steps below are performed for every timestep $t_k,\ k = 1, 2, \ldots$ of the data.

Initialization: Augment State Vector and Covariance Matrix

A preliminary step to be able to apply the UKF is to restructure the state vector, covariance matrix and process and observation models (with superscript ^{a} for "augmented"). The estimate of the state vector and its coviariance matrix are concatenated with the process and measurement noise terms, via:

$$\begin{aligned}\hat{\vec{x}}^a_{k,k} &= \begin{bmatrix}\hat{\vec{x}}^x_{k,k}\\ \hat{\vec{x}}^w_{k,k}\\ \hat{\vec{x}}^v_{k,k}\end{bmatrix} = \begin{bmatrix}\hat{\vec{x}}_{k,k}\\ \hat{\vec{w}}_k\\ \hat{\vec{v}}_k\end{bmatrix} = \begin{bmatrix}\hat{\vec{x}}_{k,k}\\ \vec{0}\\ \vec{0}\end{bmatrix}\\ P^a_{k,k} &= \begin{bmatrix}P^{xx}_{k,k} & P^{xw}_{k,k} & P^{xv}_{k,k}\\ P^{xw}_{k,k} & P^{ww}_{k,k} & P^{wv}_{k,k}\\ P^{xv}_{k,k} & P^{wv}_{k,k} & P^{vv}_{k,k}\end{bmatrix} = \begin{bmatrix}P_{k,k} & P^{xw}_{k,k} & P^{xv}_{k,k}\\ P^{xw}_{k,k} & Q_k & P^{wv}_{k,k}\\ P^{xv}_{k,k} & P^{wv}_{k,k} & R_k\end{bmatrix} = \begin{bmatrix}P_{k,k} & 0 & 0\\ 0 & Q & 0\\ 0 & 0 & R\end{bmatrix}\end{aligned} \tag{4-12}$$

Such that the augmented model description becomes a function of the augmented state vector:

$$\dot{\vec{x}}^a(t) = f(\vec{x}^a(t), \vec{u}_m(t), \vec{w}(t), t) \tag{4-13}$$

Step 1: Define Sigma Points

The first step is to define the sigma points making use of the augmented model and the procedure described in Equation (4-5), where the mean value $\hat{\vec{x}}$ for the state is now the current state estimate $\hat{\vec{x}}$. Also take into account now that L equals the number of states plus number of input noises and number of measurement noises. In matrix form this is given by:

$$\begin{aligned}\mathcal{X}_{k,k} = \mathcal{X}^a_{k,k} &= \overbrace{\begin{bmatrix}\vec{\mathcal{X}}^x_{0|k,k} & \cdots & \vec{\mathcal{X}}^x_{2L|k,k}\\ \vec{\mathcal{X}}^w_{0|k,k} & \cdots & \vec{\mathcal{X}}^w_{2L|k,k}\\ \vec{\mathcal{X}}^v_{0|k,k} & \cdots & \vec{\mathcal{X}}^v_{2L|k,k}\end{bmatrix}}^{2L+1} =\\ &= \begin{bmatrix}\hat{\vec{x}}^a_{k,k} & \overbrace{\hat{\vec{x}}^a_{k,k} + \left(\sqrt{(L+\lambda)P_{k,k}}\right)_i}^{i=1,\ldots,L} & \overbrace{\hat{\vec{x}}^a_{k,k} - \left(\sqrt{(L+\lambda)P_{k,k}}\right)_{i-L}}^{i=L+1,\ldots,2L}\end{bmatrix}\end{aligned} \tag{4-14}$$

Step 2: One Step Ahead Prediction

With the set of sigma points defined, the transformation to the prediction of the next timestep can be performed by using the actual, nonlinear system function on each column of $\mathcal{X}$ via the procedure of Equation (4-9), by integrating to the next timestamp. Note that we only need to calculate the update for states of the original $\vec{x}$, i.e. with superscript ^{x}.

$$\vec{\mathcal{X}}^x_{i|k+1,k} = \vec{\mathcal{X}}^x_{i|k,k} + \int_{t_k}^{t_{k+1}} f(\vec{\mathcal{X}}^x_{i|k,k}, \vec{u}_k, \vec{\mathcal{X}}^w_{i|k,k}, t)dt, \quad \text{for } i = 0, \ldots, 2L \tag{4-15}$$

For the integration the classical Runge-Kutta method is applied (from t_k to t_{k+1} in one step $h = \Delta t$), which is described in [27]. Applying this method to Equation (4-15) gives:

$$\vec{\mathcal{X}}^x_{i|k+1,k} = \vec{\mathcal{X}}^x_{i|k,k} + \frac{1}{6}(k_1 + 2k_2 + 2k_3 + k_4), \quad \text{for } i = 0, \ldots, 2L \tag{4-16}$$

With:

$$\begin{aligned} k_1 &= h \cdot f(\vec{\mathcal{X}}^x_{i|k,k}, \vec{u}_k, \vec{\mathcal{X}}^w_{i|k,k}, t_k) \\ k_2 &= h \cdot f(\vec{\mathcal{X}}^x_{i|k,k} + \frac{k_1}{2}, \vec{u}_k, \vec{\mathcal{X}}^w_{i|k,k}, t_k + \frac{h}{2}) \\ k_3 &= h \cdot f(\vec{\mathcal{X}}^x_{i|k,k} + \frac{k_2}{2}, \vec{u}_k, \vec{\mathcal{X}}^w_{i|k,k}, t_k + \frac{h}{2}) \\ k_4 &= h \cdot f(\vec{\mathcal{X}}^x_{i|k,k} + k_3, \vec{u}_k, \vec{\mathcal{X}}^w_{i|k,k}, t_k + h) \end{aligned} \tag{4-17}$$

From $\vec{\mathcal{X}}^x_{i|k+1,k}$ the one step ahead prediction of the state vector can be calculated according to Equation (4-10):

$$\hat{\vec{x}}^x_{k+1,k} = \sum_{i=0}^{2L} W_i^{(m)} \vec{\mathcal{X}}^x_{i|k+1,k} \tag{4-18}$$

Step 3: Covariance Matrix of State Prediction Error

As linearization and discretization is not needed in the UKF one can continue immediately with the update of the covariance matrix, which is calculated via the procedure of Equation (4-11):

$$P_{k+1,k} = \sum_{i=0}^{2L} W_i^{(c)} (\vec{\mathcal{X}}^x_{i|k+1,k} - \hat{\vec{x}}^x_{k+1,k})(\vec{\mathcal{X}}^x_{i|k+1,k} - \hat{\vec{x}}^x_{k+1,k})^T \tag{4-19}$$

Step 4: Calculate Prediction of the Measurement Equation

Now, the prediction of the measurement using the state prediction can be calculated. This is analogous to the calculation of the state prediction, however now the measurement equation is used and the state prediction sigma points. First the sigma points are transformed via:

$$\vec{\mathcal{Z}}_{i|k+1,k} = h(\vec{\mathcal{X}}^x_{i|k+1,k}, \vec{u}_k, \vec{\mathcal{X}}^v_{i|k,k}, t), \quad \text{for } i = 0, \ldots, 2L \tag{4-20}$$

Next, the prediction of the measurement at the next timestamp can be calculated via:

$$\hat{\vec{z}}_{k+1,k} = \sum_{i=0}^{2L} W_i^{(m)} \vec{\mathcal{Z}}_{i|k+1,k} \tag{4-21}$$

Step 5: Kalman Gain Calculation

The next step is to calculate the Kalman gain. For the UKF, it is needed to calculate the innovation covariance P^{zz} and cross covariance P^{xz}:

$$P^{zz}_{k+1,k} = \sum_{i=0}^{2L} W_i^{(c)} (\vec{\mathcal{Z}}_{i|k+1,k} - \hat{\vec{z}}_{k+1,k})(\vec{\mathcal{Z}}_{i|k+1,k} - \hat{\vec{z}}_{k+1,k})^T \tag{4-22}$$

$$P^{xz}_{k+1,k} = \sum_{i=0}^{2L} W_i^{(c)} (\vec{\mathcal{X}}^x_{i|k+1,k} - \hat{\vec{x}}_{k+1,k})(\vec{\mathcal{Z}}_{i|k+1,k} - \hat{\vec{z}}_{k+1,k})^T \tag{4-23}$$

After which the Kalman Gain can be calculated via:

$$K_{k+1} = P^{xz}_{k+1,k} P^{zz^{-1}}_{k+1,k} \tag{4-24}$$

Step 6: Measurement Update and Update State Estimate

Using the calculated Kalman gain, calculated predicted measurement and actual measurement at time $k+1$, the state estimate can be updated by using:

$$\hat{\vec{x}}_{k+1,k+1} = \hat{\vec{x}}_{k+1,k} + K_{k+1}(\vec{z}_{k+1} - \hat{\vec{z}}_{k+1,k}) \tag{4-25}$$

Step 7: Covariance Matrix of State Estimation Error

The last step is to update the covariance matrix of the state estimation error via:

$$P_{k+1,k+1} = P_{k+1,k} - K_{k+1} P^{zz}_{k+1,k} K^T_{k+1} \tag{4-26}$$

With all eight steps performed at this timestamp t_k, the final values $\hat{\vec{x}}_{k+1,k+1}$ and $P_{k+1,k+1}$ are set to $\hat{\vec{x}}_{k,k}$ and $P_{k,k}$ for the next timestamp t_{k+1} and all steps are repeated.

4-3 Aircraft Kinematic Model and Measurement Model

The Kalman filter makes use of the system f and measurement h equations to perform its state estimation. In this section these are discussed.

4-3-1 Kinematic Model

The equations of the kinematic model are governed by a number of general equations for the motion of the aircraft in the F_E-frame. These include a description of the aircraft's velocity in the F_E-frame ($\dot{x}$, $\dot{y}$, $\dot{z}$), accelerations along the aircraft body axes ($\dot{u}$, $\dot{v}$, $\dot{w}$) and rotation rates ($\dot{\varphi}$, $\dot{\theta}$, $\dot{\psi}$). In matrix form this is given by:

$$\vec{\dot{x}} = \begin{bmatrix} \dot{x} \\ \dot{y} \\ \dot{z} \\ \dot{u} \\ \dot{v} \\ \dot{w} \\ \dot{\varphi} \\ \dot{\theta} \\ \dot{\psi} \end{bmatrix} = \begin{bmatrix} [u\cos\theta + (v\sin\varphi + w\cos\varphi)\sin\theta]\cos\psi - (v\cos\varphi - w\sin\varphi)\sin\psi + W_{X_E} \\ [u\cos\theta + (v\sin\varphi + w\cos\varphi)\sin\theta]\sin\psi + (v\cos\varphi - w\sin\varphi)\cos\psi + W_{Y_E} \\ -u\sin\theta + (v\sin\varphi + w\cos\varphi)\cos\theta + W_{Z_E} \\ A_x - g\sin\theta + rv - qw \\ A_y + g\cos\theta\sin\varphi + pw - ru \\ A_z + g\cos\theta\cos\varphi + qu - pv \\ p + q\sin\varphi\tan\theta + r\cos\varphi\tan\theta \\ q\cos\varphi - r\sin\varphi \\ q\frac{\sin\varphi}{\cos\theta} + r\frac{\cos\varphi}{\cos\theta} \end{bmatrix} \tag{4-27}$$

The inputs to this system are the *actual* specific accelerations A_x, A_y and A_z and the rotational rates p, q and r. For practical application in the FPR one can use the measured signals. However, as discussed in chapter 3, the AHRS measurements are susceptible to a certain bias λ and measurement noise w (with variance σ^2) and thus do not directly reflect the actual acceleration. To include these bias and noise terms one can write for the *actual* accelerations and rotations:

$$\begin{aligned} A_x &= A_{x_{\text{AHRS}}} - \lambda_x - w_x \\ A_y &= A_{y_{\text{AHRS}}} - \lambda_y - w_y \\ A_z &= A_{z_{\text{AHRS}}} - \lambda_z - w_z \\ p &= p_{\text{AHRS}} - \lambda_p - w_p \\ q &= q_{\text{AHRS}} - \lambda_q - w_q \\ r &= r_{\text{AHRS}} - \lambda_r - w_r \end{aligned} \tag{4-28}$$

Where the subscript $_{\text{AHRS}}$ means "measured by the AHRS". Implementing this, the system becomes:

$$\vec{\dot{x}} = \begin{bmatrix} \dot{x} \\ \dot{y} \\ \dot{z} \\ \dot{u} \\ \dot{v} \\ \dot{w} \\ \dot{\varphi} \\ \dot{\theta} \\ \dot{\psi} \end{bmatrix} = \begin{bmatrix} [u\cos\theta + (v\sin\varphi + w\cos\varphi)\sin\theta]\cos\psi - (v\cos\varphi - w\sin\varphi)\sin\psi + W_{X_E} \\ [u\cos\theta + (v\sin\varphi + w\cos\varphi)\sin\theta]\sin\psi + (v\cos\varphi - w\sin\varphi)\cos\psi + W_{Y_E} \\ -u\sin\theta + (v\sin\varphi + w\cos\varphi)\cos\theta + W_{Z_E} \\ (A_{x_{\text{AHRS}}} - \lambda_x - w_x) - g\sin\theta + (r_{\text{AHRS}} - \lambda_r - w_r)v - (q_{\text{AHRS}} - \lambda_q - w_q)w \\ (A_{y_{\text{AHRS}}} - \lambda_y - w_y) + g\cos\theta\sin\varphi + (p_{\text{AHRS}} - \lambda_p - w_p)w - (r_{\text{AHRS}} - \lambda_r - w_r)u \\ (A_{z_{\text{AHRS}}} - \lambda_z - w_z) + g\cos\theta\cos\varphi + (q_{\text{AHRS}} - \lambda_q - w_q)u - (p_{\text{AHRS}} - \lambda_p - w_p)v \\ (p_{\text{AHRS}} - \lambda_p - w_p) + (q_{\text{AHRS}} - \lambda_q - w_q)\sin\varphi\tan\theta + (r_{\text{AHRS}} - \lambda_r - w_r)\cos\varphi\tan\theta \\ (q_{\text{AHRS}} - \lambda_q - w_q)\cos\varphi - (r_{\text{AHRS}} - \lambda_r - w_r)\sin\varphi \\ (q_{\text{AHRS}} - \lambda_q - w_q)\frac{\sin\varphi}{\cos\theta} + (r_{\text{AHRS}} - \lambda_r - w_r)\frac{\cos\varphi}{\cos\theta} \end{bmatrix} \tag{4-29}$$

In this system the bias and wind terms remain unknown. For that reason, they should be included as states in the model such that they can be estimated too. For the bias terms, it is known these are constants and as such they can be modeled as:

$$\begin{aligned}\dot{\lambda}_x &= 0\\ \dot{\lambda}_y &= 0\\ \dot{\lambda}_z &= 0\\ \dot{\lambda}_p &= 0\\ \dot{\lambda}_q &= 0\\ \dot{\lambda}_r &= 0\end{aligned} \tag{4-30}$$

The wind terms are not constant, such that an assumption on their behaviour has to be made. As mentioned before by findings of [22], random walk may be applicable to model relatively -but not entirely- constant states to improve convergence. In [57, 58] this has been applied to the wind equations via:

$$\begin{aligned}\dot{W}_{X_E} &= 0.01 w_{\text{walk}}\\ \dot{W}_{Y_E} &= 0.01 w_{\text{walk}}\\ \dot{W}_{Z_E} &= 0.01 w_{\text{walk}}\end{aligned} \tag{4-31}$$

With w_{walk} a random-walk white noise signal with zero mean and standard deviation $\sigma = 1$. This is incorporated into the kinematic model equation by randomly selecting a value every time this function is evaluated in the program code.

Last, a correction has to be implemented due to the angle-of-attack and angle-of-sideslip measurements of the boom [6]. Rather than measuring the actual α and β and velocities u, v and w, these instruments measure the local boom angle-of-attack and angle-of-sideslip α_b and β_b, and velocities u_b, v_b and w_b. This is due to three main reasons. The first are upwash and sidewash components at the boom vane locations due to the fuselage's shape. The second are rotational effects which occur due to the fact that the boom is mounted on the nose of the aircraft -significantly far before the c.g.- such that rotations of the aircraft influence the measurement of the vanes as these start measuring their own movement relative to the air. The last are wind components in the upwash and sidewash. The approximations of the local boom angle of attack and angle of sideslip due to these three effects have also been given by [57, 58]:

$$\begin{aligned}\alpha_b = \arctan\frac{w_b}{u_b} \approx\\ \approx (1 + C_{\alpha_{up}}) \arctan\frac{w}{u} + (x_{b_\alpha} - x_{c.g.})\frac{(q_{\text{AHRS}} - \lambda_q - w_q)}{\sqrt{u^2+v^2+w^2}} + C_{\alpha_0}\end{aligned} \tag{4-32}$$

$$\begin{aligned}\beta_b = \arctan\frac{v_b}{\sqrt{u_b^2 + w_b^2}} \approx\\ \approx (1+C_{\beta_{side}}) \arctan\frac{v}{\sqrt{u^2+w^2}} - (x_{b_\beta} - x_{c.g.})\frac{(r_{\text{AHRS}} - \lambda_r - w_r)}{\sqrt{u^2+v^2+w^2}} + (z_{b_\beta} - z_{c.g.})\frac{(p_{\text{AHRS}} - \lambda_p - w_p)}{\sqrt{u^2+v^2+w^2}} + C_{\beta_0}\end{aligned} \tag{4-33}$$

In which the x and z locations of the vanes are known constants in the vehicle reference frame and are given in Table 4-1, and the location of the c.g. is known from the massmodel data. The terms $C_{\alpha_{up}}$ and $C_{\beta_{side}}$ model the upwash and sidewash effects and C_{α_0} and C_{β_0} are coefficients to model wind components which must all be estimated. In the papers [57, 58] it was found that these can be introduced in the kinematics as random walk for the upwash and sidewash coefficients as these have been found to vary over time. The wind bias terms can assumed to be constant. Such that:

$$\begin{aligned} \dot{C}_{\alpha_{up}} &= 0.01 w_{\text{walk}} \frac{\pi}{180} \\ \dot{C}_{\beta_{side}} &= 0.01 w_{\text{walk}} \frac{\pi}{180} \\ \dot{C}_{\alpha_0} &= 0 \\ \dot{C}_{\beta_0} &= 0 \end{aligned} \tag{4-34}$$

Table 4-1: Assumed boom vane and AOA vane locations in the aircraft fuselage (datum 19 inch before and 91 inch under the aircraft nose).

Measurement	Variable	Distance from datum [inch]
Boom	x_{b_α}	$19 - 36.5 = -27.5$
	x_{b_β}	$19 - 35.3 = -16.3$
	z_{b_β}	$91 + 37.5 = 128.5$
AOA vane	x_{v_α}	$19 + 157.4 (= 4\text{ m}) = 176.4$

This results in the full time-invariant kinematic model given by:

$$\begin{aligned} \dot{\vec{x}} = f(\vec{x}, \vec{u_m}, \vec{w}) = \\ = \begin{bmatrix} \dot{x} \\ \dot{y} \\ \dot{z} \\ \dot{u} \\ \dot{v} \\ \dot{w} \\ \dot{\varphi} \\ \dot{\theta} \\ \dot{\psi} \\ \dot{\lambda}_x \\ \dot{\lambda}_y \\ \dot{\lambda}_z \\ \dot{\lambda}_p \\ \dot{\lambda}_q \\ \dot{\lambda}_r \\ \dot{W}_{X_E} \\ \dot{W}_{Y_E} \\ \dot{W}_{Z_E} \\ \dot{C}_{\alpha_{up}} \\ \dot{C}_{\beta_{side}} \\ \dot{C}_{\alpha_0} \\ \dot{C}_{\beta_0} \end{bmatrix} = \begin{bmatrix} [u\cos\theta + (v\sin\varphi + w\cos\varphi)\sin\theta]\cos\psi - (v\cos\varphi - w\sin\varphi)\sin\psi + W_{X_E} \\ [u\cos\theta + (v\sin\varphi + w\cos\varphi)\sin\theta]\sin\psi + (v\cos\varphi - w\sin\varphi)\cos\psi + W_{Y_E} \\ -u\sin\theta + (v\sin\varphi + w\cos\varphi)\cos\theta + W_{Z_E} \\ (A_{x_{\text{AHRS}}} - \lambda_x - w_x) - g\sin\theta + (r_{\text{AHRS}} - \lambda_r - w_r)v - (q_{\text{AHRS}} - \lambda_q - w_q)w \\ (A_{y_{\text{AHRS}}} - \lambda_y - w_y) + g\cos\theta\sin\varphi + (p_{\text{AHRS}} - \lambda_p - w_p)w - (r_{\text{AHRS}} - \lambda_r - w_r)u \\ (A_{z_{\text{AHRS}}} - \lambda_z - w_z) + g\cos\theta\cos\varphi + (q_{\text{AHRS}} - \lambda_q - w_q)u - (p_{\text{AHRS}} - \lambda_p - w_p)v \\ (p_{\text{AHRS}} - \lambda_p - w_p) + (q_{\text{AHRS}} - \lambda_q - w_q)\sin\varphi\tan\theta + (r_{\text{AHRS}} - \lambda_r - w_r)\cos\varphi\tan\theta \\ (q_{\text{AHRS}} - \lambda_q - w_q)\cos\varphi - (r_{\text{AHRS}} - \lambda_r - w_r)\sin\varphi \\ (q_{\text{AHRS}} - \lambda_q - w_q)\frac{\sin\varphi}{\cos\theta} + (r_{\text{AHRS}} - \lambda_r - w_r)\frac{\cos\varphi}{\cos\theta} \\ 0 \\ 0 \\ 0 \\ 0 \\ 0 \\ 0 \\ 0.01 w_{\text{walk}} \\ 0.01 w_{\text{walk}} \\ 0.01 w_{\text{walk}} \\ 0.01 w_{\text{walk}} \frac{\pi}{180} \\ 0.01 w_{\text{walk}} \frac{\pi}{180} \\ 0 \\ 0 \end{bmatrix} \end{aligned} \tag{4-35}$$

With state vector:

$$\vec{x} = \begin{bmatrix} x & y & z & u & v & w & \varphi & \theta & \psi & \lambda_x & \lambda_y & \lambda_z & \lambda_p & \lambda_q & \lambda_r & W_{X_E} & W_{Y_E} & W_{Z_E} & C_{\alpha_{up}} & C_{\beta_{side}} & C_{\alpha_0} & C_{\beta_0} \end{bmatrix}^T \tag{4-36}$$

With (measured) input vector:

$$\vec{u}_m = \begin{bmatrix} A_{x_{\text{AHRS}}} & A_{y_{\text{AHRS}}} & A_{z_{\text{AHRS}}} & p_{\text{AHRS}} & q_{\text{AHRS}} & r_{\text{AHRS}} \end{bmatrix}^T \tag{4-37}$$

And process noise vector:

$$\vec{w} = \begin{bmatrix} w_x & w_y & w_z & w_p & w_q & w_r \end{bmatrix}^T \tag{4-38}$$

4-3-2 Measurement Model

Now the measurement model must be defined. This is done by defining the available measurement signals in terms of the state, input and measurement noise vector. The required measurement model includes a description of aircraft position in the F_E-frame (x, y, z), velocity in the F_E-frame ($\dot{x}$, $\dot{y}$, $\dot{z}$) attitude angles (φ, θ, ψ) and airdata measurements (V_{TAS}, α_b, β_b).

The first nine states and true airspeed are governed by general equations. The angle-of-attack and angle-of-sideslip must be related via the defined relations as given in Equation (4-32) and Equation (4-33). However, note that the process noise terms (w_p, w_q, w_r) are dropped from the equation as via the definition of Equation (4-1) the measurement model cannot cannot contain process noise terms. Rather, it is implicitly assumed that these noises are incorporated in the measurement noises v_α and v_β.

All these measured signals contain a certain measurement noise v which is an assumed white noise signal with variances as given in Table 3-2. This results in the full time-invariant measurement model with measurement vector $\vec{z}_m$:

$$\vec{z}_m = h(\vec{x}, \vec{u}_m, \vec{v}) =$$

$$= \begin{bmatrix} x_{\text{GPS}} \\ y_{\text{GPS}} \\ z_{\text{GPS}} \\ \dot{x}_{\text{GPS}} \\ \dot{y}_{\text{GPS}} \\ \dot{z}_{\text{GPS}} \\ \varphi_{\text{AHRS}} \\ \theta_{\text{AHRS}} \\ \psi_{\text{AHRS}} \\ V_{TAS_{\text{DADC}}} \\ \alpha_{b_{\text{synchro}}} \\ \beta_{b_{\text{synchro}}} \end{bmatrix} = \begin{bmatrix} x+v_x \\ y+v_y \\ z+v_z \\ [u\cos\theta+(v\sin\varphi+w\cos\varphi)\sin\theta]\cos\psi-(v\cos\varphi-w\sin\varphi)\sin\psi+W_{X_E}+v_{\dot{x}} \\ [u\cos\theta+(v\sin\varphi+w\cos\varphi)\sin\theta]\sin\psi+(v\cos\varphi-w\sin\varphi)\cos\psi+W_{Y_E}+v_{\dot{y}} \\ -u\sin\theta+(v\sin\varphi+w\cos\varphi)\cos\theta+W_{Z_E}+v_{\dot{z}} \\ \varphi+v_\varphi \\ \theta+v_\theta \\ \psi+v_\psi \\ \sqrt{u^2+v^2+w^2}+v_V \\ (1+C_{\alpha_{up}})\arctan\frac{w}{u}+(x_{b_\alpha}-x_{c.g.})\frac{(q_{\text{AHRS}}-\lambda_q)}{\sqrt{u^2+v^2+w^2}}+C_{\alpha_0}+v_\alpha \\ (1+C_{\beta_{side}})\arctan\frac{v}{\sqrt{u^2+w^2}}-(x_{b_\beta}-x_{c.g.})\frac{(r_{\text{AHRS}}-\lambda_r)}{\sqrt{u^2+v^2+w^2}}+(z_{b_\beta}-z_{c.g.})\frac{(p_{\text{AHRS}}-\lambda_p)}{\sqrt{u^2+v^2+w^2}}+C_{\beta_0}+v_\beta \end{bmatrix} \tag{4-39}$$

With measurement noise vector:

$$\vec{v} = \begin{bmatrix} v_x & v_y & v_z & v_{\dot{x}} & v_{\dot{y}} & v_{\dot{z}} & v_\varphi & v_\theta & v_\psi & v_V & v_\alpha & v_\beta \end{bmatrix}^T \tag{4-40}$$

4-3-3 Kinematic and Measurement Model with Pseudo-β

There are many flights from Citation flights that were performed without the air data boom installed. In [58], it was concluded that the omission of the air data boom was detrimental in the aerodynamic modeling of the lateral equations and could not be used at all in this case. For the longitudinal modeling it was found if data was taken from a lateral motion, also the estimate of α from the UKF showed errors relative to the data from the boom. It was concluded that the question remained open whether the inclusion of the no-boom flights delivered more data that was valuable enough even though its lower expected accuracy. In the end it was decided to not use this data.

However, data from flights that have the boom included performed measurements at largely only one altitude. As *global* modeling is at the core of this research, data at more altitudes from more flights become of higher value than in the former research, which might warrant a different conclusion as to the inclusion of the no-boom data. Furthermore, no effect on the actual X parameters was investigated. Therefore, this investigation is performed here.

For data that does not include air data boom measurements the kinematic and measurement above does not apply. The only available data comes from the α-vane installed on the fuselage. However this vane, and as such its data, comes with a number of considerations. First, body induced velocities are present in the vane measurement, however this is also the case for the boom. Second, there is significant damping in the alpha vane, whilst the boom contains higher frequency components. Third and last, the damping of the vane also introduces a lag in its measurement. To incorporate this behaviour [57] altered the kinematic and measurement model for the α-vane, that makes use of a the following relation for the α measurement (analogous to Equation (4-32)):

$$\dot{\alpha}_v = \frac{1}{\tau_v}\left((1 + C_{\alpha_{up}}) \arctan\frac{w}{u} + (x_{v_\alpha} - x_{c.g.})\frac{(q_{\text{AHRS}} - \lambda_q - w_q)}{\sqrt{u^2 + v^2 + w^2}} + C_{\alpha_0} - \alpha_v\right) \tag{4-41}$$

With the AOA vane location given in Table 4-1. The parameter τ_v is the vane lag time constant. This is added because the AOA vane mechanics cause a lag relative to the actual angle of attack. The value for $\tau_v = 0.2$ s. This results in the following kinematic model:

$$\vec{\dot{x}} = f(\vec{x}, \vec{u_m}, \vec{w}) =$$

$$= \begin{bmatrix} \dot{x} \\ \dot{y} \\ \dot{z} \\ \dot{u} \\ \dot{v} \\ \dot{w} \\ \dot{\varphi} \\ \dot{\theta} \\ \dot{\psi} \\ \dot{\lambda}_x \\ \dot{\lambda}_y \\ \dot{\lambda}_z \\ \dot{\lambda}_p \\ \dot{\lambda}_q \\ \dot{\lambda}_r \\ \dot{W}_{X_E} \\ \dot{W}_{Y_E} \\ \dot{W}_{Z_E} \\ \dot{C}_{\alpha_{up}} \\ \dot{C}_{\alpha_0} \\ \dot{\alpha}_v \end{bmatrix} = \begin{bmatrix} [u\cos\theta + (v\sin\varphi + w\cos\varphi)\sin\theta]\cos\psi - (v\cos\varphi - w\sin\varphi)\sin\psi + W_{X_E} \\ [u\cos\theta + (v\sin\varphi + w\cos\varphi)\sin\theta]\sin\psi + (v\cos\varphi - w\sin\varphi)\cos\psi + W_{Y_E} \\ -u\sin\theta + (v\sin\varphi + w\cos\varphi)\cos\theta + W_{Z_E} \\ (A_{x_{\text{AHRS}}} - \lambda_x - w_x) - g\sin\theta + (r_{\text{AHRS}} - \lambda_r - w_r)v - (q_{\text{AHRS}} - \lambda_q - w_q)w \\ (A_{y_{\text{AHRS}}} - \lambda_y - w_y) + g\cos\theta\sin\varphi + (p_{\text{AHRS}} - \lambda_p - w_p)w - (r_{\text{AHRS}} - \lambda_r - w_r)u \\ (A_{z_{\text{AHRS}}} - \lambda_z - w_z) + g\cos\theta\cos\varphi + (q_{\text{AHRS}} - \lambda_q - w_q)u - (p_{\text{AHRS}} - \lambda_p - w_p)v \\ (p_{\text{AHRS}} - \lambda_p - w_p) + (q_{\text{AHRS}} - \lambda_q - w_q)\sin\varphi\tan\theta + (r_{\text{AHRS}} - \lambda_r - w_r)\cos\varphi\tan\theta \\ (q_{\text{AHRS}} - \lambda_q - w_q)\cos\varphi - (r_{\text{AHRS}} - \lambda_r - w_r)\sin\varphi \\ (q_{\text{AHRS}} - \lambda_q - w_q)\frac{\sin\varphi}{\cos\theta} + (r_{\text{AHRS}} - \lambda_r - w_r)\frac{\cos\varphi}{\cos\theta} \\ 0 \\ 0 \\ 0 \\ 0 \\ 0 \\ 0 \\ 0.01 w_{\text{walk}} \\ 0.01 w_{\text{walk}} \\ 0.01 w_{\text{walk}} \\ 0.01 w_{\text{walk}} \frac{\pi}{180} \\ 0.01 w_{\text{walk}} \frac{\pi}{180} \\ \frac{1}{\tau_v}\left((1 + C_{\alpha_{up}})\arctan\frac{w}{u} + (x_{v_\alpha} - x_{c.g.})\frac{(q_{\text{AHRS}} - \lambda_q - w_q)}{\sqrt{u^2 + v^2 + w^2}} + C_{\alpha_0} - \alpha_v\right) \end{bmatrix} \tag{4-42}$$

Due to the lack of the boom there are no measurements of β at all. It was found that this impairs the convergence of the state estimates. However, one can include a so-called "pseudo-β". The artificial pseudo-β noise measurement was added to the flight data in the pre-processing as described below. In practise, it is a meaningless zero mean white noise signal with variance v_β and thus adds no significant information on lateral FPR. However, it does improve the performance of the UKF related to the other states and therefore it is included.

This results in the measurement equation as given by:

$$\vec{z}_m = h(\vec{x}, \vec{u}_m, \vec{v}) =$$

$$= \begin{bmatrix} x_{\text{GPS}} \\ y_{\text{GPS}} \\ z_{\text{GPS}} \\ \dot{x}_{\text{GPS}} \\ \dot{y}_{\text{GPS}} \\ \dot{z}_{\text{GPS}} \\ \varphi_{\text{AHRS}} \\ \theta_{\text{AHRS}} \\ \psi_{\text{AHRS}} \\ V_{TAS_{\text{DADC}}} \\ \alpha_{v_{\text{analog}}} \\ \beta_{pseudo} \end{bmatrix} = \begin{bmatrix} x + v_x \\ y + v_y \\ z + v_z \\ [u\cos\theta + (v\sin\varphi + w\cos\varphi)\sin\theta]\cos\psi - (v\cos\varphi - w\sin\varphi)\sin\psi + W_{X_E} + v_{\dot{x}} \\ [u\cos\theta + (v\sin\varphi + w\cos\varphi)\sin\theta]\sin\psi + (v\cos\varphi - w\sin\varphi)\cos\psi + W_{Y_E} + v_{\dot{y}} \\ -u\sin\theta + (v\sin\varphi + w\cos\varphi)\cos\theta + v_{\dot{z}} \\ \varphi + v_\varphi \\ \theta + v_\theta \\ \psi + v_\psi \\ \sqrt{u^2 + v^2 + w^2} + v_V \\ \alpha_v + v_\alpha \\ \arctan\frac{v}{\sqrt{u^2 + w^2}} + v_\beta \end{bmatrix} \tag{4-43}$$

4-3-4 Model Observability and Convergence

A condition for proper convergence (however not a guarantee) is that all states of the model are *observable*. The observability can be calculated analytically. But in order to evaluate if a model can actually be used its convergence also needs to be checked experimentally.

An analytical method for observability that makes use of Lie derivatives and an observability matrix is implemented by [6]. The observability matrix is defined as:

$$\mathcal{O} = \begin{bmatrix} \partial_x h \\ \partial_x(L_f h) \\ \partial_x(L_f L_f h) \\ \partial_x(L_f L_f L_f h) \\ \vdots \\ \partial_x(\underbrace{L_f \cdots L_f}_{n-1} h) \end{bmatrix} \quad \text{with} \quad L_f h = \partial_x(h) f, \quad \text{s.t.} \quad \mathcal{O} = \begin{bmatrix} \partial_x(h) \\ \partial_x(\partial_x[h] f) \\ \partial_x(\partial_x[\partial_x\{h\} f] f) \\ \partial_x(\partial_x[\partial_x\{\partial_x(h) f\} f] f) \\ \vdots \\ \partial_x(\underbrace{\partial_x[\cdots\{\partial_x}_{n-1}(h) \underbrace{f\}\cdots]f}_{n-1}) \end{bmatrix} \tag{4-44}$$

In which n is the number of states in the system. The states are observable if the observability matrix is of full rank, meaning:

$$\text{rank } \mathcal{O} = n \tag{4-45}$$

By using MATLAB and its symbolic variables one can build the observability matrix and calculate its rank. The noise v and w terms are removed from the models for this as they do not add anything to the dynamics, only introduce noise. The matrix is calculated row-by-row as immediately calculating the full $\mathcal{O}$-matrix is an expensive operation. It was found that all states are already observable when $\mathcal{O} = \begin{bmatrix} \partial_x h \\ \partial_x(L_f h) \\ \partial_x(L_f L_f h) \end{bmatrix}$, and as such no changes are needed to the model.

The second method to explore the system's convergence is experimentally and is implemented by [57] and [58]. By investigating the behaviour of the KF estimates the best convergence was found by deleting the following states from the system. The vertical wind W_{Z_E} was deleted as it is usually rather small, but influences the estimate of the two lateral wind estimates. Coefficient C_{α_0} was deleted as it is strongly correlated to $C_{\alpha_{up}}$, and using both hinders convergence of either coefficient. Last, $C_{\beta_{side}}$ and C_{β_0} were both deleted as they led to large deviations in the estimate of u, v and w, and because of that in the reconstructed β.

The UKF of this thesis was tested and it was found that applying these exact same techniques also considerably improved the UKF's estimates. Therefore the same changes were implemented one-to-one. An advantage of knowing this is that the separately built UKF of this thesis is as such already partly verified to work correctly. This results in the final UKF model as explained below.

4-3-5 Final UKF Model

Deleting the states as explained above results in the final kinematic model given by:

$$\vec{\dot{x}} = f(\vec{x}, \vec{u_m}, \vec{w}) =$$

$$= \begin{bmatrix} \dot{x} \\ \dot{y} \\ \dot{z} \\ \dot{u} \\ \dot{v} \\ \dot{w} \\ \dot{\varphi} \\ \dot{\theta} \\ \dot{\psi} \\ \dot{\lambda}_x \\ \dot{\lambda}_y \\ \dot{\lambda}_z \\ \dot{\lambda}_p \\ \dot{\lambda}_q \\ \dot{\lambda}_r \\ \dot{W}_{X_E} \\ \dot{W}_{Y_E} \\ \dot{C}_{\alpha_{up}} \end{bmatrix} = \begin{bmatrix} [u\cos\theta + (v\sin\varphi + w\cos\varphi)\sin\theta]\cos\psi - (v\cos\varphi - w\sin\varphi)\sin\psi + W_{X_E} \\ [u\cos\theta + (v\sin\varphi + w\cos\varphi)\sin\theta]\sin\psi + (v\cos\varphi - w\sin\varphi)\cos\psi + W_{Y_E} \\ -u\sin\theta + (v\sin\varphi + w\cos\varphi)\cos\theta \\ (A_{x_{\text{AHRS}}} - \lambda_x - w_x) - g\sin\theta + (r_{\text{AHRS}} - \lambda_r - w_r)v - (q_{\text{AHRS}} - \lambda_q - w_q)w \\ (A_{y_{\text{AHRS}}} - \lambda_y - w_y) + g\cos\theta\sin\varphi + (p_{\text{AHRS}} - \lambda_p - w_p)w - (r_{\text{AHRS}} - \lambda_r - w_r)u \\ (A_{z_{\text{AHRS}}} - \lambda_z - w_z) + g\cos\theta\cos\varphi + (q_{\text{AHRS}} - \lambda_q - w_q)u - (p_{\text{AHRS}} - \lambda_p - w_p)v \\ (p_{\text{AHRS}} - \lambda_p - w_p) + (q_{\text{AHRS}} - \lambda_q - w_q)\sin\varphi\tan\theta + (r_{\text{AHRS}} - \lambda_r - w_r)\cos\varphi\tan\theta \\ (q_{\text{AHRS}} - \lambda_q - w_q)\cos\varphi - (r_{\text{AHRS}} - \lambda_r - w_r)\sin\varphi \\ (q_{\text{AHRS}} - \lambda_q - w_q)\frac{\sin\varphi}{\cos\theta} + (r_{\text{AHRS}} - \lambda_r - w_r)\frac{\cos\varphi}{\cos\theta} \\ 0 \\ 0 \\ 0 \\ 0 \\ 0 \\ 0 \\ 0.01 w_{\text{walk}} \\ 0.01 w_{\text{walk}} \\ 0.01 w_{\text{walk}} \frac{\pi}{180} \end{bmatrix} \tag{4-46}$$

And the final measurement model becomes:

$$\vec{z}_m = h(\vec{x}, \vec{u}_m, \vec{v}) =$$

$$= \begin{bmatrix} x_{\text{GPS}} \\ y_{\text{GPS}} \\ z_{\text{GPS}} \\ \dot{x}_{\text{GPS}} \\ \dot{y}_{\text{GPS}} \\ \dot{z}_{\text{GPS}} \\ \varphi_{\text{AHRS}} \\ \theta_{\text{AHRS}} \\ \psi_{\text{AHRS}} \\ V_{TAS_{\text{DADC}}} \\ \alpha_{b_{\text{synchro}}} \\ \beta_{b_{\text{synchro}}} \end{bmatrix} = \begin{bmatrix} x + v_x \\ y + v_y \\ z + v_z \\ [u\cos\theta + (v\sin\varphi + w\cos\varphi)\sin\theta]\cos\psi - (v\cos\varphi - w\sin\varphi)\sin\psi + W_{X_E} + v_{\dot{x}} \\ [u\cos\theta + (v\sin\varphi + w\cos\varphi)\sin\theta]\sin\psi + (v\cos\varphi - w\sin\varphi)\cos\psi + W_{Y_E} + v_{\dot{y}} \\ -u\sin\theta + (v\sin\varphi + w\cos\varphi)\cos\theta + v_{\dot{z}} \\ \varphi + v_\varphi \\ \theta + v_\theta \\ \psi + v_\psi \\ \sqrt{u^2 + v^2 + w^2} + v_V \\ (1 + C_{\alpha_{up}})\arctan\frac{w}{u} + (x_{b_\alpha} - x_{c.g.})\frac{(q_{\text{AHRS}} - \lambda_q)}{\sqrt{u^2 + v^2 + w^2}} + v_\alpha \\ \arctan\frac{v}{\sqrt{u^2 + w^2}} - (x_{b_\beta} - x_{c.g.})\frac{(r_{\text{AHRS}} - \lambda_r)}{\sqrt{u^2 + v^2 + w^2}} + (z_{b_\beta} - z_{c.g.})\frac{(p_{\text{AHRS}} - \lambda_p)}{\sqrt{u^2 + v^2 + w^2}} + v_\beta \end{bmatrix} \tag{4-47}$$

The same model structure is applicable to the model with the pseudo-β, but with the added α_v as state and the $\alpha_{v_{\text{analog}}}$ and β_{pseudo} in the measurement model as in Equation (4-42) and Equation (4-43).

4-4 UKF Data Pre-Processing and Post-Processing

The raw data as gathered by the aircraft's sensors cannot directly be used in the UKF but needs to be processed first for effective state estimation. Furthermore, after the UKF procedure, the estimated states can be used to calculate a number of additional parameters.

Pre-Processing 1: Adjust Data to Correct Reference Frame

First, the IMU acceleration measurement $A_{z_{\text{AHRS}}}$ is defined positive upwards in the F_b-frame while it should be downwards. The same applies to the GPS velocity measurement $\dot{z}_{\text{GPS}}$ but then in the F_E-frame. Mathematically:

$$A_{z_{\text{AHRS},F_b,+g}} = -A_{z_{\text{AHRS,measured}}} \tag{4-48}$$

$$\dot{z}_{\text{GPS}} = \dot{z}_{\text{GPS},F_E} = -\dot{z}_{\text{GPS,measured}} \tag{4-49}$$

Furthermore, in the UKF it is assumed that the signals of $A_{x,y,z_{\text{AHRS}}}$ as they appear in the kinematic model are the *specific* accelerations in the body frame, thus including a component of the gravitational acceleration. For this reason the terms $-g\sin\theta$, $+g\cos\theta\sin\phi$ and $+g\cos\theta\cos\phi$ are included in the kinematic model for state derivatives $\dot{u}$, $\dot{v}$ and $\dot{w}$, where the gravity influence is subtracted such that the *body* acceleration remains.

However, the acceleration data in the Z_b axis $A_{z_{\text{AHRS},F_b}}$ has been corrected in the IMU itself by simply adding the gravitational constant 9.80665 m/s to the signal, which is a too crude and wrong assumption. Therefore in this preprocessing step this constant is subtracted again, such that in level flight the signal measures a negative acceleration of 9.80665 m/s, such that this corresponds to the kinematic relation. Mathematically this is:

$$A_{z_{\text{AHRS},F_b}} = A_{z_{\text{AHRS},F_b,+g}} - 9.80665 \tag{4-50}$$

The accelerations in the X_b and Y_b axes are in fact already the specific acceleration and as such do not require any further pre-processing.

Pre-Processing 2: Data Prefiltering

Before use in the UKF it is needed to prefilter a number of signals as these contain vibrations measured due to the stall buffet of the aircraft when entering the stall. The focus of the research described in this thesis is on the dynamics of the aircraft itself and lesser on the stall buffet. But, the stall buffet *does* affect the measurements and thus the FPR and modeling. Therefore it needs to be filtered out before the UKF such that the FPR is not affected by the buffet signal and only aircraft dynamic features remain in the signal.

The buffet is filtered out by using a 6th order Butterworth filter as this is realistically one of the closest options to an ideal lowpass filter by minimizing ripple effects. This is done via the MATLAB `butter()` and `filtfilt()` functions on the signals in Table 4-2. In the same table the filter properties are also given. The sample frequency is always 100 Hz, as the flight data is based on timesteps of 0.01 s. The signal of the α-vane does not need to be pre-filtered as the damping in the vane causes a lack of higher frequency features in the signal, as was discussed earlier.

The passband frequency was chosen manually in a rough manner. In the case that any significant secondary peak could be observed the passband frequency was chosen to be just before the beginning of the peak, or if no clear peak could be observed 1 Hz was chosen. The filters were designed with a cutoff frequency of the desired passband +0.5 Hz margin, to not filter out frequencies below the desired passband. The -0.01 dB point is just under 0.5 dB under the chosen cutoff frequency, so therefore this was chosen. The numbers in Table 4-2 include this margin.

An example of the filtered signals in the data of a stall is given in Figure 4-2. One can clearly see that the high frequencies are filtered out of all the signals. Also one can clearly see the

Table 4-2: Filter properties for UKF prefiltering.

Signal	Sample freq f_s [Hz]	Passband freq f_{pass} [Hz]
$A_{x_{\text{AHRS,nose}}}$, $A_{y_{\text{AHRS,nose}}}$, $A_{z_{\text{AHRS,nose}}}$	100	1.5
p_{AHRS}, q_{AHRS}, r_{AHRS}	100	1.5
$\alpha_{b_{\text{synchro}}}$, $\beta_{b_{\text{synchro}}}$	100	5.5

secondary peak around the frequencies of the stall buffet in the signals of $\alpha_{b_{\text{synchro}}}$ and $\beta_{b_{\text{synchro}}}$ around $10 - 12$ Hz in Figure 4-2c.

Pre-Processing 3: Calculate Center of Gravity Accelerations

The accelerations and rotations measured by the AHRS are measured in the IMU unit of the AHRS itself. However, the accelerations and rotations of the state variables are by definition those in the aircraft center of gravity. These are thus not the same. Therefore an adjustment should be made to the AHRS measurements via the procedure described by [57]:

$$A_{x_{\text{AHRS}}} = A_{x_{\text{AHRS,nose}}} + (x_{c.g.} - x_{\text{AHRS}})(q^2 + r^2) - (y_{c.g.} - y_{\text{AHRS}})(pq - \dot{r}) - (z_{c.g.} - z_{\text{AHRS}})(pr - \dot{q}) \tag{4-51}$$

$$A_{y_{\text{AHRS}}} = A_{y_{\text{AHRS,nose}}} + (y_{c.g.} - y_{\text{AHRS}})(r^2 + p^2) - (z_{c.g.} - z_{\text{AHRS}})(qr - \dot{p}) - (x_{c.g.} - x_{\text{AHRS}})(qp - \dot{r}) \tag{4-52}$$

$$A_{z_{\text{AHRS}}} = A_{z_{\text{AHRS,nose}}} + (z_{c.g.} - z_{\text{AHRS}})(p^2 + q^2) - (x_{c.g.} - x_{\text{AHRS}})(rp - \dot{q}) - (y_{c.g.} - y_{\text{AHRS}})(rq - \dot{p}) \tag{4-53}$$

In which the x, y and z locations of the AHRS are constants assumed from the vehicle reference frame (see Table 4-3) and the location of the c.g. is known from the massmodel data. The rotational accelerations are not known from the data but are calculated from the rotation rates via backwards Newton differentiation.

Table 4-3: Assumed AHRS locations in the aircraft fuselage (datum 19 inch before and 91 inch under the aircraft nose).

Variable	Distance from datum [inch]
x_{AHRS}	$19 + 75 = 94$
y_{AHRS}	$0 + 3.94 (= 0.1 \text{ m}) = 3.94$
z_{AHRS}	$91 + 0 = 91$

Pre-Processing 4: Adding Pseudo-β

The last step in pre-processing is to add the pseudo-β measurement for the flight data in which no boom data is available. This is simply done by using MATLAB's `randn()`-function and multiplying by a user-defined variance v_β, resulting in a white noise signal with this specified variance. Usually v_β is set to 0.01 deg.

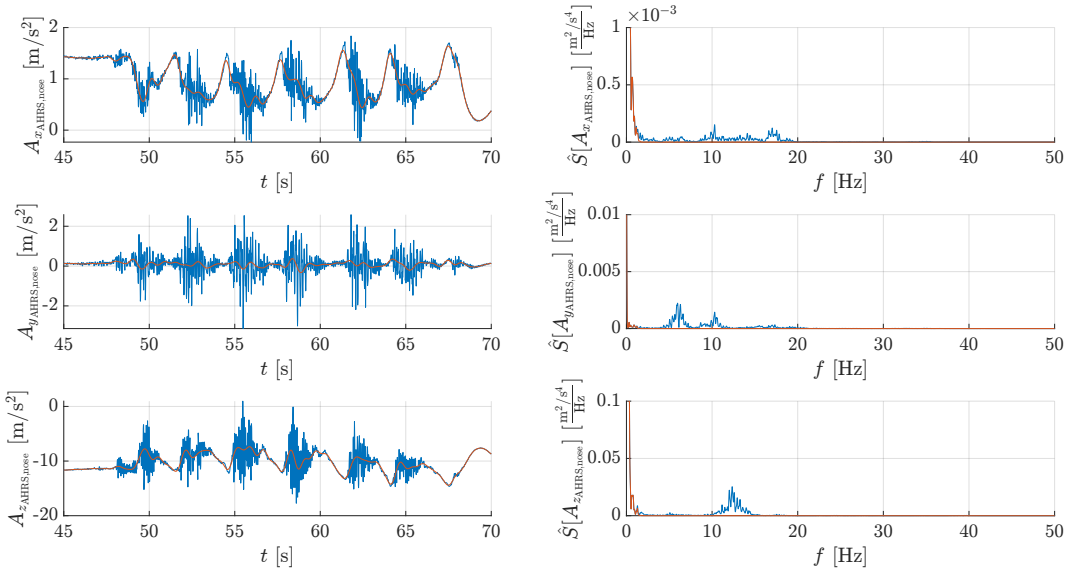

(a) AHRS accelerations.

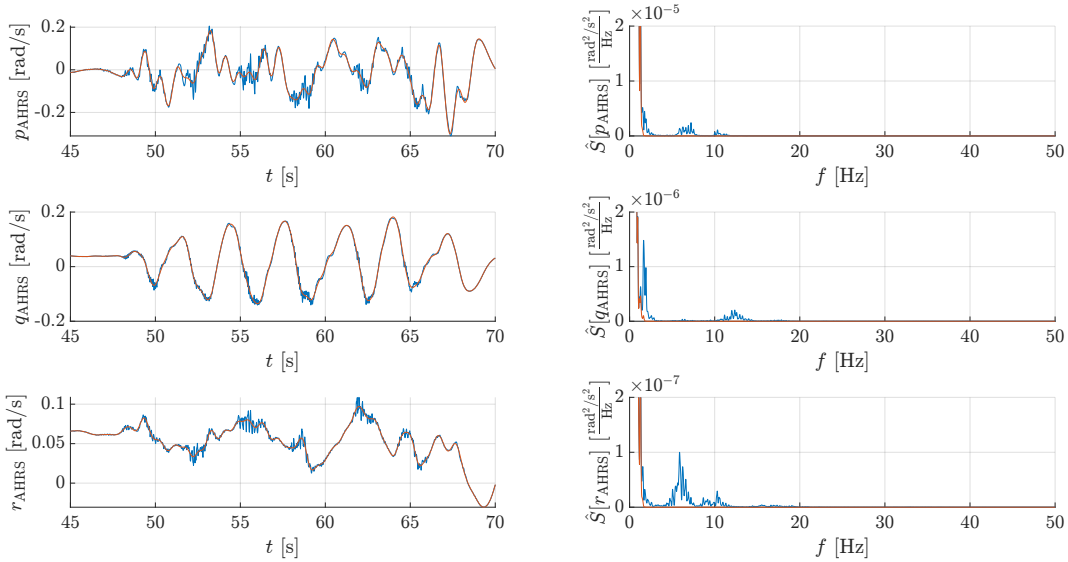

(b) AHRS rotation rates.

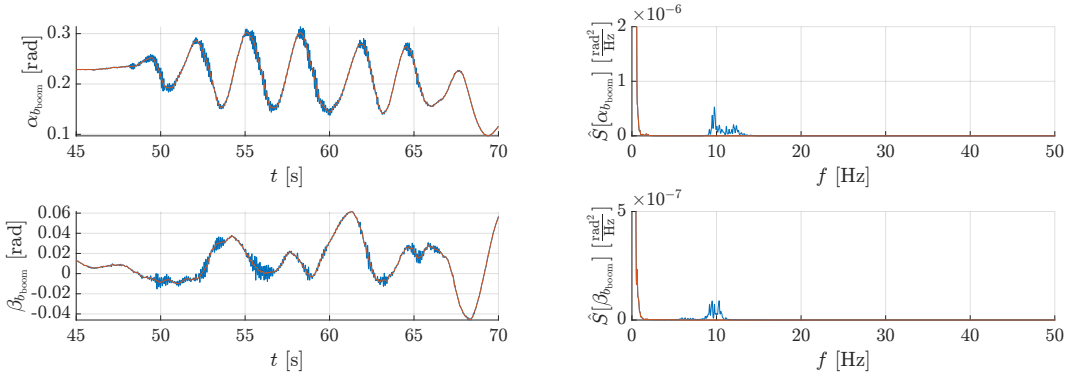

(c) Boom air angels.

Figure 4-2: Example of the pre-filtered signals in the dataset of a stall. Blue is non-filtered data and red is filtered data.

Post-Processing 1: Input and Measurement Reconstruction

After application of the UKF, the state estimates $\hat{\vec{x}}$ can be used to also reconstruct input ($\hat{\vec{u}}$) and measurement ($\hat{\vec{z}}$) data such that also an UKF filtered estimate of those is available for use. For the inputs, the estimated biases are simply subtracted from the input signals:

$$\begin{aligned}
\hat{A}_x &= A_{x_{\text{AHRS}}} - \hat{\lambda}_x \\
\hat{A}_y &= A_{y_{\text{AHRS}}} - \hat{\lambda}_y \\
\hat{A}_z &= A_{z_{\text{AHRS}}} - \hat{\lambda}_z \\
\hat{p} &= p_{\text{AHRS}} - \hat{\lambda}_p \\
\hat{q} &= q_{\text{AHRS}} - \hat{\lambda}_q \\
\hat{r} &= r_{\text{AHRS}} - \hat{\lambda}_r
\end{aligned} \tag{4-54}$$

For reconstruction of the measurements, the state estimates can directly be put into the measurement system of Equation (4-47), *except* for the angle of attack and the angle of sideslip. The measurement model contains the boom $\alpha_{b_{\text{synchro}}}$ and $\beta_{b_{\text{synchro}}}$ and the actual α and β are needed. Thus for those the general definition in terms of u, v and w are used. The result is (for the measurements that are not the same as a state):

$$\begin{aligned}
\hat{\dot{x}} &= [\hat{u}\cos\hat{\theta} + (\hat{v}\sin\hat{\varphi} + \hat{w}\cos\hat{\varphi})\sin\hat{\theta}]\cos\hat{\psi} - (\hat{v}\cos\hat{\varphi} - \hat{w}\sin\hat{\varphi})\sin\hat{\psi} + \hat{W}_{X_E} \\
\hat{\dot{y}} &= [\hat{u}\cos\hat{\theta} + (\hat{v}\sin\hat{\varphi} + \hat{w}\cos\hat{\varphi})\sin\hat{\theta}]\sin\hat{\psi} + (\hat{v}\cos\hat{\varphi} - \hat{w}\sin\hat{\varphi})\cos\hat{\psi} + \hat{W}_{Y_E} \\
\hat{\dot{z}} &= -\hat{u}\sin\hat{\theta} + (\hat{v}\sin\hat{\varphi} + \hat{w}\cos\hat{\varphi})\cos\hat{\theta} \\
\hat{V}_{TAS} &= \sqrt{\hat{u}^2 + \hat{v}^2 + \hat{w}^2} \\
\hat{\alpha} &= \arctan\frac{\hat{w}}{\hat{u}} \\
\hat{\beta} &= \arctan\frac{\hat{v}}{\sqrt{\hat{u}^2 + \hat{w}^2}}
\end{aligned} \tag{4-55}$$

Post-Processing 2: Add Rotational Accelerations, Air Angle Rates and Thrust Data

Also for further use the rotational accelerations, air angle rates and thrust data from the engines must be added to the data.

First, the rotational accelerations $\hat{\dot{p}}$, $\hat{\dot{q}}$ and $\hat{\dot{r}}$. As mentioned before when calculating the c.g. specific accelerations during pre-processing of the data, the rotational accelerations can simply be found by using backwards Newton differentiation of the reconstructed rotation rates $\hat{p}$, $\hat{q}$ and $\hat{r}$.

For the air angle rates $\hat{\dot{\alpha}}$ and $\hat{\dot{\beta}}$ also a backwards Newton differentiation is used on the reconstructed air angles $\hat{\alpha}$ and $\hat{\beta}$.

The engine thrust data is found by using the engine thrust look-up table of the Cessna Citation's JT15 engines. This gives the engine thrust as a function of engine fan speed in

$\%N1$ and Mach number when using the MATLAB `interp2()`-function. The Mach number of the aircraft is found by using the reconstructed true airspeed:

$$\hat{M} = \frac{\hat{V}}{\hat{a}} \tag{4-56}$$

With $\hat{a}$ the estimated speed of sound found by the MATLAB `atmosisa()`-function with the reconstructed altitude $-\hat{z}$ as input. This is performed for both the left and right engine with their respective $N1$ fan speeds. When adding both together, the final estimated total thrust $\hat{T}$ is found.

However, when performing the local estimation in chapter 5 it was found that the model contained considerate peaks in the model residual. Investigating this behaviour it was found that the $\%N1$ contained significant outliers in the data where the $\%N1$ suddenly had a very low reading not physically attainable by the actual engine in such a short time. As this could not be solved by filtering of the data because of the introduction of resonance peaks around the outliers, a separate outlier removal has to be performed before filtering the signal. For this the Matlab `filloutliers()`-function was used with a moving median with a window width of 25 and a removed outlier was given the value of the foregoing measurement. This was found to effectively remove the largest outliers. Some non-outlying measurements were also removed, but the main signal features were not affected. Also, as the signal is filtered in the step hereafter, the removal of these tiny peaks should not affect the reconstruction of the signal. For the effect of the outlier removal see Figure 4-3.

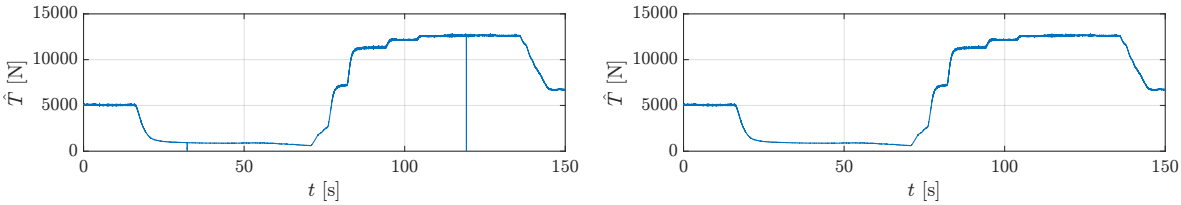

(a) Engine thrust with outliers.

(b) Engine thrust after outlier removal.

Figure 4-3: Example of the thrust outlier removal.

Post-Processing 3: Data Postfiltering

After reconstructing or adding all needed data, some signals must also be post-filtered. The rotational accelerations $\hat{\dot{p}}$, $\hat{\dot{q}}$ and $\hat{\dot{r}}$ and air angle rates $\hat{\dot{\alpha}}$ and $\hat{\dot{\beta}}$ may have amplified noise in their signals due to the performed numerical differentiation. Therefore filtering is necessary to counter this. Also the control surface deflections $\delta_{a_{\text{synchro}}}$, $\delta_{e_{\text{synchro}}}$ and $\delta_{r_{\text{synchro}}}$ must be filtered as these may still have stall buffet effects in the signal. Last, the measurements of the $\%N1$ and the subsequent estimate of $\hat{T}$ are very noisy which introduced very noisy errors in the local model of chapter 5 and thus need to be filtered, too.

Just as for the prefiltering, the filtering here is performed by using the MATLAB `butter()` and `filtfilt()`-functions on the signals in Table 4-4. In the same table the filter properties are also given. The procedure for choosing the passband frequency for the derivatives, of which the primary peak is relatively wide, the end of the peak plus the 0.5 Hz margin was

chosen. For the control surface deflections a very slight secondary peak could be observed for the aileron deflection, so the same passband as for α in pre-filtering was chosen.

Table 4-4: Filter properties for UKF postfiltering.

Signal	Sample freq f_s [Hz]	Passband freq f_{pass} [Hz]
$\hat{\dot{p}}$, $\hat{\dot{q}}$, $\hat{\dot{r}}$	100	3.5
$\hat{\dot{\alpha}}$, $\hat{\dot{\beta}}$	100	3.5
$\delta_{a_{\text{synchro}}}$, $\delta_{e_{\text{synchro}}}$, $\delta_{r_{\text{synchro}}}$	100	4.5
$\hat{T}$	100	2.5

An example of the post-filtered data around a stall can be found in Figure 4-4.

4-5 Applying the UKF

The Kalman Filter procedure as explained above was developed using a selection of stalls and flights from the available data to keep the computational cost lower whilst testing, adapting and tuning the UKF. Data from the flights including the boom was used so that the UKF could be tested for both the boom and no-boom data and a comparison between the two can be made. In this section as an example 150 s of data from a dynamic stall is used, to give an overviewable insight into the UKF behaviour.

First, the tuning of the UKF parameters and initial conditions is discussed. Second, the performance of the UKF itself is evaluated. Last, the most significant differences for the UKF performance between the data with and without boom is discussed.

4-5-1 Tuning UKF Parameters

For the UKF there are three main parameters that can be "tuned": the specific UKF parameters, the initial conditions of the filter and the Q and R matrices.

UKF Parameters

As mentioned before, the UKF can be tuned via the weights of the sigma point matrix. It was found that the standard setting of the parameters from [58] already provided desirable results. Therefore no further tuning was performed on these parameters and they were chosen as: $\alpha = 0.3$, $\kappa = 0$ and $\beta = 2$.

State Initial Conditions

It was found that the UKF performance increases if particular initial conditions are chosen that are relatively close to the actual value of the state. Even though the actual state is unknown, it can be assumed that the available measurements say at least *something* about the actual state, or is at least close to it. Therefore the initial conditions $\hat{\vec{x}}_0$ were chosen as:

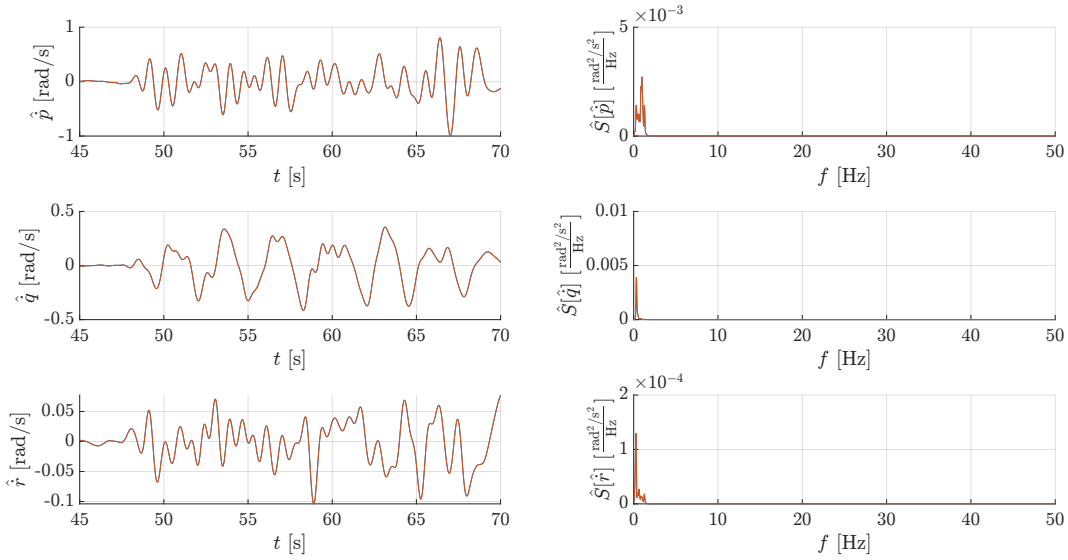

(a) Rotational accelerations.

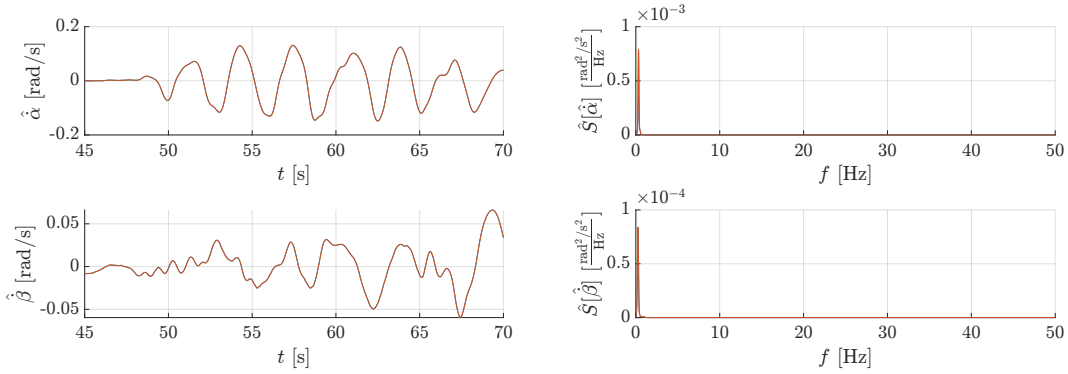

(b) Air angle rates.

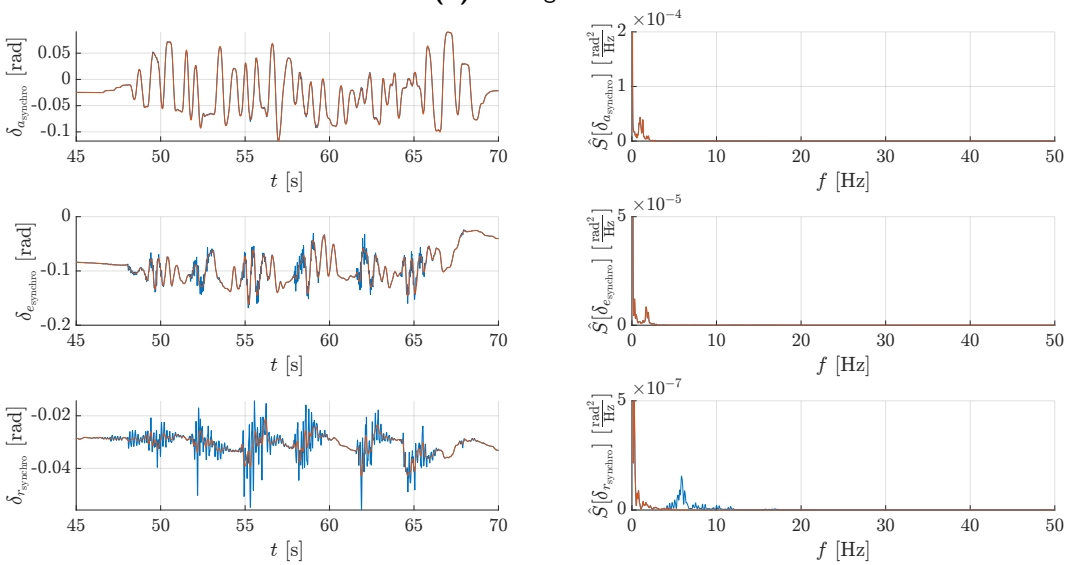

(c) Control surface deflections.

Figure 4-4: (1/2) Example of the post-filtered signals in the dataset of a stall. Blue is non-filtered data and red is filtered data.

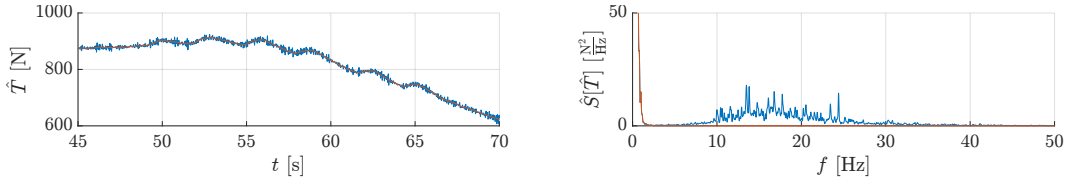

(d) Engine thrust.

Figure 4-4: (continued, 2/2) Example of the post-filtered signals in the dataset of a stall. Blue is non-filtered data and red is filtered data.

$$\hat{\vec{x}}_0 = \begin{bmatrix} x \\ y \\ z \\ u \\ v \\ w \\ \varphi \\ \theta \\ \psi \\ \lambda_x \\ \lambda_y \\ \lambda_z \\ \lambda_p \\ \lambda_q \\ \lambda_r \\ W_{X_E} \\ W_{Y_E} \\ C_{\alpha_{up}} \end{bmatrix} = \begin{bmatrix} x_{\text{GPS}} \\ y_{\text{GPS}} \\ -z_{\text{GPS}} \\ V_{TAS_{\text{DADC}}} \cos\beta_{b_{\text{synchro}}} \cos\alpha_{b_{\text{synchro}}} \\ V_{TAS_{\text{DADC}}} \sin\beta_{b_{\text{synchro}}} \cos\alpha_{b_{\text{synchro}}} \\ V_{TAS_{\text{DADC}}} \cos\beta_{b_{\text{synchro}}} \sin\alpha_{b_{\text{synchro}}} \\ \varphi_{\text{AHRS}} \\ \theta_{\text{AHRS}} \\ \psi_{\text{AHRS}} \\ 0 \\ 0 \\ 0 \\ 0 \\ 0 \\ 0 \\ 0 \\ 0 \\ 0 \end{bmatrix} \tag{4-57}$$

For the covariance matrix P simply 100 was chosen as the initial condition for each of the states.

Q and R Matrices

When building the UKF, it was found that the selection of values in the Q and R matrices *does* greatly influence the performance of the UKF. Using the values of Table 3-2 results in diverging filter estimates and non-desirable results.

It was considered to perform a small research into the best and optimal values of the Q and R matrices, however it quickly became clear that this would take a considerable amount of effort for only a small expected improvement of the UKF performance relative to the performance as reported by [57, 58]. Therefore it was decided to not further investigate the optimal Q and R tuning and directly apply the values as used by [58]. An overview of the difference between the theoretical values of Table 3-2 and the used values has been given in Table 4-5.

It can be seen that there are significant differences between the measurement equipment value and the used value in the filter, sometimes even significant differences in the order of

Table 4-5: Differences between the theoretical variances of Table 3-2 and the used variances in the UKF.

Variable	Noise σ^2			Unit
	Table 3-2	Q **matrix**	R **matrix**	
A_x	$3.9 \cdot 10^{-5}$	$4 \cdot 10^{-4}$	-	m/s^2
A_y	$3.8 \cdot 10^{-4}$	$4 \cdot 10^{-4}$	-	m/s^2
A_z	$2.7 \cdot 10^{-3}$	$4 \cdot 10^{-4}$	-	m/s^2
p	$9.1 \cdot 10^{-4}$	$1 \cdot 10^{-6}$	-	rad/s
q	$1.5 \cdot 10^{-4}$	$1 \cdot 10^{-6}$	-	rad/s
r	$5.4 \cdot 10^{-5}$	$1 \cdot 10^{-6}$	-	rad/s
x	$1.1 \cdot 10^{-1}$	-	$1 \cdot 10^{-0}$	m
y	$1.1 \cdot 10^{-0}$	-	$1 \cdot 10^{-0}$	m
z	$2.2 \cdot 10^{-2}$	-	$1 \cdot 10^{-0}$	m
$\dot{x}$	$2.3 \cdot 10^{-5}$	-	$1 \cdot 10^{-2}$	m/s
$\dot{y}$	$2.4 \cdot 10^{-5}$	-	$1 \cdot 10^{-2}$	m/s
$\dot{z}$	$1.0 \cdot 10^{-4}$	-	$1 \cdot 10^{-2}$	m/s
φ	$2.8 \cdot 10^{-6}$	-	$3.0 \cdot 10^{-6}$	rad
θ	$4.5 \cdot 10^{-7}$	-	$3.0 \cdot 10^{-6}$	rad
ψ	$1.9 \cdot 10^{-6}$	-	$6.8 \cdot 10^{-6}$	rad
V_{TAS}	$2.5 \cdot 10^{-2}$	-	$1 \cdot 10^{-2}$	m/s
α_b	$4.4 \cdot 10^{-4}$	-	$3.0 \cdot 10^{-6}$	rad
β_b	$2.1 \cdot 10^{-4}$	-	$3.0 \cdot 10^{-6}$	rad
α_v	$4.4 \cdot 10^{-8}$	-	$3.0 \cdot 10^{-6}$	rad

magnitude. The reason as to why this is has, as mentioned, not been further investigated.

4-5-2 Testing the UKF

With the initial conditions and tuning parameters defined the UKF is ready for use. In this section it is tested and its performance is assessed.

Filter Innovation

As the actual states are not known (which of course is the reason that the KF is used) the estimates cannot be compared to what they should be. In order to be able to say something useful about the UKF performance one can make use of the filter "Innovation" (Inn), which is defined as the difference between the predicted measurement at time $k+1$ $\hat{\vec{z}}_{k+1,k}$ and the actual measurement at time $k+1$ $\vec{z}_{k+1}$:

$$\text{Inn}[\vec{z}] = \hat{\vec{z}}_{k+1,k} - \vec{z}_{k+1} \tag{4-58}$$

This can then be plotted for each of the measurements. To draw a conclusion about the proper functioning of the filter one has to calculate whether the innovation behaves according to the standard deviation from the measurement covariance matrix P^{zz}. This means that for

at least 68.2% (one standard deviation) of the timesteps the innovation needs to be between the bounds. In that case the performance of the KF is deemed acceptable. The innovation is also plotted for the example plotted below.

UKF Results

The UKF was run on a dataset of 150 s of a dynamic stall at an altitude of 5700 m (stall run 19 of Table A-2). The results of running the UKF on this dataset are given in Figure 4-5, Figure 4-6, Figure 4-7 and Figure 4-8.

Looking at the data the UKF performs as desired. The behaviour of the states is as expected. For the data were a measurement is available there is a significant deviation for the state $\hat{w}$, but no conclusion may be drawn from this as it is the task of the UKF to reconstruct the flight path and differences can thus be expected.

Also, the estimate $\hat{w}$ is heavily influenced by the air data measurements which are interesting in itself and might explain partly the behaviour of $\hat{w}$. Looking at the reconstructed measurements of $\hat{\alpha}$ and $\hat{\beta}$, one can observe significant differences between the reconstruction and the actual measurement.

- *Angle of attack.* The raw measurement of the angle of attack shows constantly a higher angle of attack than the reconstructed angle of attack. This seems very intuitive due to the location of boom vanes in the upwash present in front of the aircraft's nose, which can be explained by the positive estimate of $C_{\alpha_{up}}$ as well. This is thus also as expected.
- *Angle of sideslip.* The raw measurement of the angle of sideslip is also slightly higher than the estimated angle. For this dataset, the aircraft is in a right turn, resulting a relatively constant positive yaw rate (see states). According to Equation (4-33) this results in a higher measurement by the boom than the actual angle of sideslip. This indeed confirms the observation.

Last, the measurement innovations are investigated as these say the most about the behaviour of the UKF. It can be observed that the innovations are generally within the 40-60% range, or higher (except for the vertical acceleration) This is just, but not significantly, below the 68.2% that can be expected for crisp signals of a nonlinear system. As the flight data used in this thesis contains many disturbances and unknowns (e.g. the noise variances which are not the theoretical values) it can be expected that the innovations fall slightly below the 1σ bound. As also can be observed, after the stall the innovations tend to return to between the bounds again, which also speaks for its effectiveness. However, the UKF performance within the actual stall might be a topic that needs further research. That is however not the topic of this thesis and it was decided that the desired performance of the UKF is reached in this case.

Another observation worth noting is the behaviour of the x_{GPS} and y_{GPS} innovations. It can be seen that the innovation behaves almost like a "bouncing ball". This is actually behaviour that reinforces the trust in the UKF behaviour. As known, the sampling rate of the GPS is 1 Hz, but the UKF reconstructs the flight path in 100 Hz; the reconstruction is "smoother" than the actual signal. Thus, from the last measurement point of the GPS, the

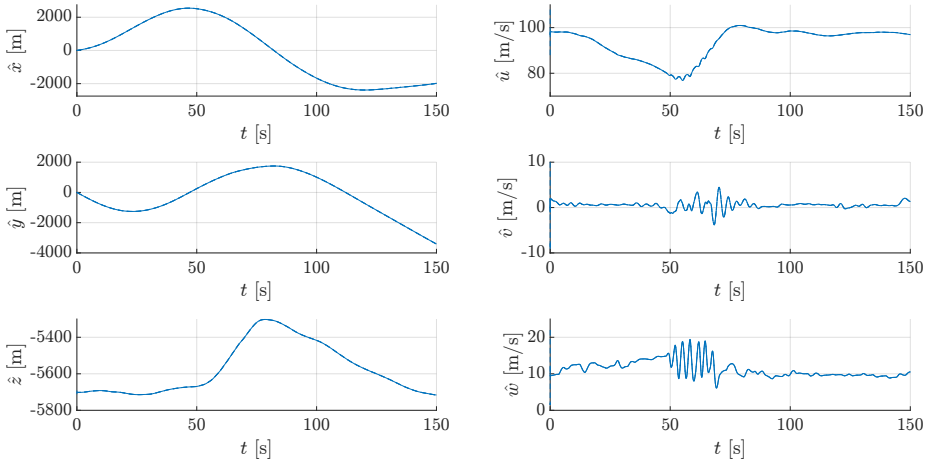

(a) State estimates $\hat{x}$, $\hat{y}$, $\hat{z}$, $\hat{u}$, $\hat{v}$, $\hat{w}$.

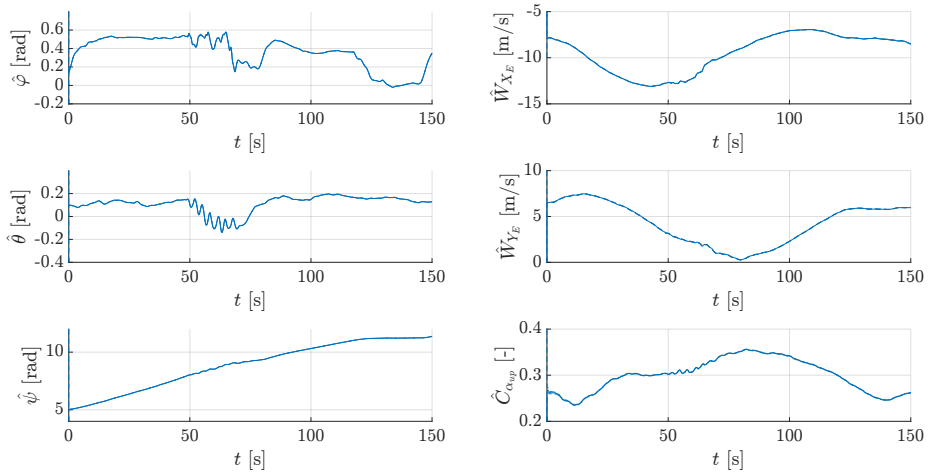

(b) State estimates $\hat{\varphi}$, $\hat{\theta}$, $\hat{\psi}$, $\hat{W}_{X_E}$, $\hat{W}_{X_E}$, $\hat{C}_{\alpha_{up}}$.

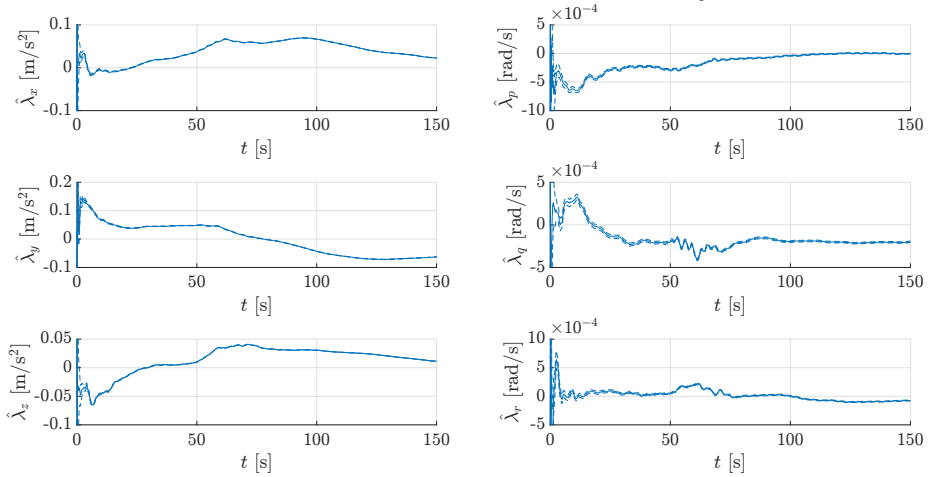

(c) State estimates $\hat{\lambda}_x$, $\hat{\lambda}_y$, $\hat{\lambda}_z$, $\hat{\lambda}_p$, $\hat{\lambda}_q$, $\hat{\lambda}_r$.

Figure 4-5: UKF estimated states.

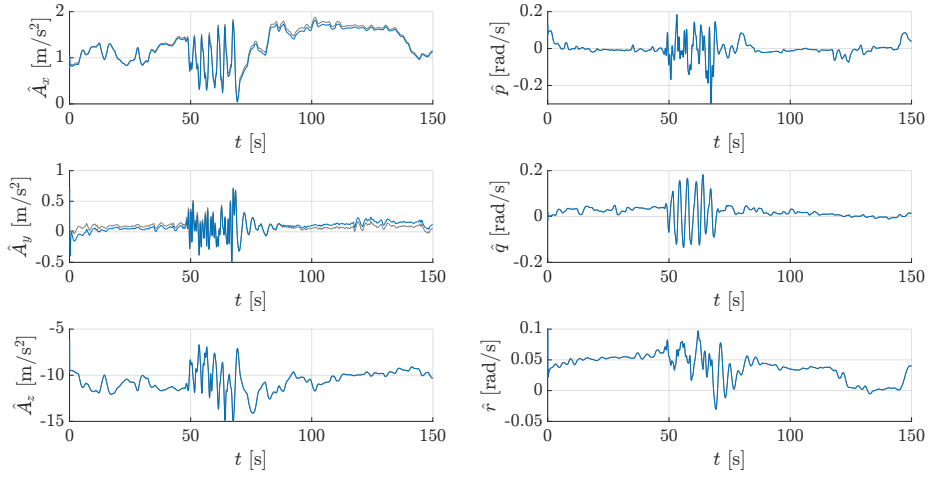

(a) Input estimates $\hat{A}_x$, $\hat{A}_y$, $\hat{A}_z$, $\hat{p}$, $\hat{q}$, $\hat{r}$.

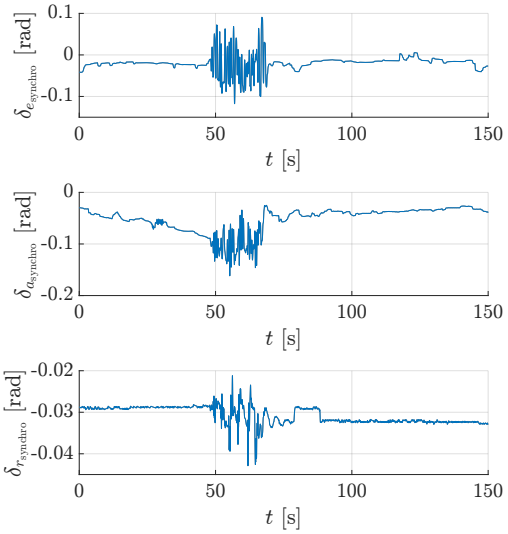

(b) Input estimates $\delta_{e_{\text{synchro}}}$, $\delta_{a_{\text{synchro}}}$, $\delta_{r_{\text{synchro}}}$.

Figure 4-6: UKF estimated inputs. Blue is the estimated input and grey is the input from raw measurements (if available).

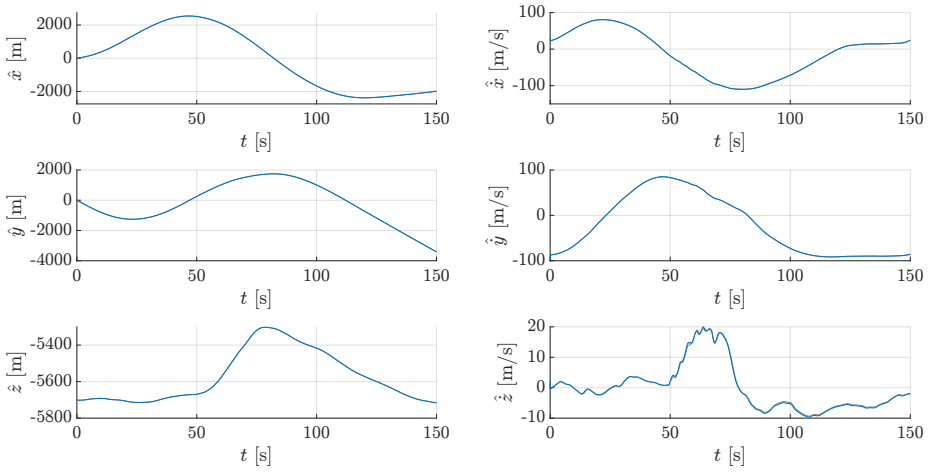

(a) Reconstructed measurements $\hat{x}$, $\hat{y}$, $\hat{z}$, $\dot{\hat{x}}$, $\dot{\hat{y}}$, $\dot{\hat{z}}$.

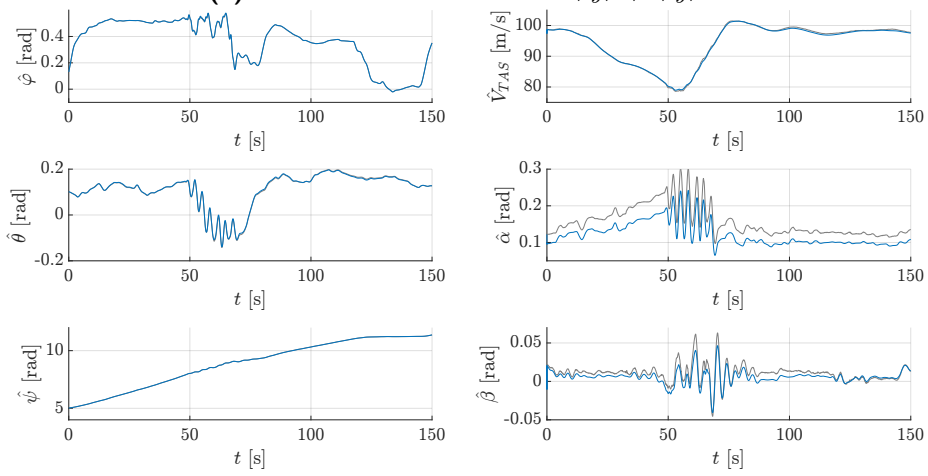

(b) Reconstructed measurements $\hat{\varphi}$, $\hat{\theta}$, $\hat{\psi}$, $\hat{V}_{TAS}$, $\hat{\alpha}$, $\hat{\beta}$.

Figure 4-7: UKF reconstructed measurements. Blue is the reconstructed measurement and grey is the raw measurement.

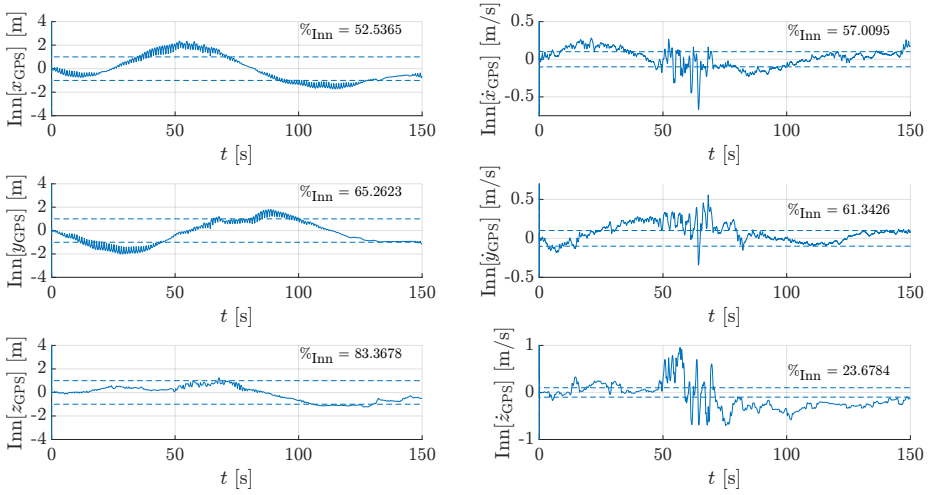

(a) Measurement innovations x_{GPS}, y_{GPS}, z_{GPS}, $\dot{x}_{\text{GPS}}$, $\dot{y}_{\text{GPS}}$, $\dot{z}_{\text{GPS}}$.

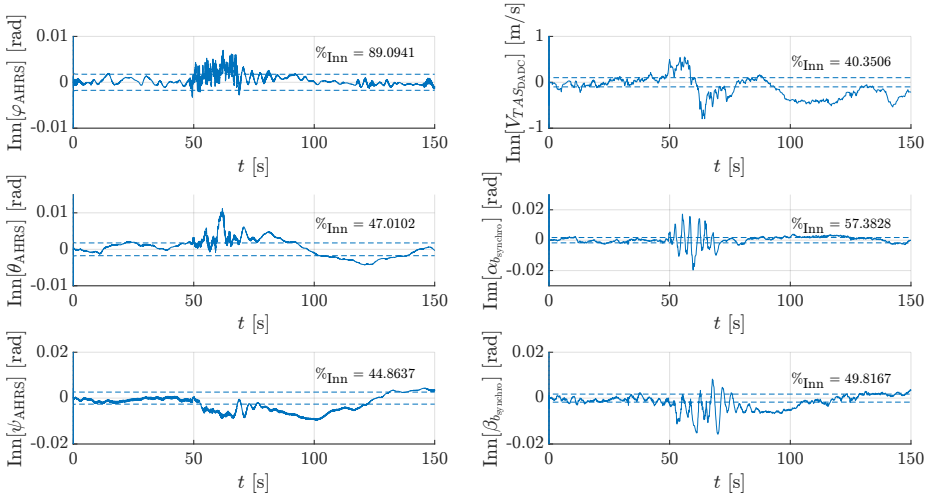

(b) Measurement innovations φ_{AHRS}, θ_{AHRS}, ψ_{AHRS}, $V_{TAS_{\text{DADC}}}$, $\alpha_{b_{\text{synchro}}}$, $\beta_{b_{\text{synchro}}}$.

Figure 4-8: UKF measurement innovations. Solid is the innovation and dashed is the measurement covariance.

UKF prediction and measurement start to diverge as the measurement is actually linear to the next measurement point 100 timesteps later, while the prediction is actually moves only 1 timestep. Thus they diverge until 50 timesteps, and then start to converge again to the next measurement point, after which a sudden diversion starts again, causing the "bouncing ball" effect in the innovation. But actually, it can thus be concluded that the UKF does a more accurate reconstruction than the measurement is able to give.

4-5-3 Comparison of Boom Data and AOA Vane Data

As the kinematic model of the case where the boom is used and where no boom is available differ significantly, it is interesting to look at the main differences between the two on the exact same dataset. It may also indicate something about the reliability of the no-boom data. In this chapter a comparison is made of the filtered data for both cases. For the UKF results of both cases see Figure 4-9, Figure 4-10, Figure 4-11 and Figure 4-12.

For most of the estimated states the UKF performs comparatively to the UKF with the boom data, but significant differences exist for $\hat{v}$ and $\hat{C}_{\alpha_{up}}$. Basically, it becomes clear that without an angle of sideslip measurement the lateral velocity v cannot be estimated correctly. It should thus be concluded that one should take the utmost care when no-boom data is regarded for lateral modeling of the aircraft, or it should simply not be used at all. Another difference is for the upwash coefficient, which is significantly lower than that with the boom, but it shows the same behaviour. The lower value can be explained by the fact that the AOA vane is further down the fuselage where the effect is less present. As it *does* show the same behaviour, it can be regarded as a trustworthy estimate. The biases show the same behaviour, although more excitations are present in $\hat{\lambda}_r$.

The measurements also show comparative behaviour, but extra interesting are the air angles. For $\hat{\alpha}$, the estimate of the no-boom data is significantly good and almost the same as that of the boom data. More interesting is when the estimate is compared to the AOA vane measurement. The vane measurement is very different from that of the boom, but still they result in the same estimate, proving the performance of the UKF. Also note that the slight vane measurement delay can be seen observed, but due to the modeled time constant this does not affect the estimate. Another conclusion must be drawn for $\hat{\beta}$. Due to the lack of β measurement without the boom the estimate of $\hat{\beta}$ is very unreliable. Again, one should consider not using the no-boom data for lateral modeling.

The last interesting differences can be found in the innovations. A comparison of the 1σ-bound performance is given in Table 4-6.

When looking at the innovation time series, the largest differences can be observed in that of the aircraft rotation angles, especially θ and ψ show larger excitation around the stall, even though the percentage bound is higher for θ, but lower for ψ. Why this excitation is larger is unknown, but it may be due to the fact that with the boom, more information is available about u, v and w and as such a better prediction can be made of the rotational velocities when evaluating $f()$, which then in return delivers a more trustworthy integration and prediction of θ and ψ, while for the no-boom data this information is not available. For α, the no-boom UKF also shows good performance. While, as seen, for the performance related to β, the no-boom UKF is significantly worse.

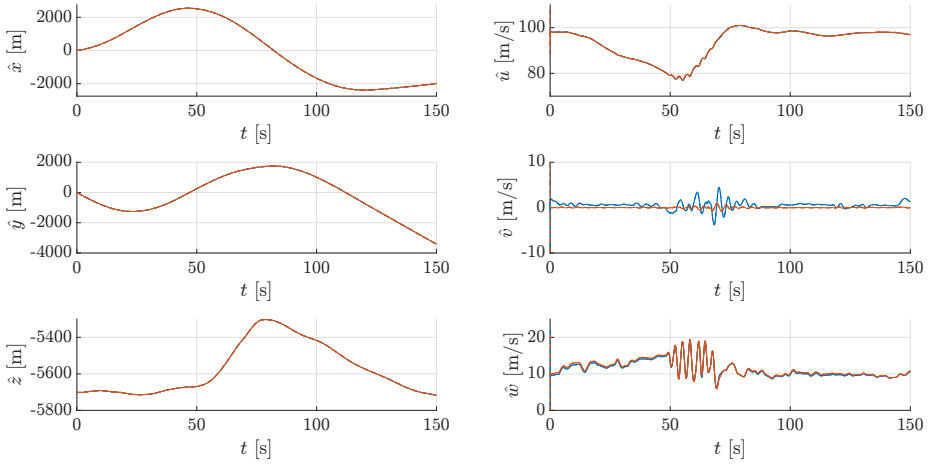

(a) State estimates $\hat{x}$, $\hat{y}$, $\hat{z}$, $\hat{u}$, $\hat{v}$, $\hat{w}$.

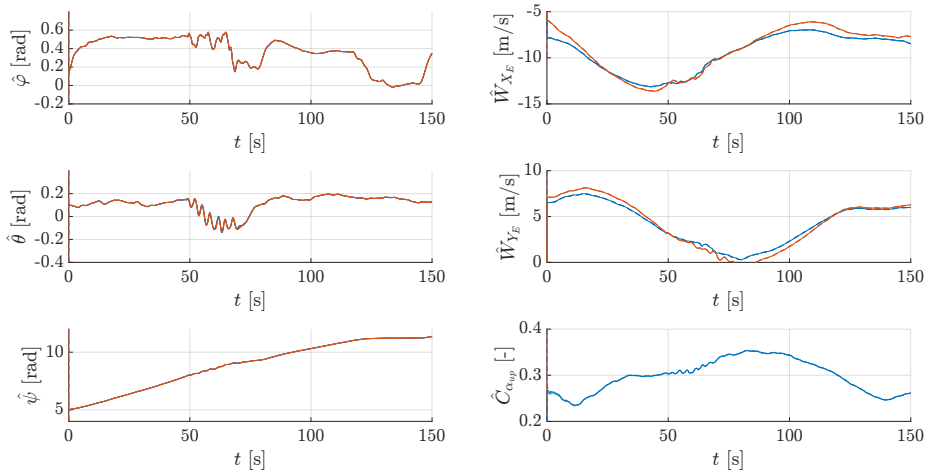

(b) State estimates $\hat{\varphi}$, $\hat{\theta}$, $\hat{\psi}$, $\hat{W}_{X_E}$, $\hat{W}_{X_E}$, $\hat{C}_{\alpha_{up}}$.

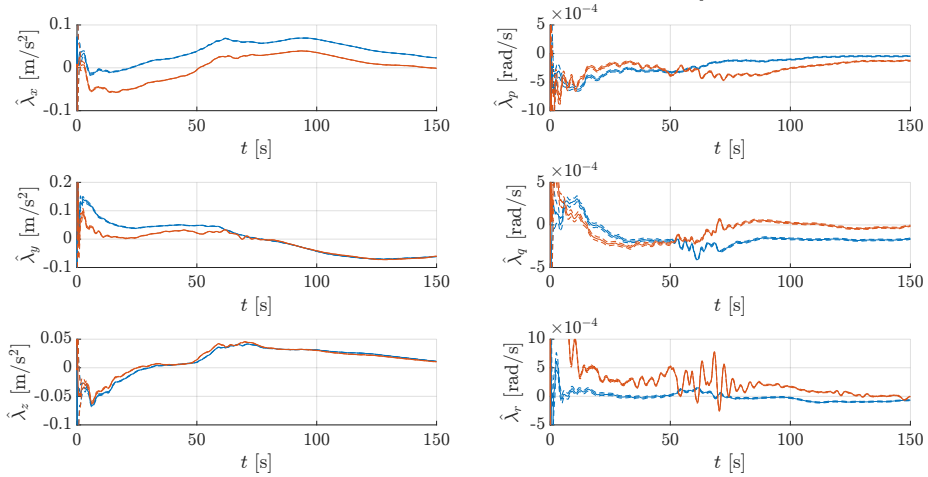

(c) State estimates $\hat{\lambda}_x$, $\hat{\lambda}_y$, $\hat{\lambda}_z$, $\hat{\lambda}_p$, $\hat{\lambda}_q$, $\hat{\lambda}_r$.

Figure 4-9: (1/2) UKF estimated states comparison. Blue is the estimated state from the boom data and red is the estimated state from the no-boom data.

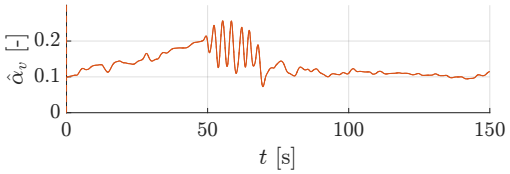

(d) State estimate α_v.

Figure 4-9: (continued, 2/2) UKF estimated states comparison. Blue is the estimated state from the boom data and red is the estimated state from the no-boom data.

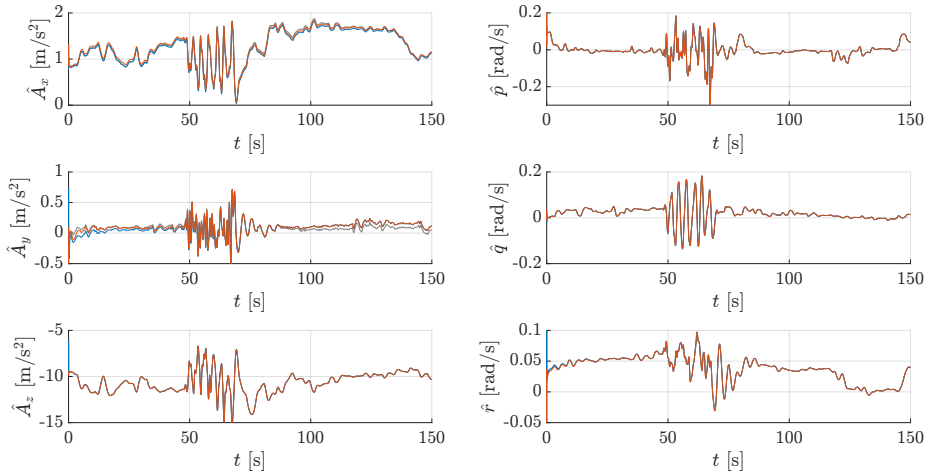

(a) Input estimates $\hat{A}_x$, $\hat{A}_y$, $\hat{A}_z$, $\hat{p}$, $\hat{q}$, $\hat{r}$.

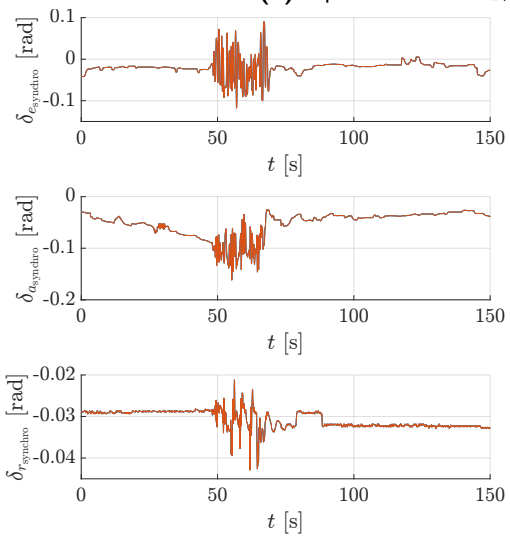

(b) Input estimates $\delta_{e_{\text{synchro}}}$, $\delta_{a_{\text{synchro}}}$, $\delta_{r_{\text{synchro}}}$.

Figure 4-10: UKF estimated inputs comparison. Blue is the estimated state from the boom data, red is the estimated state from the no-boom data and grey is the input from raw measurements (if available).

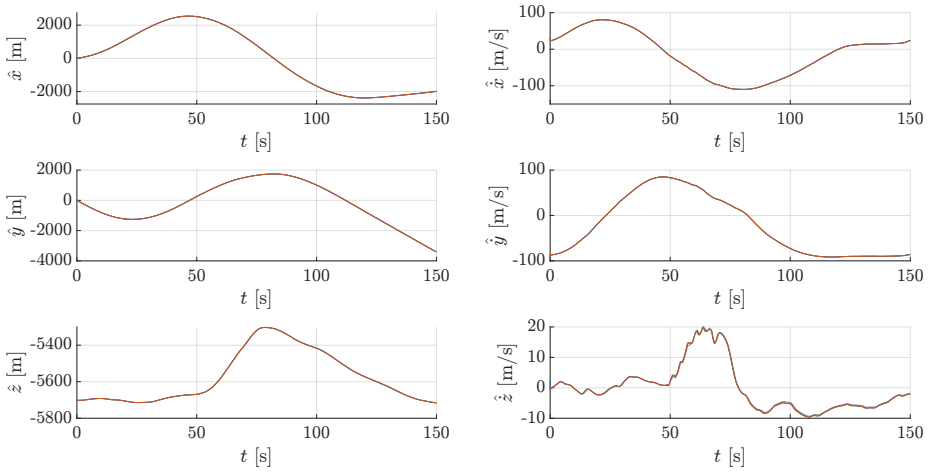

(a) Reconstructed measurements $\hat{x}$, $\hat{y}$, $\hat{z}$, $\hat{\dot{x}}$, $\hat{\dot{y}}$, $\hat{\dot{z}}$.

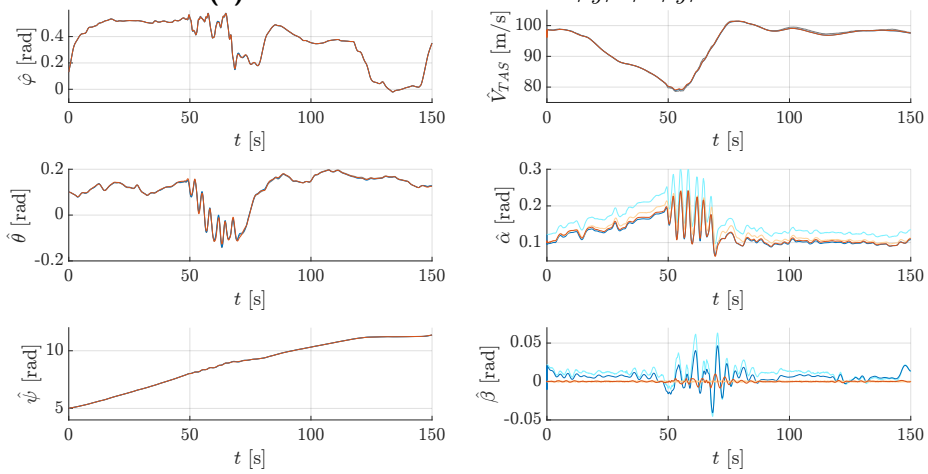

(b) Reconstructed measurements $\hat{\varphi}$, $\hat{\theta}$, $\hat{\psi}$, $\hat{V}_{TAS}$, $\hat{\alpha}$, $\hat{\beta}$.

Figure 4-11: UKF reconstructed measurements comparison. Blue is the estimated state from the boom data, red is the estimated state from the no-boom data and grey is the raw measurement (for $\hat{\alpha}$ and $\hat{\beta}$: lightblue are the raw measurements of the boom and lightred is the vane AOA and pseudo-β).

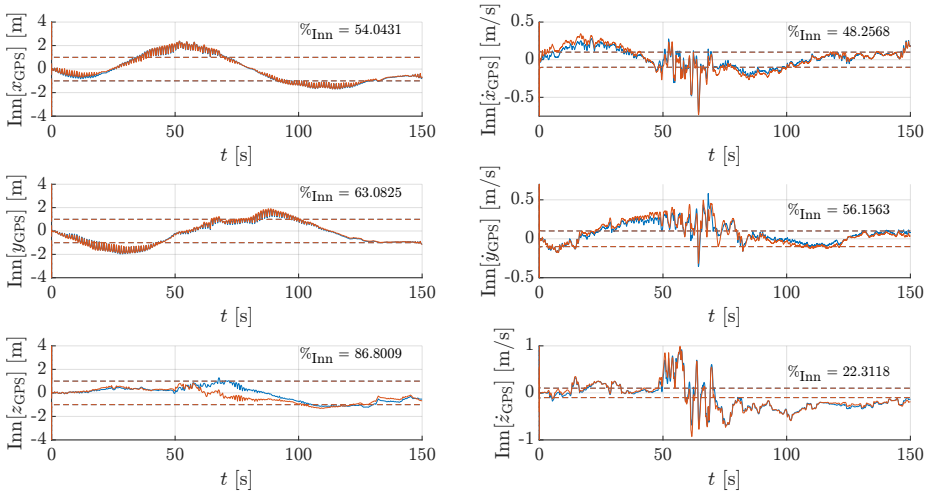

(a) Measurement innovations x_{GPS}, y_{GPS}, z_{GPS}, $\dot{x}_{\text{GPS}}$, $\dot{y}_{\text{GPS}}$, $\dot{z}_{\text{GPS}}$.

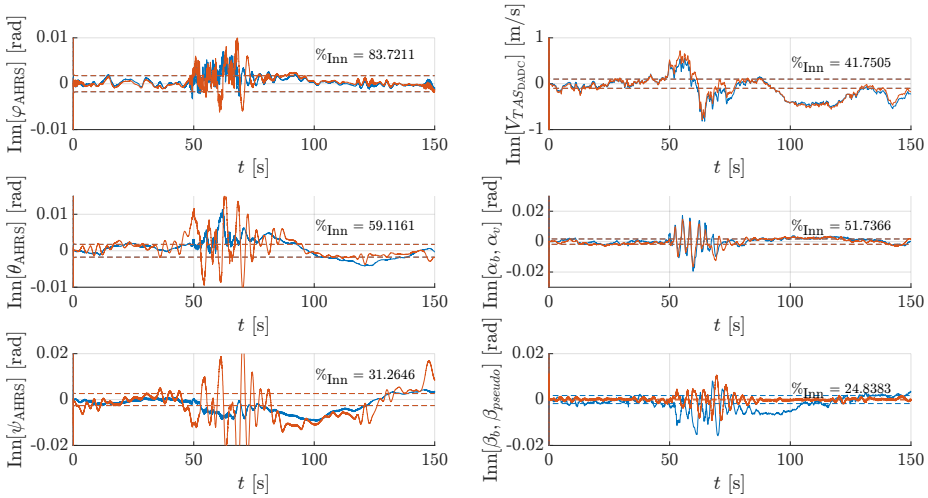

(b) Measurement innovations φ_{AHRS}, θ_{AHRS}, ψ_{AHRS}, $V_{TAS_{\text{DADC}}}$, $\alpha_{b_{\text{synchro}}}/\alpha_{v_{\text{analog}}}$, $\beta_{b_{\text{synchro}}}/\beta_{pseudo}$.

Figure 4-12: UKF measurement innovations comparison. Blue is the estimated state from the boom data and red is the estimated state from the no-boom data, and solid is the innovation and dashed is the measurement covariance. The percentage shown is for the UKF with the pseudo-β.

Table 4-6: Comparison of innovation percentages of boom and no-boom data.

Measurement	$\%_{\mathbf{Inn}_b}$	$\%_{\mathbf{Inn}_v}$
x_{GPS}	54.0364	54.0431
y_{GPS}	66.2223	63.0825
z_{GPS}	82.9345	86.8009
$\dot{x}_{\text{GPS}}$	57.7095	48.2568
$\dot{y}_{\text{GPS}}$	60.0227	56.1563
$\dot{z}_{\text{GPS}}$	23.9051	22.3118
φ_{AHRS}	88.5874	83.7211
θ_{AHRS}	47.7168	59.1161
ψ_{AHRS}	45.417	31.2646
$V_{TAS_{\text{DADC}}}$	39.2907	41.7505
$\alpha_{\text{synchro}}/\alpha_{v_{\text{analog}}}$	57.2429	51.7366
$\beta_{\text{synchro}}/\beta_{pseudo}$	50.3633	24.8383

4-6 Conclusion on Flight Path Reconstruction

From the results in the above sections it can be concluded that the UKF performs the FPR reasonably well for the stall manoeuvre in consideration with the air data boom installed. It performs as good as may be expected for a reconstruction on real data from a flight where still some unknown disturbances remain that are not captured in the kinematic or measurement model. As for the innovations of the UKF, they approach the theoretically expected performance of 66% , even though some innovations are lower, especially the case for the vertical velocity, pitch and yaw angle and the true airspeed. However it is deemed that these innovations are the highest achievable in this case. The obtained results are comparable to earlier research [57, 58].

Comparing the results with the air data boom measurements the FPR results of the same flight with the pseudo-β, it can be seen that comparable results are found and the latter case also achieves the same reasonably good performance for the longitudinal states. However, it is evident that the no-boom data cannot be used when regarding the lateral motions of the aircraft.

Even though the UKF thus has reasonable performance, it should be kept in mind that there are a significant number of assumption made in the process of building the entire FPR procedure, which may effect its reliability. This should thus be taken into regard when assessing the reliability of further results making use of the reconstructed data. Nevertheless, based on the observed performance it is concluded that the UKF can be used in further research of this thesis to perform the Flight Path Reconstruction.

Chapter 5

Local Aerodynamic Modeling and Parameter Estimation

With the results from the FPR the estimated states and reconstructed measurements are now "trustworthy" and, more importantly, accurate enough to be used as variables in the aerodynamic modeling of the aircraft. This accuracy is required such that any movement of the aircraft is captured, but also any input or state that caused these movements is known accurately, such that the inputs, states can be linked to the output accurately, which together results in a reliable aerodynamic model of the aircraft, which -when used- delivers results that mimic the actual aircraft as close as possible.

This chapter aims to develop such a model for the Citation in stall. First, the basics of aircraft modeling are reviewed, along with common model structures. Then, the model is extended to incorporate specific stall behaviour, making use of Kirchoff's theory as explained in chapter 2. This includes the origins of the chosen stall model as designed via Orthogonal Function Modeling. Next, the procedure to estimate the chosen aircraft aerodynamic stall model is explained step by step. This starts with nonlinear estimation methods needed for the estimation of the X parameters in Kirchoff's theory, as well as the linear regression methods used to find the parameters of the final aerodynamic model. Last, the found model is evaluated, verified and validated.

5-1 General Aircraft Aerodynamic Model

In this section the basics of aircraft aerodynamic modeling are discussed. Thereafter it is discussed how the model has been extended to stall modeling by Kirchoff's theory of flow separation via Orthogonal Function Modeling. This model is used in the next section to perform the parameter estimation.

5-1-1 Aircraft Reference Frames

A very important part in aircraft modeling is the use of different reference frames, as any model is usually only applicable to that specifically chosen frame. The aircraft equations of motion are usually given in a form that define the aircraft flight dynamics in terms of forces, moments and angles respective to that frame. Two important frames for aircraft modeling are the aircraft body frame and aircraft vehicle-carried normal Earth reference frame.

The first is the aircraft body-fixed frame which is fixed to the aircraft. The origin is in the aircraft c.g., with the x-axis pointing forward in the plane of symmetry through the aircraft's nose, the z-axis is pointing down in this plane of symmetry and the y-axis is pointed right, perpendicular to the plane of symmetry. The Figure 5-1 shows the aircraft body-frame F_b.

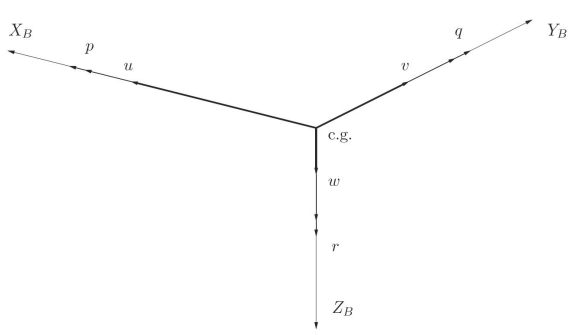

(a) The six degrees of freedom of a rigid aircraft.

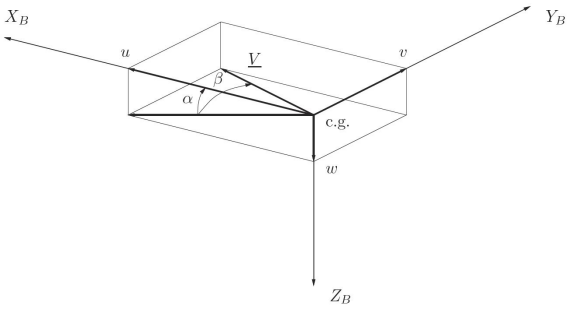

(b) Definition of the angle of attack α and sideslip angle β.

Figure 5-1: Overview of the aircraft body frame F_b [42].

The variables in these figures are defined as below:

F_b : aircraft body-frame
$c.g.$: center of gravity
X_B : aircraft body x-axis
Y_B : aircraft body y-axis
Z_B : aircraft body z-axis
u : velocity in direction X_B
v : velocity in direction Y_B
w : velocity in direction Z_B
X : aerodynamic force in direction of u
Y : aerodynamic force in direction of v
Z : aerodynamic force in direction of w
p : angular velocity around X_B
q : angular velocity around Y_B
r : angular velocity around Z_B
ℓ : aerodynamic moment in direction of p
m : aerodynamic moment in direction of q
n : aerodynamic moment in direction of r
α : angle between $\vec{V}$ and the X_B, Y_B-plane
β : angle between $\vec{V}$ and the X_B, Z_B-plane
δ_a : aileron deflection (right wing down positive)
δ : elevator deflection (down positive)
δ_r : rudder deflection (left positive)

Furthermore, there are a number of variables used in aircraft modeling that do not come from the aircraft F_b frame, but from the aircraft "vehicle-carried normal Earth reference frame" F_E, also known as the "navigation frame" or "NED"-frame (for North, East, Down) or simply just "earth-frame". This frame has its origin in the aircraft c.g., with the x-axis pointing North normal to the Earth's geoid surface, the y-axis pointing east and z-axis pointing down normal to the Earth's geoid surface. See Figure 5-2.

Important variables in this frame are:

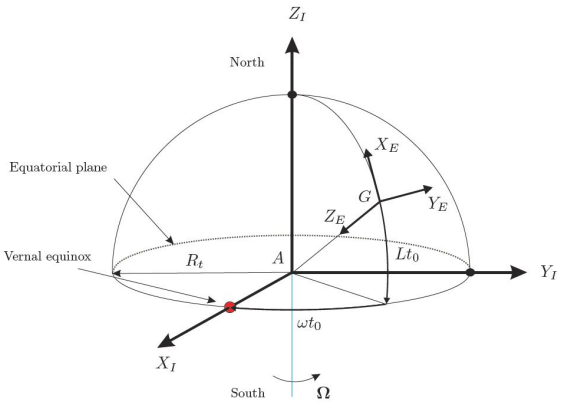

Figure 5-2: Overview of the aircraft vehicle-carried normal Earth reference frame F_E [42].

F_E : aircraft earth-frame
X_E : earth frame x-axis, pointing North
Y_E : earth frame y-axis, pointing East (90 deg from X_E)
Z_E : earth frame z-axis, pointing Down (for flat earth assumption, normal to earth surface)
$\dot{x}$: velocity in direction X_E
$\dot{y}$: velocity in direction Y_E
$\dot{z}$: velocity in direction Z_E
ψ : aircraft yaw angle about X_E (derivative of ψ is r)
θ : aircraft pitch angle between X_B and the X_E, Y_E-plane (derivative of θ is q)
φ : aircraft roll angle about X_B (derivative of φ is p)

Both reference frames are used interchangeably in flight simulation models, which is further elaborated upon below.

5-1-2 Aircraft Equations of Motion for Flight Simulation

Often the final goal of aircraft modeling is to reproduce the aircraft's motion as realistically as possible for use in flight simulation. Therefore aerodynamic models of aircraft usually have a (mathematical) structure that is applicable for this purpose.

The core of any flight simulator is this mathematical model. It comes in two main forms, the first being the general nonlinear equations of motion that apply in the entire flight envelope, and the second their derivatives; the so-called small perturbation equations which can be used to calculate the aircraft behaviour closely around a certain speed and altitude of steady, trimmed, symmetric flight [2]. To simulate a complete flight from take-off to landing one needs to make use of the general nonlinear equations.

The general equations of motion in the F_b-frame are given by:

$$F_{X_B} = X - W\sin\theta = m(\dot{u} + qw - rv) \tag{5-1}$$
$$F_{Y_B} = Y + W\cos\theta\sin\varphi = m(\dot{v} + ru - pw) \tag{5-2}$$
$$F_{Z_B} = Z + W\cos\theta\cos\varphi = m(\dot{w} + pv - qu) \tag{5-3}$$
$$M_{X_B} = L = \dot{p}I_{xx} + qr(I_{zz} - I_{yy}) - (pq + \dot{r})I_{xz} \tag{5-4}$$
$$M_{Y_B} = M = \dot{q}I_{yy} + rp(I_{xx} - I_{zz}) - (p^2 - r^2)I_{xz} \tag{5-5}$$
$$M_{Z_B} = N = \dot{r}I_{zz} + pq(I_{yy} - I_{xx}) + (qr - \dot{p})I_{xz} \tag{5-6}$$

Which can be rewritten into six equations for $\dot{u}$, $\dot{v}$, $\dot{w}$, $\dot{p}$, $\dot{q}$ and $\dot{r}$. Next to these equations for the body linear and rotational accelerations, it is important to incorporate the relation between the accelerations in the body frame to the movement of the aircraft in the F_E-frame and Euler angle rates in the F_E-frame, as given by:

$$V_{X_E} = \dot{x} = [u\cos\theta + (v\sin\varphi + w\cos\varphi)\sin\theta]\cos\psi - (v\cos\varphi - w\sin\varphi)\sin\psi \tag{5-7}$$
$$V_{Y_E} = \dot{y} = [u\cos\theta + (v\sin\varphi + w\cos\varphi)\sin\theta]\sin\psi + (v\cos\varphi - w\sin\varphi)\cos\psi \tag{5-8}$$
$$V_{Z_E} = \dot{z} = -u\sin\theta + (v\sin\varphi + w\cos\varphi)\cos\theta \tag{5-9}$$
$$\omega_{X_E} = \dot{\varphi} = p + q\sin\varphi\tan\theta + r\cos\varphi\tan\theta \tag{5-10}$$
$$\omega_{Y_E} = \dot{\theta} = q\cos\varphi - r\sin\varphi \tag{5-11}$$
$$\omega_{Z_E} = \dot{\psi} = q\frac{\sin\varphi}{\cos\theta} + r\frac{\cos\varphi}{\cos\theta} \tag{5-12}$$

Note the correspondence between the above equations and the FPR navigation equations of Equation (4-27). With the above equations the entire path and orientation of the aircraft during the flight can be simulated by calculating the accelerations in the body frame and then using the relations to the ECEF frame to calculate the aircraft's trajectory.

However, to calculate the accelerations in the body frame in the first place, one needs to know the forces and moments F_{X_B}, F_{Y_B}, F_{Z_B}, M_{X_B}, M_{Y_B} and M_{Z_B} in that frame. For this an additional *aerodynamic model* is used [2].

5-1-3 Aircraft Aerodynamic Model

The aircraft's aerodynamic model describes the forces and moments in the body frame as a function of the aircraft's current state and any given inputs. Instead of body axes X and Z often the drag and lift coefficients D and L along and perpendicular to the aircraft speed vector $\vec{V}$ are used, but can be converted back to X and Y via α and β for calculation in the equations of motion (see Equation (5-55) and Equation (5-56)). Rather than using a dimensional version of the force and moment equations it is customary to use the form of dimensionless coefficients [2]. This is defined as:

$$C_D = \frac{D}{\frac{1}{2}\rho V^2 S}, \quad C_Y = \frac{Y}{\frac{1}{2}\rho V^2 S}, \quad C_L = \frac{L_{(\text{lift})}}{\frac{1}{2}\rho V^2 S}, \quad C_\ell = \frac{L}{\frac{1}{2}\rho V^2 S b}, \quad C_m = \frac{M}{\frac{1}{2}\rho V^2 S \bar{c}}, \quad C_n = \frac{N}{\frac{1}{2}\rho V^2 S b} \tag{5-13}$$

The most common model structure for the calculation of the force and moment coefficients for operation within the largest part of the envelope when using flight test data is given by [28]:

$$C_i = C_i\left(\frac{V}{V_0}, \alpha, \beta, \frac{pb}{2V}, \frac{q\bar{c}}{V}, \frac{rb}{2V}, \frac{\dot{\alpha}\bar{c}}{V}, \frac{\dot{\beta}b}{2V}, \delta\right), \quad \text{for } i = D, Y, L, \ell, m, n \tag{5-14}$$

Which in practise are the aircraft states V, α, β, p, q and r and control deflections δ, which can be aileron, elevator and rudder deflections, but also any other control input like flap or thrust setting. For any force related to the state α the resulting force does not only relate to the instantaneous state, but also its entire time history that effects the current flow. However, for practical applications it is generally assumed that the flow is quasi-steady such that these effects are not present and any α-related coefficient is only affected by its current state. However as discussed in chapter 2 this cannot be assumed for the stall region, where the flow is significantly unsteady and time-related effects are significant such that a more complex model structure is desired. This is discussed later in this chapter.

In order to be able to make practical use of the force and moment coefficients these are often linearized via a first order Taylor series expansion about a certain trimming point, denoted by the subscript "$_0$". A first order is chosen as higher order effects are often negligible because of the only small perturbations. For example, for the lift force the Taylor series expansion becomes:

$$\begin{aligned} C_L = C_{L_0} + C_{L_V}\frac{(V-V_0)}{V_0} + C_{L_\alpha}(\alpha-\alpha_0) + C_{L_\beta}(\beta-\beta_0) + \dots \\ \cdots + C_{L_p}\frac{(p-p_0)b}{2V_0} + C_{L_q}\frac{(q-q_0)\bar{c}}{V_0} + C_{L_r}\frac{(r-r_0)b}{2V_0} + \dots \\ \dots + C_{L_{\dot{\alpha}}}\frac{(\dot{\alpha}-\dot{\alpha}_0)\bar{c}}{V_0} + C_{L_{\dot{\beta}}}\frac{(\dot{\beta}-\dot{\beta}_0)b}{2V_0} + \dots \\ \dots + C_{L_{\delta_a}}(\delta_a-\delta_{a_0}) + C_{L_{\delta_e}}(\delta_e-\delta_{e_0}) + C_{L_{\delta_r}}(\delta_r-\delta_{r_0}) + C_{L_{\delta_t}}(\delta_t-\delta_{t_0}) \end{aligned} \tag{5-15}$$

In which (a number of) the stability and control derivatives are defined as:

$$\begin{aligned} C_{L_V} = V_0\left.\frac{\partial C_L}{\partial V}\right|_0, \quad C_{L_\alpha} = \left.\frac{\partial C_L}{\partial \alpha}\right|_0, \quad C_{L_p} = \frac{2V_0}{b}\left.\frac{\partial C_L}{\partial p}\right|_0, \\ C_{L_q} = \frac{V_0}{\bar{c}}\left.\frac{\partial C_L}{\partial q}\right|_0, \quad C_{L_{\dot{\alpha}}} = \frac{V_0}{\bar{c}}\left.\frac{\partial C_L}{\partial \dot{\alpha}}\right|_0, \quad C_{L_{\delta_a}} = \left.\frac{\partial C_L}{\partial \delta_a}\right|_0 \end{aligned} \tag{5-16}$$

As these derivatives are only valid for the trimming conditions or small perturbations therefrom and differ for other conditions, a flight simulator model needs a large database containing the values for these parameters based on the current flight condition [2]. Usually these conditions can be described by current angle of attack α_0, velocity V_0, altitude h_0 and mass and inertia parameters m_0 and I_0. For turns and climbs or descends bank angle φ_0 and climb angle γ_0 are also needed, respectively.

Not all terms in Equation (5-16) have the same influence on the lift coefficient C_L, as is also the case for the other coefficients. The equations can be simplified by neglecting symmetric forces on the asymmetric states and vice versa [28]. This leads to the most common expressions for the aerodynamic model in aircraft simulations. The expression itself can also be simplified by stating just the state α instead of $(\alpha - \alpha_0)$. The result is, for the symmetric motions:

$$C_L = C_{L_0} + C_{L_V}\frac{V}{V_0} + C_{L_\alpha}\alpha + C_{L_q}\frac{q\bar{c}}{V_0} + C_{L_{\dot{\alpha}}}\frac{\dot{\alpha}\bar{c}}{V_0} + C_{L_{\delta_e}}\delta_e + C_{L_{\delta_t}}\delta_t \tag{5-17}$$

$$C_D = C_{D_0} + C_{D_V}\frac{V}{V_0} + C_{D_\alpha}\alpha + C_{D_q}\frac{q\bar{c}}{V_0} + C_{D_{\dot{\alpha}}}\frac{\dot{\alpha}\bar{c}}{V_0} + C_{D_{\delta_e}}\delta_e + C_{D_{\delta_t}}\delta_t \tag{5-18}$$

$$C_m = C_{m_0} + C_{m_V}\frac{V}{V_0} + C_{m_\alpha}\alpha + C_{m_q}\frac{q\bar{c}}{V_0} + C_{m_{\dot{\alpha}}}\frac{\dot{\alpha}\bar{c}}{V_0} + C_{m_{\delta_e}}\delta_e + C_{m_{\delta_t}}\delta_t \tag{5-19}$$

And for the asymmetric motions:

$$C_Y = C_{Y_0} + C_{Y_V}\frac{V}{V_0} + C_{Y_\beta}\beta + C_{Y_p}\frac{pb}{2V_0} + C_{Y_r}\frac{rb}{2V_0} + C_{Y_{\dot{\beta}}}\frac{\dot{\beta}b}{2V_0} + C_{Y_{\delta_a}}\delta_a + C_{Y_{\delta_r}}\delta_r \tag{5-20}$$

$$C_\ell = C_{\ell_0} + C_{\ell_V}\frac{V}{V_0} + C_{\ell_\beta}\beta + C_{\ell_p}\frac{pb}{2V_0} + C_{\ell_r}\frac{rb}{2V_0} + C_{\ell_{\dot{\beta}}}\frac{\dot{\beta}b}{2V_0} + C_{\ell_{\delta_a}}\delta_a + C_{\ell_{\delta_r}}\delta_r \tag{5-21}$$

$$C_n = C_{n_0} + C_{n_V}\frac{V}{V_0} + C_{n_\beta}\beta + C_{n_p}\frac{pb}{2V_0} + C_{n_r}\frac{rb}{2V_0} + C_{n_{\dot{\beta}}}\frac{\dot{\beta}b}{2V_0} + C_{n_{\delta_a}}\delta_a + C_{n_{\delta_r}}\delta_r \tag{5-22}$$

In these equations, the terms $\dot{\alpha}$ and $\dot{\beta}$ are related to unsteady aerodynamics and might also be left out when manoeuvres are in the quasi-steady regime. Also, instead of having both q and $\dot{\alpha}$ in the equations, often one is chosen as strong correlations between the two make identification difficult [28]. In general, any terms can be added or removed from the above model at will (e.g. higher order terms, cross-terms or even spline functions, as discussed later in this chapter), the only requirement being that a reflection of the real-world and sufficient model fidelity is still pursued. This last fact is important especially when trying to describe aircraft behaviour in unsteady conditions (i.e. near stall) where this first-order linearization based model is often not exact enough.

5-2 Extending the Aircraft Aerodynamic Model to Stalls

A key point in the research of the Citation Stall Modeling Group is to create a model that is able to capture the nonlinearities and unsteady conditions of the aircraft in the stall regime, without resorting to overly complicated or complex models. At the core of this method is Kirchoff's Theory. It is found by the method of Orthogonal Function Modeling (OFM) in order to find the most "powerful" model, meaning: the model that describes the aircraft behaviour the best, for the least amount of model terms, exactly as is the goal of the Stall Modeling Group. This method and the final model is explained in this section.

5-2-1 Ordinary Least Squares Estimation

The basic principle upon which OFM is built is Ordinary Least Squares (OLS) parameter estimation. OLS is a simple but powerful tool to estimate the parameters when a certain model structure is known. Therefore it is also the first step of the local estimation performed for this thesis, as explained later in this chapter. However, as the workings of OLS are needed to be known for OFM it is already discussed here.

Consider an assumed linear model structure which to model a certain output with. The standard model structure for OLS problems of order n is given by:

$$y = a_1\theta_1 + a_2\theta_2 + \ldots + a_n\theta_n + \varepsilon = \begin{bmatrix} a_1 & a_2 & \ldots & a_n \end{bmatrix} \begin{bmatrix} \theta_1 \\ \theta_2 \\ \vdots \\ \theta_n \end{bmatrix} + \varepsilon \tag{5-23}$$

With y the measurement value, θ the to-be-estimated parameters, a the known model regressors and ε any remaining residual. When regarding a measurement series of $k = 1, \ldots, N$ measurements, this becomes the vector equation:

$$\vec{y} = A\vec{\theta} + \vec{\varepsilon} = \begin{bmatrix} \vec{a_1} & \vec{a_2} & \ldots & \vec{a_n} \end{bmatrix} \vec{\theta} + \vec{\varepsilon} = \\ = \begin{bmatrix} y_{k=1} \\ \vdots \\ y_{k=N} \end{bmatrix} = \begin{bmatrix} a_{1,k=1} & a_{2,k=1} & \ldots & a_{n,k=1} \\ \vdots & \vdots & \ddots & \vdots \\ a_{1,k=N} & a_{2,k=N} & \ldots & a_{n,k=N} \end{bmatrix} \begin{bmatrix} \theta_1 \\ \theta_2 \\ \vdots \\ \theta_n \end{bmatrix} + \begin{bmatrix} \varepsilon_{k=1} \\ \vdots \\ \varepsilon_{k=N} \end{bmatrix} \tag{5-24}$$

The goal of the OLS is to find a parameter vector $\hat{\vec{\theta}}$ that minimizes the least-squares cost function:

$$J = \frac{1}{2}\left(\vec{y} - A\vec{\theta}\right)^T \left(\vec{y} - A\vec{\theta}\right) = \frac{1}{2}\vec{\varepsilon}^T\vec{\varepsilon} \tag{5-25}$$

Which can be calculated by:

$$\hat{\vec{\theta}} = \left(A^T A\right)^{-1} A^T \vec{y} \tag{5-26}$$

With this result, the best estimated output for the model can be calculated via:

$$\hat{\vec{y}} = A\hat{\vec{\theta}} \tag{5-27}$$

This results in a set of estimated parameters $\hat{\vec{\theta}}$ which best approximates the output signal $\hat{\vec{y}}$ *for the chosen model structure*. This model structure must thus be chosen up front by the user based on insight about what model structure is best applicable to the case. This process can be very arbitrary. In order to make the model structure selection quasi-objective OFM can be used.

5-2-2 Orthogonal Function Modeling

This is indeed the large challenge in the parameter estimation process: often not the parameter estimation itself, but the step foregoing the parameter estimation. A certain model structure is assumed, however, it might be the case that this normal polynomial model is not optimal in itself and contains non-optimal regressors, regardless of the estimated parameters. This may result in correct global fits of the model, but significant discrepancies locally, especially when locally non-linearities exist. This problem may be countered by applying OFM and structure selection.

Parameter Estimation via OFM

By use of OFM, before the parameter estimation is applied, first a procedure is performed that decouples the OLS, such that any regressor's ability to improve the OLS fit can be evaluated independently regardless of which other regressors are already chosen for the model. The main advantage of this is that the model regressors are chosen such that the final model structure itself will also add to improving the model fit, and not only the estimation of the parameters. This method was first applied in combination with the use of flight data in [37]. The used procedure is described below.

For a pair of orthogonal regressors, the following applies:

$$\vec{a}_i^T \vec{a}_j = 0, \quad i \neq j, \quad i, j = 1, 2, \ldots, n \tag{5-28}$$

Such that follows, from implementing matrix A of Equation (5-24) and the function of Equation (5-28) into Equation (5-26) for the orthogonal estimated parameters (equivalent to $\hat{\vec{\theta}}$):

$$\hat{\vec{\varphi}} = \frac{\vec{a}_j^T \vec{y}}{\vec{a}_j^T \vec{a}_j} \tag{5-29}$$

And implementing Equation (5-24), Equation (5-28) and Equation (5-29) into Equation (5-25):

$$\hat{J} = \frac{1}{2}\left[\vec{y}^T\vec{y} - \sum_{j=1}^{n} \frac{\left(\vec{a}_j^T \vec{y}\right)^2}{\vec{a}_j^T \vec{a}_j}\right] \tag{5-30}$$

Which is only dependent on the measurement data $\vec{y}$ and only the specific regressor a_j, meaning that the performance of the regressor on its own to minimize the cost function can be evaluated.

Continuing, it must be evaluated which model regressors to include or not include in the model. The metric used for this is the specific regressor's ability to minimize Predicted Square Error (PSE), defined by:

$$PSE = \frac{\left(\vec{y} - A\hat{\vec{\theta}}\right)^T \left(\vec{y} - A\hat{\vec{\theta}}\right)}{N} + \sigma_{max}^2 \frac{n}{N} \quad \xrightarrow{\text{orthogonal}} \quad \frac{2\hat{J}}{N} + \sigma_{max}^2 \frac{n}{N} \tag{5-31}$$

In order to practically implement the PSE in an algorithm, it is needed to evaluate for every orthogonalized regressor its own contribution to the PSE. The regressor with the smallest contribution is then chosen to be an actual regressor in the model. This individual contribution of the jth regressor is given by [58] and is basically the derivative $\frac{\Delta PSE}{\Delta j}$:

$$\Delta PSE_j = -\frac{\left(\vec{a}_j^T \vec{y}\right)^2}{\vec{a}_j^T \vec{a}_j} + \sigma_{max}^2 \frac{1}{N} \tag{5-32}$$

In these equations σ_{max}^2 is the upper-bound estimate of the squared error between future data and the current model, governed by:

$$\sigma_{max}^2 = \frac{1}{N-1} \sum_{i=1}^{N} (y_i - \bar{y})^2 \tag{5-33}$$

And:

$$\bar{y} = \frac{1}{N} \sum_{i=1}^{N} y_i \tag{5-34}$$

Of the orthogonal PSE in Equation (5-31), the left term decreases with additional model terms and the right term increases with additional terms. This means that the PSE always has just one single global optimum. This makes it fit for structure selection as it weighs on one hand gaining a better fit by adding terms, but also keeping the resulting model simple as a penalty is imposed for adding too many model terms.

Orthogonalizing Regressors

The important assumption of the above procedure is that all the regressors are orthogonal. As this is usually not the case, they need to be orthogonalized first by the Gram-Schmidt orthogonalization procedure as also explained in [37].

Normally the first orthogonal regressor is associated with the bias-term and set to 1 as in:

$$\vec{a}_1 = \vec{b}_1 = \vec{1} \tag{5-35}$$

In which the original regressors are denoted by $\vec{a}$ and the orthogonalized regressors by $\vec{b}$. Next, any function of the regressor candidates can be chosen next and defined as the next $\vec{a_j}$ and can be orthogonalized via:

$$\vec{b}_j = \vec{a}_j - \sum_{k=1}^{j-1} \gamma_{kj} \vec{b}_k, \quad j = 2, 3, \ldots, n_t \tag{5-36}$$

With n_t the number of candidate regressors (including the bias term). The scalar γ_{kj} can be calculated via:

$$\gamma_{kj} = \frac{\vec{b}_k^T \vec{a}_j}{\vec{b}_k^T \vec{b}_k}, \quad k = 1, 2, \ldots, j-1 \tag{5-37}$$

As candidate regressors any function of the original regressors can be chosen up to a certain order. A valuable property of the selection process is that choosing more regressors that may not be important, or including higher order functions of them does not affect the final selected orthogonal regressors. The only cost is additional computation time.

The original regressor matrix A is already known, then one can also define the orthogonal regressor matrix B. This can be done via the matrix G, which is defined as:

$$G = \begin{bmatrix} 1 & \gamma_{12} & \gamma_{13} & \cdots & \gamma_{1n_t} \\ 0 & 1 & \gamma_{23} & \cdots & \gamma_{2n_t} \\ 0 & 0 & 1 & \cdots & \gamma_{3n_t} \\ \vdots & \vdots & \vdots & \ddots & \vdots \\ 0 & 0 & 0 & \cdots & 1 \end{bmatrix} \tag{5-38}$$

These matrices make it possible to calculate and convert between the original and orthogonal regressor model outputs:

$$A = BG \;\Leftrightarrow\; B = AG^{-1} \quad \text{s.t.} \quad \hat{\vec{y}} = B\hat{\vec{\varphi}} \;\Leftrightarrow\; \hat{\vec{y}} = AG^{-1}\hat{\vec{\varphi}} \tag{5-39}$$

Furthermore this also gives an expression to convert between the orthogonal and original estimated parameters:

$$\hat{\vec{\theta}} = G^{-1}\hat{\vec{\varphi}} \;\Leftrightarrow\; \hat{\vec{\varphi}} = G\hat{\vec{\theta}} \tag{5-40}$$

Use of Spline Functions in OFM

As mentioned before, the challenge in global parameter estimation is to also accommodate local variations in the model. The sole practise of incorporating the model structure selection is already a step in this. But additionally, not only functions of regressors but also spline functions that consist of candidate regressors can be added to the regressor pool. These splines are mathematically defined as:

$$(x - x_i)_+^m = \begin{cases} 0 & \text{when } x \leq x_i \\ (x - x_i)^m & \text{when } x > x_i \end{cases} \tag{5-41}$$

Where the variable x can be any other candidate regressor that is already considered. Based on insights into aircraft behaviour, one can choose the specific regressor that might profit from being included in a spline as well as the specific point (or "knot") where the spline becomes turned "on" (or multiple options can be included and the OFM algorithm will choose the most applicable one).

For example, if one knows that the behaviour of the angle of attack α significantly changes above 10 degrees, one could include the spline $(\alpha - 10)_+^1$ as a regressor as well. Based on the chosen candidates' orders, also higher orders of the spline can be included (i.e. $(\alpha - 10)_+^2$).

Conclusion on OFM in Parameter Estimation

The above procedure as described and used in [37] can offer significant increases in model fidelity. The paper concludes that, even though only data from one flight test is used, the model produces reasonable predictions of flight behaviour that can be compared to the accuracy that is normally achieved in extensive wind tunnel testing. The final model consisted of regressors and splines that were automatically chosen by the OFM structure selection process.

In the Citation Stall Modeling Group, OFM was used in two previous researches: for the normal flight envelope in [54] and for stall modeling in [58]. Both these papers made use of multiple flight tests, in the contrary to [37]. This made it possible to extend the algorithm with two additional steps. First, if for a certain set the regressors are chosen and the algorithm ended, each of their contributions to the final model output was checked via their individual Root Mean Square ($RMS = \frac{1}{N}\sqrt{\hat{\tilde{y}}^T\hat{\tilde{y}}}$) by calculating the RMS with the regressor and without it. If the difference was less than 0.5% the regressor was still deleted. This to further simplify the model. Second, as multiple flight tests with test runs were available, the algorithm was run for each run. Each run may result in different outcomes with different chosen regressors. To come to a final model that only consisted of regressors that were chosen in at least 50% of the flight test runs, or when practically a significant reason could be found that increased model accuracy. This to increase the model global performance.

5-2-3 Final Aerodynamic Stall Model

The final aerodynamic stall model of the Cessna Citation PH-LAB was found by applying the algorithm as discussed above by [58]. The candidate regressor pool consisted of the following regressors and any combination of those up to order 2:

$$1,\ \alpha,\ \dot{\alpha},\ \beta,\ \dot{\beta},\ p,\ q,\ r,\ \delta_a,\ \delta_e,\ \delta_r,\ C_T,\ M,$$
$$X,\ (1-X),\ \left(\frac{1+\sqrt{X}}{2}\right)^2,\ \max(\frac{1}{2}, X)$$

In which C_T is the thrust coefficient, which is related to δ_t and used instead thereof, and is defined as the total engine thrust made non-dimensional:

$$C_T = \frac{T}{\frac{1}{2}\rho V_{TAS}^2 S} \tag{5-42}$$

The final aerodynamic stall model that was identified, and which is further used in this thesis, is:

$$C_L = C_{L_0} + C_{L_\alpha}\left(\frac{1+\sqrt{X}}{2}\right)^2 \alpha + C_{L_{\alpha^2}}(\alpha - 6^\circ)^2_+ \tag{5-43}$$

$$C_D = C_{D_0} + C_{D_\alpha}\alpha + C_{D_{\delta_e}}\delta_e + C_{D_X}(1-X) + C_{D_{C_T}}C_T \tag{5-44}$$

$$C_Y = C_{Y_0} + C_{Y_\beta}\beta + C_{Y_p}\frac{pb}{2V} + C_{Y_r}\frac{rb}{2V} + C_{Y_{\delta_a}}\delta_a \tag{5-45}$$

$$C_\ell = C_{\ell_0} + C_{\ell_\beta}\beta + C_{\ell_p}\frac{pb}{2V} + C_{\ell_r}\frac{rb}{2V} + C_{\ell_{\delta_a}}\delta_a \tag{5-46}$$

$$C_m = C_{m_0} + C_{m_\alpha}\alpha + C_{m_{X\delta_e}}\max(\frac{1}{2}, X)\delta_e + C_{m_{C_T}}C_T \tag{5-47}$$

$$C_n = C_{n_0} + C_{n_\beta}\beta + C_{n_r}\frac{rb}{2V} + C_{n_{\delta_r}}\delta_r \tag{5-48}$$

In this set of equations one regressor spline term is present that was not included in the regressor pool. This was added to the model as the coefficient C_{L_α} also incorporated the Kirchoff term X, which significantly reduces the lift as the separation point moves to the leading edge of the wing. However, Kirchoff's theory is applicable to airfoils, whilst the estimation of the Citation models the entire aircraft. It was found that the spline regressor $(\alpha - 6^\circ)^2_+$ effectively counters the somewhat overestimated lift decrease related to X at higher angles of attack from 6 deg onwards.

5-3 Estimating the Aerodynamic Stall Model from Flight Data

With the final Citation aerodynamic stall model structure known, it is possible to perform the parameter estimation on the model. The used procedure for this is discussed in this section.

5-3-1 Calculating Force and Moment Coefficients

The first step to perform parameter estimation of the aerodynamic stall model is to calculate the actual output $\vec{y}$ that the to-be-estimated model needs to model. These are the coefficients from Equation (5-43) through Equation (5-48).

The aerodynamic force and moment coefficients can be calculated from the reconstructed inputs and reconstructed measurements from the FPR and the massmodel data. Note that in this chapter the FPR estimated values are regarded as the "true" values so that from now on the superscript "^" is dropped for those, while the "^" is now only used for the parameter estimation estimates. The dimensionless aerodynamic forces in the aircraft body frame can be calculated and modeled as:

$$C_X = \frac{X}{\frac{1}{2}\rho V^2 S} = \frac{mA_x}{\frac{1}{2}\rho V^2 S} \tag{5-49}$$

$$C_Y = \frac{Y}{\frac{1}{2}\rho V^2 S} = \frac{mA_y}{\frac{1}{2}\rho V^2 S} \tag{5-50}$$

$$C_Z = \frac{Z}{\frac{1}{2}\rho V^2 S} = \frac{mA_z}{\frac{1}{2}\rho V^2 S} \tag{5-51}$$

The dimensionless aerodynamic moments in the aircraft body frame can be calculated and modeled as:

$$C_\ell = \frac{L}{\frac{1}{2}\rho V^2 S b} = \frac{\dot{p}I_{xx} + qr(I_{zz} - I_{yy}) - (pq + \dot{r})I_{xz}}{\frac{1}{2}\rho V^2 S b} \tag{5-52}$$

$$C_m = \frac{M}{\frac{1}{2}\rho V^2 S \bar{c}} = \frac{\dot{q}I_{yy} + rp(I_{xx} - I_{zz}) - (p^2 - r^2)I_{xz}}{\frac{1}{2}\rho V^2 S \bar{c}} \tag{5-53}$$

$$C_n = \frac{N}{\frac{1}{2}\rho V^2 S b} = \frac{\dot{r}I_{zz} + pq(I_{yy} - I_{xx}) + (qr - \dot{p})I_{xz}}{\frac{1}{2}\rho V^2 S b} \tag{5-54}$$

Last, the dimensionless lift and drag coefficients can be calculated from the force coefficients in the body frame:

$$C_L = C_X \sin\alpha - C_Z \cos\alpha \tag{5-55}$$

$$C_D = -C_X \cos\alpha \cos\beta - C_Y \sin\beta - C_Z \sin\alpha \cos\beta \tag{5-56}$$

Now all $\vec{y}$ outputs are known and can be used to estimate the parameters in Equation (5-43) through Equation (5-48).

5-3-2 Nonlinear Estimation

The preferred method to estimate the parameters of Equation (5-43) through Equation (5-48) is simply via linear regression via OLS. However, this is not possible as the variable X in equations of C_L and C_m is governed by an ODE and thus non-linear. A method to be able to still do this is by first performing a nonlinear parameter estimation to estimate X and its parameters a_1, α^*, τ_1 and τ_2 before the linear regression. Then, it is possible to regard X as "just" a part of the regressor $\left(\frac{1+\sqrt{X}}{2}\right)^2 \alpha$.

Preparing Regressors

The first step in any estimation, be it linear or nonlinear, is to calculate the regressors that appear in the to-be-estimated model structure. Recall Equation (2-6):

$$\tau_1 \frac{dX}{dt} + X = \frac{1}{2}\{1 - \tanh\left[a_1(\alpha - \tau_2\dot{\alpha} - \alpha^*)\right]\}$$

Which is the to-be-esimated model structure for the nonlinear estimation part. The regressors that appear in this equation are α and $\dot{\alpha}$ which van be obtained from the Kalman filtered flight data. The regressor time series in the nonlinear estimation are denoted by $\vec{x}_n$ and the to-be-estimated parameters a_1, α^*, τ_1 and τ_2 by $\vec{\theta}_{nonlin}$, rather than $\vec{a}_n$ and just θ of the linear estimation to distinct them from the linear estimation.

For the final aerodynamic model equations some regressors must be made dimensionless (like $\frac{\dot{\alpha}\bar{c}}{V}$). However, the ODE of X applies to the *actual* values of α and $\dot{\alpha}$, so no further preparation is needed to these regressors and the nonlinear estimation can be performed directly.

Nonlinear Estimation Procedure

The basic method of nonlinear estimation is to minimize a specific cost function. For a nonlinear cost function, the cost function can be regarded as being a surface. In order to find a minimum on this surface, one starts at a certain point and calculates the gradient in all directions. The direction with the highest decrease is then chose and a step is taken in that direction. This is repeated until at some point no further decrease appears in any direction, which means a minimum is reached. The method to find out if a local or global optimum is reached is discussed later in this section.

As X is described by a nonlinear ODE a nonlinear estimation procedure is necessary to solve for its parameters. One can make use of any equation containing X, thus Equation (5-43) or Equation (5-47). The Equation (5-43) was chosen as the data for C_L contains most information related to angle of attack and the airfoil separation point. The accompanying cost function to find the parameters of X is defined by [58]:

$$\hat{\vec{\theta}} = \arg\min_{\vec{\theta}} J(\vec{\theta}, x), \quad \text{with } J(\vec{\theta}, x) = \frac{1}{n}\left(\hat{\vec{y}}_{C_L} - \vec{y}_{C_L}\right)^T \left(\hat{\vec{y}}_{C_L} - \vec{y}_{C_L}\right) \tag{5-57}$$

In which θ is the to-be-estimated nonlinear parameter vector given by:

$$\vec{\theta} = \vec{\theta}_{nonlin} = \begin{bmatrix} a_1 & \alpha^* & \tau_1 & \tau_2 & C_{L_0} & C_{L_\alpha} & C_{L_{\alpha^2}} \end{bmatrix}^T \tag{5-58}$$

Further, x are the regressors, $\vec{y}_{C_L}$ are the measurements of C_L and $\hat{\vec{y}}_{C_L}$ is the calculated value of C_L via the estimated parameters and model structure of Equation (5-43). For clarity repeated here:

$$C_L = C_{L_0} + C_{L_\alpha}\left(\frac{1+\sqrt{X}}{2}\right)^2 \alpha + C_{L_{\alpha^2}}(\alpha - 6°)_+^2$$

Last, the derivative of X in time, $\frac{dX}{dt}$, is given by a rewritten version of Equation (2-6):

$$\frac{dX(t,\theta,x)}{dt} = \frac{\frac{1}{2}\{1 - \tanh\left[a_1(\alpha - \tau_2\dot{\alpha} - \alpha^*)\right]\} - X}{\tau_1} \tag{5-59}$$

The nonlinear optimization makes use of the gradient of the cost function surface relative to the parameters, but this may encounter numerical difficulties when regarding an ODE. The gradient of $J(\vec{\theta}, x)$ with regard to the parameters $\frac{\partial J(\vec{\theta},x)}{\partial \vec{\theta}}$ depends both on the parameters that constitute X and those that do not. Through differentiation via the chain rule one then finds that:

$$\frac{\partial J(\vec{\theta}, x)}{\partial \theta_i} = \begin{cases} \frac{\partial J}{\partial \hat{C}_L}\frac{\partial \hat{C}_L}{\partial X}\frac{\partial X}{\partial \theta_i} & \text{when } \theta_i \in \{a_1, \alpha^*, \tau_1, \tau_2\} \\ \frac{\partial J}{\partial \hat{C}_L}\frac{\partial \hat{C}_L}{\partial \theta_i} & \text{when } \theta_i \in \{C_{L_0}, C_{L_\alpha}, C_{L_{\alpha^2}}\} \end{cases} \tag{5-60}$$

All but one of the partial derivatives can be found analytically quite straightforwardly, except for $\frac{\partial X}{\partial \theta_i}$. To find this derivative, first one can define:

$$\frac{dX(t,\theta,x)}{dt} = G(X,t,\theta,x) \tag{5-61}$$

Then one can define for the to-be-found derivative:

$$\frac{\partial X(t,\theta,x)}{\partial \theta} = S(t,\theta,x) \tag{5-62}$$

Then, taking the partial derivative of G with respect to the parameters θ gives:

$$\frac{\partial}{\partial \theta}\frac{dX(t,\theta,x)}{dt} = \frac{\partial G(X,t,\theta,x)}{\partial \theta} = \frac{\partial G(X,t,\theta,x)}{\partial X}\frac{\partial X(t,\theta,x)}{\partial \theta} + \frac{\partial G(X,t,\theta,x)}{\partial \theta} \tag{5-63}$$

Then substituting S into this equation yields:

$$\frac{dS(t,\theta,x)}{dt} = \frac{\partial G(X,t,\theta,x)}{\partial X}S(t,\theta,x) + \frac{\partial G(X,t,\theta,x)}{\partial \theta} \tag{5-64}$$

Both derivatives of G can be derived straightforwardly from Equation (5-59). With this final equation a second ODE has been obtained which can be solved numerically rather than analytically. The solution can be substituted into Equation (5-60) to complete the chain rule and as such being able to calculate the gradients relative to all parameters.

The derivatives when $\theta_i \in \{C_{L_0}, C_{L_\alpha}, C_{L_{\alpha^2}}\}$ become:

$$\frac{\partial J}{\partial \hat{C}_L} = \frac{2}{n}\left(\hat{\vec{y}}_{C_L} - \vec{y}_{C_L}\right) \tag{5-65}$$

$$\frac{\partial \hat{C}_L}{\partial \theta_i} = \begin{cases} 1 & \text{when } \theta_i = C_{L_0} \\ \left(\frac{1+\sqrt{X}}{2}\right)^2 \alpha & \text{when } \theta_i = C_{L_\alpha} \\ \max(0, \alpha - 6^\circ)^2 & \text{when } \theta_i = C_{L_{\alpha^2}} \end{cases} \tag{5-66}$$

While the derivatives when $\theta_i \in \{a_1, \alpha^*, \tau_1, \tau_2\}$ become, via the procedure described above:

$$\frac{\partial J}{\partial \hat{C}_L} = \frac{2}{n}\left(\hat{\vec{y}}_{C_L} - \vec{y}_{C_L}\right) \tag{5-67}$$

$$\frac{\partial \hat{C}_L}{\partial X} = \frac{1}{4}C_{L_\alpha}\alpha\left(1 + \frac{1}{\sqrt{X}}\right) \tag{5-68}$$

$$\frac{\partial G}{\partial X} = -\frac{1}{\tau_1} \tag{5-69}$$

$$\frac{\partial G}{\partial \theta_i} = \begin{cases} -\frac{\frac{1}{2}\{1-\tanh^2\left[a_1(\alpha-\tau_2\dot{\alpha}-\alpha^*)\right]\}\{\alpha-\tau_2\dot{\alpha}-\alpha^*\}}{\tau_1} & \text{when } \theta_i = a_1 \\ -\frac{\frac{1}{2}\{1-\tanh^2\left[a_1(\alpha-\tau_2\dot{\alpha}-\alpha^*)\right]\}\{-a_1\}}{\tau_1} & \text{when } \theta_i = \alpha^* \\ -\frac{\frac{1}{2}\{1-\tanh\left[a_1(\alpha-\tau_2\dot{\alpha}-\alpha^*)\right]\}-X}{\tau_1^2} & \text{when } \theta_i = \tau_1 \\ -\frac{\frac{1}{2}\{1-\tanh^2\left[a_1(\alpha-\tau_2\dot{\alpha}-\alpha^*)\right]\}\{-a_1\dot{\alpha}\}}{\tau_1} & \text{when } \theta_i = \tau_2 \end{cases} \tag{5-70}$$

(5-71)

After which $\frac{\partial X}{\partial \theta_i} = S$ is the value found when numerically integrating the ODE $\frac{dS}{dt} = \frac{\partial G}{\partial X}S + \frac{\partial G}{\partial \theta_i}$.

In order to perform the nonlinear estimation the MATLAB `fmincon()`-function was used, in which the cost function was defined as Equation (5-57) and the gradient of the cost function surface was specified by the user as Equation (5-60).

For any dataset (i.e. one stall run) the optimization was run for 500 randomized initial conditions, uniformly selected within the bounds given by Table 5-1. The bounds were chosen according to [58]. All initial conditions were normalized by dividing by their own upper bound before being used as input for the `fmincon()`-procedure to increase performance.

Table 5-1: Nonlinear estimation parameter initial condition specifications.

Parameter	Lower bound	Upper bound	Unit
a_1	15	40	-
α^*	0.1	0.35	rad
τ_1	0.001	0.8	s
τ_2	0	0.5	s
C_{L_0}	0.1	0.4	-
C_{L_α}	2	6	-
$C_{L_{\alpha^2}}$	0	20	-

By using this method it is never certain if the global optimum is *actually* reached. However, the more initial conditions are optimized, the more certain it is that one of them is in fact the global optimum. A significant number of final estimates were found that came significantly close to the estimate with the lowest cost function value of J. This is to be expected. First, the lowest value of J is not necessarily the *exact* global optimum, nor are the found optima that lay close to it. Due to the calculated gradients, the direction in which these are calculated and reaching of the initial condition tolerance the algorithm may never reach the singular point that is the global optimum. Therefore the median of all optima that came within 5% of the lowest found optimum was regarded to represent the global optimum best and therefore assumed to *be* the global optimum from the nonlinear estimation. More details about the distribution of the found optima is discussed below.

With the found parameters the modeled value of C_L, $\hat{y}_{C_L}$, was calculated for the time series of the stall run and compared to the "actual" value of C_L, y_{C_L}, that was calculated from the Kalman filtered data. The results hereof are also discussed below.

Results Specific to the Nonlinear Estimation

As an example to discuss the workings and results of the nonlinear estimation it was performed with 500 initial conditions on the same dataset as with the discussion of the UKF: 150 s of data from a dynamic stall that includes boom measurements.

The distribution of the 500 optima that are found with the nonlinear estimation procedure are shown in Figure 5-3. Where Figure 5-3a shows the optima of all 500 initial conditions and Figure 5-3b shows the selected initial conditions that results in an optimum that is within 5% of the lowest cost function found of all initial conditions. This is the case for 20 initial

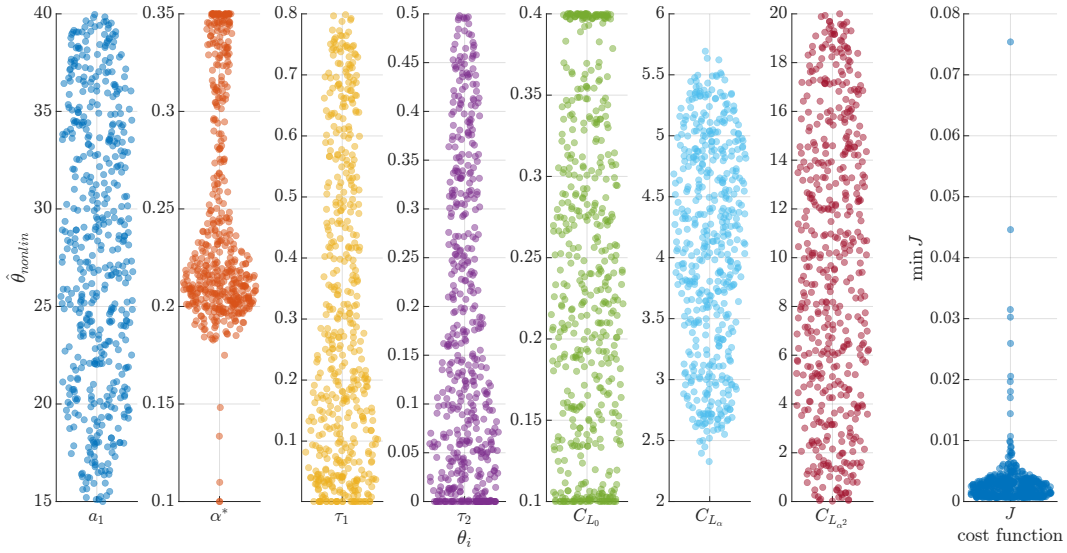

(a) All initial conditions ($n = 500$).

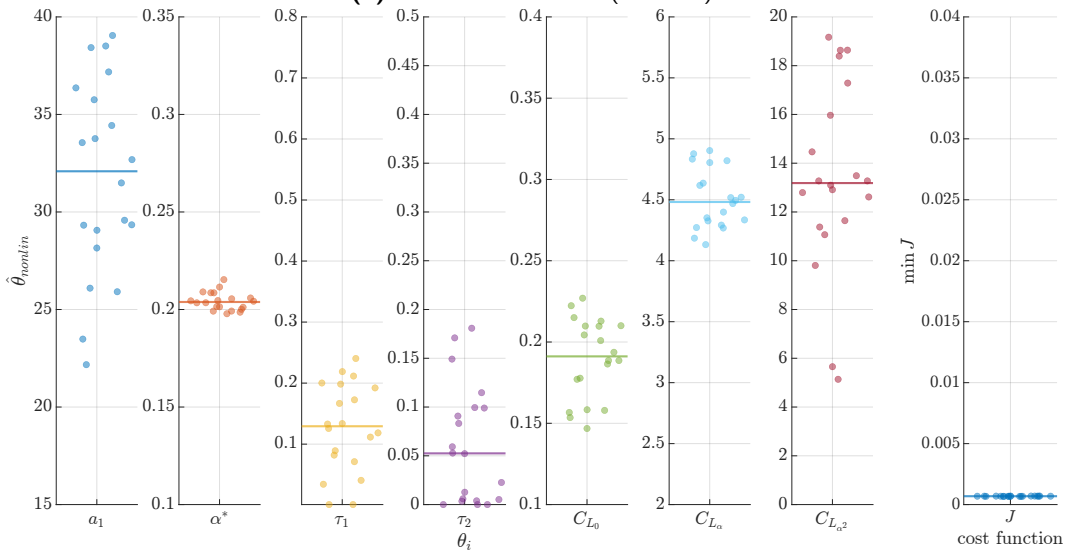

(b) Selected initial conditions ($n = 20$) with median.

Figure 5-3: Distribution of the parameters and cost function values found by the nonlinear estimation procedure.

conditions. Also, the median of the parameters is shown for these 20 optima, which is assumed to be the *actual* global optimum of the nonlinear estimation.

From all initial conditions it can be observed that the optima are distributed quite widely within the upper and lower bounds of the parameters. This may indicate that there are many local optima on the cost function surface. This does however reinforce the choice for as many initial conditions as chosen. What is also clear is that all distributions do possess a concentration in their distribution. Not coincidentally, when looking at the distribution of the selection of best optima and their median, these *do* coincide with where the highest concentrations roughly are. Therefore, even though the spread is quite significant, this does increase the reliability of the found best optima. In this case, the parameter best estimates are thus found to be: $a_1 = 32.0864$, $\alpha^* = 0.2039$ rad, $\tau_1 = 0.1293$ s, $\tau_2 = 0.0525$ s, $C_{L_0} = 0.1912$, $C_{L_\alpha} = 4.4819$ and $C_{L_{\alpha^2}} = 13.1858$ where the cost function has a value of $J = 6.8562 \cdot 10^{-4}$.

In order to explain the behaviour and these relatively "spreaded" results of the optima of the parameters it is useful to investigate the cost function surface and its derivatives at the found global optimum. See Figure 5-4 and Figure 5-5 for the cost function surface and its derivatives at the global optimum and Figure 5-6 shows the surface zoomed in on a local optimum.

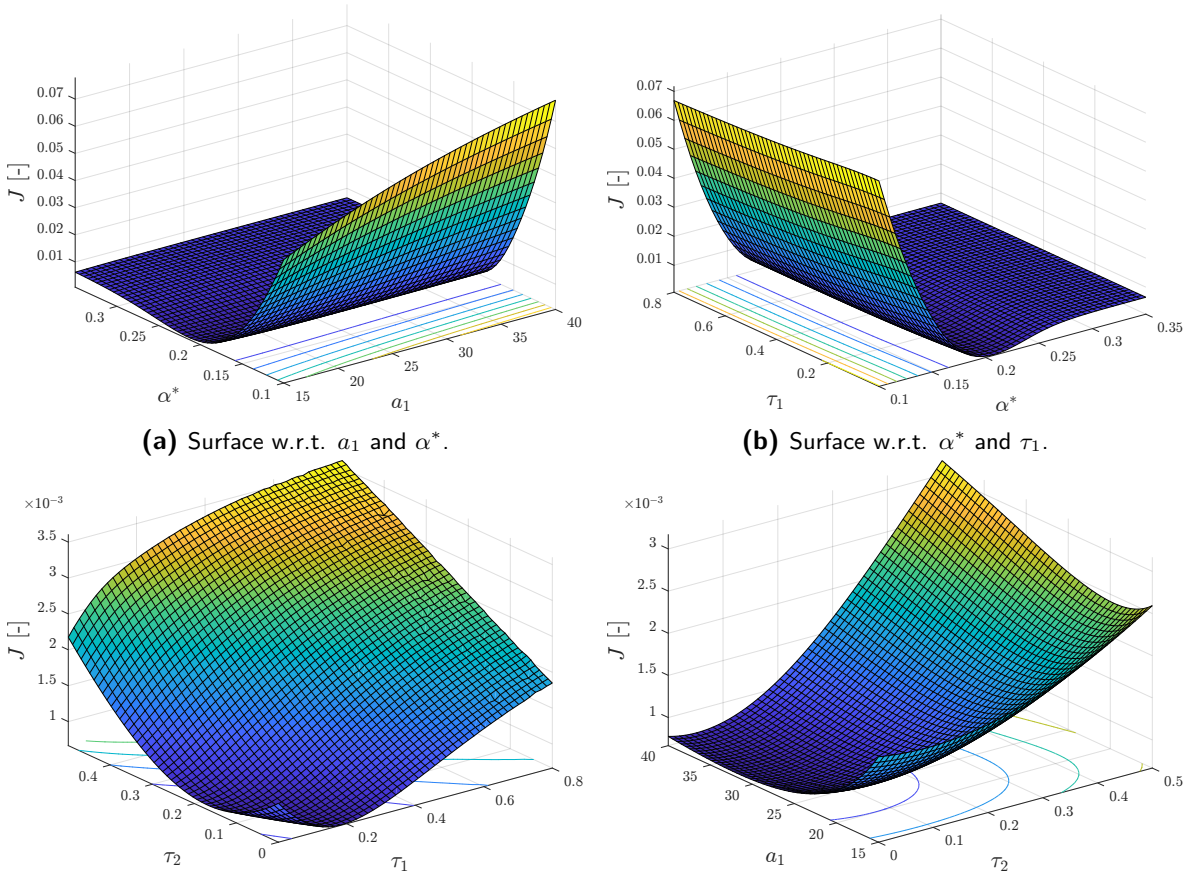

(a) Surface w.r.t. a_1 and α^*.

(b) Surface w.r.t. α^* and τ_1.

(c) Surface w.r.t. τ_1 and τ_2.

(d) Surface w.r.t. τ_2 and a_1.

Figure 5-4: Surface of cost function J at the found global optimum ($a_1 = 32.0864$, $\alpha^* = 0.2039$ rad, $\tau_1 = 0.1293$ s, $\tau_2 = 0.0525$ s).

The behaviour of the large spread of all 500 found can be expected. It is visible in Figure 5-

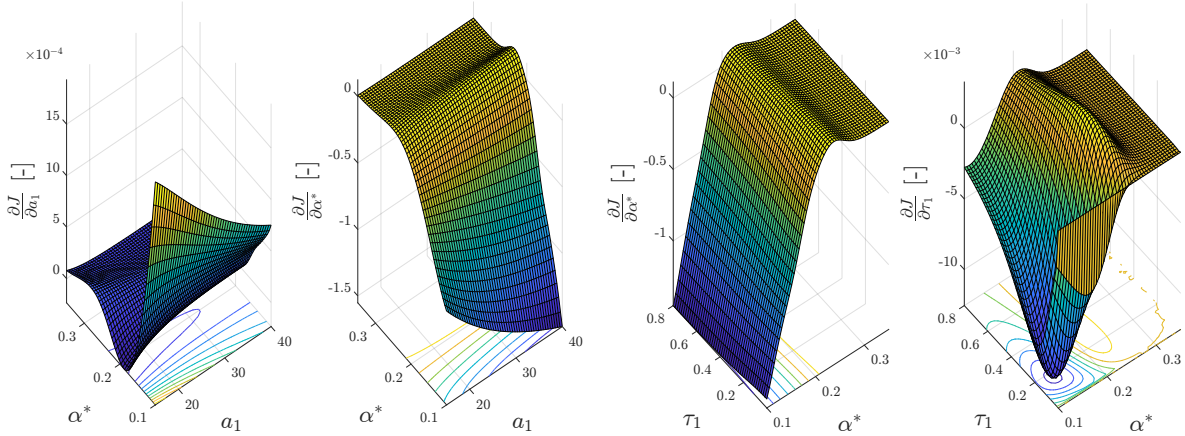

(a) Derivatives w.r.t. a_1 and α^*.

(b) Derivatives w.r.t. α^* and τ_1.

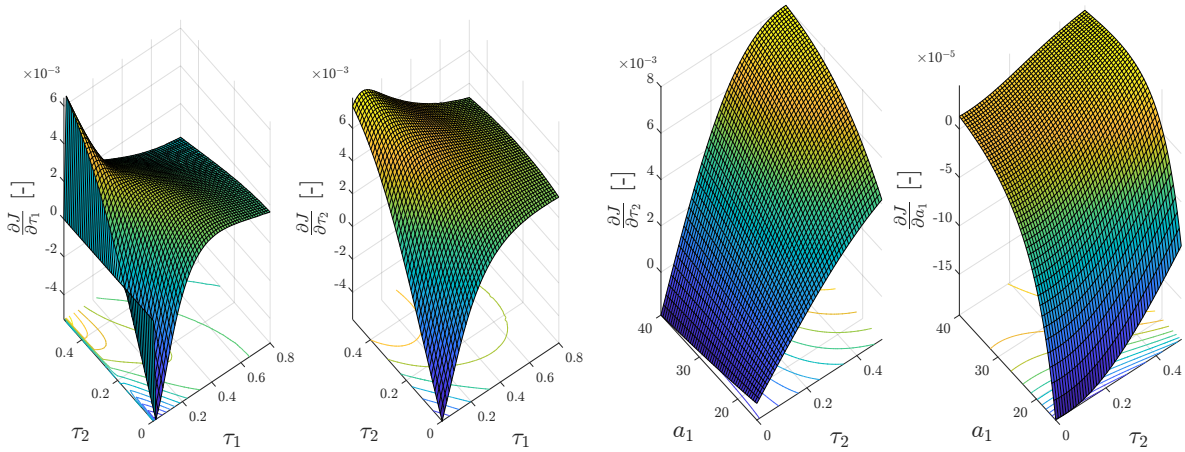

(c) Derivatives w.r.t. τ_1 and τ_2.

(d) Derivatives w.r.t. τ_2 and a_1.

Figure 5-5: Derivatives of cost function J at the found global optimum ($a_1 = 32.0864$, $\alpha^* = 0.2039$ rad, $\tau_1 = 0.1293$ s, $\tau_2 = 0.0525$ s).

4c. As τ_1 and τ_2 increase some significant roughness appears on the surface in which the optimization algorithm might find an optimum, even this close to the global optimum. This roughness was also found by [58]. As an example, in Figure 5-6 the cost function surface at an optimum for $J = 0.0170$ at $a_1 = 27.4739$, $\alpha^* = 0.2365$ rad, $\tau_1 = 0.0119$ s and $\tau_2 = 0.0874$ s is shown with a higher resolution, and indeed it can be seen the rough cost function surface creates many local optima, even though at the specified point there is clearly not a global optimum.

However, also a smaller but still significant spread is present in the selected parameters that make up the global optimum. This is also not unexpected as it can be seen in Figure 5-4 that the surface at the global optimum is very "flat". Thus, the optimization algorithm decides that another step on the surface does not increase the cost function value *enough* even though the singular global optimum is not yet reached. That the spread of these final 20 optima is rather large and may differ significantly from the chosen median is no problem, however. The flat surface of the cost function namely has as result that a change in this parameter does not deteriorate the model fit and is still a good representation of the actual data, which is

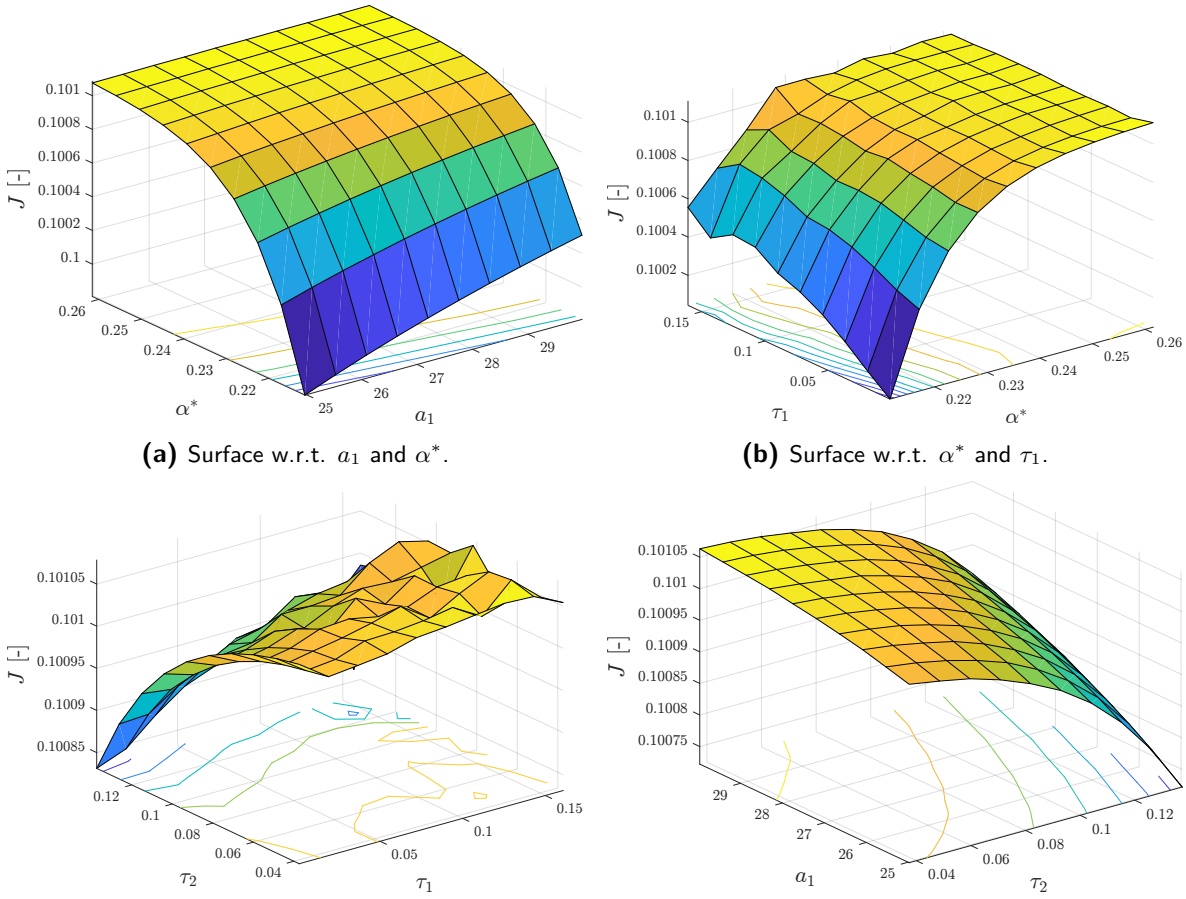

(a) Surface w.r.t. a_1 and α^*.

(b) Surface w.r.t. α^* and τ_1.

(c) Surface w.r.t. τ_1 and τ_2.

(d) Surface w.r.t. τ_2 and a_1.

Figure 5-6: Surface of cost function J at a local optimum ($a_1 = 27.4739$, $\alpha^* = 0.2365$ rad, $\tau_1 = 0.0119$ s, $\tau_2 = 0.0874$ s) where $J = 0.0170$.

ultimately the only goal of the model.

With the estimated parameters the C_L can be modeled by calculating X and the other regressors for the entire time series of the data and multiplying with the estimated parameters, resulting in $\hat{y}_{C_L}$. A number of metrics are calculated to give an indication of the model fitting performance (for their explanation see later in this chapter). See Table 5-2.

Indeed the MSE is the same (with a small numerical difference) as was found for the optimum of J in the nonlinear optimization, verifying that the nonlinear optimization works correctly. The modeled C_L differs less than 3% from the measurements, which are low enough values that prove the nonlinear estimation estimates the model parameter with quite some accuracy. It might be interesting to see if these values significantly change when the linear estimation is applied below.

5-3-3 Linear Estimation

Now that for the data set the nonlinear X parameters have been estimated, it is possible to calculate X throughout the time series of the data and regard it as a regressor that can

Table 5-2: Performance metrics of the nonlinear parameter estimation.

Model	Metric	Value
C_L	MSE	$6.6661 \cdot 10^{-4}$
	RMS	0.0258
	$RRMS$	2.9568%
	R^2	0.9625

be utilized in this second part of the parameter estimation, which is the linear estimation of the stability and control derivatives of the model described by Equation (5-43) through Equation (5-48).

Preparing Regressors

The first step is to prepare the regressors for use in the parameter estimation. The first step in this is to calculate X by means of the estimated nonlinear parameters. Recall Equation (5-59):

$$\frac{dX}{dt} = \frac{\frac{1}{2}\{1 - \tanh\left[a_1(\alpha - \tau_2\dot{\alpha} - \alpha^*)\right]\} - X}{\tau_1}$$

With this equation X can be calculated for the entire time series by using the Matlab `ode45()`-function on the equation. The parameters a_1, α^*, τ_1 and τ_2 are taken directly from the nonlinear estimation, α and $\dot{\alpha}$ from the UKF data and the initial condition is set to the steady-state separation point X_0 at the first timestamp of the data governed by:

$$X_0 = \frac{1}{2}\{1 - \tanh\left[a_1(\alpha - \tau_2\dot{\alpha} - \alpha^*)\right]\} \tag{5-72}$$

Next, the regressors are calculated according to how they appear in Equation (5-43) through Equation (5-48) which also makes the regressors dimensionless for which it is required that they are dimensionless. Gathering these into the regression matrix A for each of the six force and moment equations results in:

$$
\begin{aligned}
A_{C_L} &= \begin{bmatrix} 1 & \left(\frac{1+\sqrt{X}}{2}\right)^2 \alpha_{k=1} & \max(0, \alpha - 6°)^2_{k=1} \\ \vdots & \vdots & \vdots \\ 1 & \left(\frac{1+\sqrt{X}}{2}\right)^2 \alpha_{k=N} & \max(0, \alpha - 6°)^2_{k=N} \end{bmatrix} \\
A_{C_D} &= \begin{bmatrix} 1 & \alpha_{k=1} & \delta_{e_{k=1}} & (1-X)_{k=1} & C_{T_{k=1}} \\ \vdots & \vdots & \vdots & \vdots & \vdots \\ 1 & \alpha_{k=N} & \delta_{e_{k=N}} & (1-X)_{k=N} & C_{T_{k=N}} \end{bmatrix} \\
A_{C_Y} &= \begin{bmatrix} 1 & \beta_{k=1} & \frac{pb}{2V}_{k=1} & \frac{rb}{2V}_{k=1} & \delta_{a_{k=1}} \\ \vdots & \vdots & \vdots & \vdots & \vdots \\ 1 & \beta_{k=N} & \frac{pb}{2V}_{k=N} & \frac{rb}{2V}_{k=N} & \delta_{a_{k=N}} \end{bmatrix} \\
A_{C_\ell} &= \begin{bmatrix} 1 & \beta_{k=1} & \frac{pb}{2V}_{k=1} & \frac{rb}{2V}_{k=1} & \delta_{a_{k=1}} \\ \vdots & \vdots & \vdots & \vdots & \vdots \\ 1 & \beta_{k=N} & \frac{pb}{2V}_{k=N} & \frac{rb}{2V}_{k=N} & \delta_{a_{k=N}} \end{bmatrix} \\
A_{C_m} &= \begin{bmatrix} 1 & \alpha_{k=1} & \max(\frac{1}{2}, X)\delta_{e_{k=1}} & C_{T_{k=1}} \\ \vdots & \vdots & \vdots & \vdots \\ 1 & \alpha_{k=N} & \max(\frac{1}{2}, X)\delta_{e_{k=N}} & C_{T_{k=N}} \end{bmatrix} \\
A_{C_n} &= \begin{bmatrix} 1 & \beta_{k=1} & \frac{rb}{2V}_{k=1} & \delta_{r_{k=1}} \\ \vdots & \vdots & \vdots & \vdots \\ 1 & \beta_{k=N} & \frac{rb}{2V}_{k=N} & \delta_{r_{k=N}} \end{bmatrix}
\end{aligned}
\tag{5-73}
$$

In which C_T is as defined in Equation (5-42). With the regression matrices defined, the linear estimation procedure can be commenced.

Linear Estimation Procedure

The linear estimation procedure is via OLS and works exactly as described earlier in this chapter. The linear to-be-estimated parameters θ_{lin} are given by:

$$
\begin{aligned}
\vec{\theta}_{C_L} &= \begin{bmatrix} C_{L_0} & C_{L_\alpha} & C_{L_{\alpha^2}} \end{bmatrix}^T \\
\vec{\theta}_{C_D} &= \begin{bmatrix} C_{D_0} & C_{D_\alpha} & C_{D_{\delta_e}} & C_{D_X} & C_{D_{C_T}} \end{bmatrix}^T \\
\vec{\theta}_{C_Y} &= \begin{bmatrix} C_{Y_0} & C_{Y_\beta} & C_{Y_p} & C_{Y_r} & C_{Y_{\delta_a}} \end{bmatrix}^T \\
\vec{\theta}_{C_\ell} &= \begin{bmatrix} C_{\ell_0} & C_{\ell_\beta} & C_{\ell_p} & C_{\ell_r} & C_{\ell_{\delta_a}} \end{bmatrix}^T \\
\vec{\theta}_{C_m} &= \begin{bmatrix} C_{m_0} & C_{m_\alpha} & C_{m_{X\delta_e}} & C_{m_{C_T}} \end{bmatrix}^T \\
\vec{\theta}_{C_n} &= \begin{bmatrix} C_{n_0} & C_{n_\beta} & C_{n_r} & C_{n_{\delta_r}} \end{bmatrix}^T
\end{aligned}
\tag{5-74}
$$

Then applying Equation (5-26) with the A matrices from Equation (5-73) and the parameter vectors $\vec{\theta}_{lin}$ from Equation (5-74) results in the best estimate parameter estimates $\hat{\vec{\theta}}_{lin}$. These

best estimates can subsequently be used in Equation (5-27) to calculate the best estimated model outputs $\hat{\vec{y}}_{C_L}$, $\hat{\vec{y}}_{C_D}$, $\hat{\vec{y}}_{C_Y}$, $\hat{\vec{y}}_{C_\ell}$, $\hat{\vec{y}}_{C_m}$ and $\hat{\vec{y}}_{C_n}$.

Results Specific to the Linear Estimation

The result of the linear estimation constitutes the final model of the Citation in stall. Its results and performance are discussed in the section hereafter as they are thus not specific to the linear estimation only.

An interesting feature that should still be discussed here is the difference between the nonlinear estimates of C_{L_0}, C_{L_α} and $C_{L_{\alpha^2}}$ and its linear estimates. See Table 5-3.

Table 5-3: Differences in the estimates of the C_{L_0}, C_{L_α} and $C_{L_{\alpha^2}}$ parameters between the nonlinear and linear estimation.

Parameter	$\hat{\theta}_{nonlin}$	$\hat{\theta}_{lin}$
C_{L_0}	0.1912	0.1910
C_{L_α}	4.4819	4.4832
$C_{L_{\alpha^2}}$	13.1858	13.6978

As can be seen, no significant differences occur in the linear estimates of the stability and control derivatives of C_L, even though $C_{L_{\alpha^2}}$ differs the most. It is also interesting to look at the difference in performance metrics in Table 5-2 and Table 5-5, where the metrics of the C_L model performance are slightly lower for the linear than the nonlinear estimation. This can be attributed to the fact that the nonlinear estimation results in parameters that are the median of a wider spread of optima. And for $C_{L_{\alpha^2}}$ this spread is the most irregular, as can be seen in Figure 5-3b, so it can be expected the median of this parameter deviated the most from the optimal value. The linear estimation does not have this problem as it is calculated analytically, and therefore the model performance slightly improves. However, as the results *are* very close, more than disregarding the nonlinear estimation reliability, it strengthens the reliability of using both methods consecutively.

All other results of the full estimation that do not relate to differences between the linear and nonlinear estimation are discussed below.

5-4 Evaluating the Aircraft Local Aerodynamic Model

The local with the two steps from the local aerodynamic modeling performed, its results can be investigated and its performance evaluated.

5-4-1 Model Validation Methods

Of course, the main model validation method is by plotting the modeled data ($\hat{\vec{y}}$), comparing it to the measured data from the UKF ($\vec{y}$) and to identify differences in the model behaviour. Next to this, in this case two other methods can be applied as well. First there are some specific OLS validation methods in order to assess if the the OLS delivered reliable results.

Second, by investigating the model output a lot of information can be obtained, but it is also worthwhile to extract a quantative measure. The Means Squared Error, Root Mean Square and Relative Root Mean Square are often used methods for this. They are both explained below.

OLS Validation

One can investigate the performance of the OLS application as this may indicate something about the reliability of the estimated model and its parameters. The validation of the linear regression model can be performed in two manners by use of:

- analysis of model residuals, and;
- analysis of parameter covariances.

Below, the application of both procedures is discussed.

- *Analysis of Model Residuals.* The performance of the model and its parameters can be analysed via its residuals. Rewriting the equation for the measurement vector $\vec{y}$ and using the best estimated output for the model $\hat{\vec{y}}$, one gets the residual vector $\vec{\varepsilon}$:

$$\vec{\varepsilon} = \hat{\vec{y}} - \vec{y} \tag{5-75}$$

  For a good estimator, the mean $\bar{\vec{\varepsilon}}$ of all residuals should be very close to 0 (and *should* be 0 in theory).

  The second condition for estimator performance related to the residuals is that the residuals should be uncorrelated. That means: to check whether the residuals (as much as possible) represent white noise. This can be calculated via the auto-correlation function $\gamma(l)$. Also a 95% confidence bound should be included. These are defined as:

$$\gamma(l) = \sum_{i=-N}^{N} \varepsilon(i)\varepsilon(i+l) \tag{5-76}$$

$$\text{conf} = 1.96/\sqrt{N} \tag{5-77}$$

  Where N is the number of measurements. The indication if the residuals have a white noise character is if the autocorrelation function resembles a Dirac-pulse, meaning $\gamma = 1$ at $l = 0$ and $\gamma = 0$ anywhere else. As in practise this is never the case, the 95% confidence bounds are added. Very close to $l = 0$ the autocorrelation is allowed to vaguely exceed the bounds, but broader this should not be the case.

- *Analysis of Parameter Covariances.* Next to analysing the actual residuals of the models, one can also perform an analysis on the OLS estimator itself to examine the reliability of its own estimated parameters. This is done by calculating the covariance of the estimated parameters, given by:

$$\text{Cov}[\hat{\vec{\theta}}] = \sigma^2 P = \sigma^2 \left(A^T A\right)^{-1}, \quad \text{with: } \sigma^2 \approx \hat{\sigma}^2 = \frac{\vec{\varepsilon}^T \vec{\varepsilon}}{N-k} \tag{5-78}$$

Where N is again the number of measurements and k is the number of regressor terms. The values on the diagonals of the covariance matrix show the variance that the model produces for that specific related parameter. The off-diagonal elements show the correlation between the different parameters. If all values in the matrices are significantly small, one can say that the estimator estimates significantly reliable parameters under the influence of noise.

Model Performance Metrics

A number of common metrics used are:

- the Mean Squared Error (MSE), which gives the average squared error of the residuals;
- the Root Mean Square (RMS), which is the root of the MSE giving the average residual (but positive);
- the Relative Root Mean Square ($RRMS$), which is the RMS as a percentage of the band that the measurements span;
- the coefficient of determination (R^2), which gives a measure of how much of the modeled outcome has been predictable from its parameters on a scale of 0 to 1.

These metrics are mathematically defined as:

$$MSE = \frac{1}{n}\sum_{i=1}^{n}(\hat{\vec{y}}_i - \vec{y}_i)^2 = \frac{1}{n}\sum_{i=1}^{n}\varepsilon_i^2 = \frac{1}{n}\vec{\varepsilon}^T\vec{\varepsilon} \tag{5-79}$$

$$RMS = \sqrt{MSE} = \sqrt{\frac{1}{n}\vec{\varepsilon}^T\vec{\varepsilon}} \tag{5-80}$$

$$RRMS = \sqrt{\frac{MSE}{|\max\vec{y} - \min\vec{y}|}} \times 100\% = \sqrt{\frac{1}{n}\frac{\vec{\varepsilon}^T\vec{\varepsilon}}{|\max\vec{y} - \min\vec{y}|}} \times 100\% \tag{5-81}$$

$$R^2 = 1 - \frac{\sum_{i=1}^{n}\varepsilon_i^2}{\sum_{i=1}^{n}(y_i - \bar{y})^2} \tag{5-82}$$

With $\bar{y}$ the mean of the measurements. All may give some insight into the behaviour of the model and therefore they are all calculated for the dataset. Especially R^2 calculates a very different essence of the model than the first three metrics that are basically a residual analysis of the models. While the former analyses more the response of the system. Other than the OLS validation, these metric can also be used to compare model output to an unrelated validation dataset.

5-4-2 Results of the Local Aerodynamic Model

In this section the results of the local estimation on the example dataset are discussed and the performance of the local aerodynamic model is assessed.

The values of the stability and control derivatives found by the linear OLS estimation are given in Table 5-4. The resulting model output by applying these parameters in the six aerodynamic force and moment equations is given in Figure 5-7. The performance metrics of the model are given in Table 5-5.

Table 5-4: Parameter estimates in the aerodynamic force and moment equations.

Model	Parameter	Value
X	a_1	32.0864
	α^*	0.2039 rad
	τ_1	0.1293 s
	τ_2	0.0525 s
Model	**Parameter**	**Value**
C_L	C_{L_0}	0.1910
	C_{L_α}	4.4832
	$C_{L_{\alpha^2}}$	13.6978
C_D	C_{D_0}	0.0133
	C_{D_α}	0.1788
	$C_{D_{\delta_e}}$	-0.1697
	C_{D_X}	0.0696
	$C_{D_{C_T}}$	-0.6073
C_Y	C_{Y_0}	0.0070
	C_{Y_β}	-0.5605
	C_{Y_p}	-0.5637
	C_{Y_r}	-0.9068
	$C_{Y_{\delta_a}}$	-0.2294
C_ℓ	C_{ℓ_0}	-0.0013
	C_{ℓ_β}	-0.0622
	C_{ℓ_p}	-0.1234
	C_{ℓ_r}	-0.0954
	$C_{\ell_{\delta_a}}$	-0.0968
C_m	C_{m_0}	0.0334
	C_{m_α}	-0.6014
	$C_{m_{X\delta_e}}$	-0.8784
	$C_{m_{C_T}}$	-0.0511
C_n	C_{n_0}	$-9.0476 \cdot 10^{-4}$
	C_{n_β}	0.0572
	C_{n_r}	0.0024
	$C_{n_{\delta_r}}$	-0.0181

Table 5-5: Performance metrics of the full parameter estimation.

Model	Metric	Value
C_L	MSE	$6.6409 \cdot 10^{-4}$
	RMS	0.0258
	$RRMS$	2.9512%
	R^2	0.9626
C_D	MSE	$1.6805 \cdot 10^{-5}$
	RMS	0.0041
	$RRMS$	0.9897%
	R^2	0.9904
C_Y	MSE	$2.5271 \cdot 10^{-5}$
	RMS	0.0050
	$RRMS$	1.7196%
	R^2	0.6256
C_ℓ	MSE	$1.1555 \cdot 10^{-6}$
	RMS	0.0011
	$RRMS$	0.6444%
	R^2	0.7207
C_m	MSE	$4.3408 \cdot 10^{-5}$
	RMS	0.0066
	$RRMS$	1.4857%
	R^2	0.8514
C_n	MSE	$4.8400 \cdot 10^{-7}$
	RMS	$6.9570 \cdot 10^{-4}$
	$RRMS$	0.4334%
	R^2	0.3473

Each of the aerodynamic force and moment models are discussed below.

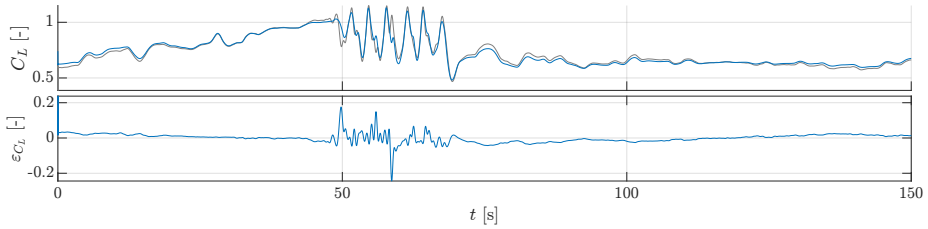

(a) Aerodynamic force C_L.

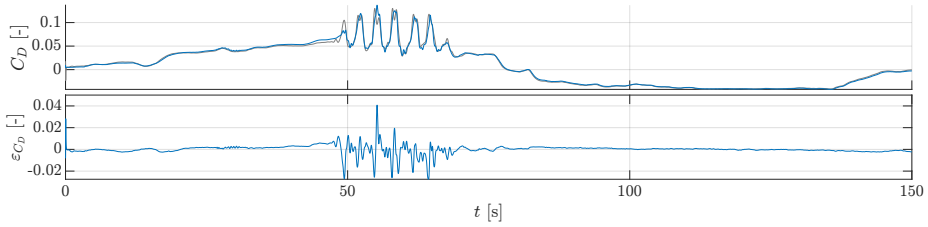

(b) Aerodynamic force C_D.

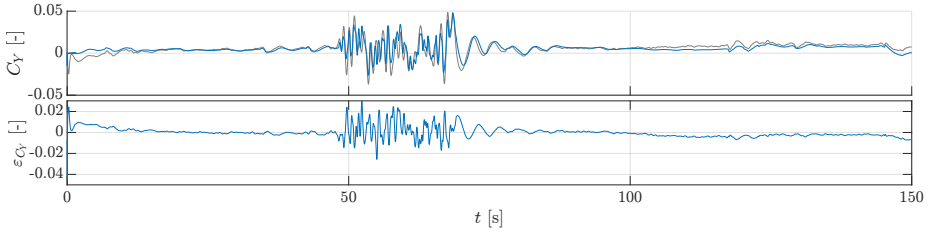

(c) Aerodynamic force C_Y.

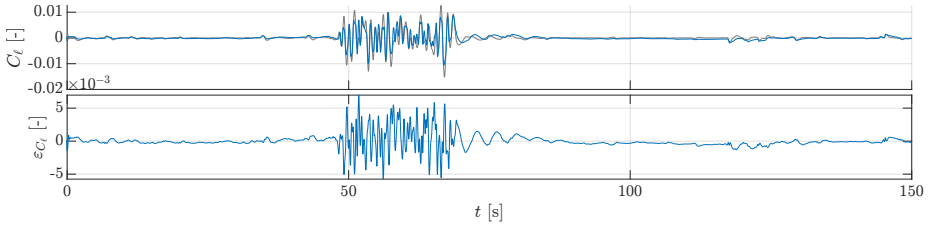

(d) Aerodynamic moment C_ℓ.

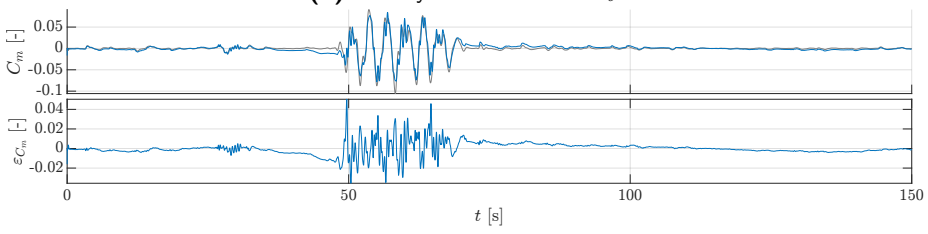

(e) Aerodynamic moment C_m.

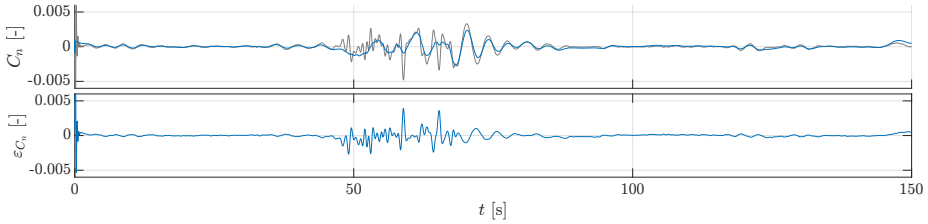

(f) Aerodynamic moment C_n.

Figure 5-7: Local aerodynamic model output and residuals for the example dataset. Blue is the model output $\hat{\vec{y}}$ and grey is the measurement $\vec{y}$.

- *Aerodynamic model force C_L.* The values of the stability and control parameters found are within a standard deviation of the values from all datasets as found in Table 6 of [58] which supports the findings here. Judging from the metrics the C_L model performs rather well, even though when compared to the other force and moment models it is the worst, with an $RRMS$ of 2.9%. Based on R^2 it does perform quite well though, but this can be expected due to the C_L having by far the largest variations of all forces and moments.

  The largest differences in the C_L model are because of two reasons that can be observed in the plot. First, there appear "almost" steady state residuals during the time of the dataset, with first a positive, then a negative after the stall and then a positive error again towards the end of the dataset. Second, during the stall the model performs quite well in representing the nonlinear behaviour during the stall. Especially note the small positive peaks after the larger peaks in C_L. The only problem seems to be however that the timing and size of these peaks is different than for the measurements, which also cause the largest peaks in the residual plot. This was also observed in [58], but no specific reason was found for this.

  It can be concluded however, that with the obtained metrics the model still is a satisfying representation of reality and therefore it is concluded that the model is of sufficient quality for further use in this thesis.

- *Aerodynamic model force C_D.* For the C_D all-but-one of the found values are also within a standard deviation of the values found by [58]. This is however not the case for $C_{D_{C_T}}$. In [58], the reconstructed thrust was subtracted from the C_D measurement, but it was still found that the thrust coefficient needed to be added to the model for C_D and C_m as a "fix" for errors in the engine model estimates. But as was argued in [28] via Equation (5-14) it is not uncommon to include thrust inputs in the aerodynamic model equations. Thus, as C_T was included in the equations of [58] anyways, it was decided to *not* subtract the thrust from the reconstructed C_D or C_m measurement and keep the C_T derivatives in the equation as full parameters to give the most complete representation of all effects on C_D and C_m. Of course, this may not lead to very different estimates for the other parameters or worse performance parameters of the model.

  The metrics of the C_D model are rather good, with an $RRMS$ of 1.0210% and R^2 of 0.9898. In the plot of the model behaviour it is clear that the residuals are significantly smaller than for the C_L. The nonlinear effects with the secondary peaks are present and follow the measurements better than for C_L, even though not perfectly. This can be expected as the nonlinear effects are indeed known to have the largest effect on C_L and as such errors related to this are less pronounced in the C_D.

- *Aerodynamic model force C_Y.* The C_Y coefficient model relatively shows the least accurate (but still absolutely accurate) behaviour with a $RRMS$ of 1.7196%. In this case it cannot be contributed to large nonlinearities that are hard to model as for the C_L as there are no X terms in the equation for C_Y. Also from the plot is is clear that the excitations are more frequent than for the C_L and C_D, but the model is able to follow them well. There appear some residuals but these are never large. However the R^2 is quite low, but this can be expected as the variance of C_Y is neither this large. This may automatically be the reason of the slightly lower $RRMS$: the Y force is less excited during the maneuver which may make identification more difficult. A last observation

is that the residuals do show some offset, where until the stall the model overestimates and underestimates thereafter. Looking at the found stability and control derivatives they are also comparable to those found by [58] and all fall within a standard deviation found in that paper, except for C_{Y_r} which has an unexpected sign.

- *Aerodynamic model moment C_ℓ.* The rolling moment shows a very good fit with an $RRMS$ of 0.6444%. In the time series there can only be found two main types of deviations from the measurement, even though these are not very large in magnitude. The main errors are found during the stall, where the model is not able to reach the exact same intensity of the peaks that are found in the measurements, and just after the stall where the model does not timely estimate the rolling behaviour that exists there, even though the intensity of this roll behaviour is modeled well. Again, looking at [58] the values found for the stability and control derivatives are within a standard deviation of the estimates found there. Surprisingly, the yaw rate coefficient C_{ℓ_r} again has an unexpected sign.

- *Aerodynamic model moment C_m.* The pitching moment model shows the same behaviour as for the lift coefficient. The values are within a standard deviation from the values found by [58], but again except for the one related to C_T, because of the reason as discussed above. The sign of this derivative can be expected, though. The engines are located relatively high on the fuselage above the *c.g.*, such that an increase in thrust results in a nose down pitching moment. The $RRMS$ value of 1.4857% shows a sufficient model fit, but is quite high relative to the other model equations. Looking at the data in time it can be seen that the nonlinearities during the stall are accurately modeled, but the main error lies mainly in the high angles of attack just before and after the stall, which may still be attributed to any nonlinear behaviour around the stall angle of attack. The R^2 value of 0.8514 is somewhat lower than for the C_L, but again may be attributed to the lower variance present in the measurement.

- *Aerodynamic model moment C_n.* The last model for the yawing moment C_n shows metrics that deem the model very reliable with an $RRMS$ of only 0.4334%. The R^2 shows less fit of the model with the measurements with a value of only 0.3473. Partly this can be attributed to the fact that the yawing rate is not very significant in the maneuver leading to a low variance. But, when investigating the time series it can also be seen that the model does not very accurately model the measurements. Especially there is a significant lack of higher frequency, higher amplitude behaviour in the model relative to the data. This behaviour was also found to be hard to replicate by [58], primarily thought to occur because of less distinct excitations in this direction during the flight testing. Also when comparing the found stability and control derivatives with this paper, there are larger differences amongst them, not falling within one standard deviation but outside of it, including the yaw rate derivative C_{n_r} with, again, a wrong sign.

For the the last aerodynamic moment and all the yaw-rate derivatives with the wrong sign, it is expected that other stall runs may provide better data. Because of this, care must be taken to make a new comparison with [58] when more stall runs have been estimated by the procedure of this thesis. Additionally, the results of the models with those estimated parameters should be compared to the outcomes of other, unrelated, validation datasets.

The full parameter estimation does not only consist of the "top-level" equations as described above, but the calculation of X can also be seen as sub-model of its own. The values of the X parameters as found earlier in the nonlinear estimation are given in Table 5-4. The resulting model output by applying these parameters in the ODE for X and the resulting regressors containing X is given in Figure 5-8. As there is no measurement of X it is unfortunately not possible to calculate performance metrics.

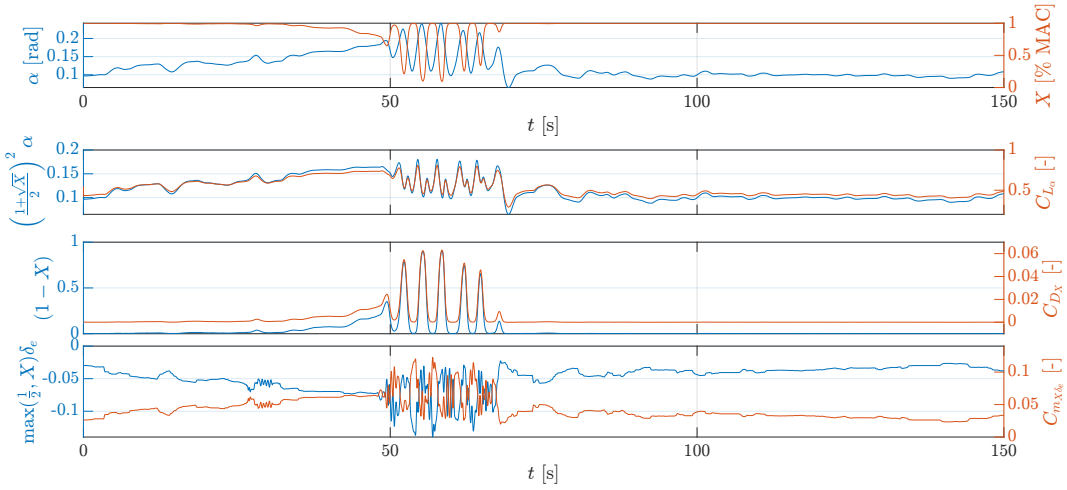

Figure 5-8: Output of the model for X and the effect of the X parameter on the stability and control derivatives of C_L, C_D and C_m.

The modeling of X is discussed below.

- *Separation point model parameter X.* First looking at the behaviour of the separation point as a function of angle of attack, it can be seen that the model properly imitates the expected behaviour of X. As the angle of attack increases towards the stall angle of attack the separation point starts to move forward along the wing until the first drop just before 50 s, after which the increasing of angle of attack after this point lead to a second stall where the separation point moves significantly to the leading edge of the wing, after almost reattaching entirely when the angle of attack is lowered again. This behaviour is repeated a number of times until at 70 s the angle of attack is kept low for full recovery from the stall and the flow reattaches to the wing for the remainder of the dataset.

  It is worthwhile to investigate the effect of the separation point on the regressors used in the aerodynamic model and the subsequent value of the stability and control contribution. First for the C_L, the most visible effect is the aim of the modeling of Kirchoff's theory is immediately visible: the "smoothening and flattening" of the peaks in angle of attack to reduce the lift when the angle of attack is high, but the airflow is significantly separated. Also here becomes visible what also has been observed in the time series for the C_L: the introduction of the smaller "secondary peaks", where the angle of attack is decreased, but the airflow reattaches, such that counterintiutively the lift increases with decreasing angle of attack.

  For the C_D the worth of the X parameter also becomes clearly visible. In normal models the drag only increases with the angle of attack, but here it can be seen that separated

flow imposes an enormous penalty on the efficiency of the aircraft. With a forward moving separation point the drag also increases with it very heavily.

Last, the effect of X is also present in the effectiveness of the elevator. The multiplication of X with the elevator deflection mimics the effect of degrading control effectiveness during the stall. For the pitching moment this is mainly due to the elevator being in the wake of the separated airflow, such that the air is not as efficient anymore in creating lift at the horizontal stabilizer, as well as that the elevator itself also reaches higher angles of attack and may experience some separation as well. The max-operator is present to make sure that the effectiveness of the elevator is never fully degraded with the wing. This is true as the elevator is designed to always stall later than the wing and does thus always remains effective even in the stall to make recovery possible.

Last, the performance and efficiency of the linear estimation can be evaluated via the residual and parameter covariance analysis, as discussed earlier in this chapter. See Figure 5-9 and Table 5-6.

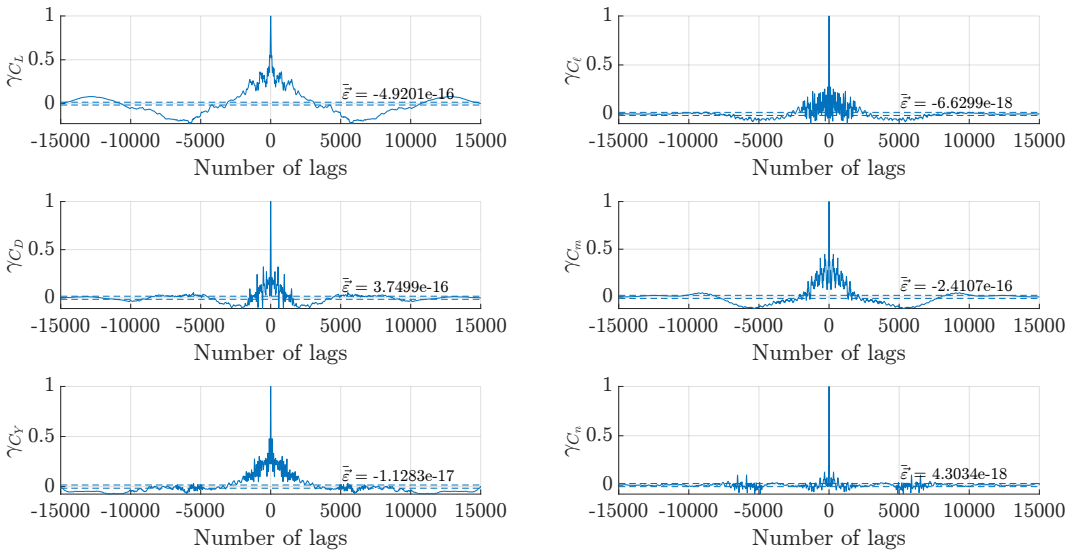

Figure 5-9: Local aerodynamic model residual analysis of correlation function and residual mean. Solid is the correlation function, dashed is the confidence bound.

First looking at the mean of the residuals it becomes clear that the OLS is effective in minimizing the error over the entire time series with mean values no higher than in the order of 10^{-16}. The second important behaviour related to the residuals is the correlation that they have along the time series. What already has been observed when analysing the time series for C_L, C_D and C_m is that they have some sort of constant deviation along larger parts of the data set. This behaviour can directly be observed in the correlation function, where for these three models there is a significant deviation from the confidence bounds even far from the 0 lags, with the largest in that of C_L. Normally this would say something about the model: that the introduced parameters and regressors are not able to converge completely to the measurement and some additional terms are needed. However, in this case it is still decided to retain the model as found by [58] as the OFM is expected to come to a model which for a reason only contains a maximum number of terms to keep model complexity low.

Table 5-6: Parameter covariances of the OLS in the linear estimation.

Model	$\mathbf{Cov}[\hat{\vec{\theta}}]$					
C_L	$10^{-0}\times$	$\begin{bmatrix} \mathbf{0.0000} & -0.0000 & 0.0001 \\ -0.0000 & \mathbf{0.0001} & -0.0006 \\ 0.0001 & -0.0006 & \mathbf{0.0086} \end{bmatrix}$				
C_D	$10^{-5}\times$	$\begin{bmatrix} \mathbf{0.0105} & -0.0765 & -0.0042 & 0.0099 & -0.0276 \\ -0.0765 & \mathbf{0.7331} & 0.3443 & -0.0809 & 0.1433 \\ -0.0042 & 0.3443 & \mathbf{0.6401} & 0.0192 & -0.0175 \\ 0.0099 & -0.0809 & -0.0036 & \mathbf{0.0192} & -0.0175 \\ -0.0276 & 0.1433 & -0.0609 & -0.0175 & \mathbf{0.1213} \end{bmatrix}$			
C_Y	$10^{-3}\times$	$\begin{bmatrix} \mathbf{0.0000} & -0.0001 & 0.0003 & -0.0013 & 0.0001 \\ -0.0001 & \mathbf{0.0243} & -0.0145 & -0.0059 & 0.0005 \\ 0.0003 & -0.0145 & \mathbf{0.1442} & 0.0182 & 0.0096 \\ -0.0013 & -0.0059 & 0.0182 & \mathbf{0.4422} & 0.0050 \\ 0.0001 & 0.0005 & 0.0096 & 0.0050 & \mathbf{0.0057} \end{bmatrix}$			
C_ℓ	$10^{-4}\times$	$\begin{bmatrix} \mathbf{0.0000} & -0.0001 & 0.0001 & -0.0006 & 0.0000 \\ -0.0001 & \mathbf{0.0111} & -0.0066 & -0.0027 & 0.0003 \\ 0.0001 & -0.0066 & \mathbf{0.0659} & 0.0083 & 0.0044 \\ -0.0006 & -0.0027 & 0.0083 & \mathbf{0.2022} & 0.0023 \\ 0.0000 & 0.0003 & 0.0044 & 0.0023 & \mathbf{0.0026} \end{bmatrix}$			
C_m	$10^{-4}\times$	$\begin{bmatrix} \mathbf{0.0015} & -0.0071 & 0.0055 & -0.0055 \\ -0.0071 & \mathbf{0.0596} & 0.0288 & 0.0200 \\ 0.0055 & 0.0288 & \mathbf{0.1510} & -0.0257 \\ -0.0055 & 0.0200 & -0.0257 & \mathbf{0.0284} \end{bmatrix}$			
C_n	$10^{-4}\times$	$\begin{bmatrix} \mathbf{0.0001} & 0.0002 & -0.0017 & 0.0032 \\ 0.0002 & \mathbf{0.0047} & -0.0038 & 0.0063 \\ -0.0017 & -0.0038 & \mathbf{0.1030} & -0.0442 \\ 0.0032 & 0.0063 & -0.0442 & \mathbf{0.1012} \end{bmatrix}$			

Adding additional terms may increase the model, but only with inefficient incremental steps such that it might be more worthwhile to keep the model simpler even though absolutely speaking the error is larger this way.

Last, in the analysis of the parameter covariances no significant variances are found for any parameter other than $C_{L_{\alpha^2}}$. This means that the reliability that this parameter *is* actually the best parameter or very close to the best estimate is less than for the other parameters. This can be expected for this parameter as its associated regressor is of order 2 and it is thus more sensitive to changes in this regressor value. But still, the value of 0.0086 is not *very* high, such that it can still be said the OLS delivers overall reliable results.

5-4-3 Application of the Local Aerodynamic Model to a Validation Dataset

The above analysis performed for the local aerodynamic model shows that the parameter estimation technique works, i.e. the model outcome behaves as expected and estimates the data it is based on sufficiently well. However, the real power of models is to create outputs

based on an independent input signal. For this a unrelated validation dataset can be used. In this case stall run 27 from Table A-2 is chosen. This is a symmetric and different type of stall with a different control input as the training stall run 19, and thus quite unrelated to the training run.

The model output compared to the validation run measurement is given in Figure 5-10 and the performance metrics are given in Table 5-7.

Table 5-7: Performance metrics of the model from training run 19 on validation run 27.

Model	Metric	Value
C_L	MSE	0.0016
	RMS	0.0399
	$RRMS$	4.5944%
	R^2	0.9448
C_D	MSE	$5.3448 \cdot 10^{-5}$
	RMS	0.0073
	$RRMS$	1.7536%
	R^2	0.9347
C_Y	MSE	$2.2489 \cdot 10^{-4}$
	RMS	0.0150
	$RRMS$	3.0614%
	R^2	0.6056
C_ℓ	MSE	$8.2327 \cdot 10^{-6}$
	RMS	0.0029
	$RRMS$	1.5976%
	R^2	-0.0139
C_m	MSE	$1.2541 \cdot 10^{-4}$
	RMS	0.0112
	$RRMS$	2.5240%
	R^2	0.6360
C_n	MSE	$2.5410 \cdot 10^{-5}$
	RMS	0.0050
	$RRMS$	2.2669%
	R^2	0.1101

From the time series data in Figure 5-10 it can be seen that the longitudinal motions are approximated rather well, also in the stall where the nonlinearites can be captured quite well. For the lateral motions this seems to be less so. The lateral force C_Y follows the main measurement in the stall quite well, although during the stall the nonlinearities are not very well estimated. The moments C_ℓ and C_n have rather bad estimates.

This behaviour is partly reflected by the metrics in Table 5-7. The $RRMS$ values are still within a reasonable range for both the longitudinal as the lateral motions, but this could be expected as during a large part of the validation run there are not that many excitations and the error is small. Looking at the low R^2 values for the lateral motions substantiates better what is also observed in the time series data: the variations in the measurements cannot be well predicted from the parameters of the model. Normally this would definitely constitute a

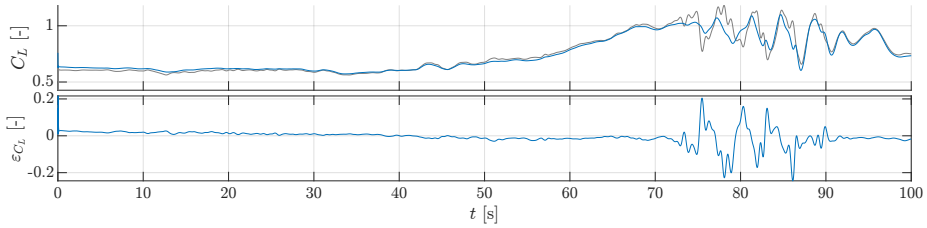

(a) Aerodynamic force C_L.

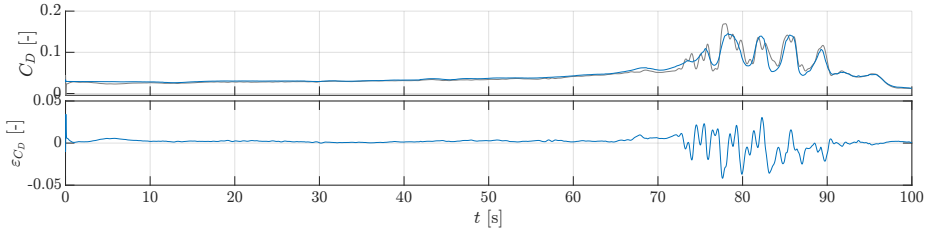

(b) Aerodynamic force C_D.

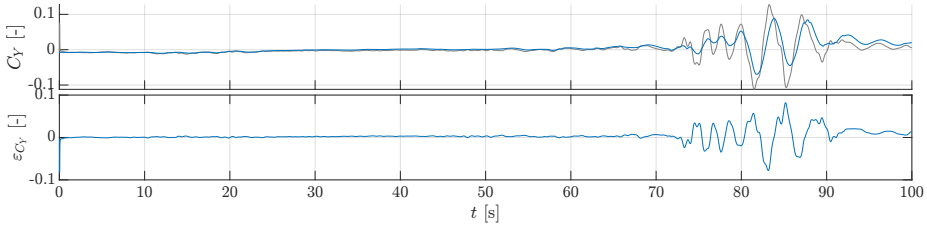

(c) Aerodynamic force C_Y.

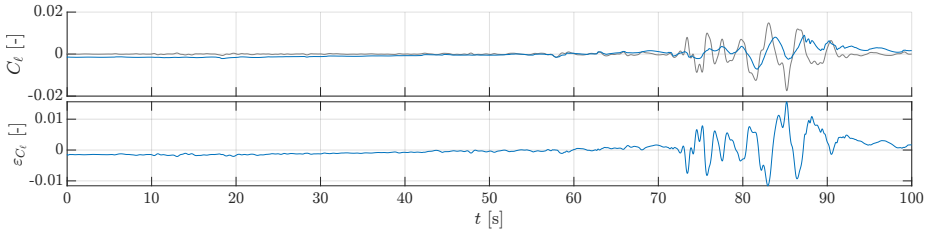

(d) Aerodynamic moment C_ℓ.

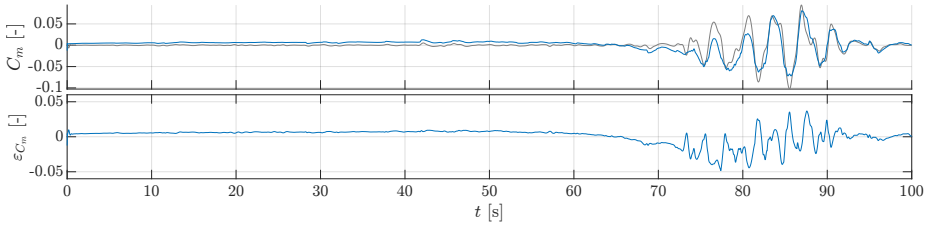

(e) Aerodynamic moment C_m.

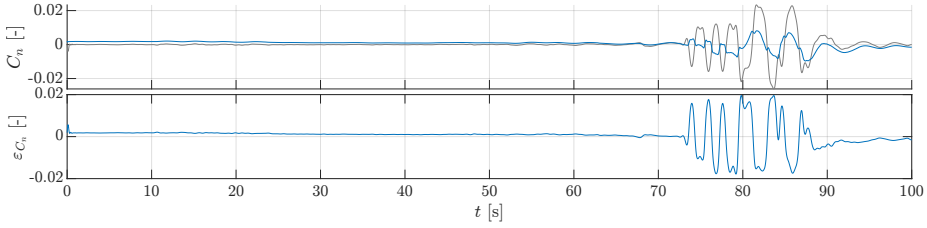

(f) Aerodynamic moment C_n.

Figure 5-10: Local aerodynamic model output from training run 19 on measurements from validation run 27. Blue is the model output $\hat{\vec{y}}$ of training run 19 and grey is the measurement $\vec{y}$ from validation run 27.

"bad" model. However as mentioned, it must be kept in mind that this is based on only one training run. The bad performance for the lateral motions may very well be attributed to the unexpected sign of the yaw-rate derivatives, for example. Again, as was concluded above as well, when more training runs and training data is used this problem might very well solve itself as better overall parameter estimates are found.

5-5 Conclusion on the Applicability of the Local Aerodynamic Stall Model

Overall, the estimation of the local aerodynamic model delivers satisfyingly reliable results. With the complexity of the entire procedure in mind it is concluded that the estimation procedure as designed is reliable and can be used for the remainder of this thesis. However, it is at this point still only a "$n = 1$" experiment. Other data sets may yield very different results, or: the model is not proven until further used.

What the main takeaway of the above analysis *does* provide however is an indication that is has some degree of reliability that is deemed enough for further use in the thesis. The main found drawbacks were the lacking accuracy for the very nonlinear behaviour of the stall for the C_L model and relatively (but not absolutely!) high $RRMS$, a non-satisfactory model for C_n during the stall, high correlation of some residuals, especially just before stall entry and after stall exit and significant correlation for some parameters. However, the first is not necessarily a problem as it *does* model the most important nonlinear characteristic, the second was accepted because of the explicit reasoning that was behind the model structure selection and the last can be experimentally checked by actually performing the estimation on more datasets and doing statistical analysis on the spread and means of the found parameters. Of course, it is actually also interesting if any change in method or selection of time window which is used for the estimation may even improve any lacking behaviour as found in the comparison of the model output with the measurements.

In conclusion, this chapter does *not* prove the entire validity of the model, but *does* shows that any shortcomings now can be explained and thus the model is reliable enough to perform further research with, which will only prove its validity even further.

Chapter 6

Global Modeling Methods

The local estimated model of chapter 5 is very valuable to the modeling of aircraft as it has very accurate performance with a Relative Root Mean Square ($RRMS$) performance of no higher than 2.9512%, even for the very nonlinear C_L equation. It is thus represents the actual aircraft in a significantly accurate manner. However, the local model cannot practically be used on its own as it is only valid closely around the point where its values are estimated, as explained in chapter 5 according to [2]. One method to make the model globally applicable is by estimating the parameters at a large range of points in the flight envelope, and saving those in a database, then the model basically consists of many separate local models.

Another method is not to create a model that consists of many local models, but one that consists of only one *global* model that is valid over the entire envelope and includes variables as angle of attack α_0, velocity V_0, altitude h_0 and mass and inertia parameters m_0 and I_0. For turns and climbs or descends bank angle φ_0 and climb angle γ_0 are also needed, respectively. A reason for this method is to decrease model complexity which also introduced the possibility for higher computational efficiency. Global models differ from local models in two ways. First, where a local model has limited applicability (e.g. close around a trimming point), a global model is widely applicable (e.g. in the entire flight envelope). On the other hand, a local model is often very accurate in its domain, while a global model usually lacks accuracy on the local level, especially when more detailed, nonlinear maneuvers need to be modeled. A goal in global modeling is increase the local applicability while still retaining the less complex model structure.

Normally this is can be done in two ways: via direct estimation with one model structure (as with simplex splines or neural networks), or via an intermediate step where first many local models are estimated and these are globally coupled via equations for the stability and control derivatives (as with OFM or DOE methods) or coupled via more elaborate stitching techniques (as e.g. in [32] but not further discussed here).

In this chapter, three methods to achieve this are discussed that aim at the global aerodynamic modeling of aircraft. First, orthogonal function modeling is applied to find powerful regressors that may be used in global modeling. A problem that often occurs is that global data is

very scattered which makes identification with some methods difficult. By using design of experiment methods, a polynomial method is developed that aims to accurately model the aircraft behaviour with the least needed information. Also, multivariate splines are discussed that try to increase local applicability even further than polynomials, but may also be used on scattered data. Last, neural networks for global modeling are discussed and all different methods are compared.

6-1 Global Modeling via OFM

In chapter 5 orthogonal function modeling was applied to find the most effective *local* model structure for the Citation in stall and it was shown that this can be a very powerful tool in keeping the model as simple as possible, but all the while keeping its modeling performance up to a high standard. As mentioned, the goal of aerodynamic *global* is somewhat the same: creating accurate models which are more simple than a large collection of local models. Naturally, the question follows whether it is possible to also use OFM for global modeling. This has been investigated by [34].

In this paper, the OFM technique is applied to create an aerodynamic model of an F-16 aircraft from wind tunnel data. As a starting point the equations that govern the wind tunnel measurements were taken, given by:

$$
\begin{aligned}
C_X &= C_X(\alpha, \delta_e) + C_{X_q}(\alpha)\frac{q\bar{c}}{2V} \\
C_Y &= C_Y(\beta, \delta_a, \delta_r) + C_{Y_p}(\alpha)\frac{pb}{2V} + C_{Y_r}(\alpha)\frac{rb}{2V} \\
C_Z &= C_Z(\alpha, \beta, \delta_e) + C_{Z_q}(\alpha)\frac{q\bar{c}}{2V} \\
C_\ell &= C_\ell(\alpha, \beta) + C_{\ell_p}(\alpha)\frac{pb}{2V} + C_{\ell_r}(\alpha)\frac{rb}{2V} + C_{\ell_{\delta_a}}(\alpha, \beta)\delta_a + C_{\ell_{\delta_r}}(\alpha, \beta)\delta_r \\
C_m &= C_m(\alpha, \delta_e) + C_{m_q}(\alpha)\frac{q\bar{c}}{2V} + C_Z\left(x_{c.g._{ref}} - x_{c.g.}\right) \\
C_n &= C_n(\alpha, \beta) + C_{n_p}(\alpha)\frac{pb}{2V} + C_{n_r}(\alpha)\frac{rb}{2V} + C_{n_{\delta_a}}(\alpha, \beta)\delta_a + C_{n_{\delta_r}}(\alpha, \beta)\delta_r - C_Y\left(x_{c.g._{ref}} - x_{c.g.}\right)\frac{\bar{c}}{b}
\end{aligned}
\tag{6-1}
$$

Immediately the difference between the global and local modeling becomes clear in the fact that the stability and control derivatives are not a constant but a function of parameters itself. The "old-fashioned" manner to find these values are in the large set of tables but in this case OFM is used to find a polynomial parametrization for these values, i.e. an actual function. For every derivative the candidate regressor pool consists of the variables as given in Equation (6-1), higher order terms of those regressors and combinations of both. The selection algorithm then lead to 19 further equations. As an example, for derivative $C_Z(\alpha, \beta, \delta_e)$:

$$\left(f_0 + f_1\alpha + f_2\alpha^2 + f_3\alpha^3 f_4\alpha^4\right)\left(1 - \beta^2\right) + f_5\delta_e$$

In this equation the f_n are then constants found by performing an OLS procedure, which is performed for all 19 equations for the derivatives.

The output of the model when run in nonlinear simulations of the F-16 found that the polynomial model differed less than 10% from the data found by the original database version of the model. Regarding the high nonlinearity of the F-16 aerodynamic model this is quite good, even though 10% is also not of very high quality. Also, this model does not incorporate any envelope-related regressors like altitude or Mach number, which may be interesting as they directly say something about the global applicability of a certain stability and control derivative. Therefore it is interesting to research further methods.

6-2 Global Aerodynamic-Propulsive Modeling via Design of Experiment Methods

A second method that aims to more explicitly introduce flight envelope related regressors into the model has been developed by [44] which makes use of Design of Experiment (DOE) methods. First the mathematical global modeling procedure is explained, then the application of DOE methods to flight envelope testing is considered and last, the model is compared to the OFM global model.

6-2-1 DOE Mathematical Global Modeling Procedure

The method as designed by [44] has the same structure as for the OFM global model. First a local model definition is chosen and the force and moment coefficient are estimated at that particular location in the flight envelope, and is then repeated for a number of other different locations in the flight envelope. Then every stability and control derivative is modeled according to the flight envelope regressors altitude h, true airspeed V_{TAS}, aircraft mass m and center of gravity location $\left(\frac{x}{\bar{c}}\right)_{c.g.}$. The final model then has the following structure (in this case for pitching moment C_m):

$$C_m = C_{m_0}(h, V_{TAS}, m, \left(\frac{x}{\bar{c}}\right)_{c.g.}) + C_{m_u}(h, V_{TAS}, m, \left(\frac{x}{\bar{c}}\right)_{c.g.})\frac{u}{V_{TAS}} + C_{m_\alpha}(h, V_{TAS}, m, \left(\frac{x}{\bar{c}}\right)_{c.g.})\alpha + \ldots$$
$$\ldots + C_{m_q}(h, V_{TAS}, m, \left(\frac{x}{\bar{c}}\right)_{c.g.})\frac{q\bar{c}}{2V_{TAS}} + C_{m_{\delta_e}}(h, V_{TAS}, m, \left(\frac{x}{\bar{c}}\right)_{c.g.})\delta_e \quad (6\text{-}2)$$

For every required DOE measurement point multiple runs are performed (i.e. at one specific combination of h, V_{TAS}, m and $\left(\frac{x}{\bar{c}}\right)_{c.g.}$). In this case via an optimized orthogonal multisine input as developed by [36]. Then for the runs at that condition a simple least-squares regression is performed to find the stability and control derivatives. This concludes the local estimation part of this method.

After having performed the *local* parameter estimation on each of the tested flight conditions, phase 2 of the algorithm is performed to find the *global* model based on the variables describing the flight condition. A resource- and time-efficient method for this is a DOE (Design of Experiments) technique, which delivers an approximate model that is still able to describe the characteristics of the design space including the influence of each factor in the response behaviour and factor interactions. This approach is discussed below.

The first step is to define a 2^k Full Factorial Design (FFD) as a baseline structure for the model. It includes modeling responses of up to first, second and third order factor interactions and bias terms (zero order). The general structure is given by:

$$\begin{aligned} &y_n = f(x_{i,n}) = \\ &= \gamma_0 + \sum_{i=1}^{k} \gamma_i x_{i,n} + \sum_{i=1,j=i+1}^{k-1,k} \gamma_{ij} x_{i,n} x_{j,n} + \sum_{i=1,j=i+1,l=j+1}^{k-2,k-1,k} \gamma_{ijl} x_{i,n} x_{j,n} x_{l,n} + \varepsilon_n, \quad \text{with } n = 1, 2, \ldots, N \end{aligned} \tag{6-3}$$

In which k is the number of factors (i.e. in this case $k = 4$: h, V_{TAS}, m and $\left(\frac{x}{\bar{c}}\right)_{c.g.}$), n is one certain flight condition with N the total number of flight conditions conducted and γ are the coefficients.

If a higher order model is needed to capture any quadratic characteristics, pure quadratic terms can be added by making used of Central Composite Design (CCD) rather than FFD. This is by adding a quadratic term in the following manner:

$$\begin{aligned} &y_n = f(x_{i,n}) = \\ &= \gamma_0 + \sum_{i=1}^{k} \gamma_i x_{i,n} + \sum_{i=1}^{k} \gamma_{ii} x_{i,n}^2 \sum_{i=1,j=i+1}^{k-1,k} \gamma_{ij} x_{i,n} x_{j,n} + \sum_{i=1,j=i+1,l=j+1}^{k-2,k-1,k} \gamma_{ijl} x_{i,n} x_{j,n} x_{l,n} + \varepsilon_n, \quad \text{with } n = 1, 2, \ldots, N \end{aligned} \tag{6-4}$$

Non-dependent which of the two methods is used, the coefficients of the model may be estimated via least-squares. In case of the defined model structure using CCD, one can write Equation (6-4) in matrix form as:

$$Y = X\vec{\gamma} + \vec{\varepsilon} = \begin{bmatrix} y_1 \\ y_2 \\ \vdots \\ y_N \end{bmatrix} = \begin{bmatrix} 1 & X_{i,1} & X_{ii,1} & X_{ij,1} & X_{ijl,1} \\ 1 & X_{i,2} & X_{ii,2} & X_{ij,2} & X_{ijl,2} \\ \vdots & \vdots & \vdots & \vdots & \vdots \\ 1 & X_{i,N} & X_{ii,N} & X_{ij,N} & X_{ijl,N} \end{bmatrix} \begin{bmatrix} \gamma_0 \\ \vec{\gamma}_i \\ \vec{\gamma}_{ii} \\ \vec{\gamma}_{ij} \\ \vec{\gamma}_{ijl} \end{bmatrix} + \begin{bmatrix} \varepsilon_1 \\ \varepsilon_2 \\ \vdots \\ \varepsilon_N \end{bmatrix} \tag{6-5}$$

In which:

$$
\begin{aligned}
\vec{\gamma}_i &= \begin{bmatrix} \gamma_1 & \gamma_2 & \cdots & \gamma_k \end{bmatrix}^T \\
\vec{\gamma}_{ii} &= \begin{bmatrix} \gamma_{11} & \gamma_{22} & \cdots & \gamma_{kk} \end{bmatrix}^T \\
\vec{\gamma}_{ij} &= \begin{bmatrix} \gamma_{12} & \gamma_{13} & \cdots & \gamma_{1k} & \gamma_{23} & \cdots & \gamma_{(k-1)k} \end{bmatrix}^T \\
\vec{\gamma}_{ijl} &= \begin{bmatrix} \gamma_{123} & \gamma_{124} & \cdots & \gamma_{12k} & \gamma_{234} & \cdots & \gamma_{2(k-1)k} & \gamma_{345} & \cdots & \gamma_{(k-2)(k-1)k} \end{bmatrix}^T \\
X_{i,n} &= \begin{bmatrix} x_{1,n} & x_{2,n} & \cdots & x_{k,n} \end{bmatrix} \\
X_{ii,n} &= \begin{bmatrix} x_{1,n}x_{1,n} & x_{2,n}x_{2,n} & \cdots & x_{k,n}x_{k,n} \end{bmatrix} \\
X_{ij,n} &= \begin{bmatrix} x_{1,n}x_{2,n} & x_{1,n}x_{3,n} & \cdots & x_{1,n}x_{k,n} & x_{2,n}x_{3,n} & \cdots & x_{k-1,n}x_{k,n} \end{bmatrix} \\
X_{ijl,n} &= \begin{bmatrix} x_{1,n}x_{2,n}x_{3,n} & x_{1,n}x_{2,n}x_{4,n} & \cdots & x_{1,n}x_{2,n}x_{k,n} & x_{2,n}x_{3,n}x_{4,n} & \cdots & x_{2,n}x_{k-1,n}x_{k,n} & x_{3,n}x_{4,n}x_{5,n} & \cdots & x_{k-2,n}x_{k-1,n}x_{k,n} \end{bmatrix}
\end{aligned}
\tag{6-6}
$$

Then one can simply perform the OLS procedure as explained in chapter 5 and calculate the residuals ε and variance σ^2 via Equation (5-75) and Equation (5-78), respectively. Next, a t statistic is used to calculate the significance of of each parameter, via:

$$
t_m = \frac{|\gamma_m|}{\sqrt{(\mathrm{Cov}[\hat{\vec{\gamma}}])_{m,m}}} > t_{crit}, \quad \text{with: } m = 1, 2, \ldots, k \tag{6-7}
$$

With k the number of regressor terms, i.e. the size of $\vec{\gamma}$, and $(\mathrm{Cov}[\hat{\vec{\gamma}}])_{m,m}$ is the m-th diagonal entry of the covariance matrix, i.e. the variance related to regressor number m. The t_{crit} is the t-test statistic based on the degrees of freedom and a certain level of desired significance. If this regressor does not meet the required t_{crit} it may be removed from the global model, for example via a standard backwards regression procedure via the t-test statistic and analysing the regressors by means of half-normal probability plots [33]. When all these steps have been performed a final model remains that describes the flight envelope effects on each of the stability and control coefficients as a function of the factors defining flight condition.

An example of the global model for the stability and control derivative C_{m_q} that has been found via the above procedure (with the CCD structure) is:

$$
\begin{aligned}
C_{m_q} = -25.8 + 0.53 \left(\frac{x}{\bar{c}}\right)_{c.g.} - 0.039h + 9.4 \cdot 10^{-3} V_{TAS} + 5.5 \cdot 10^{-3} m - 3 \cdot 10^{-4} \left(\frac{x}{\bar{c}}\right)_{c.g.} h - \ldots \\
\ldots - 3.8 \cdot 10^{-5} \left(\frac{x}{\bar{c}}\right)_{c.g.} V_{TAS} + 1.8 \cdot 10^{-5} h V_{TAS} - 1.3 \cdot 10^{-7} V_{TAS} m - 3.9 \cdot 10^{-6} V_{TAS}^2 + \ldots \\
\ldots + 1.7 \cdot 10^{-6} m^2 + 2.3 \cdot 10^{-7} \left(\frac{x}{\bar{c}}\right)_{c.g.} h V_{TAS} - 1.5 \cdot 10^{-4} \left(\frac{x}{\bar{c}}\right)_{c.g.} m
\end{aligned}
$$

Such an equation exists for every stability and control derivative in Equation (6-1), which in turn exists for all six force and moment equations. These together comprise the full global model for this method.

6-2-2 Application of DOE Methods to Flight Envelope Testing

Whatever the accuracy of the DOE model may be relative to other methods (as discussed below) there is one main advantage of the DOE methods as FFD and CCD: it is a manner of collecting data in the most *efficient* manner. This means: with only limited measurement points in the experiment design space (in this case the flight envelope) collect as useful data as possible [33]. In [43], both the FFD and CCD designs have been applied to the same region of the flight envelope of the F-16 and are compared in their performance.

The principle of the FFD and CCD is practically choosing measurement points such that the most individual contribution of each of the regressors become clear, i.e. a certain form of orthogonality. The manner in which this can be achieved becomes clear via Figure 6-1.

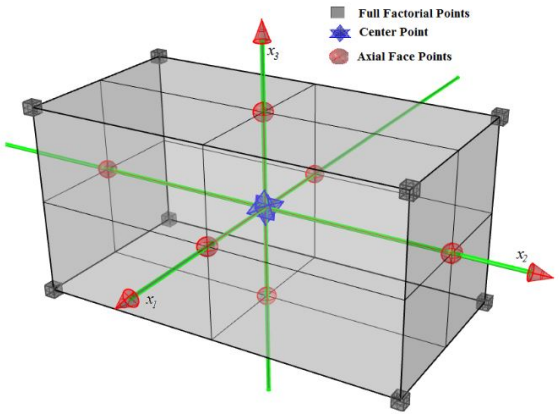

Figure 6-1: Overview of the measurement point designs of an 2^3 FFD and CCD DOE method [43].

For the FFD, the measurement points consist of the vertices of a 3D "box" and the center point. Here also the orthogonality becomes clear: at any measurement point, there exists a measurement point which is at the same location except for one of the factors, thus the effect due to that sole factor is known. The CCD makes use of the same points as the FFD but also includes measurements at the middle of the faces, such that any higher order effects can be modeled better. In the case of the factors h, V_{TAS}, m and $\left(\frac{x}{c}\right)_{c.g.}$ [43] has 20 measurement points (16 vertices of the 4D cube and 4 times the center point) and the CCD has these points and additionally 8 axial face points.

It was found that for the FFD did not provide satisfactory results for the F-16 modeling, especially because of lacking quadratic curvature modeling when tested at the center points. Therefore the CCD was chosen. This model is compared to the OFM method further below.

When analysing Figure 6-1 an important feature is that the measurement points together make a square surface. As known, the flight envelope is not square and as such the question may come to mind how applicable DOE methods actually are to come to a global model of the *entire* flight envelope. In [43] the application of the CCD design to the flight envelope is visualised in Figure 6-2.

Indeed from this figure, it becomes clear the DOE method may only have a somewhat limited applicability as a full global model that is valid in the entire flight envelope. Luckily, in

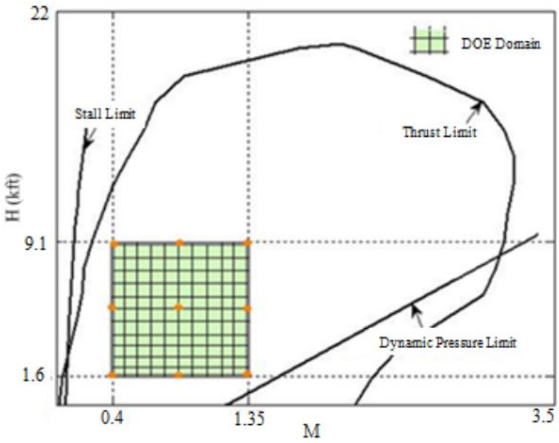

Figure 6-2: Application of the CCD to the F16 flight envelope [43].

other research by [53] the applicability of the CCD and other extended DOE designs has been evaluated in a case study of part of the flight envelope of the F16 aircraft to find the effect of active control of synthetic jets on the buffet caused by the F16's targeting pod at its ventral fin. The DOE design types related to the flight envelope and the baseline model used to compare their performance are given in Figure 6-3.

The following four cases are investigated.

- *Baseline experiment (324 test points).* The baseline experiment consists of the most legacy type of flight testing: performing measurements in a grid, consistently spaced along the edges of and at regular intervals within the flight envelope. This is a very intensive manner of testing, but delivers the most amount of data.
- *Central composite design (54 test points).* As already discussed the CCD requires measurements on the vertices but adds the central points. In this case the axial central points are not exactly placed on an edge to gather more info outside of the square box. An extra point was added in a particularly interesting region, too, also resulting in a CCD+1 design. This is a flexibility that the CCD design allows.
- *Face-centered central composite design (54 test points).* An extended version of the CCD, the FCD has the benefit that the axial points can be placed even more remotely from the rest of the design, including additional smaller designs that can be combined to get measurements from an even wider range within the envelope.
- *Embedded face-centered central composite design (108 test points).* The embedded design allows for placing a design within the other that allows for modeling with third order polynomials, while the CCD and FCD only allow for second order. This may improve performance of the model even further.

By means of statistical tests it was found that either design would come to the same conclusion that the synthetic jets did not have a significant effect on the vibrations of the ventral fin. When investigating the statistical power it *was* found that the highest power was still achieved

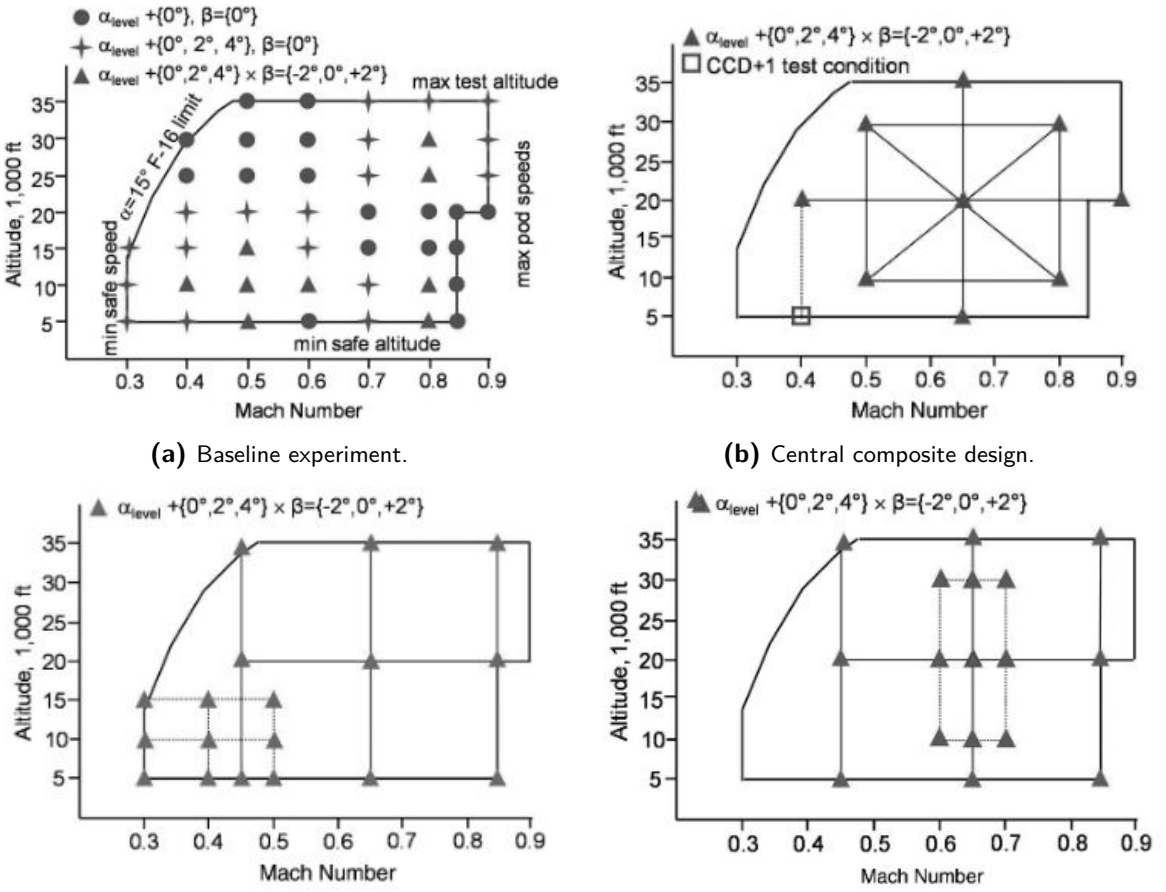

(a) Baseline experiment.

(b) Central composite design.

(c) Face-centered central composite design.

(d) Embedded face-centered central composite design.

Figure 6-3: Overview of the application of different DOE types to the F16 flight envelope [53].

by the baseline model. But, the other designs have an enormous lower impact on testing resources.

Even though the findings by [53] do not give any conclusion on the performance of aerodynamic models found by DOE methods, it *does* prove that DOE methods can be made flexible enough to gather data efficiently throughout larger parts of a flight envelope, ultimately helping to further any global modeling effort.

6-2-3 Comparison of the DOE Method with the OFM Method

The results of [44] indicate that the DOE approach to flight envelope modeling results in a feasible model for a significantly large part of the envelope (with the design factor ranges of $V_{TAS} = 500 - 1500$ ft/s, $h = 5000 - 30000$ ft, $m = 636 - 836$ slug, $\bar{x}_{cg} = 20 - 30$ %).

The final model is the CCD model from [43] and this model is compared this model to the F-16 global model from [34] as discussed above for verification. Validation was performed by using the new model and comparing it to the existing F-16 simulator model that makes use of the common tabular modeling. The DOE model showed comparable performance to the

global model by Morelli and both have high qualitative accuracy and can acquire reasonable quantitative accuracy.

For the CCD method, the found stability and control derivatives differed less than 6% from the tabular value for one coefficient and less than 2% for all other derivatives. This is reasonable performance as a model for further use in research models, however not as good for use in e.g. flight training. The primary finding is that the DOE method *is* a method that can result in satisfying global models with significantly less flight testing, where the aircraft behaviour is described by flight envelope parameters.

6-3 Global Aerodynamic Modeling with Multivariate Splines

The DOE method as described above may thus acquire relatively good fits by using the defined polynomial. However the polynomials have one significant disadvantage which is that they often provide accurate global approximations but at the same time have difficulties approximating local features, especially when these features acquire a significant degree of nonlinearity. Even with the significant complexity that the polynomials possess for the stability and control derivatives. To counter this one can make use of spline functions which are piecewise defined polynomials on distinct pieces of a certain factor's space. This makes it possible to use simpler polynomials that are able to approximate local nonlinearities very well, while the combined set of polynomials also acquire great global performance. A specific type of spline is the multivariate simplex spline, which was applied to perform global modeling of an F-16 in [8], which is further explained below.

Additionally, multivariate splines have the ability to fit very well to scattered datasets by forming an applicable triangulation [1] (see further below), making them particularly useful for flight data as this often is very scattered as it is of course not gathered in a controlled experiment environment.

6-3-1 Mathematical Description of the Multivariate Simplex B-Spline

A mathematical description of the multivariate simplex spline is given below.

Introduction to Simplex Splines

The individual spline pieces of the simplex spline are defined on simplices. A simplex is defined as follows. When V is a set of $n+1$ unique, non-degenerate points in n-dimensional space:

$$V = \{v_0, v_1, \ldots, v_n\} \in \mathbb{R}^n \tag{6-8}$$

The the convex hull of V is the n-simplex t:

$$t = \langle V \rangle \tag{6-9}$$

Any point x inside and outside the simplex can be defined by the simplex's own normalized barycentric coordinate system, which is a weighted vector sum of the simplex vertices. The barycentric coordinate $b(x) = (b_0, b_1, \ldots, b_n)$ of point x with respect to simplex t are the weighted vertices:

$$x = \sum_{i=0}^{n} b_i v_i = b_0 v_0 + b_1 v_1 + \ldots + b_n v_n, \quad \text{with } \sum_{i=0}^{n} b_i = 1 \tag{6-10}$$

The polynomial $p()$ of a simplex spline can be expressed in the so-called B-form. Its derivation starts with the multimodal theorem as defined by:

$$p(b_0, b_1, \ldots, b_n) = (b_0 + b_1 + \ldots + b_n)^d = \sum_{\kappa_0+\kappa_1+\ldots+\kappa_n=d} \frac{d!}{\kappa_0!\kappa_1! \ldots \kappa_n!} \prod_{i=0}^{n} b_i^{\kappa_i} \tag{6-11}$$

In which κ is the "multi-index" defined as:

$$\kappa = (\kappa_0, \kappa_1, \ldots, \kappa_n) \in \mathbb{N}^{n+1} \tag{6-12}$$

And its 1-norm given by:

$$|\kappa| = \kappa_0 + \kappa_1 + \ldots + \kappa_n = d, \quad \text{with } d \geq 0 \tag{6-13}$$

When making use of the multi-index form this expression can be simplified. The multi-index is governed by the maximum number of permutations of κ, namely $\hat{d}$:

$$\hat{d} = \frac{(d+n)!}{n!d!} \tag{6-14}$$

With these properties it is possible to rewrite Equation (6-11) into a simpler form via:

$$\begin{aligned} p(b_0, b_1, \ldots, b_n) = (b_0 + b_1 + \ldots + b_n)^d &= \sum_{\kappa_0+\kappa_1+\ldots+\kappa_n=d} \frac{d!}{\kappa_0!\kappa_1! \ldots \kappa_n!} \prod_{i=0}^{n} b_i^{\kappa_i} \\ &= \sum_{\kappa_0+\kappa_1+\ldots+\kappa_n=d} \frac{d!}{\kappa_0!\kappa_1! \ldots \kappa_n!} b_0^{\kappa_0} b_1^{\kappa_1} \ldots b_n^{\kappa_n} \\ &= \sum_{\kappa_0+\kappa_1+\ldots+\kappa_n=|\kappa|=d} \frac{d!}{\kappa!} b_0^{\kappa_0} b_1^{\kappa_1} \ldots b_n^{\kappa_n} \\ &= \sum_{|\kappa|=d} \frac{d!}{\kappa!} b^{\kappa} \\ &= \sum_{|\kappa|=d} B_{\kappa}^{d}(b) \\ &= 1 \end{aligned} \tag{6-15}$$

With $B^d_\kappa(b)$ the basis function of the multivariate simplex spline. After this the B-form of the multivariate spline becomes:

$$p(b) = \sum_{|\kappa|=d} c_\kappa B^d_\kappa(b) \tag{6-16}$$

In which the c_κ are called the "B-coefficients" of the polynomial, which ultimately are the coefficients that need to be estimated for locally fitting the simplex polynomial to the data. The full vector form notation of this expression for a certain simplex t_j is:

$$p(b(x)) = \begin{cases} B^d(b_{t_j}(x))\vec{c}^{t_j} & \forall\ x \in t_j \\ 0 & \forall\ x \notin t_j \end{cases} \tag{6-17}$$

With:

$$\begin{aligned} B^d(b_{t_j}(x)) &= \begin{bmatrix} B^d_{d,0,0}(b_{t_j}(x)) & B^d_{d-1,1,0}(b_{t_j}(x)) & \cdots & B^d_{0,1,d-1}(b_{t_j}(x)) & B^d_{0,0,d}(b_{t_j}(x)) \end{bmatrix} \\ \vec{c}^{t_j} &= \begin{bmatrix} c^{t_j}_{d,0,0} & c^{t_j}_{d-1,1,0} & \cdots & c^{t_j}_{0,1,d-1} & c^{t_j}_{0,0,d} \end{bmatrix}^T \end{aligned} \tag{6-18}$$

When integrating or differentiating B-spline polynomials one can make use of the following properties:

$$\begin{aligned} \int_t (B^d(b_{t_j}(x))\vec{c}^{t_j})db &= \frac{\mathrm{vol}[t] \cdot n!d!}{(d+n)!} \sum_{|\kappa|=d} c^t_\kappa \\ D^m_u(B^d(b_{t_j}(x))\vec{c}^{t_j}) &= \frac{d!}{(d-m)!} B^{d-m}(b_{t_j}(x)) \cdot P^{d,d-m}(a_{t_j}(u)) \cdot \vec{c} \end{aligned} \tag{6-19}$$

A important aspect of the B-coefficients is that they locally control the shape of the simplex polynomial, at their own unique spatial location within the simplex. This depends on the degree of polynomial used, which gives the total of B-coefficients $\hat{d}$ for this degree polynomial d and dimensions n, given by:

$$\hat{d} = \frac{(d+n)!}{n!d!} \tag{6-20}$$

The location of the specific B-coefficients in the simplex can then be calculated via:

$$b(c_\kappa) = \frac{\kappa}{d} = \frac{\kappa_0 + v_{p_0} + \kappa_1 + v_{p_1} + \ldots + \kappa_n + v_{p_n}}{d}, \quad |\kappa| = d \tag{6-21}$$

The locations of the B-coefficients form a structure which is called the "B-net". Effectively, introducing a higher degree d for a certain simplex polynomial introduces more B-coefficient location effectively increasing the "resolution"[1] of the B-net, through which better fits of the

[1] Even though the term "resolution" is cognitively logical for the structure of the B-net with increasing the degree d, it actually is a false term as the polynomial is continuous and not discrete. "Density" might also be a term used to describe this phenomenon.

polynomial to a certain shape can be acquired. A convention for the orientation of the B-net is agreed upon, in which the B-coefficient with the highest multi-index (i.e. $c_{d,0,0}$) is located at the vertex with the lowest index (i.e. v_0) and vice versa (i.e. $c_{0,0,d}$ at v_n).

Linear Regression with Simplex Splines on a Single Simplex

A useful property of the simplex splines it that is is possible to perform linear regression to fit it to some sort of dataset. The regression of a simplex spline consists of eight steps, explained below.

1. Let one have a set of measurements on the points $\vec{x}$ with values $\vec{y}$. This may be scattered data. The size of $\vec{x}$ is the number of measurements m by the dimension n, and $\vec{y}$ consists of m measurements:

$$\vec{x} \in \mathbb{R}^{m \times n}, \quad \vec{y} \in \mathbb{R}^{m \times 1} \tag{6-22}$$

2. Define a set of $n+1$ vertices as in Equation (6-8):

$$V \in \mathbb{R}^{n+1 \times n} \tag{6-23}$$

3. Define simplex t as the convex hull of V, as in Equation (6-9). A particular choice of V is better than the other, however V may be chosen freely. In mathematical terms:

$$t = \langle V \rangle \tag{6-24}$$

4. Perform a data membership search, i.e. checking which data points x are inside of simplex t. The MATLAB function `tsearchn()` is able to perform this and return the barycentric coordinates of those points. Mathematically one is looking for:

$$\vec{x} \in t \tag{6-25}$$

5. Transform all point inside t to barycentric coordinates. As mentioned, the MATLAB function `tsearchn()` is able to perform this operation. Mathematically:

$$b = b_{t_j}(x_i) \tag{6-26}$$

6. Formulate the simplex polynomial structure in B-form. For one simplex this can be performed by choosing degree d, getting a structure as in Equation (6-17):

$$p(x) = B^d(b_{t_j}(x))\vec{c}^{t_j} \tag{6-27}$$

7. Create the sorted B-form regression matrix for all measurements $m = 1, 2, \ldots, M$, as in Equation (6-18):

$$B = \begin{bmatrix} B^d_{d,0,0}(b(1)) & B^d_{d-1,1,0}(b(1)) & \cdots & B^d_{0,1,d-1}(b(1)) & B^d_{0,0,d}(b(1)) \\ B^d_{d,0,0}(b(2)) & B^d_{d-1,1,0}(b(2)) & \cdots & B^d_{0,1,d-1}(b(2)) & B^d_{0,0,d}(b(2)) \\ \vdots & \vdots & \ddots & \vdots & \vdots \\ B^d_{d,0,0}(b(M)) & B^d_{d-1,1,0}(b(M)) & \cdots & B^d_{0,1,d-1}(b(M)) & B^d_{0,0,d}(b(M)) \end{bmatrix} \tag{6-28}$$

8. Formulate the OLS estimator for the estimated B-coefficients $\hat{\vec{c}}$ as described in chapter 5:

$$\hat{\vec{c}} = \left(B^T B\right)^{-1} B^T \vec{y} \tag{6-29}$$

Making use of the quite straightforward OLS estimator one can fit the polynomial of chosen degree d to the data.

Continuity of Simplex B-Spline Polynomials

Even though it is thus possible to fit one simplex spline polynomial to one simplex's data, for large spaces where data is available multiple simplices are needed with each their own polynomial. In order to smooth their boundaries one has to choose and enforce a certain continuity order of the different polynomials.

The continuity of simplex B-splines is governed by its continuity equation given by:

$$c^{t_2}_{\kappa_0,m,\kappa_1} = \sum_{|\gamma|=m} c^{t_1}_{(\kappa_0,0,\kappa_1)+\gamma} B^m_\gamma(v_*), \quad \text{for } 0 \leq m \leq r \tag{6-30}$$

With r the desired order of continuity (with $r < d$), γ a multi-index independent of κ and v_* the out-of-edge vertex of t_2, which is the only vertex of t_2 not on the edge of the two adjacent simplices. It is further defined that:

$$\begin{aligned} \kappa_0 + m + \kappa_1 &= d \\ (\kappa_0 + d + \kappa_1) + (\gamma_0 + \gamma_1 + \gamma_2) &= d \end{aligned} \tag{6-31}$$

This equation may not be trivial but can be visualized via the so-called "structure of continuity" in the B-net. See Figure 6-4.

In the figure, three simplices (t_i, t_j and t_k) are shown with their B-net coefficients for polynomials of degree $d = 3$ and continuity order $r = 1$ (first derivative continuity). In such a B-net for this degree and continuity structure, the continuity equation states for, e.g. c^i_{201}, that:

$$c^i_{111} = c^j_{210} b_0(v_a) + c^j_{111} b_1(v_a) + c^j_{120} b_2(v_a) \tag{6-32}$$

In practice, a certain desired continuity requires that the value of a certain B-coefficient c equals the sum of all B-coefficients in the adjacent simplex, contained within the mirrored version of the "sub"-simplex formed from that B-coefficient to the edge of the simplex that is

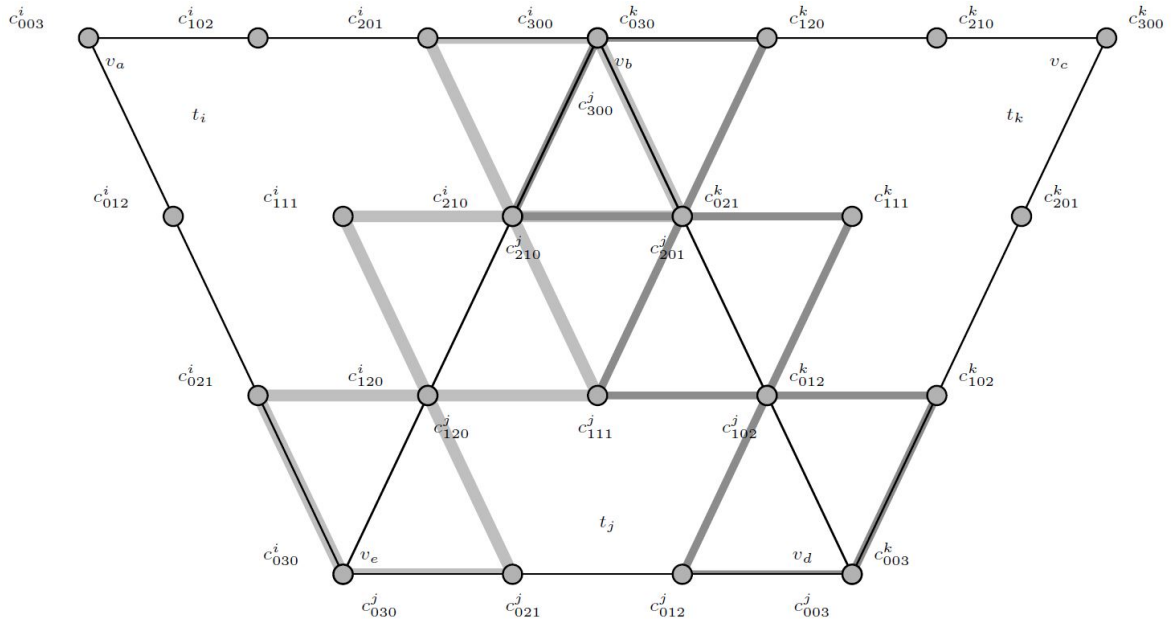

Figure 6-4: B-net for third degree ($d = 3$) basis function on 3 simplices together with first order ($r = 1$) continuity structure [8].

adjacent to it. This sum is then multiplied with the barycentric coordinate of the out-of-edge vertex of that simplex.

The procedure to enforce these continuities is described below, based on the case of Figure 6-4 and Equation (6-32) ($d = 3$ and $r = 1$).

1. Construct the global B-coefficient vector $\vec{c}$:

$$\begin{aligned}\vec{c} &= \begin{bmatrix} \vec{c}^{\,t_i}_{\kappa} \\ \vec{c}^{\,t_j}_{\kappa} \end{bmatrix}_{|\kappa|=d} = \\ &= \begin{bmatrix} c^{t_i}_{3,0,0} & c^{t_i}_{2,1,0} & c^{t_i}_{2,0,1} & c^{t_i}_{1,2,0} & c^{t_i}_{1,1,1} & c^{t_i}_{1,0,2} & c^{t_i}_{0,3,0} & c^{t_i}_{0,2,1} & c^{t_i}_{0,1,2} & c^{t_i}_{0,0,3} & \cdots \\ \cdots & c^{t_j}_{3,0,0} & c^{t_j}_{2,1,0} & c^{t_j}_{2,0,1} & c^{t_j}_{1,2,0} & c^{t_j}_{1,1,1} & c^{t_j}_{1,0,2} & c^{t_j}_{0,3,0} & c^{t_j}_{0,2,1} & c^{t_j}_{0,1,2} & c^{t_j}_{0,0,3} \end{bmatrix}^T \end{aligned} \tag{6-33}$$

2. Write the continuity equation in vector form. First substract the left-hand side of the equation and then rewrite it to vector form:

$$\begin{aligned} c^i_{111} &= c^j_{210} b_0(v_a) + c^j_{111} b_1(v_a) + c^j_{120} b_2(v_a) \\ 0 &= c^j_{210} b_0(v_a) + c^j_{111} b_1(v_a) + c^j_{120} b_2(v_a) - c^i_{111} \\ 0 &= \begin{bmatrix} 0 & \cdots & 0 & -1 & 0 & \cdots & 0 & b_0(v_a) & 0 & b_2(v_a) & b_1(v_a) & 0 & \cdots & 0 \end{bmatrix} \vec{c} \end{aligned} \tag{6-34}$$

3. Compile the complete smoothness matrix H for all of the continuity constraints needed for the desired continuity. In this example this is a row for the coefficients c^i_{201}, c^i_{111}

and c^i_{021} for the first order continuity, but also a row for all the lower order continuities below $r = 1$, i.e. c^i_{300}, c^i_{210}, c^i_{120} and c^i_{030}. Additionally, all rows must be added for *all* edges of *all* simplices in the entire to be modeled domain, and as such H can become significantly large. Then H is multiplied by $\vec{c}$ and set it equal to 0:

$$H \cdot \vec{c} = \begin{bmatrix} \vdots & \ddots & \vdots & \vdots & \vdots & \ddots & \vdots & \vdots & \vdots & \vdots & \vdots & \vdots & \ddots & \vdots \\ 0 & \cdots & 0 & -1 & 0 & \cdots & 0 & b_0(v_a) & 0 & b_2(v_a) & b_1(v_a) & 0 & \cdots & 0 \\ \vdots & \ddots & \vdots & \vdots & \vdots & \ddots & \vdots & \vdots & \vdots & \vdots & \vdots & \vdots & \ddots & \vdots \end{bmatrix} \vec{c} = 0 \tag{6-35}$$

This matrix equation is solely responsible for enforcing the chosen continuity of the spline functions, and is used in the parameter estimation of the entire spline function.

Linear Regression with Simplex Splines on an Entire Triangulation Domain

Above the parameter estimation of a single spline polynomial of one simplex has been discussed. However, the power of the spline function of course lies on an estimation over an entire domain with a (large) number of simlices including a certain enforced continuity.

One starts with the definition of the (entire) multivariate simplex spline:

$$s^d_r(x) = B \cdot \vec{c}, \quad \in S^r_d(T_J) \tag{6-36}$$

In which s^d_r is the simplex spline with degree d and continuity r as a function of a Cartesian coordinate x, B the global regression matrix and $\vec{c}$ the global B-coefficient vector as described for continuity above. The $S^d_r(T_J)$ is defined as the "spline-space" on a triangulation T consisting of J simplices.

An additional step needed for splines is to define the triangulation T_J on which the spline pieces are defined, as described in [9]. The triangulation T is a partitioning of a domain into J non-overlapping simplices, mathematically:

$$T := \bigcup \{t_i,\ i = 0, 1, \ldots, J\} \tag{6-37}$$

A spline space is also described in [9] as being the space of all spline functions s of a given degree d and continuity order r on a given triangulation T. The spline space is defined as:

$$S^r_d(T) := \{s \in r(T) : s|_t \in \mathbb{P}^d, \quad \forall\ t \in T\} \tag{6-38}$$

In which $\mathbb{P}$ is the space of all polynomials of total degree d. The meaning of this spline space is that it is the space that consists of all the degree d spline functions with continuity order r on the triangulation T. The model structure for the regression is, in fact, the spline space itself. This means for a certain model the required choices for model structure are the spline space dimension (which is the dimension of T), spline polynomial degree d and triangulation T.

The global regression matrix B for the spline $s_r^d(x)$ on triangulation T_J is defined as:

$$B = \begin{bmatrix} B_{t_1} & 0 & 0 & 0 \\ 0 & B_{t_2} & 0 & 0 \\ \vdots & \vdots & \ddots & \vdots \\ 0 & 0 & 0 & B_{t_J} \end{bmatrix}, \quad \in \mathbb{R}^{N \times J \cdot \hat{d}} \tag{6-39}$$

In which the B_{t_j} are matrices as defined for one simplex t_j as in Equation (6-28). The number N equals the total number of measurements, which is the number of measurements M for one simplex times the number of simplices J in the triangulation.

In order to perform an parameter estimation that not free but subject to the continuity condition $H\vec{c} = 0$, one can use Lagrangian multiplication to derive the constraint OLS estimator as given by [7]:

$$\begin{bmatrix} \hat{\vec{c}} \\ \hat{\vec{\lambda}} \end{bmatrix} = \begin{bmatrix} B^T B & H^T \\ H & 0 \end{bmatrix}^{-1} \begin{bmatrix} B^T \vec{y} \\ 0 \end{bmatrix} \tag{6-40}$$

In which $\hat{\vec{\lambda}}$ is the estimated Lagrangian parameter vector. As one is not directly interested in these parameters, but only in the B-coefficients $\vec{c}$, it is possible to further simplify Equation (6-40) into the equivalent:

$$\begin{bmatrix} \hat{\vec{c}} \\ \hat{\vec{\lambda}} \end{bmatrix} = \begin{bmatrix} C_1 & C_2 \\ C_3 & C_4 \end{bmatrix} \begin{bmatrix} B^T \vec{y} \\ 0 \end{bmatrix} \tag{6-41}$$

Through which follows that the OLS estimator for the B-coefficients is defined as:

$$\hat{\vec{c}} = C_1 B^T \vec{y} \tag{6-42}$$

The OLS estimator statistics for the spline functions are related to Equation (5-78), and for the spline functions it is given by [7]:

$$\begin{aligned} \text{Cov}\left[\hat{\vec{c}}\right] &= C_1 \\ \text{Var}\left[\hat{\vec{c}}\right] &= \text{Diag}[C_1] \end{aligned} \tag{6-43}$$

The covariances can then be used to perform an analysis on the reliability of the estimation, just as has been performed in chapter 5.

Constructing an Applicable Triangulation of Simplices

Before estimation of the spline function the triangulation of simplices needs to be defined. The process to create a valid triangulation is explained in [9]. The definition of a triangulation was given in Equation (6-37) as:

$$T := \bigcup \{t_i,\ i = 0, 1, \ldots, J\}$$

In a valid triangulation the simplices a defined such that any simplex does is not within the convex hull of other simplices:

$$t_i \cap t_j \in \{\%_0, \tilde{t}\}, \quad \forall t_i, t_j \in T \tag{6-44}$$

Where $\tilde{t}$ is a k-simplex with $0 \leq k \leq n-1$. An often used technique is the Delaunay triangulation but it was found that when using this on the gathered flight data of the Cessna Citation this leads to numerical instability in the estimated simplex polynomials. Therefore a simpler but powerful method has been developed in [6]. This has for now not been further studied.

6-3-2 Using Simplex Splines for Global Aerodynamic Modeling

The use of multivariate splines for estimating a global model as explained above was performed for an F-16 in [8]. A modeling by use of multivariate splines versus a polynomial fit this was performed for the C_X, C_Z and C_m coefficients of the F-16 for a number of large-amplitude manoeuvres.

The model structure for the polynomial (for all three longitudinal aerodynamic coefficients) was assumed as:

$$\begin{aligned} F_p(\alpha, \beta, \delta_e, \delta_{lef}, q) = C_0 + C_\alpha \alpha + C_{\alpha^2}\alpha^2 + C_{\alpha^3}\alpha^3 + C_{\alpha^4}\alpha^4 + C_{\alpha^5}\alpha^5 + \ldots \\ \ldots + C_\beta \beta + C_{\beta^2}\beta^2 + C_{\beta^3}\beta^3 + C_{\beta^4}\beta^4 + C_{\beta^5}\beta^5 + \ldots \\ \ldots + C_q \frac{q\bar{c}}{V} + C_{\alpha q}\alpha\frac{q\bar{c}}{V} + C_{\delta_e}\delta_e + C_{\delta_{lef}}\delta_{lef} \end{aligned} \tag{6-45}$$

And the structure for the multivariate splines as:

$$\begin{aligned} F_s(\alpha, \beta, \delta_e, \delta_{lef}, \frac{q\bar{c}}{V}) = f_1(\alpha, \beta, \delta_e) + f_2(\alpha, \beta) \cdot \delta_{lef} + f_3(\alpha) \cdot \frac{q\bar{c}}{V} + f_4(\alpha) \cdot \frac{q\bar{c}}{V}\delta_{lef} = \\ = \begin{bmatrix} B_1 & B_2\delta_{lef} & B_3\frac{q\bar{c}}{V} & B_4\frac{q\bar{c}}{V}\delta_{lef} \end{bmatrix} \begin{bmatrix} \vec{c}_1 & \vec{c}_2 & \vec{c}_3 & \vec{c}_4 \end{bmatrix}^T \end{aligned} \tag{6-46}$$

After which the regression procedure was applied as explained above. The results showed significant decreases in RMS values, and thus increase in model quality from the polynomial model to spline model (C_X: 4.77 vs. 0.43, C_Z: 0.89 vs. 0.50 and C_m: 2.30 vs. 0.35), indicating the superior performance of the multivariate spline in global modeling over the ordinary polynomial, especially when significant nonlinearities are present.

The same method was also applied to the TU Delft Citation II in [9] and validated in [10]. In [9] actual flight test data gathered by the Citation was used to develop a global model for the same aircraft. The selected model structures for the aerodynamic coefficient were:

$$\begin{aligned} C_X &= f_X(\alpha, \delta_e, M), \quad \in S_3^1(T_X) \\ C_Z &= f_Z(\alpha, \delta_e, M), \quad \in S_3^1(T_Z) \\ C_m &= f_m(\alpha, q, \delta_e), \quad \in S_3^1(T_m) \\ C_\ell &= f_\ell(\alpha, \beta, p, r, \delta_a), \quad \in S_3^1(T_\ell) \\ C_n &= f_n(\alpha, \beta, \delta_r), \quad \in S_3^1(T_n) \end{aligned} \tag{6-47}$$

The model structure selection process was performed by a simple algorithm explained via the pseudo-code below.

1. Select a set of model dimensions D organized in order of relevance, based on model insight.
2. From the set D, select an active set to initialize the identification process.
3. Identify a $d = 1$ model on a triangulation T consisting of a simple simplex.
4. Increase the degree d by one and check if the performance of the modeling has increased. If not, stop increasing the degree and continue.
5. Increase the resolution of the triangulation T, then re-perform the previous step of increasing degree d.
6. If both increasing degree d or resolution of the triangulation does not increase performance, additional dimensions should be added to the active set, then repeat the above two steps. If this does not increase the performance the added dimension is deleted again.
7. The optimization stops when a desired performance has been achieved or when the simplices in the triangulation have become so small that the matrix $\begin{bmatrix} B^T B & H^T \\ H & 0 \end{bmatrix}$ becomes singular.

The performance of the model for C_Z, C_m and C_ℓ was around 2% $RRMS$ but the performance for C_X and C_n was slightly lower around 7% and 5%, respectively. It shows the splines are actually significantly capable in modeling the aircraft global behaviour, and the main drawbacks are due to inadequate filling of some simplices with data and lack of excitation in some axes (i.e. for C_n).

The model as developed was validated for the identified spline function of the C_m coefficient, in [10]. Two validation methods were used, the first by analysing model residuals and the second by the estimated variances of the B-coefficients.

First the model output was compared to a validation dataset not used for and independent from the data used for model identification. The error is then given by:

$$\varepsilon_m(\alpha, q, \delta_e) = C_{m,\text{measured}} - f_m(\alpha, q, \delta_e) \tag{6-48}$$

Then Chebyshev's inequality can be employed to calculate the confidence bound of the residuals, which states about the standard deviation for the error ε_m of the model that:

$$P(|\varepsilon_m - \mu| \geq k\sigma) \leq \frac{1}{k^2} \tag{6-49}$$

For the mean μ of the error and with k an integer. For the error the bounds were calculated with $k = 4$ for 1300 subregions and then these were modeled by a spline function f_{bound} of the same degree as f_m. This function showed that the model quality was lowest around the edges of the domain, especially for $q < -4$ and $q > 4$.

The second method of analysis comprises the expected variances and coviariances of the expected parameters, as earlier explained for OLS in chapter 5. These are given by Equation (6-43). The Cramér-Rao Lower Bound $CRLB$ for the B-coefficients are then given by:

$$CRLB\left[\hat{\vec{c}}\right] \geq \text{Var}\left[\hat{\vec{c}}\right] \tag{6-50}$$

As is known, the B-coefficients have each their own spatial location on the B-net, such that also the $CRLB$ can be visualised by a function f_{CRLB} over the domain. This function primarily shows high bounds for the region bounded by $\alpha < -2$ and $q < -3$ and the region bounded by $\alpha > 4$ and $q > 4$, which can be explained by the fact that there are only lower amounts of data in those regions.

The method explained above also has broader applications outside normal aerodynamic model identification in control design like nonlinear dynamic inversion controllers. As model quality is of very high importance for the proper design of these controllers the simplex spline is a powerful tool in making this possible [51]. Even when aerodynamic uncertainties are introduced the modeling power of the spline proves its worth also when considering adaptive control [50].

6-3-3 Comparison of the Simplex Spline Method with the OFM and DOE Methods

For the simplex spline models two cases were primarily researched: the global modeling of the F-16 and modeling of the Cessna Citation II. It was found that the $RRMS$ values for the Cessna Citation II were significantly higher than for the F16 model. The percentages also seem relatively high when compared to the $RRMS$ values found in chapter 5 for the stall model, however this is for a very local estimation. Having a global model valid for significantly larger domains with and $RRMS$ around 2% and not higher than 7% for the "worst" fit, counterintuitively argues in favor of the spline function.

One should also keep in mind that this model is based on flight data which is inherently unreliable as it is subject to many uncertainties. It thus makes more sense to compare the simplex spline's performance in the case of the F16, even though this is based on wind tunnel data which is other than the scope of this thesis. Also, it compares more directly with the OFM and DOE methods which also make use of F16 wind tunnel data. If the spline functions perform better on this data it can then also be concluded that the other global modeling types would probably result in an even worse performance than the splines when regarding real flight data of for example the Cessna Citation II.

Making this comparison the strength of the multivariate simplex spline becomes clear immediately: where the OFM and DOE methods achieve a $RRMS$ of "about lower than 10%" (see

earlier in this chapter) and the polynomial type in [8] achieves at the lowest quality 5%, the simplex spline consistently achieves $RRMS$ lower than 1%. This is even with a relatively simple model structure that is only based on one spline function for an entire aerodynamic force or moment equation, where the [34] and [44] need elaborate equations for every stability and control derivative.

6-4 Global Modeling Using Neural Networks

A last manner in which global models can be created is by the use of neural networks. Neural networks might be very valuable as they can not only perform very global fits, but it is also able to estimate the measurement data locally, because the neural network estimation is not necessarily binded to an a-priori model structure that may degrade fit. The neural network prioritizes fit over form, which might be an advantage that also proves valuable if significant local nonlinearities must met modeled in a further global model.

The basic working principle of the neural network consists of nodes in an input layer, output layer and hidden layer(s). Between each of those layers links exists that are each given a certain weight. These relations can be represented in matrix form. The goal is then to tune the weights of the links such that the input and outputs of the neural network converge. Many methods exist to optimize these weights, but the main feature is that the optimization aims to minimize the difference between the predicted outcome of certain changes in weights and the available measurements.

As mentioned, many different types of neural network optimization techniques exist. The most extensively used methods are the feed forward neural network and the recurrent neural network. The largest difference in the two is that the feed forward approach is a pure "black box" that gives no insight whatsoever in the structure of the model, whilst the recurrent approach is able to work partly with explicit parameter estimation [45].

For example, the research by [29] and [60] aim to use the high approximating power of the feed forward neural network by letting go of any a-priori model structure for the global modeling of the longitudinal behaviour of the F16 aircraft. E.g. in [60] it was found that the neural network estimates a model which has high correspondence with the F16 aerodynamic database, even for angles of attack up to 30 [deg].

The research by [45] uses the recurrent neural networks to estimate actual parameters of a defined model structure, and is able to find parameters that equates the approximating power of conventional methods. A drawback is that the recurrent neural network is limited by a maximum number of neurons that may hinder further approximating power. A solution to this is given by [17] which uses an extension of the feed forward method but with implemented a-priori knowledge such that still explicit parameters can be estimated. It also finds comparable accuracy to conventional methods.

More recent research making use of modeling techniques using neural networks is also focused on stall conditions and the nonlinearities that occur in that region. And example is [52], that performs both a feed forward and recurrent neural network global modeling of lift and drag during stall with different optimization algorithms on data from the entire envelope of a Level D CRJ700 simulator. Both models are very successful in modeling the nonlinear and even the stall hysteresis behaviour in the stall with average Mean Absolute Relative Error

($MARE$) relative to validation data from the simulator of at most 0.53%, which is highly accurate. However, of course there is no explicit model structure that governs this behaviour due to the "black box" nature of the models.

Even thought the literature gives an indication that neural networks may be a good method to perform global modeling, it is decided to not consider it further for this thesis. A large disadvantage is that the neural network is that if one want to use it to its full potential, it will be a "black box" that does not give sufficient insight into the analytics of the model. In this thesis the fundamentals of the nonlinear behaviour and estimates of the parameters are valued as these give better insights into the behaviour of the aircraft in stall. A more transparent estimation method gives this valuable information about the manner the parameters are estimated and is therefore preferred. On the other hand, using neural networks that *do* incorporate a-priori knowledge does not seem to significantly improve estimates that can also be found with conventional methods.

6-5 Conclusion on the Applicability of Global Aerodynamic Modeling Methods to Stall Modeling

As can be concluded from all described methods above it is very much possible to achieve the goal of global modeling: finding more simple models that globally describe the aircraft behaviour throughout the entire flight envelope but do not deteriorate on the local domain.

However a question that is not disregardable is the following: how applicable *are* global modeling methods to model the stall in "the entire flight envelope"? This depends on two factors.

The first factor is how applicable the methods are with regard to the independent variables that are at the basis of the global model and the added value such a global model thus would have for stall modeling. For the OFM method the main independent variables for the global part of the model are α, β, δ_r and δ_e. For the DOE model the variables are h, V_{TAS}, m and $\left(\frac{x}{\bar{c}}\right)_{c.g.}$. Last, for the multivariate splines the global independent variables are α, β, δ_e, δ_a, δ_r, p, r and M. Which of these independent variable are expected to have a significant effect on the Kirchoff parameters? The most dominant variable would be α, but the stall angle of attack is given for a certain flight condition which would remove it from the global model. The same reasoning applies to any variable regarding the velocity of the aircraft and connected to this its mass and *c.g.* location. Of the control inputs only the wing control surfaces δ_a might have significant effect, but research on this and lateral stall behaviour was still being performed by [11] during writing this thesis. Then only altitude and maybe the pitch and yaw rate would remain, but the effect of the latter two could only be reasearched with data on highly dynamic stalls which is not available for the Cessna Citation. Would global modeling then have any added value if the only one significant independent variable h remains? That could constitute a high effort for only a very limited output.

The second factor is twofold. First, research performed in preparation of the research of [58] included a very simple linear estimation of the Kirchoff parameters estimated for each of the runs in the data as a function of altitude. Two main conclusion could be drawn from this data. First, the effects found were not very significant, but secondly and more importantly the large variance of parameters estimated on roughly the same altitude could only lead to

the conclusion that such a estimation would not be reliable at all. The only fix that would be somewhat attainable is by including data from no-boom flights (as discussed in chapter 3) to have more data on more different altitudes. But this in itself has two quirks: it would not solve but may only increase the variance of data making the estimates even more unreliable and as was found in chapter 4 the UKF filtered no-boom data has many issues related to its own reliability, which would have to be researched which would demand a significantly deeper study into the UKF than allocated for the scope of this thesis.

In conclusion, the goal to create a form of global model for the Kirchoff-based stall model might very well turn out to be a very costly effort with use of complex global modeling methods for an added value that may only include a global model that has contains only one or two independent variables that make the complexity of the global modeling techniques almost superfluous. This combined with the expectation that there is a very high risk that there may not even be a demonstrable, let alone statistically relevant, effect of global independent variables on the Kirchoff parameters seems to lead to the somewhat unsatisfying conclusion that global modeling of the Cessna Citation in the stall is not a research topic worth pursuing.

Chapter 7

Preliminary Results and Research Proposal

In this chapter the literature and preliminary research as discussed in the previous chapters is reviewed. Possible research directions that follow from are taken under consideration and one is chosen. This is done in the first section. Thereafter, some preliminary results are shown that aim to substantiate the chosen direction. This chapter concludes with the final research proposal consisting of the research objectives and research question.

7-1 Considerations on Promising Research Directions

From all previous chapters four main possible research directions could be distilled. They are mentioned and explained below.

- *Global modeling of the stall-related X parameters.* This has been extensively discussed in chapter 6. The advantage of a global model would be that a relatively simple model structure could also approximate the actual aircraft behaviour locally quite well. Different methods of global modeling are possible, each with its own strong points. A drawback of global modeling techniques is however that the applicability to stall modeling only seems to be very limited. Also from earlier research related to [58] it was found that the spread of data at specific altitudes places question marks at the reliability of this data. Also, global modeling would require a need of significant data points throughout the flight envelope that, for PH-LAB data, requires the use of no-boom data of which its reliability is not yet quantified.

- *Evaluation and reliability of the no-boom data.* This immediately brings the second research option to light, which is an evaluation of the reliability of no-boom data. Especially as it is more widely available for the PH-LAB than just the stall data.

However, the question is if this would overcome the expected lesser quality of the no-boom data. In chapter 4 a preliminary comparison has been done on the boom and no-boom data and it was found that in longitudinal direction the AOA vane data actually is comparable to the boom data. For the lateral direction the AOA vane data is almost useless. A question is whether further significant findings would come up that make researching it worthwhile, especially if global modeling is not researched further.

- *Evaluation and possible improvement of the Unscented Kalman Filter.* During the construction and coding of the UKF as described in chapter 4 it was found that within it are many assumptions that are only slightly substantiated or assumed without significant background information. Also different assumptions are made for example in the research of [54] relative to [57] and relative to [58]. Also sometimes information is for example missing from the massmodel and the standard values are used. Primarily research into some of the UKF settings or noise characteristics could possibly also be improved. However, this would comprise a very significant shift of scope from the intended advances to the actual modeling, especially when it *is* known that the UKF works "well enough" despite its deficiencies.

- *Stall modeling time window slicing accuracy.* This last option was found when investigating the modeling procedure of both [57] and [58] when deciding what time window to choose for the testing of the UKF in chapter 4. Both papers use significantly different settings for the time window used in modeling, where [57] uses only data from the actual stall and is normally around 8 seconds long, whereas that of [58] always contains the approach-to-stall and a time window of about 50 seconds. Both have very different results for the parameter estimates. This could also be attributed to other factors, but it might be interesting to see what the effect actually is. A factor to be investigated is the effect of choosing not only a time window for FPR, but the entire flight -as this might also provide better FPR results- and thereafter only perform time slicing for the parameter estimation. Also no further literature was found when searching for any standardized procedure of time window selection. This, additionally with the conclusions of chapter 2 and chapter 3 that coin the question if actually enough attention is given to the quality and information content of already available signals, rather than making the usual recommendation "that more flight tests should be performed".

The decision was made to focus on the latter of the four research topics. Especially the lack of supporting literature for data slicing techniques and its possible broad application to any general research involving stall model identification are motivations for this choice. Also, with a relatively good and known model structure as developed by [58] it is actually for the first time possible to perform such research on simulated data which makes verification and validation possible, which is not the case when only real data is available. This may further help to find explicit proof for any method that may be applicable to flight data slicing.

7-2 Preliminary Results

In this section a very rudimentary analysis is done on the effect of changing the selected time window on the estimated parameters of the stall model. It is not meant to present any

explanation for the behaviour, nor make any judgement of value on which is better, rather only proof that there *exists* an effect that *can be* investigated. The selected time windows are thus also very extravagant.

The preliminary method to achieve this is by applying the exact same FPR and parameter estimation method as explained in chapter 4 and chapter 5 to two datasets of the same stall that only differ in the selected time window of the data. The first estimation is the same as in Table 5-4 where the time window $t_{window} = 150$ s and the second estimation only contains the actual stall with $t_{window} = 19$ s. To identify the stall the definition from chapter 3 was taken: stall entry is where the stall buffet starts and recovery is where the buffet ends.

The output of both models is given in Figure 7-1. The estimated stability and control derivatives and the performance metrics of the models are given in Table 7-1 and Table 7-2, respectively.

A number of top-level observations are discussed here. First, in Table 7-1 there are many differences between the stability and control derivatives of both cases, although some are relatively close the each other. However, for now these are not further investigated. Second, when looking at the performance metrics of the two cases in Table 7-2 one can see that the comparison model scores significantly worse than the model that used the longer time for identification. However one has to take into account that these metrics are based on two different observation times. Third, even though the shorter observation time model scores lower in performance, when one looks at the time series of the model outputs and the measurements in Figure 7-1, for all except the C_n the comparison model seems to still perform quite well, capturing the most featuring nonlinearities. Even compared to the model of the longer observation time, the model output of the shorter observation time does not show any significantly less behaviour of capturing the nonlinearities during the stall, despite the significantly shorter amount of available data in the short observation time.

The last observation is the very significant difference in X-parameters in Table 7-1, even though the models did not perform very differently during the stall. Parameter α^* seems is the least far off for the four parameters. For extra information on the parameters of the nonlinear estimation, just as in chapter 5 for Figure 5-3, the distribution of the 500 optima that are found with the nonlinear estimation procedure can be plotted for the comparison case. This is done in Figure 7-2. Where Figure 7-2a shows the optima of all 500 initial conditions and Figure 7-2b shows the selected initial conditions that results in an optimum that is within 5% of the lowest cost function found of all initial conditions and their median. This is the case for 49 initial conditions.

In this Figure 7-2 maybe there exists an explanation for some of the differences. When compared to Figure 5-3 only a clear difference can be seen in the parameter distributions of τ_1 and τ_2. The other distributions show no particularly striking differences in features. Especially interesting is the fact that τ_1 seems to "creep" towards the lower constraint boundary of 0.001. Interestingly, in [57], the conclusion was drawn that τ_1 could not be estimated correctly as most of the stalls in the data for that research were quasi-steady, and as such the stall buffet was used to estimate τ_1. But as seen, having a low observation time -as was the case for slicing the data in [57]- may also lead to a situation where the τ_1 estimates goes towards the constraint and becomes somewhat unreliable even for a dynamic stall as was the case for this data. It may be interesting to investigate this further, too, in the further research for this thesis, plossibly by use of the Fisher information for this parameter and the data.

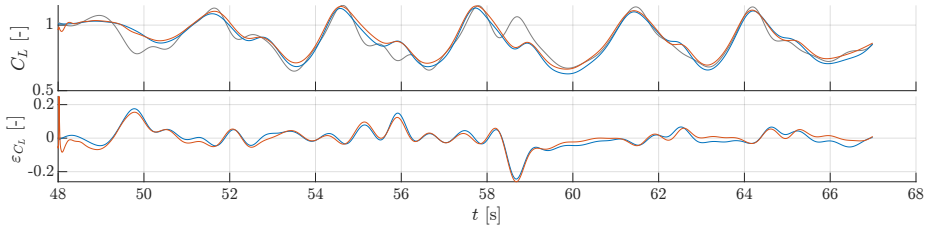

(a) Aerodynamic force C_L.

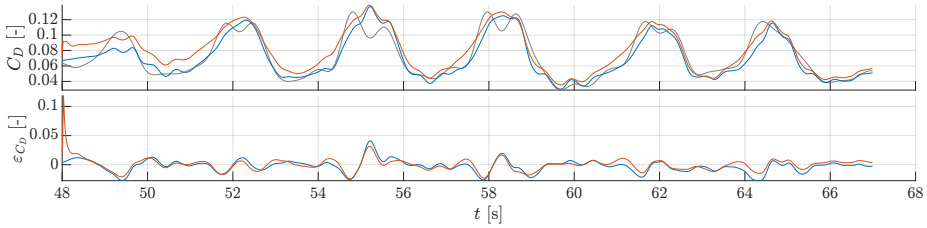

(b) Aerodynamic force C_D.

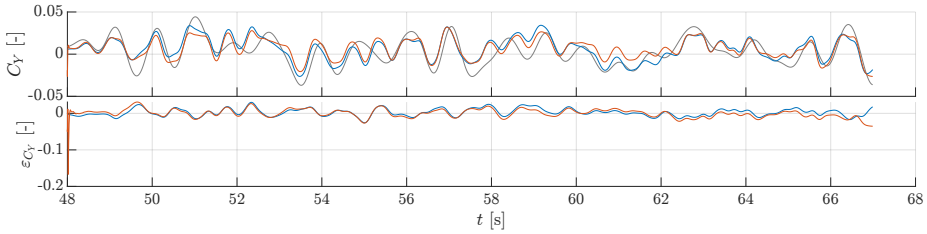

(c) Aerodynamic force C_Y.

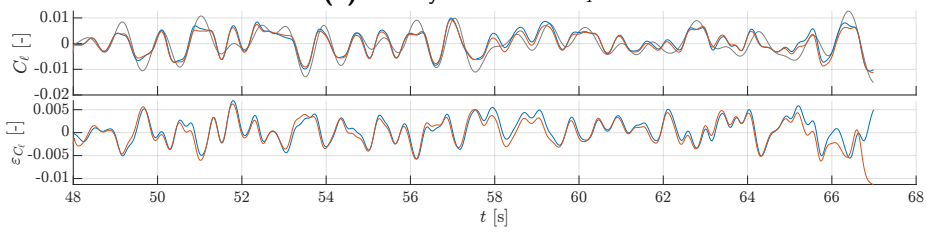

(d) Aerodynamic moment C_ℓ.

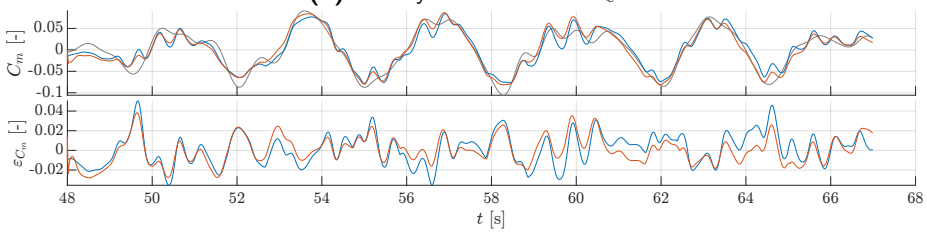

(e) Aerodynamic moment C_m.

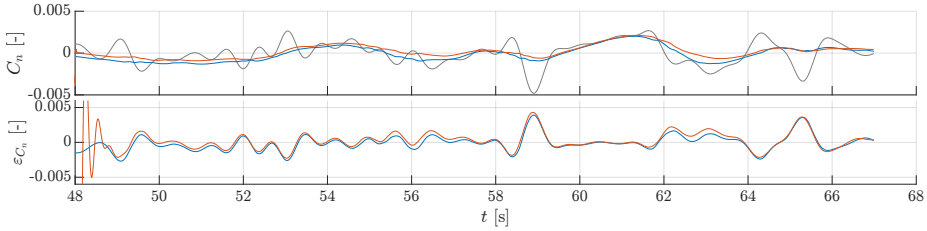

(f) Aerodynamic moment C_n.

Figure 7-1: Local aerodynamic model output and residuals for the comparison cases. Blue is the model output $\hat{\vec{y}}$ for $t_{window} = 150$ s, red the model output $\hat{\vec{y}}$ for $t_{window} = 19$ s and grey is the measurement $\vec{y}$ from the $t_{window} = 150$ s data.

A last note that should be taken into account is that the worse metrics and different results for the parameter estimation may also be partly due to a worse reconstruction for the force and moment measurements. This is because the UKF also performs better over time as it converges. This should also be taken into account in the further research for the final thesis.

7-3 Research Proposal

Based on the considerations described above and the discussed preliminary results, the following is proposed as final goal and the steps toward that goal for the research for the final thesis.

The following main research question is proposed.

> "What is the optimal manner in which to slice and/or partition flight data such that the stall related parameter estimates in a model using Kirchoff's Theory of Flow Separation acquire the highest possible reliability?"

In order to answer the main research question the following steps are proposed to be taken.

1. *Creating simulation data.*
   (a) Use the model structure and found parameter estimates from [58] to adapt the TU Delft Citation DASMAT model, if required. This is will be the baseline model.
   (b) Use the DASMAT model to create clean, unnoised data using these parameter estimates.
   (c) Add a known noise and bias to the simulation data.
   (d) Perform flight path reconstruction using the Unscented Kalman Filter to accurately reconstruct the aircraft states, inputs and measurements such that these can be used in aerodynamic modeling.
   (e) Verify the filtered outputs of the noised data with the original clean data.
2. *Empirical research.*
   (a) Define and select time slicing and independent variable partitioning domains to perform the simulation on, making use of the definition of the stall entry and recovery start as defined in chapter 3.
   (b) Perform parameter estimation on all simulated data runs.
   (c) Evaluate the empirical reliability of the stall-related parameters with the changed data slicing and partitioning by means of statistical methods and tests.
3. *Theoretical research.*
   (a) Find an analytical description for the Fisher information for all six force and moment equations of the model structure of [58].
   (b) Investigate how the Fisher information changes with the slicing and partitioning of the data.

(c) Evaluate the theoretical reliability of the stall-related parameters with the changed data slicing and partitioning by means of the Fisher information.

4. *Optimization method and verification and validation.*

   (a) Compare the results from the empirical and theoretical research.
   (b) Develop an optimized method for data slicing and partitioning that will result in the best stall-related parameter estimates, based on both the empirical simulation and the theoretical Fisher information results, if applicable.
   (c) Verify the method by applying it to the simulated flight data.
   (d) Validate the method by applying it to the real flight data.

5. *Processing real flight data.*

   (a) Slicing and partitioning the data based on the optimization method.
   (b) Perform flight path reconstruction using the Unscented Kalman Filter to accurately reconstruct the aircraft states, inputs and measurements such that these can be used in aerodynamic modeling.
   (c) Perform parameter estimation.
   (d) Compare with results from the simulated data verification.

In Figure 7-3 the above steps have been visualised by means of a flow diagram.

Table 7-1: Parameter estimates in the aerodynamic force and moment equations for the comparison cases.

Model	**Parameter**	**Value $t_{window} = 150$ s**	**Value $t_{window} = 19$ s**
X	a_1	32.0864	24.7044
	α^*	0.2039 rad	0.1983 rad
	τ_1	0.1293 s	0.0012 s
	τ_2	0.0525 s	0.2086 s
Model	**Parameter**	**Value $t_{window} = 150$ s**	**Value $t_{window} = 19$ s**
C_L	C_{L_0}	0.1910	0.2614
	C_{L_α}	4.4832	4.4001
	$C_{L_{\alpha^2}}$	13.6978	13.6919
C_D	C_{D_0}	0.0133	-0.0127
	C_{D_α}	0.1788	0.3899
	$C_{D_{\delta_e}}$	-0.1697	-0.1152
	C_{D_X}	0.0696	0.0391
	$C_{D_{C_T}}$	-0.6073	0.6075
C_Y	C_{Y_0}	0.0070	0.0015
	C_{Y_β}	-0.5605	-0.3087
	C_{Y_p}	-0.5637	-0.2838
	C_{Y_r}	-0.9068	0.2001
	$C_{Y_{\delta_a}}$	-0.2294	-0.2439
C_ℓ	C_{ℓ_0}	-0.0013	-0.0016
	C_{ℓ_β}	-0.0622	-0.0743
	C_{ℓ_p}	-0.1234	-0.0250
	C_{ℓ_r}	-0.0954	-0.0275
	$C_{\ell_{\delta_a}}$	-0.0968	-0.0923
C_m	C_{m_0}	0.0334	0.0465
	C_{m_α}	-0.6014	-0.8307
	$C_{m_{X\delta_e}}$	-0.8784	-0.6672
	$C_{m_{C_T}}$	-0.0511	2.9004
C_n	C_{n_0}	$-9.0476 \cdot 10^{-4}$	$-3.3662 \cdot 10^{-4}$
	C_{n_β}	0.0572	0.0494
	C_{n_r}	0.0024	0.0991
	$C_{n_{\delta_r}}$	-0.0181	0.0121

Table 7-2: Performance metrics of the full parameter estimation for the comparison cases.

Model	**Metric**	**Value** $t_{window} = 150$ **s**	**Value** $t_{window} = 19$ **s**
C_L	MSE	$6.6409 \cdot 10^{-4}$	0.0029
	RMS	0.0258	0.0540
	$RRMS$	2.9512%	7.5959%
	R^2	0.9626	0.8497
C_D	MSE	$1.6805 \cdot 10^{-5}$	$1.1167 \cdot 10^{-4}$
	RMS	0.0041	0.0106
	$RRMS$	0.9897%	2.5856%
	R^2	0.9904	0.8654
C_Y	MSE	$2.5271 \cdot 10^{-5}$	$1.4358 \cdot 10^{-4}$
	RMS	0.0050	0.0120
	$RRMS$	1.7196%	2.5942%
	R^2	0.6256	0.4716
C_ℓ	MSE	$1.1555 \cdot 10^{-6}$	$7.9246 \cdot 10^{-6}$
	RMS	0.0011	0.0028
	$RRMS$	0.6444%	1.7926%
	R^2	0.7207	0.6784
C_m	MSE	$4.3408 \cdot 10^{-5}$	$1.8804 \cdot 10^{-4}$
	RMS	0.0066	0.0137
	$RRMS$	1.4857%	3.0707%
	R^2	0.8514	0.9150
C_n	MSE	$4.8400 \cdot 10^{-7}$	$1.1614 \cdot 10^{-5}$
	RMS	$6.9570 \cdot 10^{-4}$	0.0034
	$RRMS$	0.4334%	1.4225%
	R^2	0.3473	0.0483

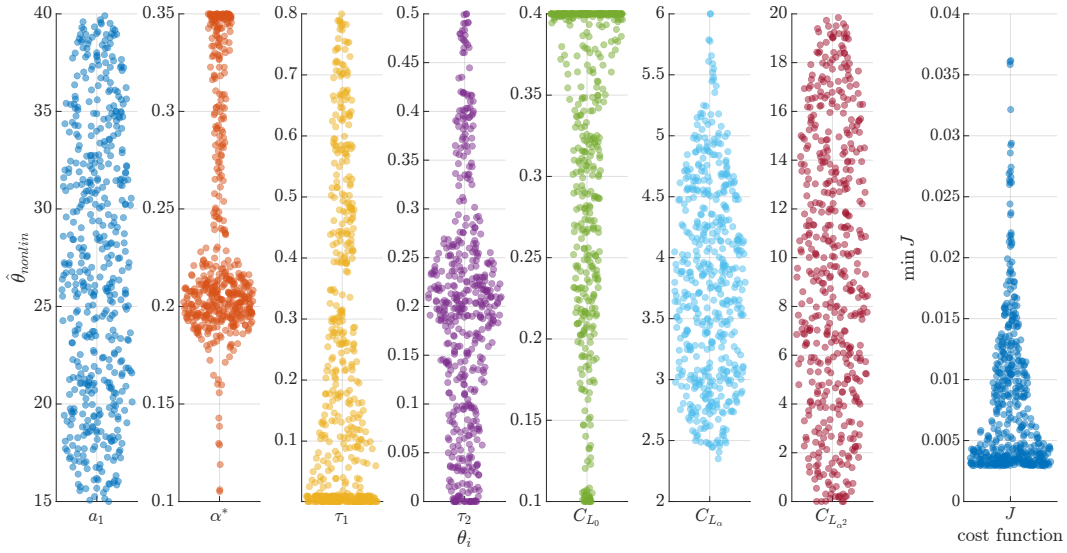

(a) All initial conditions ($n = 500$).

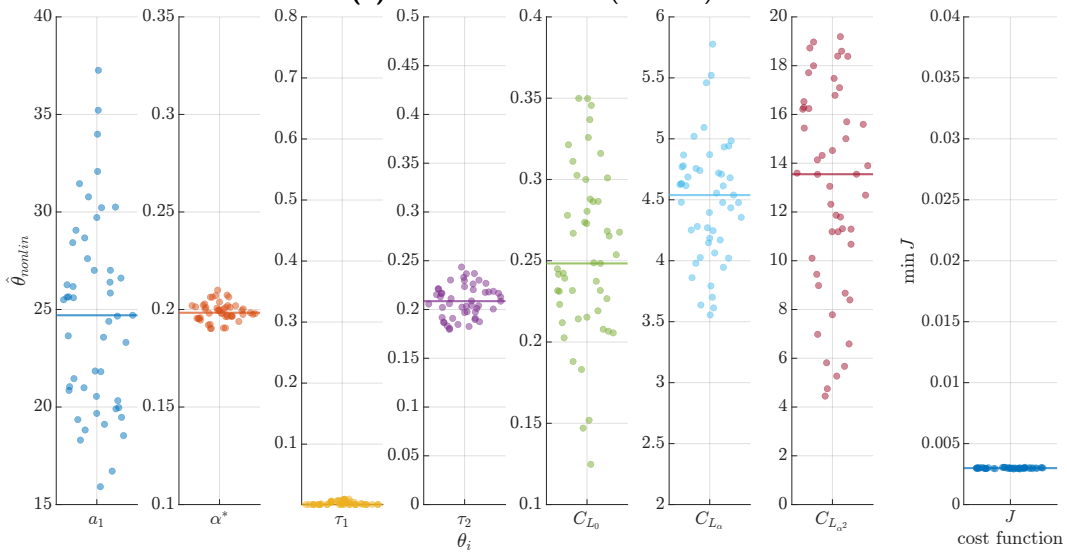

(b) Selected initial conditions ($n = 49$) with median.

Figure 7-2: Distribution of the parameters and cost function values found by the nonlinear estimation procedure for the comparison case where $t_{window} = 19$ s.

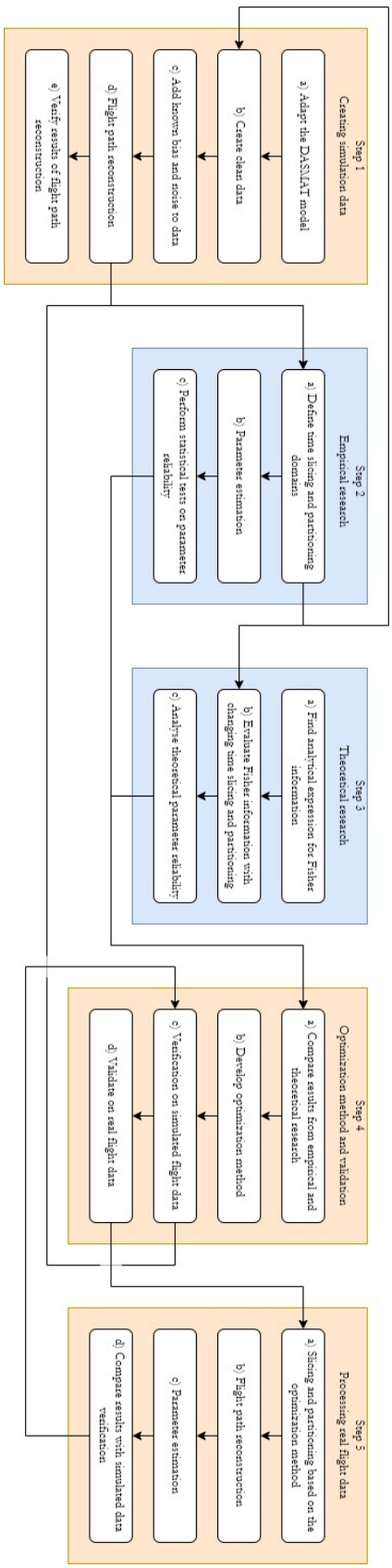

Figure 7-3: Flow diagram of for the research steps in order to answer the main research question.

Chapter 8

Conclusion

This preliminary report serves as the substantiation of the choice of research direction for the final thesis. Based on a review of applicable literature and a preliminary research, the proposed main research question is as follows:

> "What is the optimal manner in which to slice and/or partition flight data such that the stall related parameter estimates in a model using Kirchoff's Theory of Flow Separation acquire the highest possible reliability?"

The relevance of this research question stems from regulation requirements for Upset Prevention and Recovery Training for airline flight crew on Flight Simulation Training Devices. Kirchoff's Theory of Flow Separation has proven to be an applicable method to model the nonlinear behaviour of an aircraft in the stall in previous research, even though deficiencies remain in the models that cannot be solved without more flight tests, according to literature. However, no literature can be found that recommends looking at the *quality* of the data, rather than the *quantity* by doing more flight testing. It can thus be argued that the data that is available is not used in an optimal manner. The concept of Fisher information that is used in flight input design shows promise of also being used in a backwards manner, selecting the data in a manner that its quality increases with respect to the specific parameters related to the stall. The comparative case on using 150 s of data of a stall run versus only the data during the stall of 19 s showed very different results. In between these two timeframes there may be an optimum where the stall parameters achieve their highest reliability and modeling power.

Currently existing methods of Flight Path Reconstruction and parameter estimation techniques can be used. The Unscented Kalman Filter for the Flight Path Reconstruction shows a to-be-expected reliability when used on real flight data, comparative to earlier research. The quality could be improved, but this would require a more thorough investigation into a number of assumptions used in the process. The time and effort to perform this research is expected to be significant and the expected increase in quality of the results only limited. Therefore, the current method is deemed sufficient and more time can be invested in the

research on data slicing and partitioning. The combination of the nonlinear and linear parameter estimation techniques for the identification of the model shows promising results and it is decided to use this method in the to-be-performed research directly.

Other research topics such as a comparison of the usability of data from flights with and without the air data boom installed or research into global modeling methods for the stall parameters are deemed to be of only limited interest. Global modeling techniques are largely unsuitable due to the non-global appearance of the stall in the flight envelope, rendering the methods to be too complicated for only limited application. A research into the reliability of the no-boom data is expected to have a predictably outcome: it is probably significantly worse than the data with the boom. This can be substantiated by results of the Unscented Kalman Filter where the no-boom state estimates and reconstructed measurements show lesser reliability in their innovations than for the data with the boom installed.

All in all, the main research question as proposed should have an interesting, but above all, impactful answer. An answer that may not only show the effect of slicing and partitioning of flight data on the reliability of the parameter estimates, but may even be at the basis of a standardized method of selecting data that does not yet exist in the field of stall modeling.

Bibliography

[1] Gerard Awanou, Ming-Jun Lai, and Paul Wenston. The multivariate spline method for scattered data fitting and numerical solutions of partial differential equations. In *Wavelets and Splines*, pages 24–75. Nashboro Press, 2006.

[2] Max Baarspul. A review of flight simulation techniques. *Progress in Aerospace Sciences*, 27(1):1–120, 1990.

[3] James G. Batterson and Vladislav Klein. Partitioning of flight data for aerodynamic modeling of aircraft at high angles of attack. *Journal of Aircraft*, 26(4):334–339, 1989.

[4] Girish Chowdhary and Ravindra Jategaonkar. Aerodynamic parameter estimation from flight data applying extended and unscented kalman filter. *Aerospace Science and Technology*, 14(2):106–117, 2010.

[5] E.H.P. de Meester. Towards an asymmetric stall model for the fokker 100. Unpublished, 2021.

[6] C.C. de Visser. *Global Nonlinear Model Identification with Multivariate Splines, Application to Aerodynamic Model Identification of the Cessna Citation II.* Delft University of Technology, 2011.

[7] C.C. de Visser, Q.P. Chu, and J.A. Mulder. A new approach to linear regression with multivariate splines. *Automatica*, 45(12):2903–2909, 2009.

[8] C.C. de Visser, J.A. Mulder, and Q.P. Chu. Global nonlinear aerodynamic model identification with multivariate splines. In *AIAA Atmospheric Flight Mechanics Conference*. American Institute of Aeronautics and Astronautics Inc, 2009.

[9] C.C. de Visser, J.A. Mulder, and Q.P. Chu. A multidimensional spline based global nonlinear aerodynamic model for the cessna citation ii. In *AIAA Atmospheric Flight Mechanics Conference*. American Institute of Aeronautics and Astronautics Inc, 2010.

[10] C.C. de Visser, J.A. Mulder, and Q.P. Chu. Validating the multidimensional spline based global aerodynamic model for the cessna citation ii. In *AIAA Atmospheric Flight Mechanics Conference*. American Institute of Aeronautics and Astronautics Inc, 2011.

[11] Alexandre Delfosse, Daan M. Pool, and Coen de Visser. Asymmetric stall modeling of the cessna citation ii aircraft. Unpublished, 2022.

[12] Joaquim N. Dias. Unsteady and post-stall model identification using dynamic stall maneuvers. In *AIAA Atmospheric Flight Mechanics Conference*. American Institute of Aeronautics and Astronautics Inc, 2015.

[13] EASA. Annex i to ed decision 2015/012/r, 2015.

[14] EASA. Certification specifications for aeroplane flight simulation training devices 'cs-fstd(a)', 2018.

[15] D. Fischenberg. Identification of an unsteady aerodynamic stall model from flight test data. In *20th Atmospheric Flight Mechanics Conference*, pages 138–146. American Institute of Aeronautics and Astronautics Inc, 1995.

[16] D. Fischenberg and R.V. Jategaonkar. Identification of aircraft stall behavior from flight test data. In *RTO SCI Symposium in System Identification for Integrated Aircraft Development and Flight Testing*, pages 17.1–17.8. North Atlantic Treaty Organization Research and Technology Organization, 1999.

[17] A.K. Ghosh, S.C. Raisinghani, and Sunil Khubchandani. Estimation of aircraft lateral-directional parameters using neural networks. *Journal of Aircraft*, 35(6):876–881, 1998.

[18] David R. Gingras, John N. Ralston, Ryan Oltman, Chris Wilkening, Robert Watts, and Paul Desrochers. Flight simulator augmentation for stall and upset training. In *AIAA Modeling and Simulation Technologies Conference*. American Institute of Aeronautics and Astronautics Inc, 2014.

[19] D.R. Gingras and J.N. Ralston. Aerodynamics modelling for training on the edge of the flight envelope. *The Aeronautical Journal*, 116(1175):67–86, 2012.

[20] M. Goman and A. Khrabov. State-space representation of aerodynamic characteristics of an aircraft at high angles of attack. *Journal of Aircraft*, 31(5):1109–1115, 1994.

[21] Jared A. Grauer and Matthew J. Boucher. Aircraft system identification from multisine inputs and frequency responses. *Journal of Guidance, Control, and Dynamics*, 43(12):2391–2398, 2020.

[22] Jason Gross, Yu Gu, Srikanth Gururajan, Brad Seanor, and Marcello R. Napolitano. A comparison of extended kalman filter, sigma-point kalman filter, and particle filter in gps/ins sensor fusion. In *AIAA Guidance, Navigation, and Control Conference*. American Institute of Aeronautics and Astronautics Inc, 2010.

[23] IATA. Loss of control in-flight accident analysis report, 2019.

[24] ICAO. Icao doc 10011: Manual on aeroplane upset prevention and recovery training, 2014.

[25] A. Imbrechts, C.C. de Visser, and D.M. Pool. Just noticeable differences for variations in quasi-steady stall buffet model parameters. In *AIAA SciTech 2022 Forum*. American Institute of Aeronautics and Astronautics Inc, 2022.

[26] Simon J. Julier and Jeffrey K. Uhlmann. A new extension of the kalman filter to nonlinear systems. In *Signal Processing, Sensor Fusion, and Target Recognition VI*, pages 182–193. SPIE, 1997.

[27] R. Klees and R.P. Dwight. *Applied Numerical Analysis, Course AE2220-I*. Delft University of Technology, 2020.

[28] Vladislav Klein and Eugene A. Morelli. *Aircraft System Identification, Theory and Practice*. American Institute of Aeronautics and Astronautics Inc, 2006.

[29] Dennis J. Linse and Robert F. Stengel. Identification of aerodynamic coefficients using computational neural networks. In *Aerospace Sciences Meeting and Exhibit*. American Institute of Aeronautics and Astronautics Inc, 1992.

[30] Alexander Ly, Maarten Marsman, Josine Verhagen, Raoul P.P.P. Grasman, and Eric-Jan Wagenmakers. A tutorial on fisher information. *Journal of Mathematical Psychology*, 80(1):40–55, 2017.

[31] Sven Marschalk, Peter C. Luteijn, Dirk van Os, Daan M. Pool, and Coen C. de Visser. Stall buffet modeling using swept wing flight test data. In *AIAA SciTech Forum*. American Institute of Aeronautics and Astronautics Inc, 2021.

[32] Murat Millidere, Samet Uslu, and Tolga Yigit. Full-envelope stitched simulation model of an agile aircraft using lasso technique. In *AIAA SciTech Forum*. American Institute of Aeronautics and Astronautics Inc, 2022.

[33] Douglas C. Montgomery. *Design and Analysis of Experiments*. John Wiley & Sons Inc, 2013.

[34] Eugene A. Morelli. Global nonlinear parametric modeling with application to f-16 aerodynamics. In *Proceedings of the 1998 American Control Conference*, pages 997–1001. Institute of Electrical and Electronics Engineers Inc, 1998.

[35] Eugene A. Morelli. Flight test of optimal inputs and comparison with conventional inputs. *Journal of Aircraft*, 36(2):389–397, 1999.

[36] Eugene A. Morelli. Flight-test experiment design for characterizing stability and control of hypersonic vehicles. *Journal of Guidance, Control, and Dynamics*, 32(3):949–959, 2009.

[37] Eugene A. Morelli. Efficient global aerodynamic modeling from flight data. In *50th AIAA Aerospace Sciences Meeting including the New Horizons Forum and Aerospace Exposition*. American Institute of Aeronautics and Astronautics Inc, 2012.

[38] Eugene A. Morelli. Flight test maneuvers for efficient aerodynamic modeling. *Journal of Aircraft*, 49(6):1857–1867, 2012.

[39] Eugene A. Morelli, Kevin Cunningham, and Melissa A. Hill. Global aerodynamic modeling for stall/upset recovery training using efficient piloted flight test techniques. In *AIAA Modeling and Simulation Technologies (MST) Conference*. American Institute of Aeronautics and Astronautics Inc, 2013.

[40] J.A. Mulder. *Design and evaluation of dynamic flight test manoeuvres*. Delft University of Technology, 1986.

[41] J.A. Mulder, J.C. van der Vaart, W.H.J.J. van Staveren, Q.P. Chu, and M. Mulder. *Aircraft Responses to Atmospheric Turbulence, Lecture Notes AE4304*. Delft University of Technology, 2020.

[42] J.A. Mulder, W.H.J.J. van Staveren, J.C. van der Vaart, E. de Weerdt, C.C. de Visser, A.C. in 't Veld, and E. Mooij. *Flight Dynamics, Lecture Notes AE3202*. Delft University of Technology, 2013.

[43] Ashraf Omran, Drew Landman, and Brett Newman. Global stability and control derivative modeling using design of experiments. In *AIAA Atmospheric Flight Mechanics Conference*. American Institute of Aeronautics and Astronautics Inc, 2009.

[44] Ashraf Omran, Brett Newman, and Drew Landman. Global aircraft aero-propulsive linear parameter-varying model using design of experiments. *Aerospace Science and Technology*, 22(1):31–44, 2012.

[45] J.R. Raol and R.V. Jategaonkar. Aircraft parameter estimation using recurrent neural networks - a critical appraisal. In *AIAA Atmospheric Flight Mechanics Conference*, pages 119–128. American Institute of Aeronautics and Astronautics Inc, 1995.

[46] C. Seren, F. Bommier, L. Verdier, A. Bucharles, and D. Alazard. Optimal experiment and input design for flight test protocol optimization. In *AIAA Atmospheric Flight Mechanics Conference and Exhibit*. American Institute of Aeronautics and Astronautics Inc, 2006.

[47] J. Singh and R.V. Jategaonkar. Identification of lateral-directional behavior in stall from flight data. *Journal of Aircraft*, 33(3):627–630, 1996.

[48] S.C.E. Smets, C.C. de Visser, and D.M. Pool. Subjective noticeability of variations in quasi-steady aerodynamic stall dynamics. In *AIAA Scitech 2019 Forum*. American Institute of Aeronautics and Astronautics Inc, 2019.

[49] Bruno O.S. Teixeira, Leonardo A.B. Tôrres, Paulo Iscold, and Luis A. Aguirre. Flight path reconstruction - a comparison of nonlinear kalman filter and smoother algorithms. *Aerospace Science and Technology*, 15(1):60–71, 2011.

[50] H.J. Tol, C.C. de Visser, L.G. Sun, E. van Kampen, and Q.P. Chu. Multivariate spline-based adaptive control of high-performance aircraft with aerodynamic uncertainties. *Journal of Guidance, Control and Dynamics*, 39(4):781–800, 2016.

[51] H.J. Tol, C.C. de Visser, E. van Kampen, and Q.P. Chu. Nonlinear multivariate spline-based control allocation for high-performance aircraft. *Journal of Guidance, Control and Dynamics*, 37(6):1840–1862, 2014.

[52] Yvan Tondji, Georges Ghazi, and Ruxandra Mihaela Botez. Crj 700 aerodynamic coefficients identification in dynamic stall conditions using neural networks. In *AIAA SciTech Forum*. American Institute of Aeronautics and Astronautics Inc, 2022.

[53] Aaron A. Tucker, Gregory T. Hutto, and Cihan H. Dagli. Application of design of experiments to flight test: A case study. *Journal of Aircraft*, 47(2):458–463, 2010.

[54] M.A. van den Hoek, C.C de Visser, and D.M. Pool. Identification of a cessna citation ii model based on flight test data. In *Fourth CEAS Specialist Conference on Guidance, Navigation and Control*, pages 259–277. Springer, 2017.

[55] C.A.A.M. van der Linden. *DASMAT-Delft University Aircraft Simulation Model and Analysis Tool, A Matlab/Simulink Environment for Flight Dynamics and Control Analysis*. Delft University of Technology, 1998.

[56] Rudolph van der Merwe and Eric A. Wan. The square-root unscented kalman filter for state and parameter-estimation. In *IEEE International Conference on Acoustics, Speech, and Signal Processing*, pages 3461–3464. Institute of Electrical and Electronics Engineers Inc, 2001.

[57] L.J. van Horssen, C.C. de Visser, and D.M. Pool. Aerodynamic stall and buffet modeling for the cessna citation ii based on flight test data. In *2018 AIAA Modeling and Simulation Technologies Conference*. American Institute of Aeronautics and Astronautics Inc, 2018.

[58] Joost B. van Ingen, Coen C. de Visser, and Daan M. Pool. Stall model identification of a cessna citation ii from flight test data using orthogonal model structure selection. In *AIAA Scitech 2021 Forum*. American Institute of Aeronautics and Astronautics Inc, 2021.

[59] Eric A. Wan and Rudolph van der Merwe. The unscented kalman filter for nonlinear estimation. In *IEEE 2000 Adaptive Systems for Signal Processing, Communications, and Control Symposium*, pages 153–158. Institute of Electrical and Electronics Engineers Inc, 2000.

[60] Hussein M. Youssef and Jyh-Ching Juang. Estimation of aerodynamic coefficients using neural networks. In *Flight Simulation and Technologies*, pages 242–245. American Institute of Aeronautics and Astronautics Inc, 1993.

Part III

Appendices to Preliminary Thesis Report

Appendix A

Overview of Stall Test Flights

Table A-1: List of all stall experiment runs in test flight 1 of Table 3-3.

Stall #	$\sim t_{start}$ **[s]**	$\sim h$ **[m]**	**Config**	**Stall type**	**Control input**
1	1700	5700	clean	symmetric	none
2	1780	5700	clean	symmetric	none
3	1950	5700	clean	symmetric	none
4	2080	5700	clean	symmetric	δ_a wiggle, δ_e wiggle
5	2180	5700	clean	symmetric	δ_a wiggle, δ_e wiggle
6	2350	5700	clean	symmetric	δ_a wiggle, δ_e wiggle
7	2500	5700	clean	symmetric	δ_a wiggle, δ_e wiggle
8	2630	5700	clean	symmetric	δ_a wiggle, δ_e wiggle
9	2820	5700	clean	symmetric	δ_a wiggle, δ_e wiggle
10	3000	5700	clean	accelerated 1.1g (r)	none
11	3080	5700	clean	accelerated 1.1g (r)	none
12	3200	5700	clean	accelerated 1.1g (r)	none
13	3300	5700	clean	accelerated 1.1g (r)	none
14	3400	5700	clean	accelerated 1.3g (r)	none
15	3500	5700	clean	accelerated 1.3g (r)	none
16	3600	5700	clean	accelerated 1.3g (r)	none
17	3800	5700	clean	accelerated 1.1g (r)	δ_a wiggle, δ_e wiggle
18	3950	5700	clean	accelerated 1.1g (r)	δ_a wiggle, δ_e wiggle

Table A-2: List of all stall experiment runs in test flight 2 of Table 3-3.

Stall #	$\sim t_{start}$ **[s]**	$\sim h$ **[m]**	**Config**	**Stall type**	**Control input**
19	1550	5700	clean	accelerated 1.1g (r)	δ_a wiggle, δ_e wiggle
20	1670	5700	clean	accelerated 1.1g (r)	δ_a wiggle, δ_e wiggle
21	1830	5700	clean	accelerated 1.1g (r)	δ_r wiggle
22	1930	5700	clean	accelerated 1.1g (r)	δ_a wiggle, δ_e wiggle, δ_r wiggle
23	2030	5700	clean	accelerated 1.3g (l)	δ_a wiggle, δ_e wiggle, δ_r wiggle
24	2130	5700	clean	accelerated 1.3g (r)	δ_a wiggle, δ_e wiggle, δ_r wiggle
25	2230	5700	clean	accelerated 1.3g (r)	δ_a wiggle, δ_e wiggle, δ_r wiggle
26	2330	5700	clean	accelerated 1.3g (r)	δ_a wiggle, δ_e wiggle, δ_r wiggle
27	2460	5000	clean	symmetric	δ_r wiggle
28	2560	4800	clean	symmetric	δ_r wiggle
29	2820	4500	clean	symmetric	δ_a wiggle, δ_e wiggle, δ_r wiggle
30	2920	4500	clean	symmetric	δ_a wiggle, δ_e wiggle, δ_r wiggle
31	3020	4500	clean	symmetric	δ_a wiggle, δ_e wiggle, δ_r wiggle
32	3120	4500	clean	symmetric	δ_a wiggle, δ_e wiggle, δ_r wiggle

Table A-3: (1/2) List of all stall experiment runs in test flight 3 of Table 3-3.

Stall #	$\sim t_{start}$ **[s]**	$\sim h$ **[m]**	**Config**	**Stall type**	**Control input**
-	1610	2700	clean	none	$+\delta_e$ 3-2-1-1
-	1690	2700	clean	none	$-\delta_e$ 3-2-1-1
-	1780	2700	clean	none	$+\delta_r$ 3-2-1-1
-	1800	2700	clean	none	$+\delta_r$ 3-2-1-1
-	1840	2700	clean	none	$-\delta_a$ 3-2-1-1
-	1880	2700	clean	none	$-\delta_a$ 3-2-1-1
-	1920	2600	clean	none	$-\delta_a$ 3-2-1-1
-	1950	2600	clean	none	$-\delta_a$ 3-2-1-1
33	2200	2600	clean	symmetric	$-\delta_a$ 3-2-1-1, $-\delta_e$ 3-2-1-1
34	2300	2500	clean	symmetric	$-\delta_a$ 3-2-1-1, $-\delta_e$ 3-2-1-1
35	2500	2700	clean	symmetric	$-\delta_a$ 3-2-1-1, $-\delta_e$ 3-2-1-1
36	2550	2700	clean	symmetric	$-\delta_a$ 3-2-1-1, $-\delta_e$ 3-2-1-1
37	2600	2600	clean	symmetric	$-\delta_a$ 3-2-1-1, $-\delta_e$ 3-2-1-1
38	2670	2600	clean	symmetric	$-\delta_a$ 3-2-1-1, $-\delta_e$ 3-2-1-1
39	2800	2600	clean	symmetric	$+\delta_a$ 3-2-1-1, $-\delta_e$ 3-2-1-1
40	2850	2600	clean	symmetric	$+\delta_a$ 3-2-1-1, $-\delta_e$ 3-2-1-1
41	2920	2600	clean	symmetric	$-\delta_a$ 3-2-1-1, $-\delta_e$ 3-2-1-1
42	3080	2700	clean	symmetric	$-\delta_a$ 3-2-1-1, $-\delta_e$ 3-2-1-1
43	3150	2600	clean	symmetric	$-\delta_a$ 3-2-1-1, $-\delta_e$ 3-2-1-1
44	3200	2600	clean	symmetric	$-\delta_a$ 3-2-1-1, $-\delta_e$ 3-2-1-1
45	3300	2700	clean	symmetric	$-\delta_a$ 3-2-1-1, $-\delta_e$ 3-2-1-1
46	3370	2600	clean	symmetric	$-\delta_a$ 3-2-1-1, $-\delta_e$ 3-2-1-1
47	3420	2600	clean	symmetric	$-\delta_a$ 3-2-1-1, $-\delta_e$ 3-2-1-1
48	3470	2600	clean	symmetric	$-\delta_e$ 3-2-1-1, $+\delta_r$ 3-2-1-1
49	3550	2700	clean	symmetric	$-\delta_e$ 3-2-1-1, $+\delta_r$ 3-2-1-1
50	3620	2700	clean	symmetric	$-\delta_e$ 3-2-1-1, $+\delta_r$ 3-2-1-1
51	3670	2700	clean	symmetric	$-\delta_e$ 3-2-1-1, $+\delta_r$ 3-2-1-1
51	3750	2700	clean	symmetric	$-\delta_e$ 3-2-1-1, $+\delta_r$ 3-2-1-1
52	3810	2600	clean	symmetric	$-\delta_e$ 3-2-1-1, $+\delta_r$ 3-2-1-1
53	3900	2700	clean	symmetric	$-\delta_e$ 3-2-1-1, $+\delta_r$ 3-2-1-1
54	3960	2700	clean	symmetric	$-\delta_e$ 3-2-1-1, $+\delta_r$ 3-2-1-1
55	4000	2700	clean	symmetric	$-\delta_e$ 3-2-1-1, $+\delta_r$ 3-2-1-1
56	4050	2700	clean	symmetric	$-\delta_e$ 3-2-1-1, $+\delta_r$ 3-2-1-1
57	4100	2700	clean	symmetric	$-\delta_e$ 3-2-1-1, $+\delta_r$ 3-2-1-1
58	4150	2600	clean	symmetric	$-\delta_e$ 3-2-1-1, $+\delta_r$ 3-2-1-1
59	4200	2600	clean	symmetric	$-\delta_e$ 3-2-1-1, $+\delta_r$ 3-2-1-1
60	4270	2600	clean	symmetric	$-\delta_e$ 3-2-1-1, $+\delta_r$ 3-2-1-1
61	4350	2700	clean	symmetric	$-\delta_e$ 3-2-1-1, $+\delta_r$ 3-2-1-1
62	4420	2700	clean	symmetric	$-\delta_e$ 3-2-1-1, $+\delta_r$ 3-2-1-1
63	4480	2700	clean	symmetric	$-\delta_e$ 3-2-1-1, $+\delta_r$ 3-2-1-1
66	4530	2600	clean	symmetric	$-\delta_e$ 3-2-1-1, $+\delta_r$ 3-2-1-1
67	4600	2600	clean	symmetric	$-\delta_e$ 3-2-1-1, $+\delta_r$ 3-2-1-1

Table A-3: (continued, 2/2) List of all stall experiment runs in test flight 3 of Table 3-3.

Stall #	$\sim t_{start}$ [s]	$\sim h$ [m]	Config	Stall type	Control input
68	7110	2600	landing	symmetric	-δ_e 3-2-1-1, -δ_r 3-2-1-1
69	7140	2600	landing	symmetric	-δ_e 3-2-1-1, -δ_r 3-2-1-1
69	7180	2500	landing	symmetric	-δ_e 3-2-1-1, -δ_r 3-2-1-1
70	7280	2700	landing	symmetric	-δ_e 3-2-1-1, -δ_r 3-2-1-1
71	7320	2700	landing	symmetric	-δ_e 3-2-1-1, -δ_r 3-2-1-1
72	7380	2600	landing	symmetric	-δ_e 3-2-1-1, -δ_r 3-2-1-1

Table A-4: List of all stall experiment runs in test flight 4 of Table 3-3.

Stall #	$\sim t_{start}$ [s]	$\sim h$ [m]	Config	Stall type	Control input
73	1920	3200	clean	accelerated 1.3g (r)	none
74	1980	3200	clean	accelerated 1.3g (r)	none
75	2040	3200	clean	accelerated 1.3g (r)	none
76	2120	3100	clean	accelerated 1.3g (r)	none
77	2260	3200	landing	accelerated 1.3g (r)	none
78	2340	3200	landing	accelerated 1.3g (r)	none
79	2460	3200	landing	accelerated 1.3g (r)	none
80	2560	3200	landing	accelerated 1.3g (l)	none
81	2670	3200	landing	accelerated 1.3g (l)	none
82	2730	3200	landing	accelerated 1.3g (r)	none
83	2800	3300	landing	accelerated 1.3g (r)	none
84	2880	3300	landing	accelerated 1.3g (r)	none
85	3020	3300	landing	accelerated 1.3g (r)	δ_a wiggle, δ_e wiggle
86	3080	3400	landing	accelerated 1.3g (r)	δ_a wiggle, δ_e wiggle
87	3160	3400	landing	accelerated 1.3g (r)	δ_a wiggle, δ_e wiggle
88	3320	3300	landing	accelerated 1.3g (l)	δ_a wiggle, δ_e wiggle
89	3380	3300	landing	accelerated 1.3g (l)	δ_a wiggle, δ_e wiggle
90	3600	3200	landing	accelerated 1.3g (l)	δ_a wiggle, δ_e wiggle
91	3640	3300	landing	accelerated 1.3g (r)	δ_a wiggle, δ_e wiggle
92	3730	3300	landing	accelerated 1.3g (r)	δ_a wiggle, δ_e wiggle
93	3810	3300	landing	accelerated 1.3g (r)	δ_a wiggle, δ_e wiggle
94	3930	3200	landing	accelerated 1.3g (r)	δ_a wiggle, δ_e wiggle
95	4630	3200	landing	accelerated 1.3g (r)	δ_a wiggle, δ_e wiggle
96	4700	3200	landing	accelerated 1.3g (r)	δ_a wiggle, δ_e wiggle
97	4780	3100	landing	accelerated 1.3g (r)	δ_a wiggle, δ_e wiggle

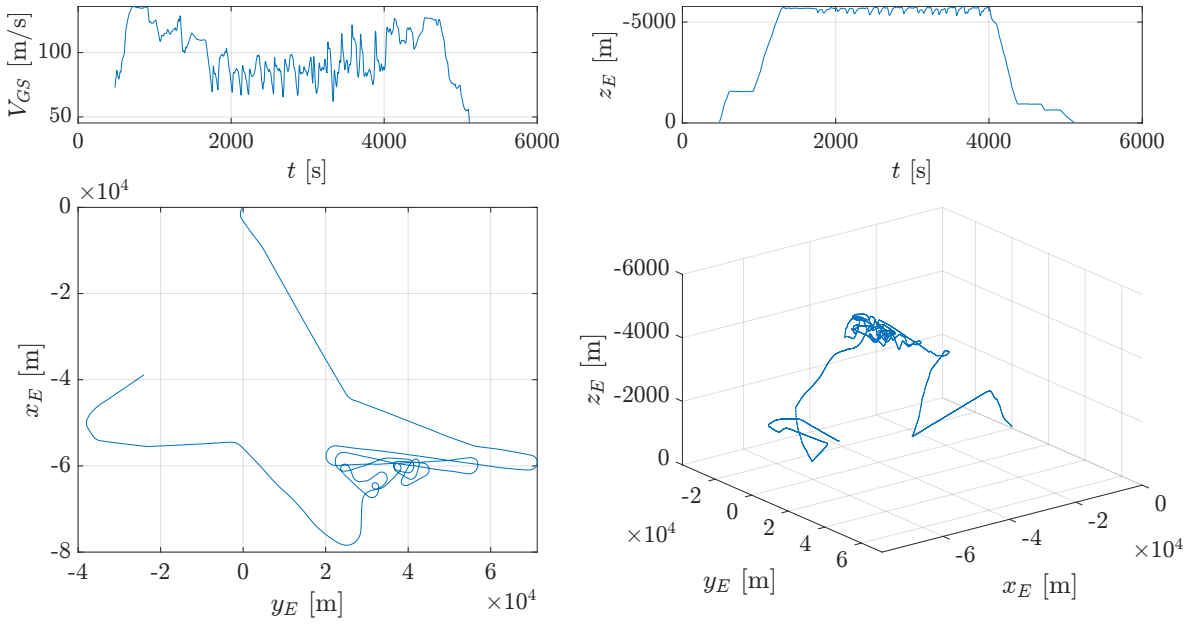

(a) Test flight trajectory.

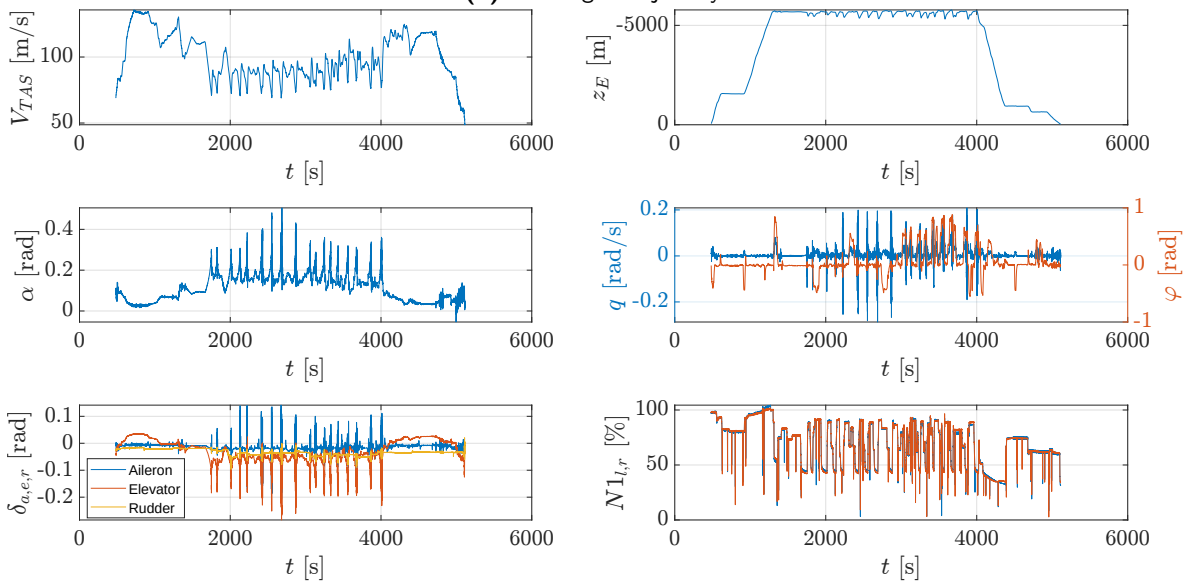

(b) Test flight stall-related parameters.

Figure A-1: Overview of test flight 1 of Table 3-3.

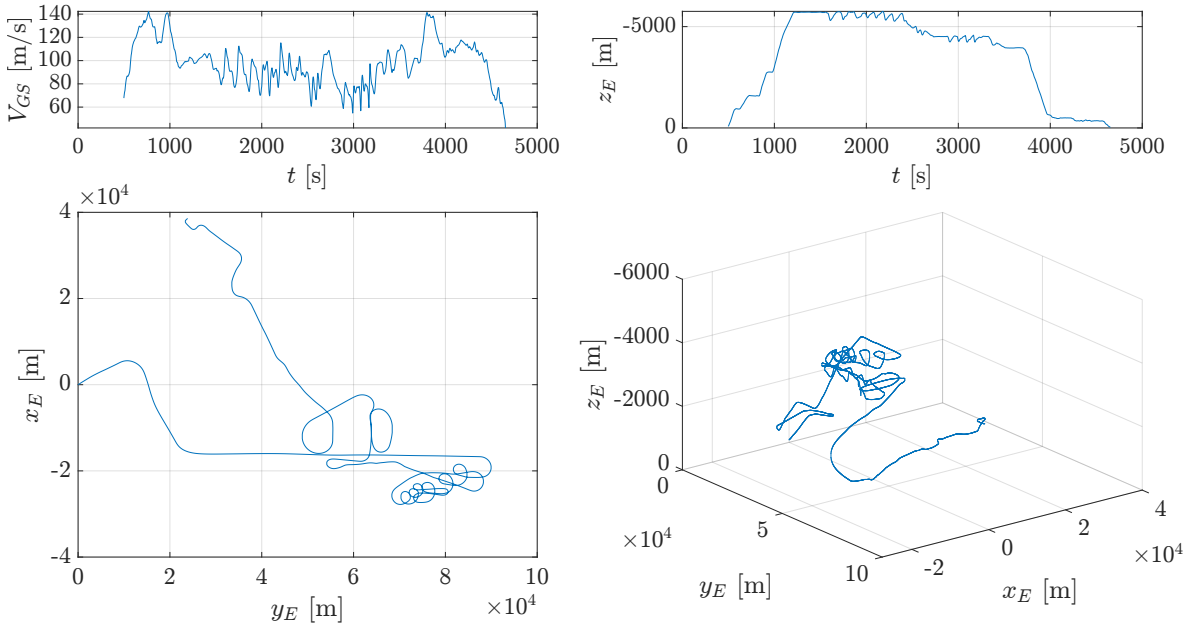

(a) Test flight trajectory.

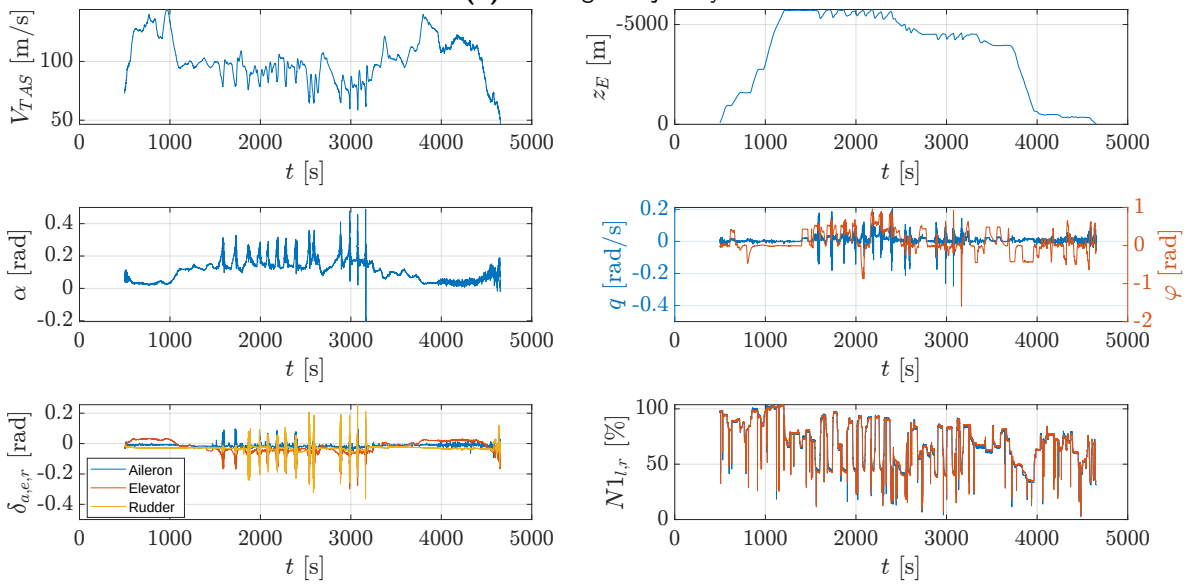

(b) Test flight stall-related parameters.

Figure A-2: Overview of test flight 2 of Table 3-3.

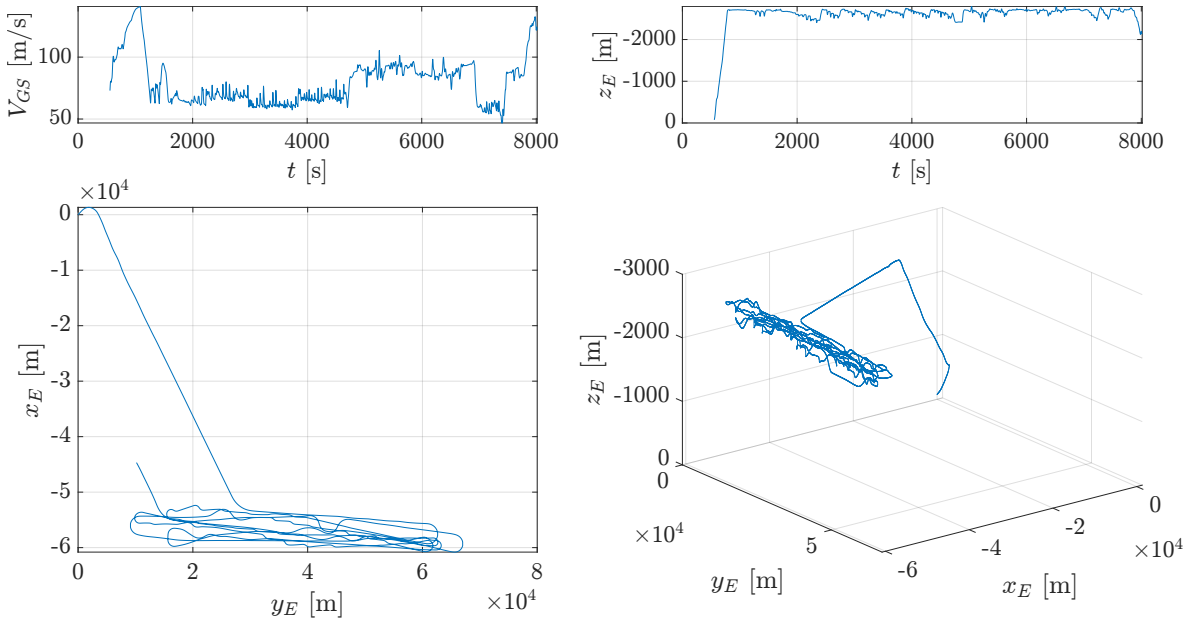

(a) Test flight trajectory.

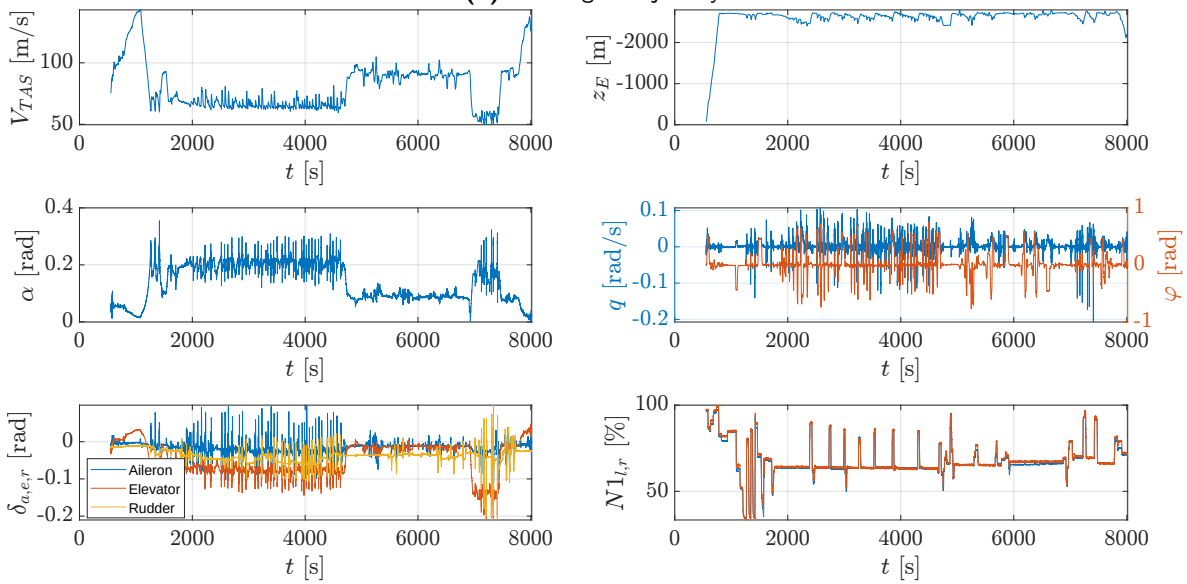

(b) Test flight stall-related parameters.

Figure A-3: Overview of test flight 3 of Table 3-3.

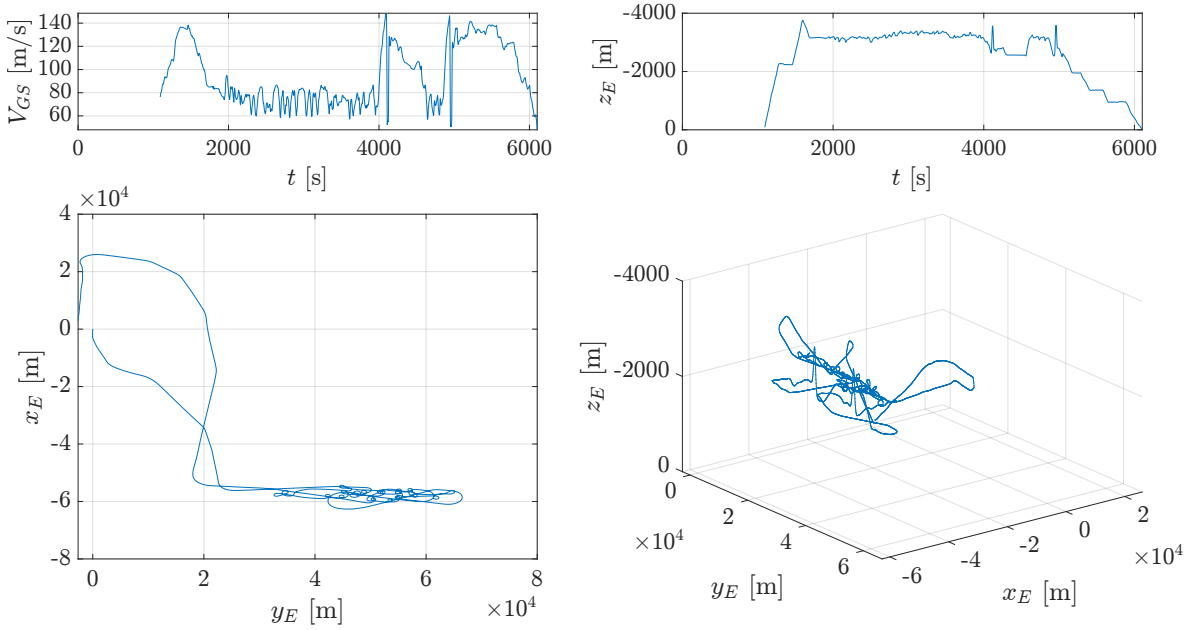

(a) Test flight trajectory.

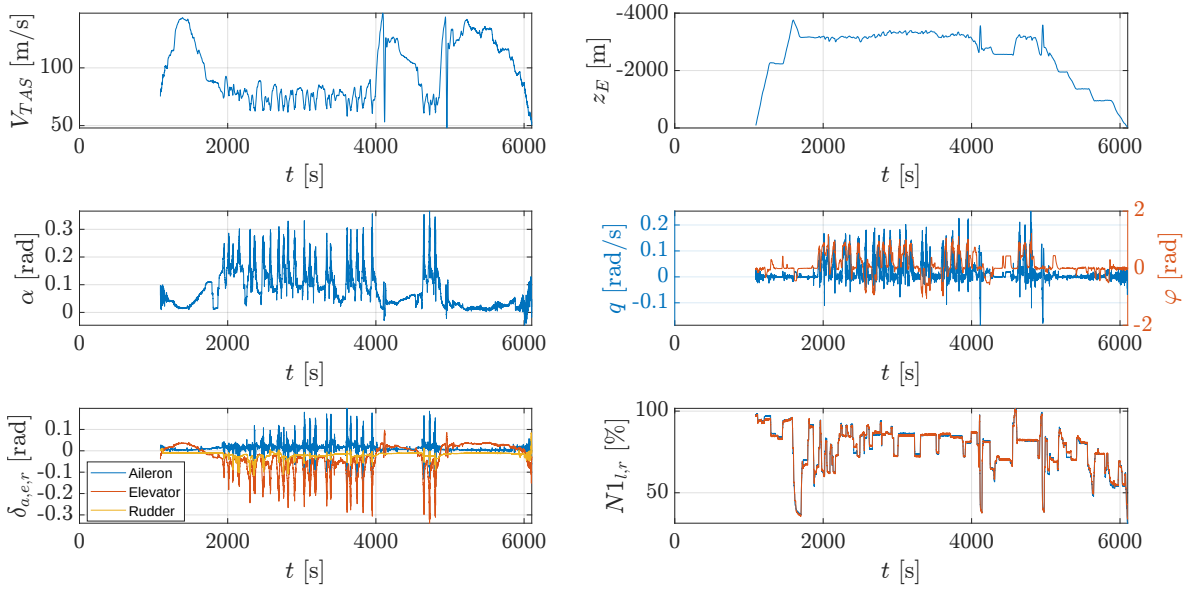

(b) Test flight stall-related parameters.

Figure A-4: Overview of test flight 4 of Table 3-3.

Part IV

Appendices to Scientific Paper

Appendix B

Compared Parameter Estimate Behaviour

B-1 No Input

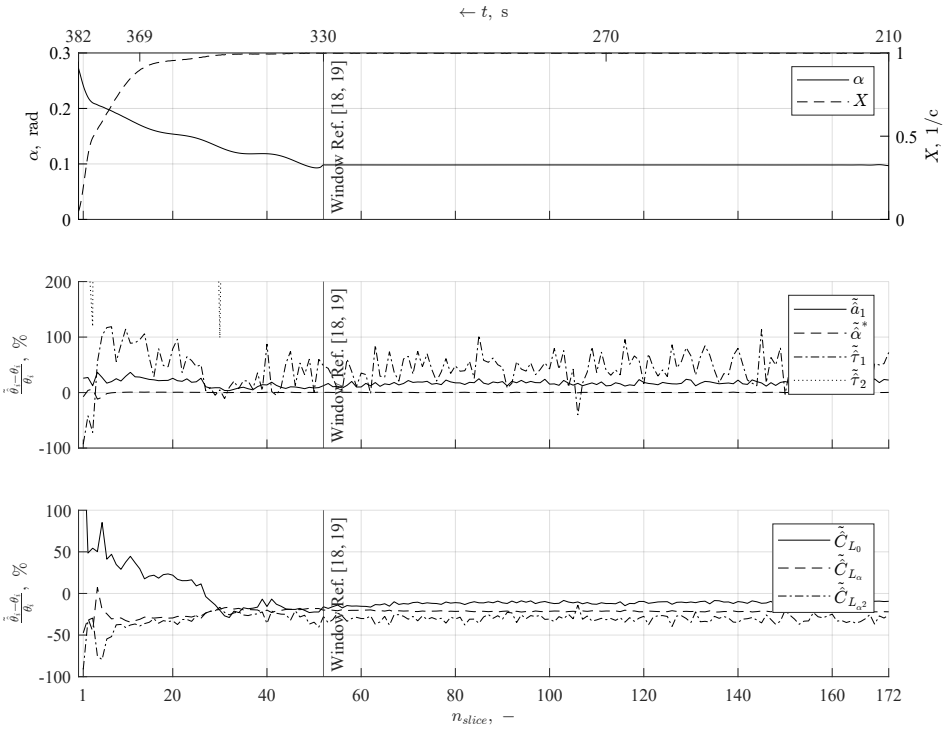

(a) Normalized bias.

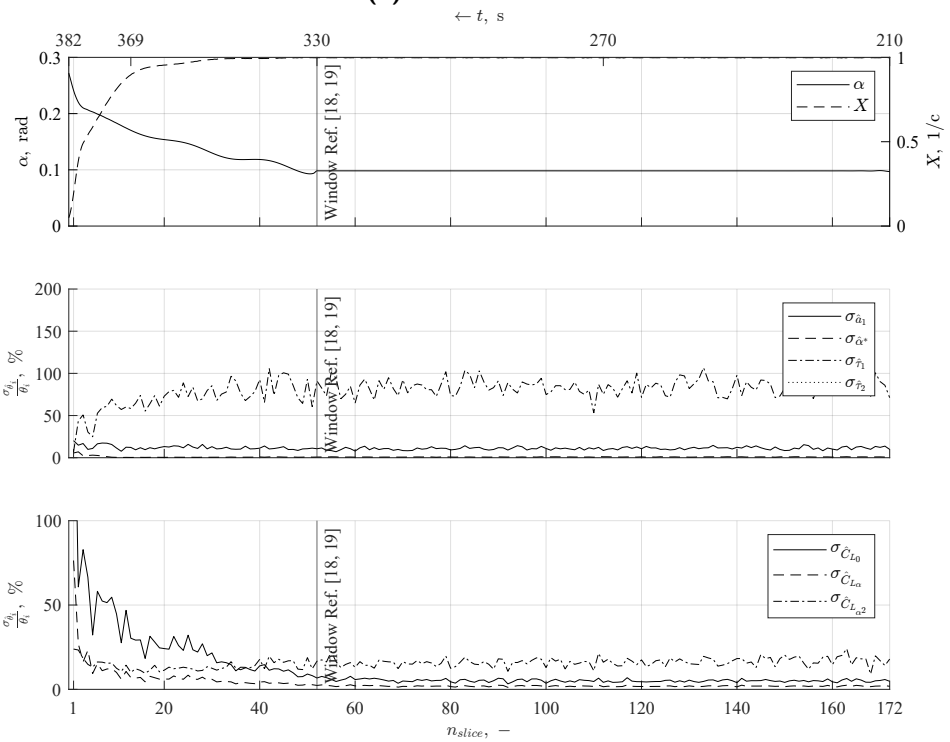

(b) Normalized standard deviation.

Figure B-1: Pre-stall.

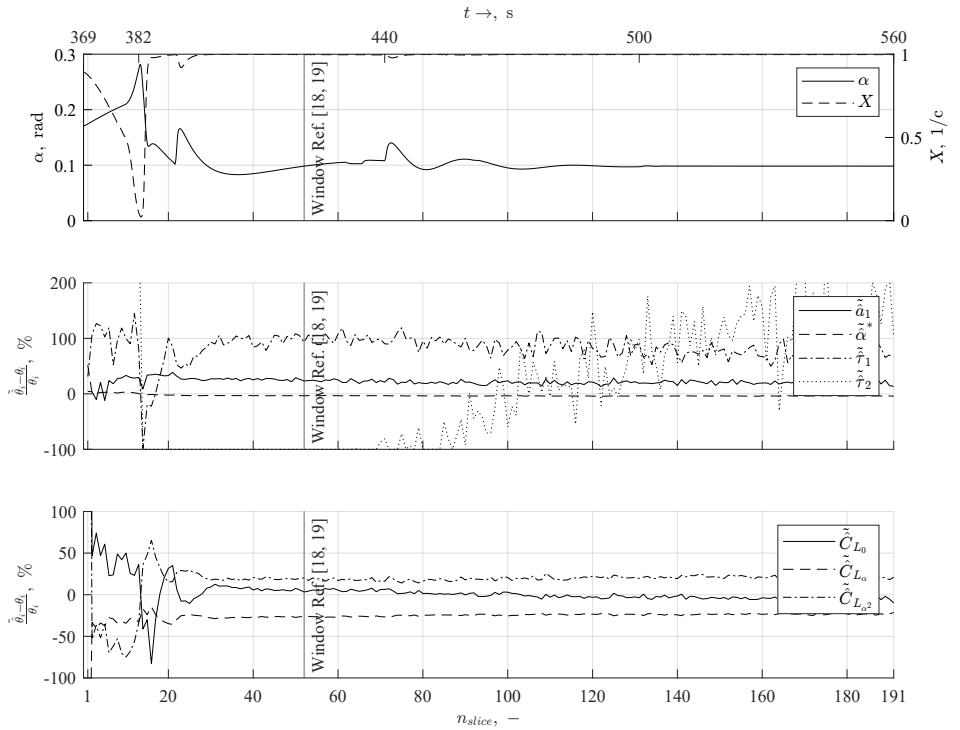

(a) Normalized bias.

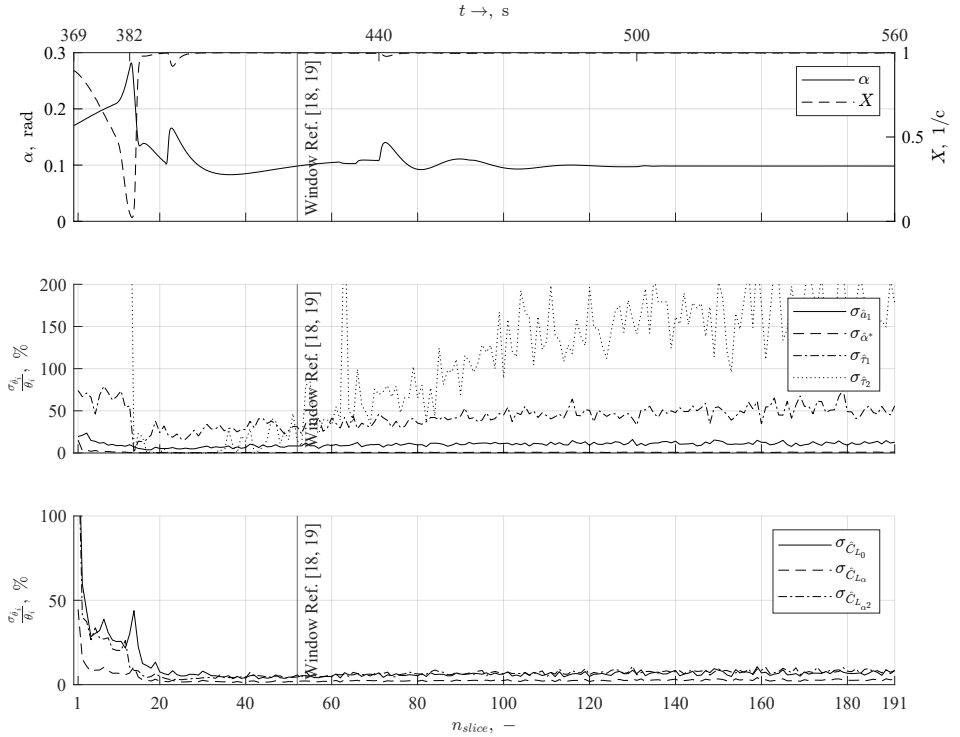

(b) Normalized standard deviation.

Figure B-2: Post-stall.

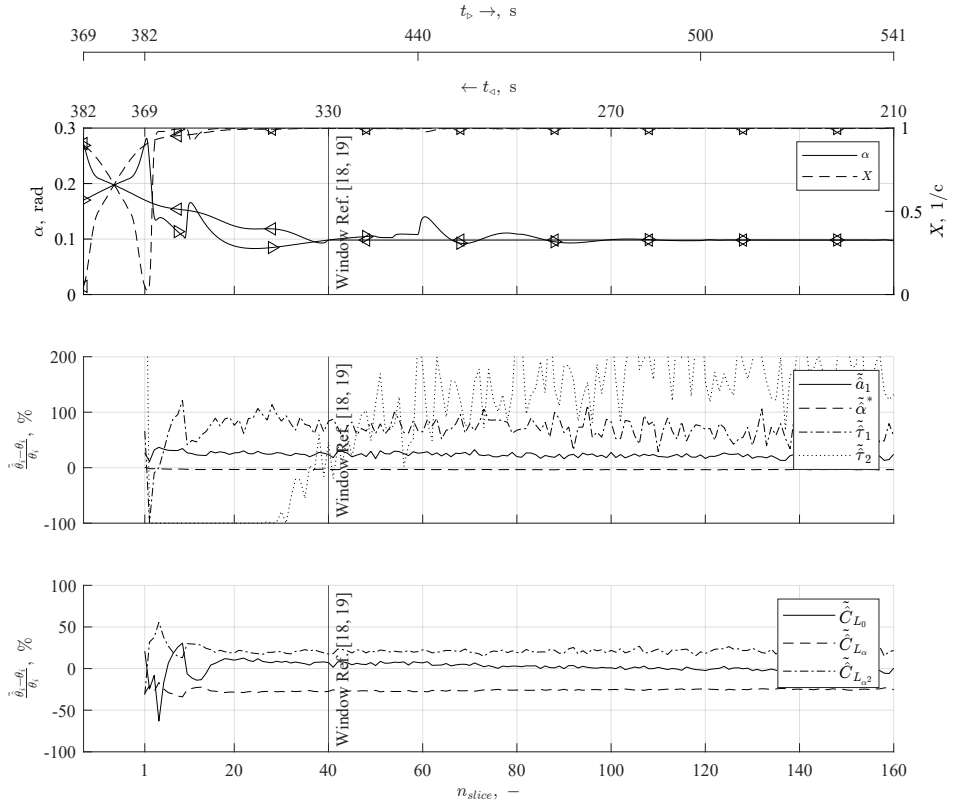

(a) Normalized bias.

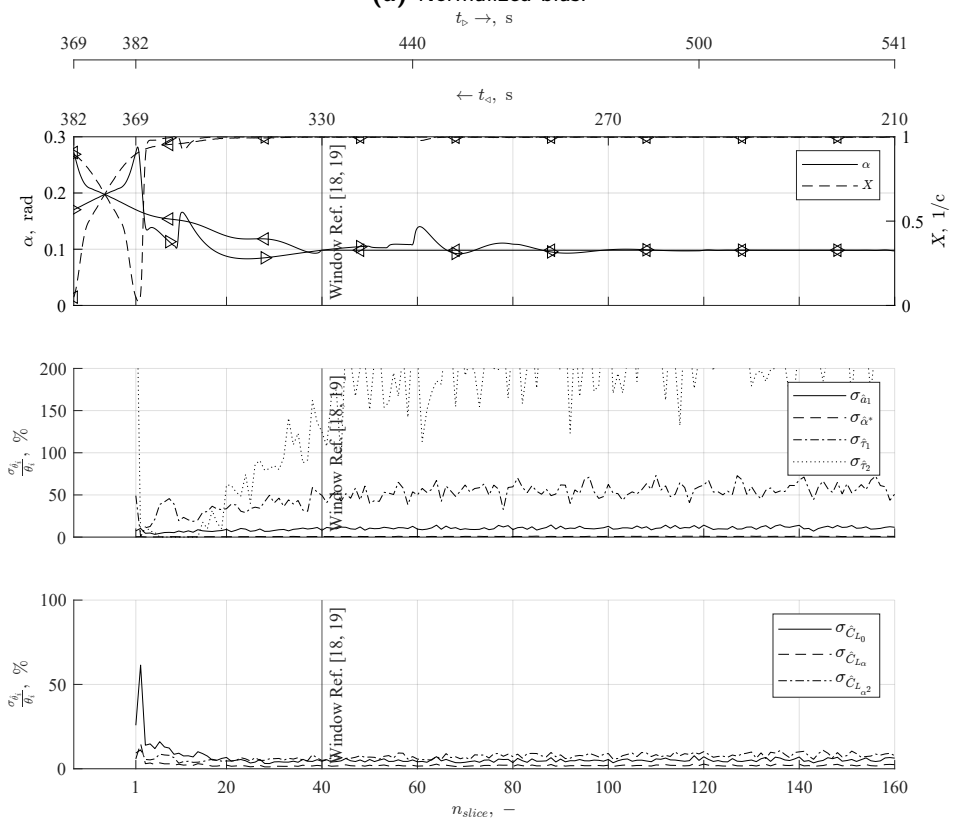

(b) Normalized standard deviation.

Figure B-3: Pre-stall and post-stall.

B-2 3-2-1-1 Input

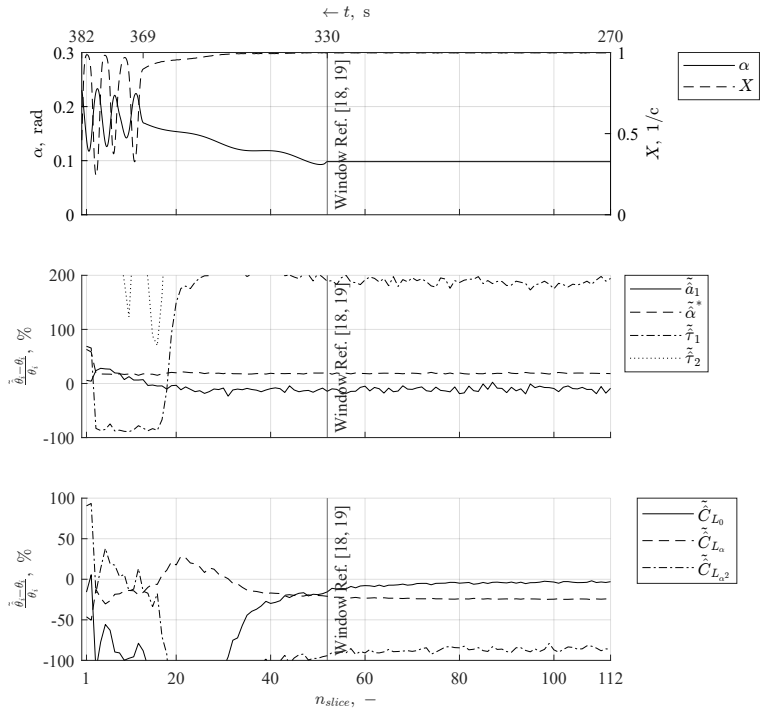

(a) Normalized bias.

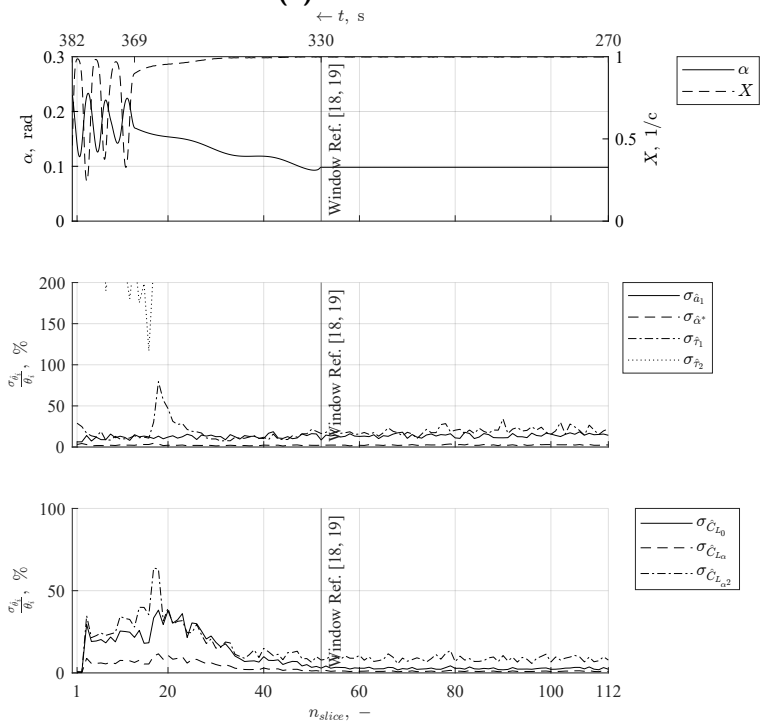

(b) Normalized standard deviation.

Figure B-4: Pre-stall.

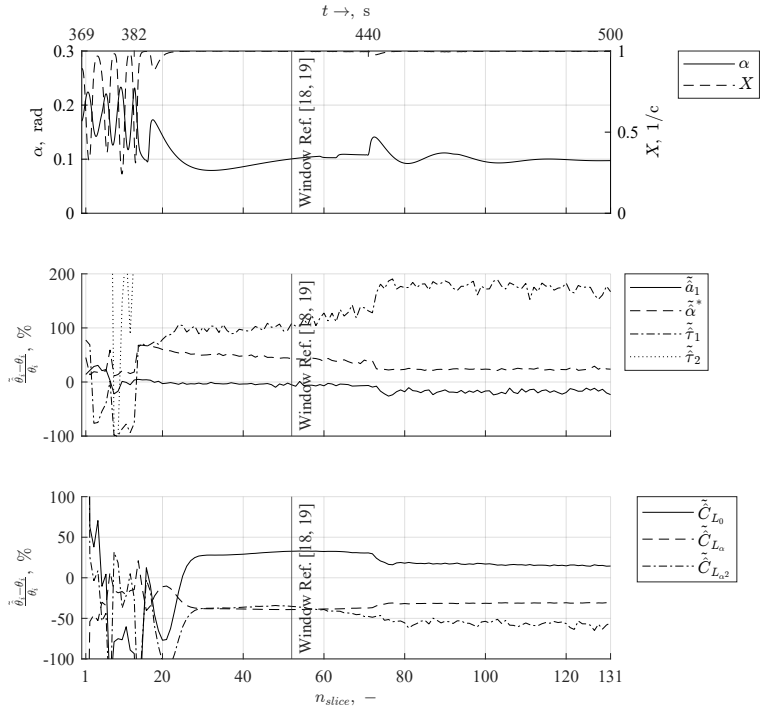

(a) Normalized bias.

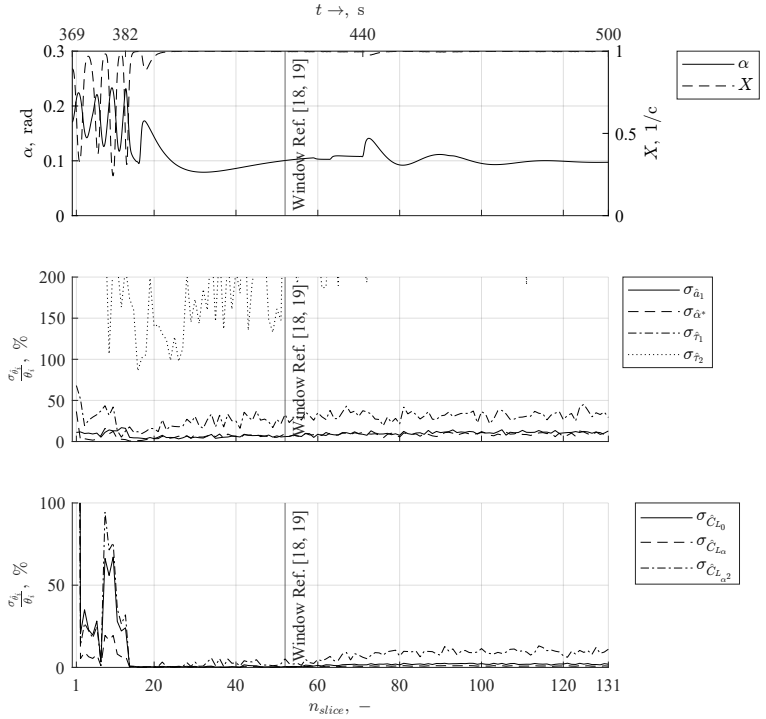

(b) Normalized standard deviation.

Figure B-5: Post-stall.

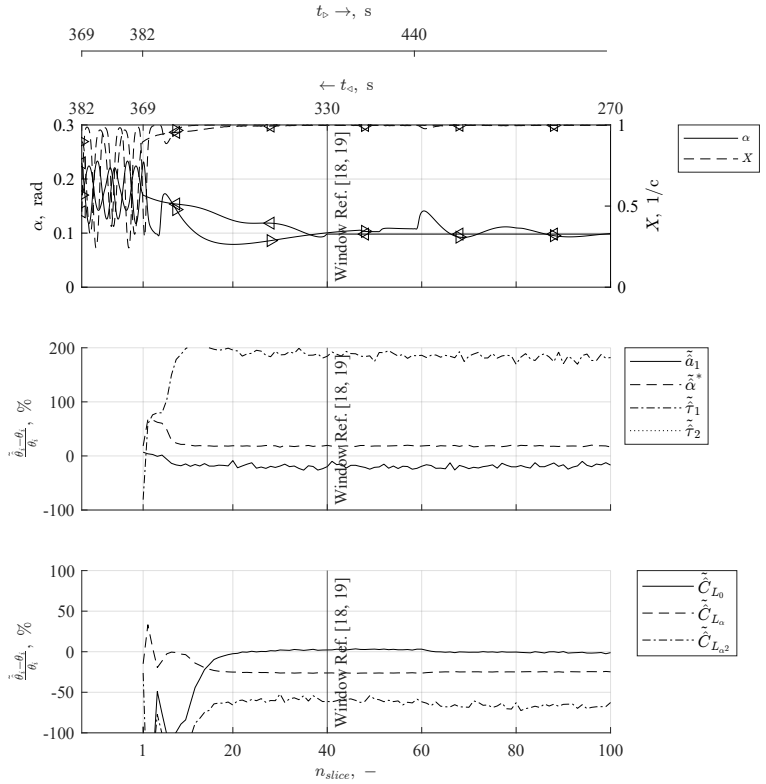

(a) Normalized bias.

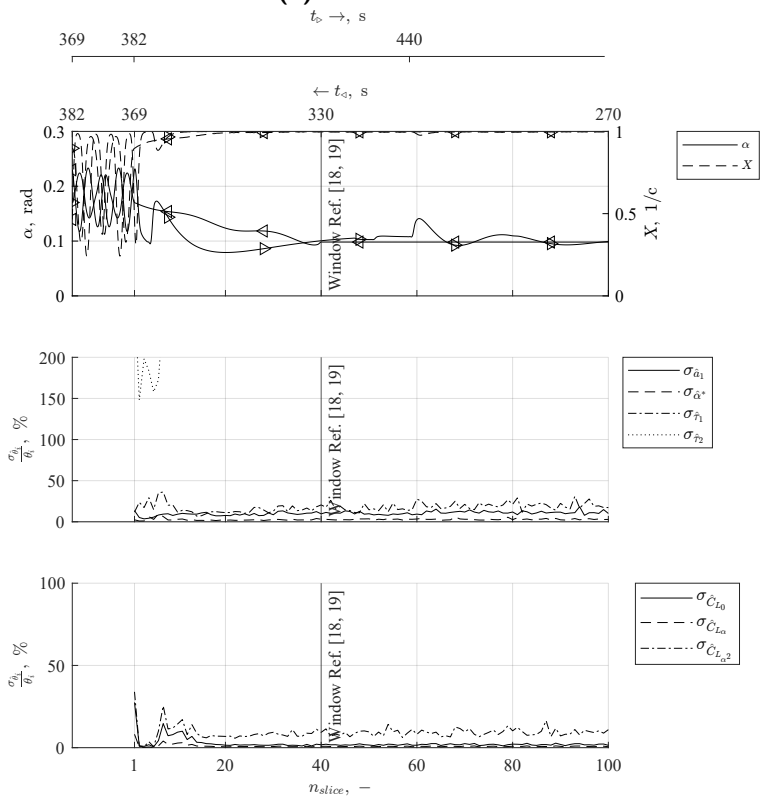

(b) Normalized standard deviation.

Figure B-6: Pre-stall and post-stall.

B-3 Wiggle Input

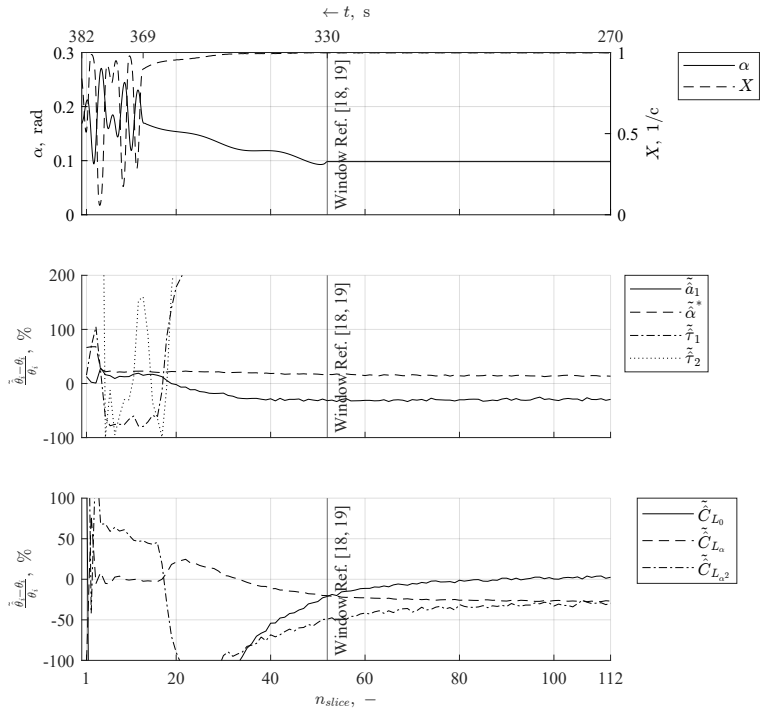

(a) Normalized bias.

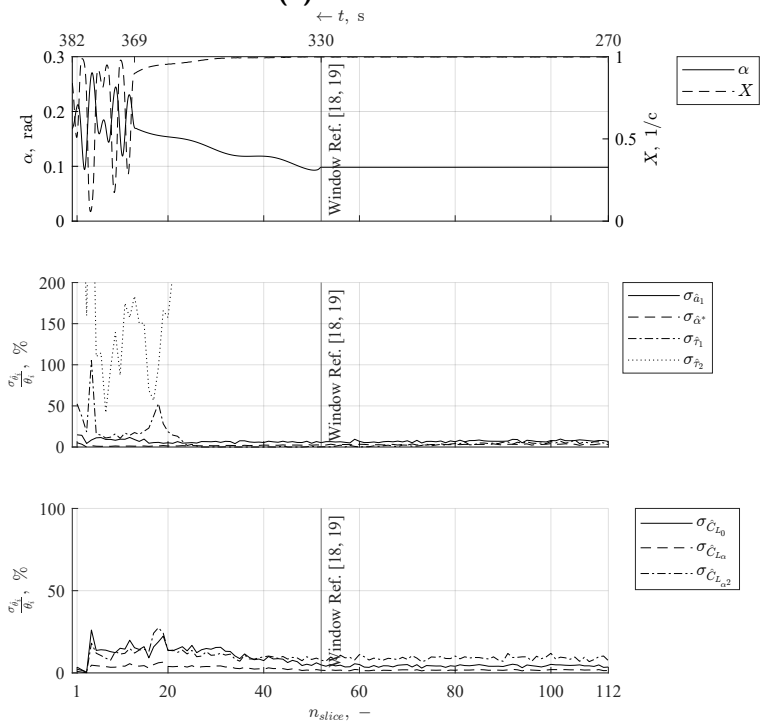

(b) Normalized standard deviation.

Figure B-7: Pre-stall.

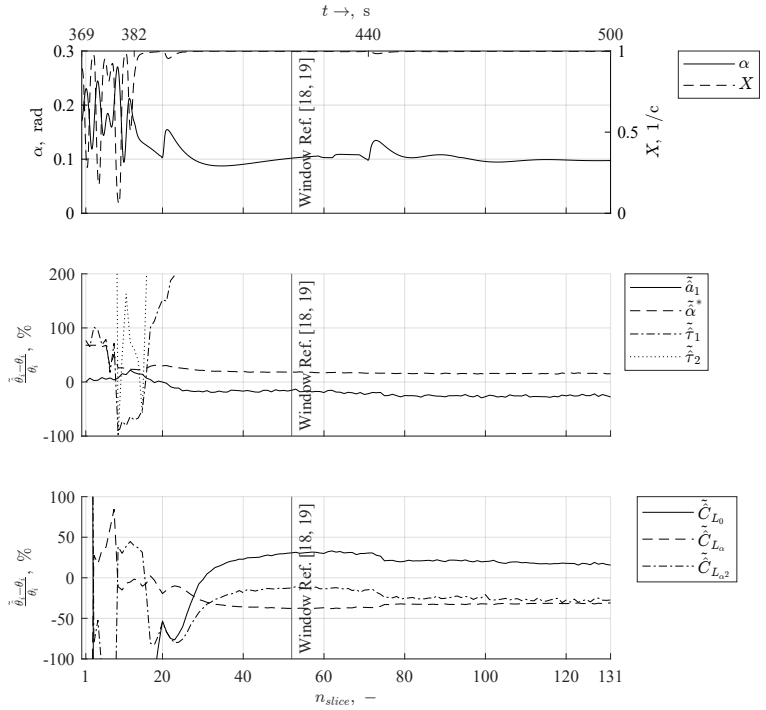

(a) Normalized bias.

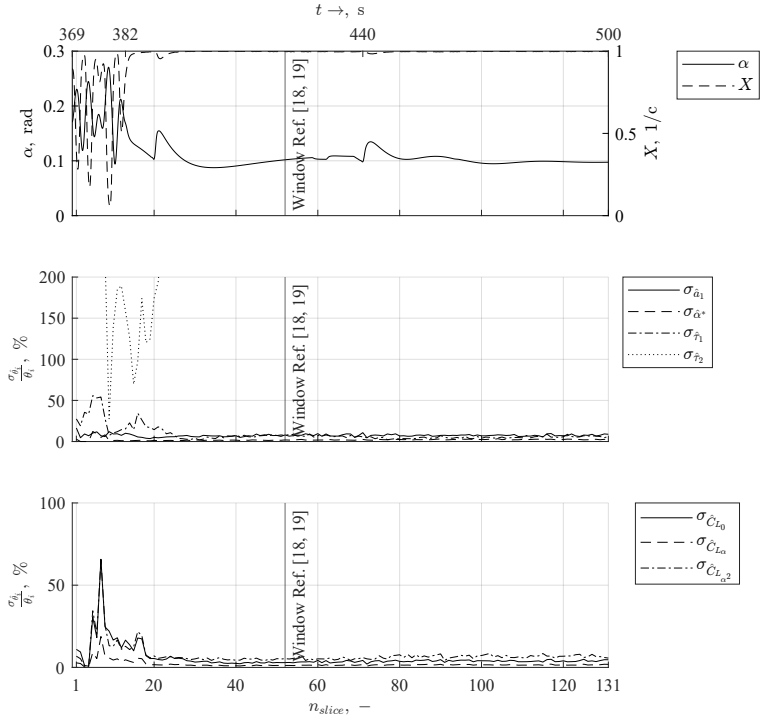

(b) Normalized standard deviation.

Figure B-8: Post-stall.

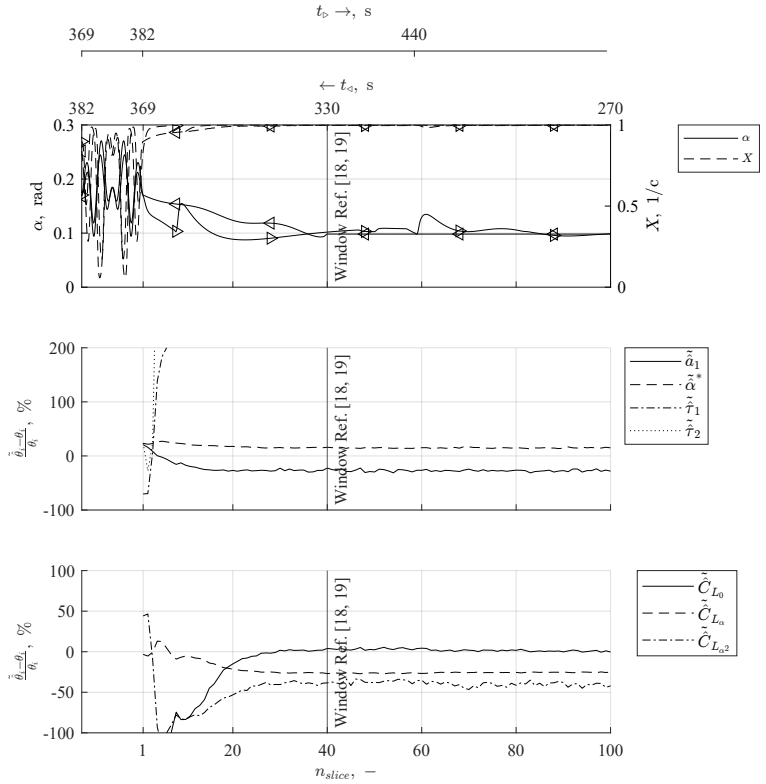

(a) Normalized bias.

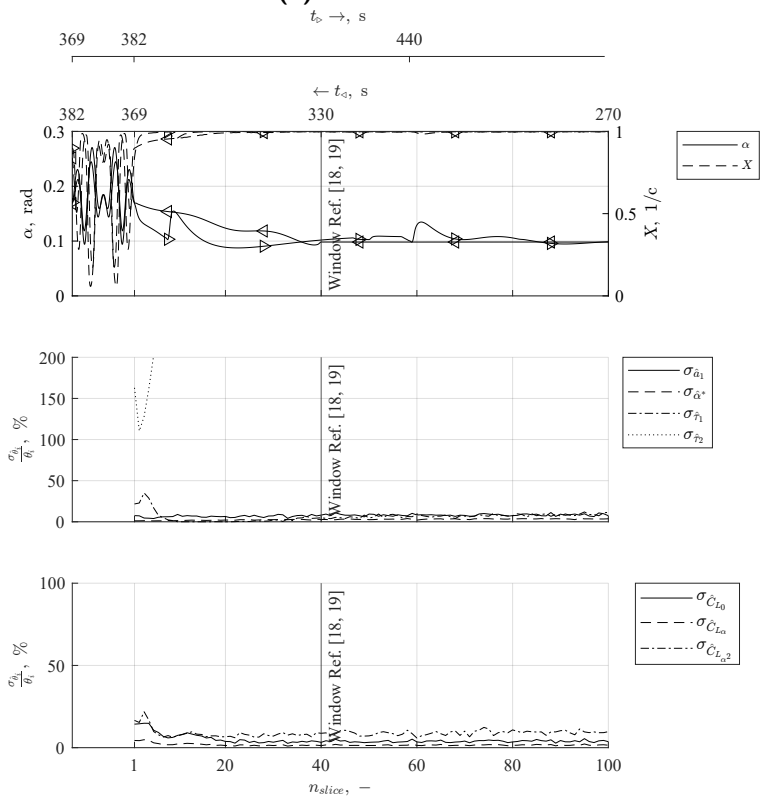

(b) Normalized standard deviation.

Figure B-9: Pre-stall and post-stall.

Appendix C

Individual Parameter Estimate Behaviour

C-1 No Input

C-1-1 Simulation Data

Pre-stall Slicing

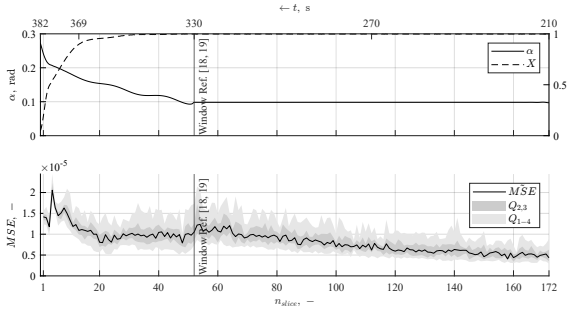

Figure C-1: Metric MSE.

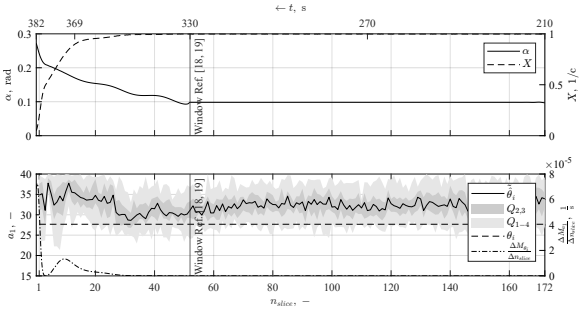

Figure C-2: Parameter a_1.

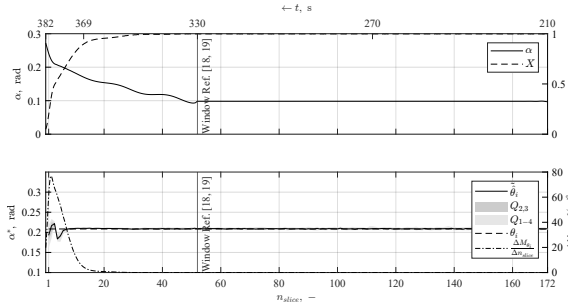

Figure C-3: Parameter α^*.

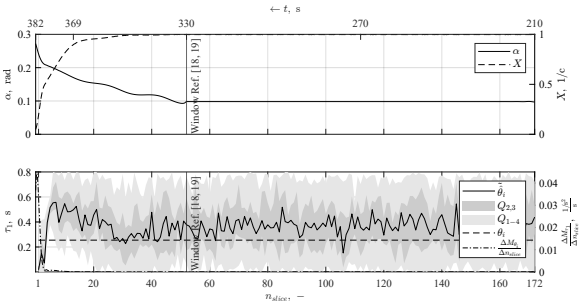

Figure C-4: Parameter τ_1.

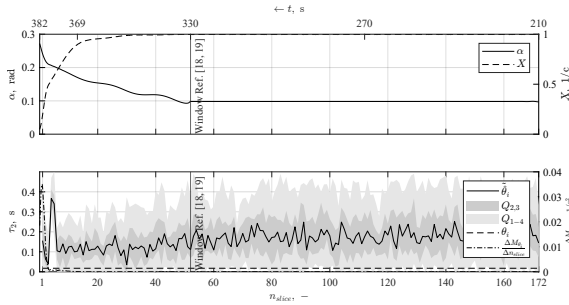

Figure C-5: Parameter τ_2.

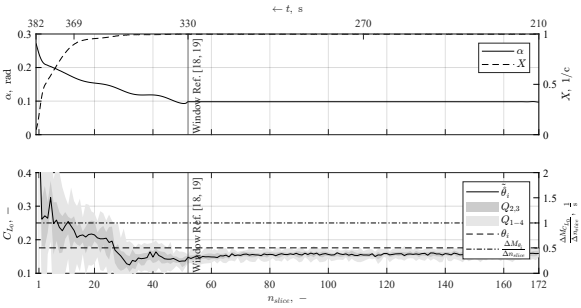

Figure C-6: Parameter C_{L_0}.

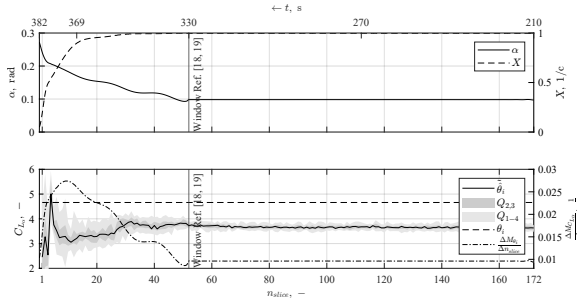

Figure C-7: Parameter C_{L_α}.

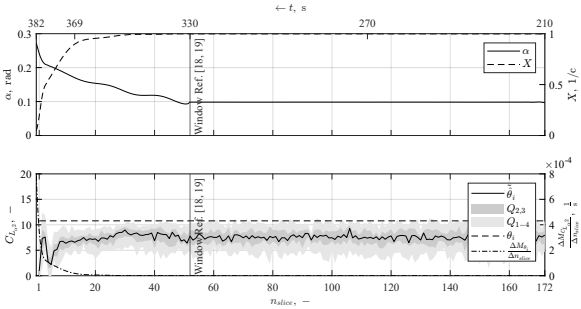

Figure C-8: Parameter $C_{L_{\alpha^2}}$.

Post-stall Slicing

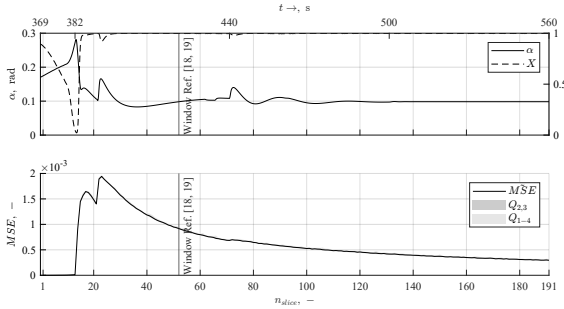

Figure C-9: Metric MSE.

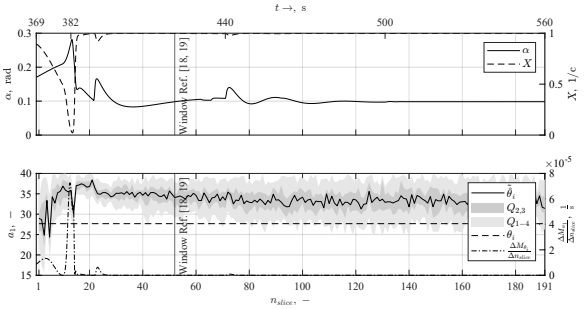

Figure C-10: Parameter a_1.

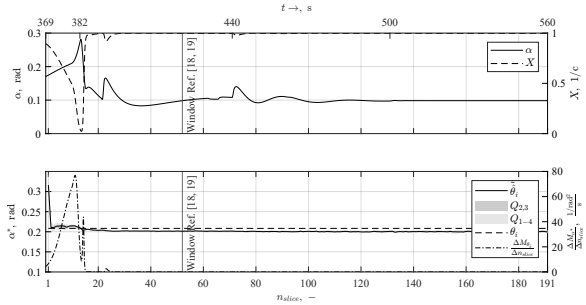

Figure C-11: Parameter α^*.

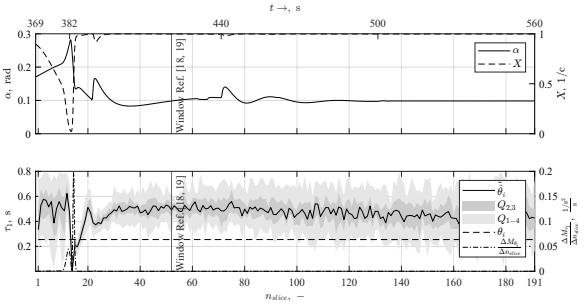

Figure C-12: Parameter τ_1.

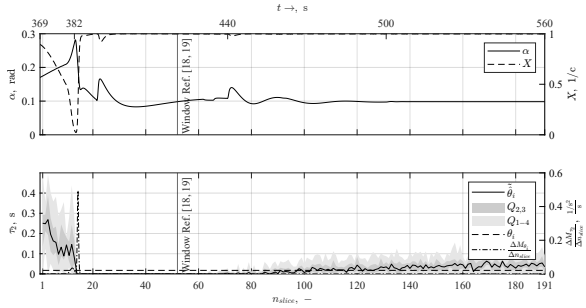

Figure C-13: Parameter τ_2.

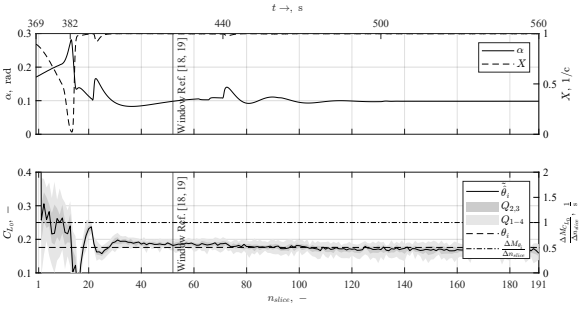

Figure C-14: Parameter C_{L_0}.

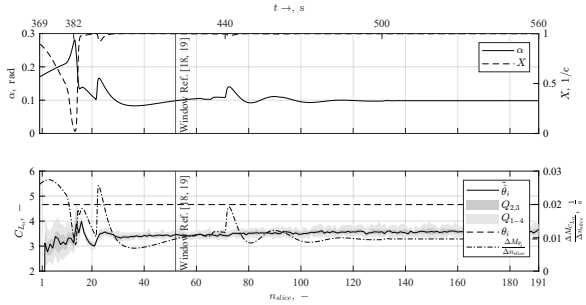

Figure C-15: Parameter C_{L_α}.

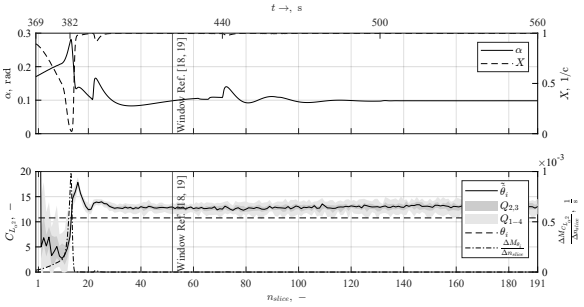

Figure C-16: Parameter $C_{L_{\alpha^2}}$.

Pre-stall and Post-stall Slicing

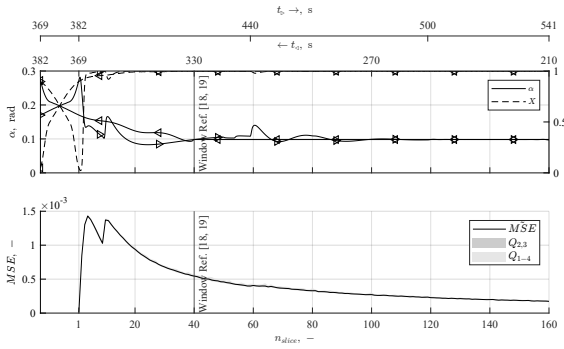

Figure C-17: Metric MSE.

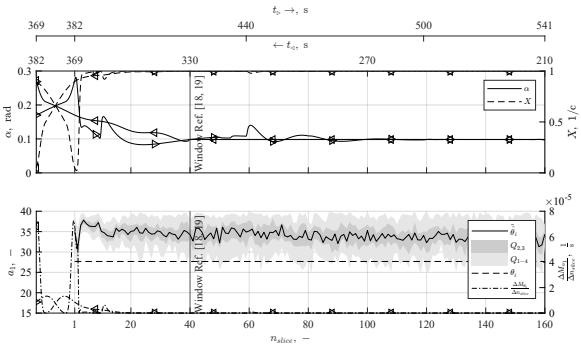

Figure C-18: Parameter a_1.

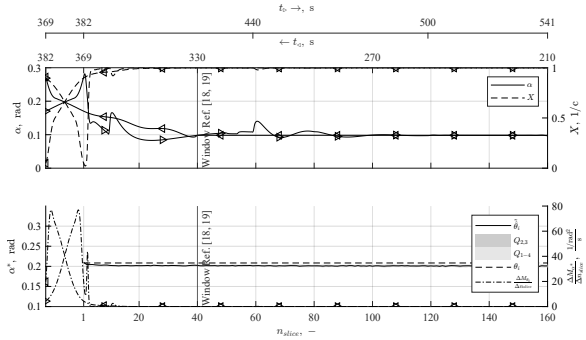

Figure C-19: Parameter α^*.

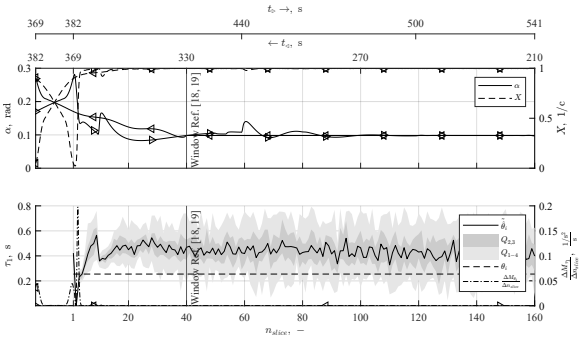

Figure C-20: Parameter τ_1.

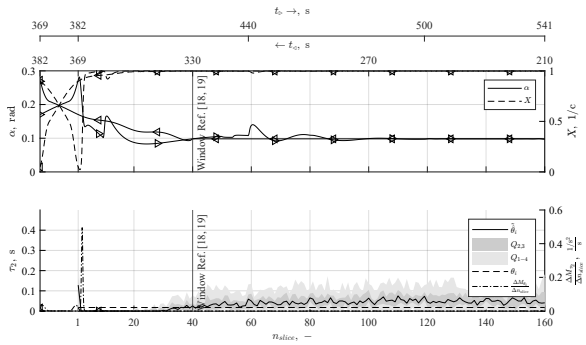

Figure C-21: Parameter τ_2.

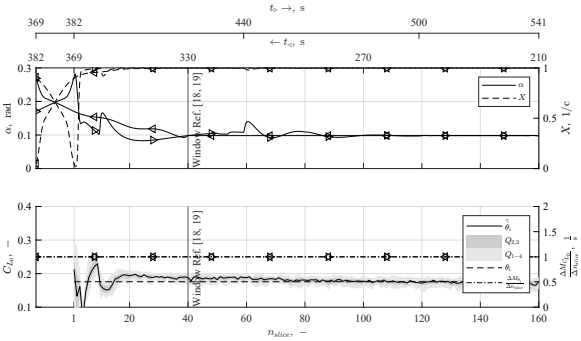

Figure C-22: Parameter C_{L_0}.

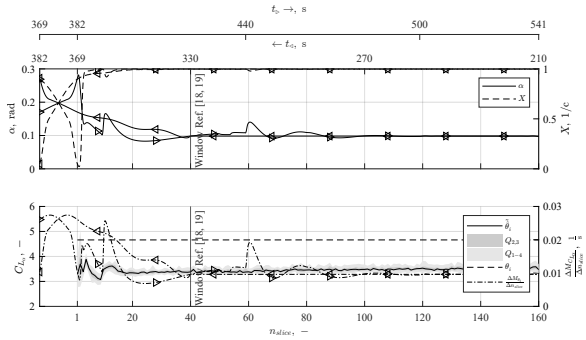

Figure C-23: Parameter C_{L_α}.

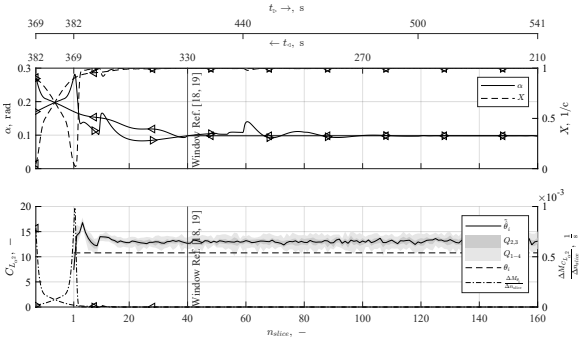

Figure C-24: Parameter $C_{L_{\alpha^2}}$.

C-1-2 Flight Test Data

Pre-stall Slicing

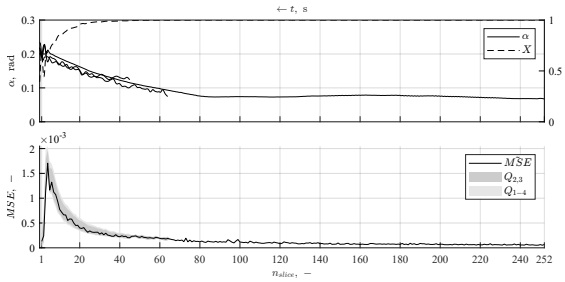

Figure C-25: Metric MSE.

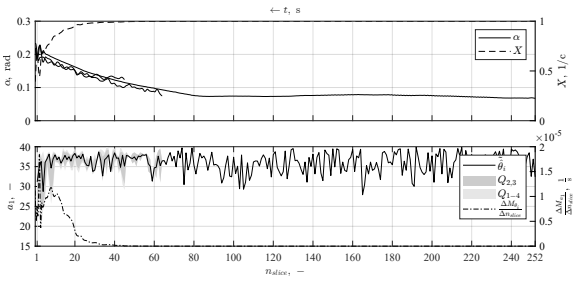

Figure C-26: Parameter a_1.

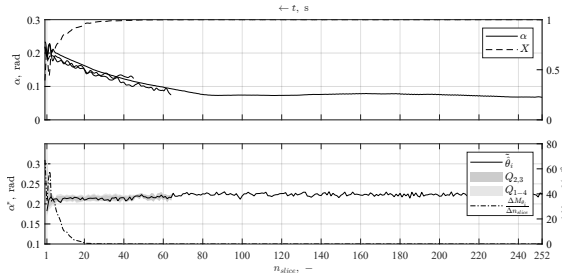

Figure C-27: Parameter α^*.

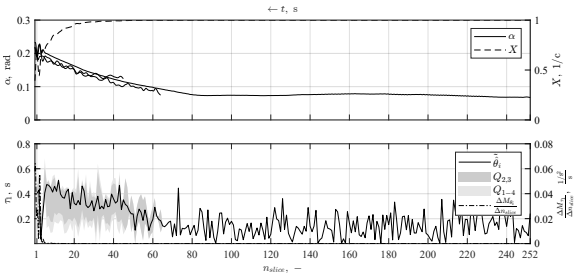

Figure C-28: Parameter τ_1.

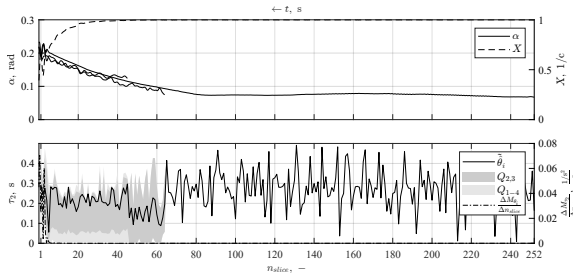

Figure C-29: Parameter τ_2.

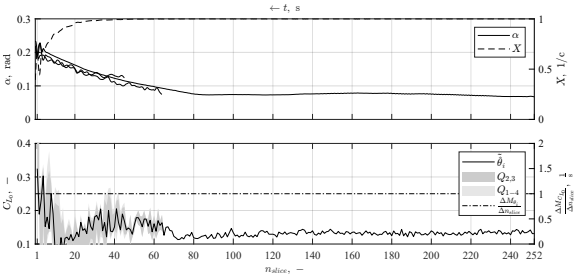

Figure C-30: Parameter C_{L_0}.

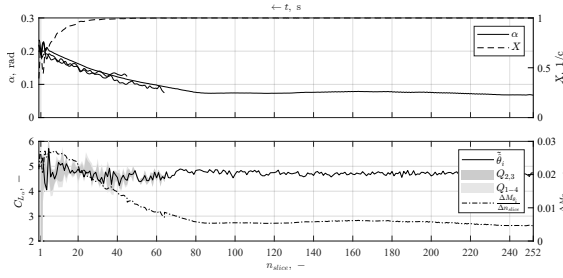

Figure C-31: Parameter C_{L_α}.

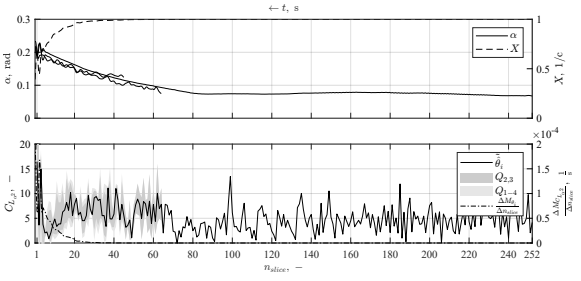

Figure C-32: Parameter $C_{L_{\alpha^2}}$.

Post-stall Slicing

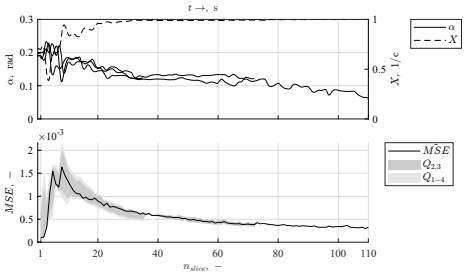

Figure C-33: Metric MSE.

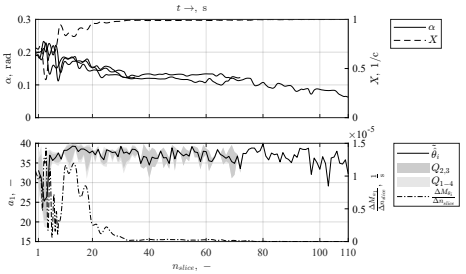

Figure C-34: Parameter a_1.

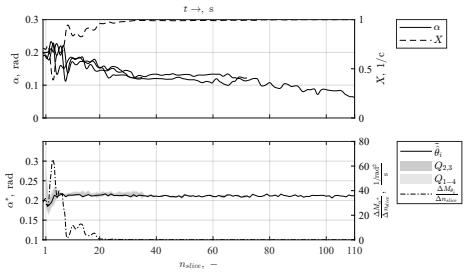

Figure C-35: Parameter α^*.

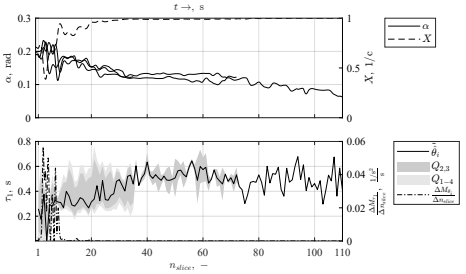

Figure C-36: Parameter τ_1.

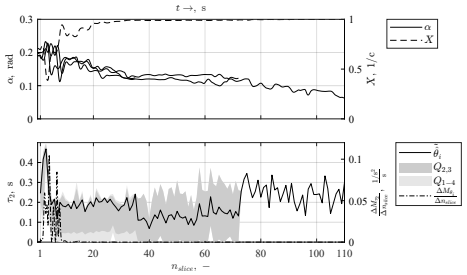

Figure C-37: Parameter τ_2.

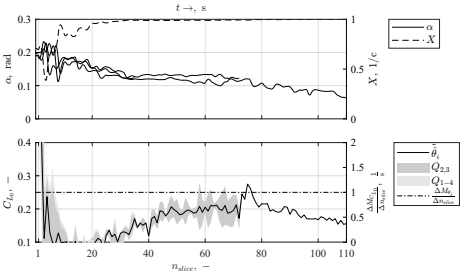

Figure C-38: Parameter C_{L_0}.

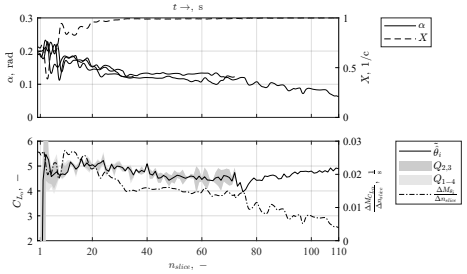

Figure C-39: Parameter C_{L_α}.

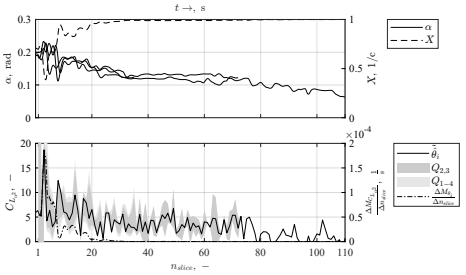

Figure C-40: Parameter $C_{L_{\alpha^2}}$.

C-2 3-2-1-1 Input

C-2-1 Simulation Data

Pre-stall Slicing

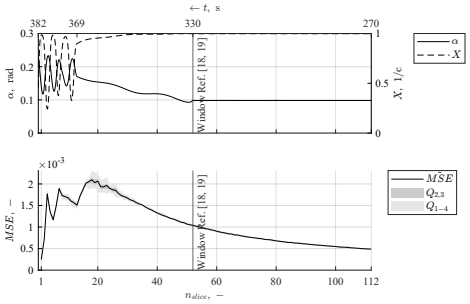

Figure C-41: Metric MSE.

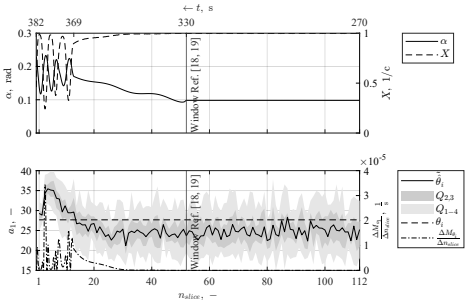

Figure C-42: Parameter a_1.

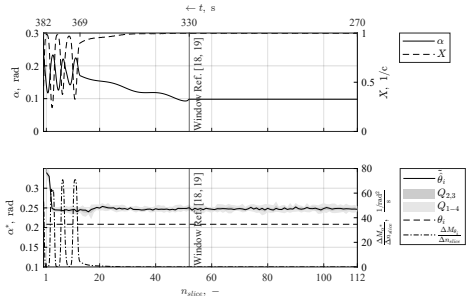

Figure C-43: Parameter α^*.

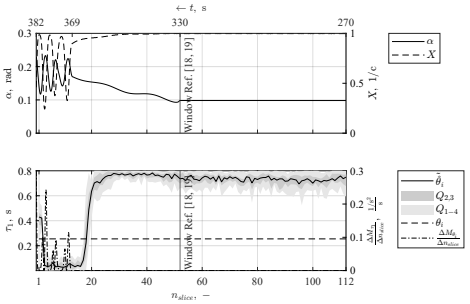

Figure C-44: Parameter τ_1.

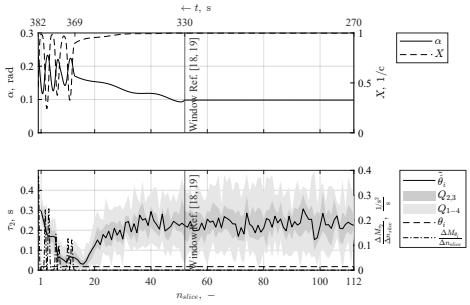

Figure C-45: Parameter τ_2.

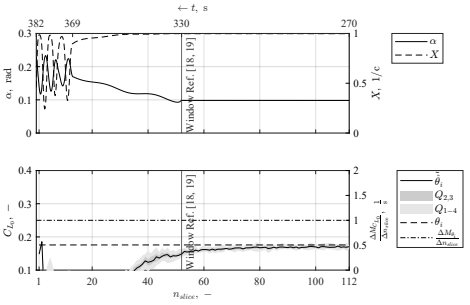

Figure C-46: Parameter C_{L_0}.

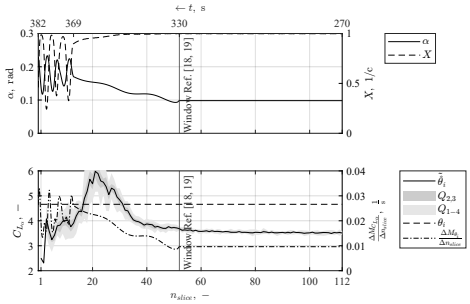

Figure C-47: Parameter C_{L_α}.

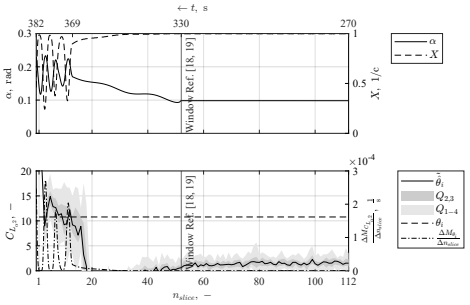

Figure C-48: Parameter $C_{L_{\alpha^2}}$.

Post-stall Slicing

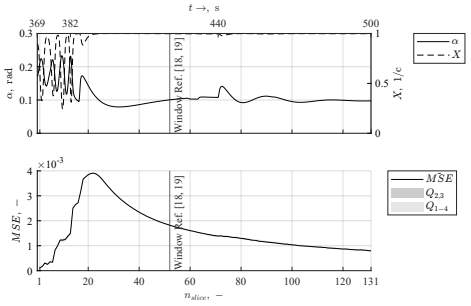

Figure C-49: Metric MSE.

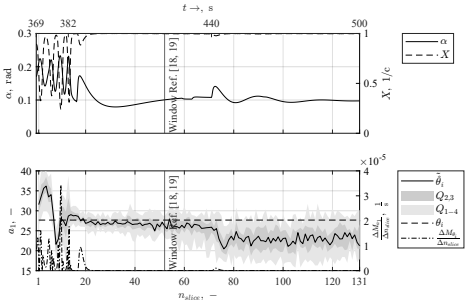

Figure C-50: Parameter a_1.

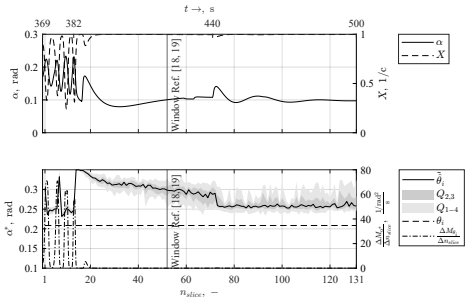

Figure C-51: Parameter α^*.

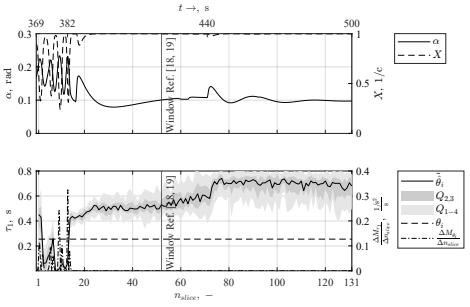

Figure C-52: Parameter τ_1.

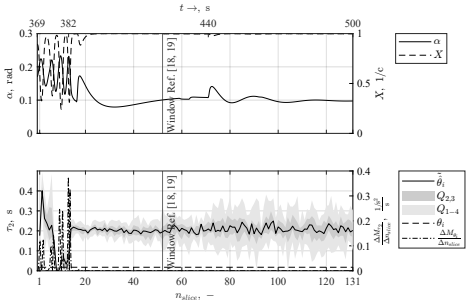

Figure C-53: Parameter τ_2.

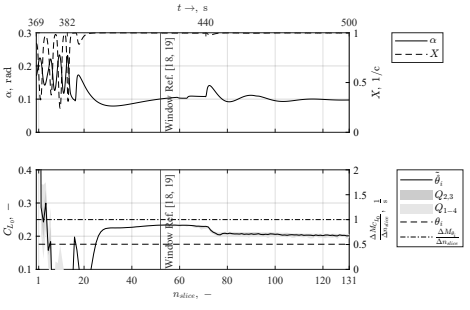

Figure C-54: Parameter C_{L_0}.

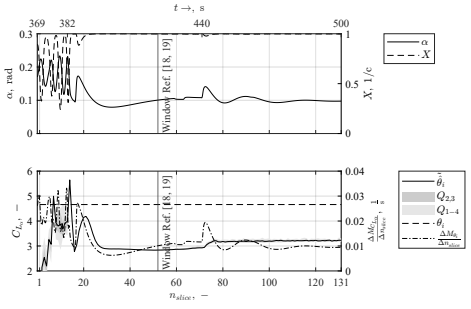

Figure C-55: Parameter C_{L_α}.

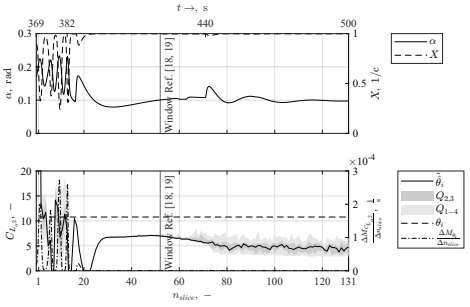

Figure C-56: Parameter $C_{L_{\alpha^2}}$.

Pre-stall and Post-stall Slicing

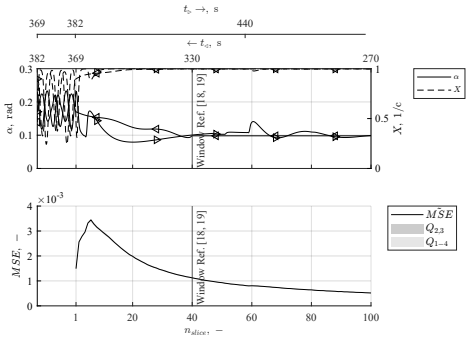

Figure C-57: Metric MSE.

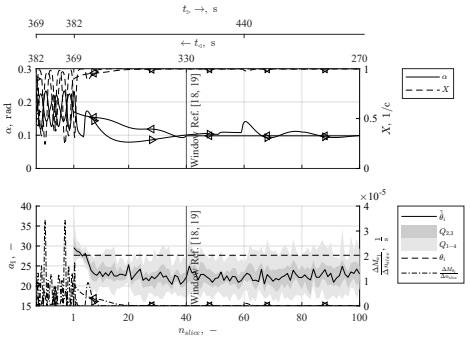

Figure C-58: Parameter a_1.

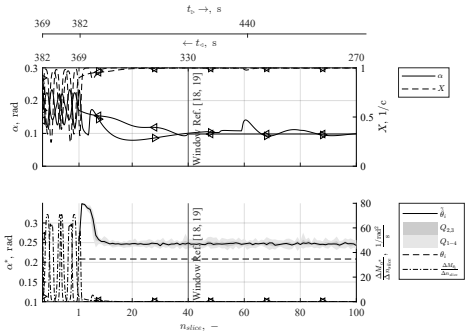

Figure C-59: Parameter α^*.

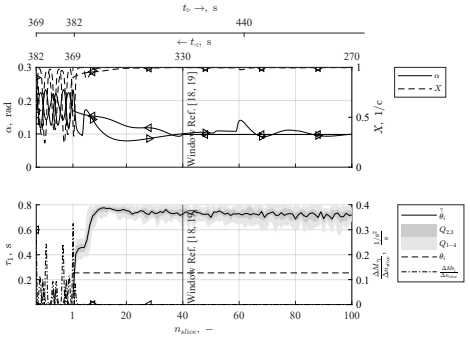

Figure C-60: Parameter τ_1.

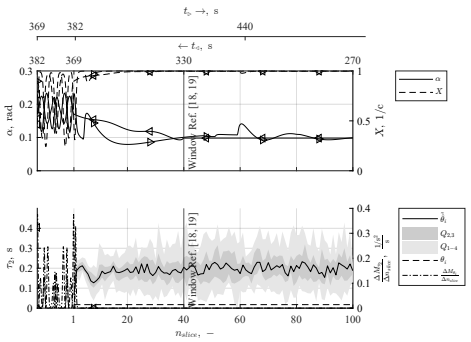

Figure C-61: Parameter τ_2.

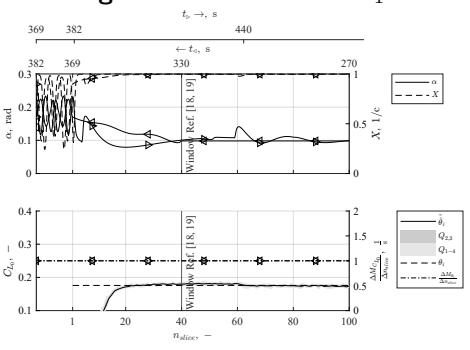

Figure C-62: Parameter C_{L_0}.

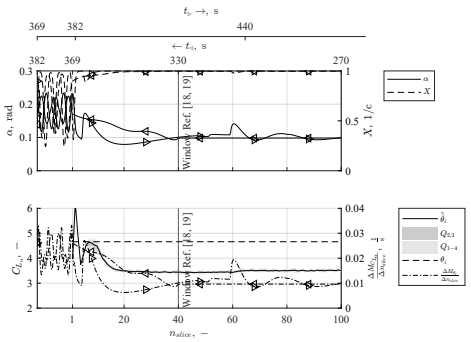

Figure C-63: Parameter C_{L_α}.

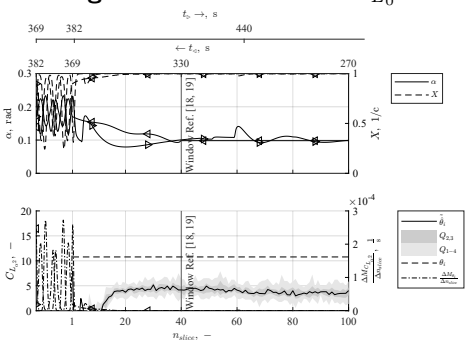

Figure C-64: Parameter $C_{L_{\alpha^2}}$.

C-2-2 Flight Test Data

Pre-stall Slicing

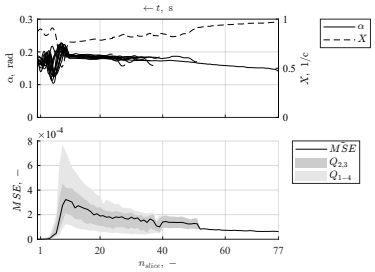

Figure C-65: Metric MSE.

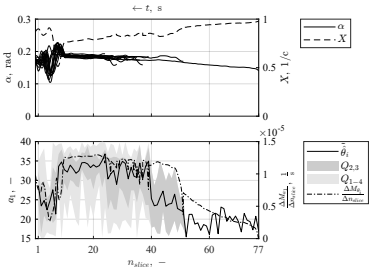

Figure C-66: Parameter a_1.

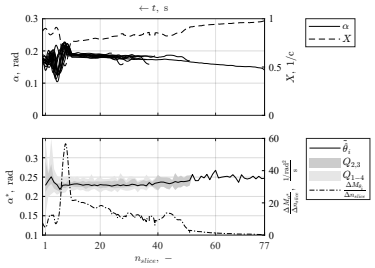

Figure C-67: Parameter α^*.

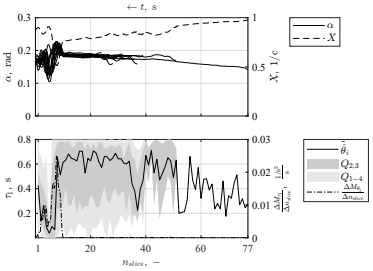

Figure C-68: Parameter τ_1.

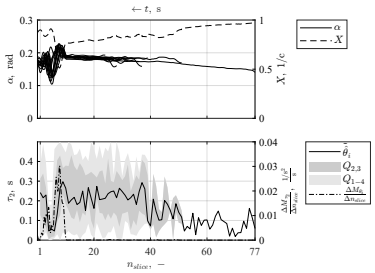

Figure C-69: Parameter τ_2.

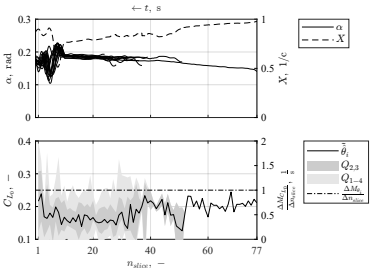

Figure C-70: Parameter C_{L_0}.

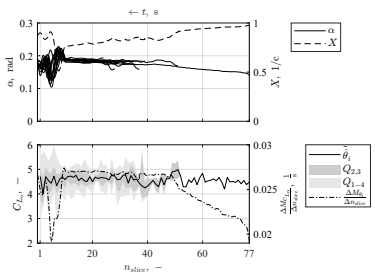

Figure C-71: Parameter C_{L_α}.

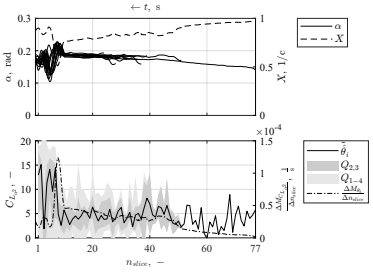

Figure C-72: Parameter $C_{L_{\alpha^2}}$.

Post-stall Slicing

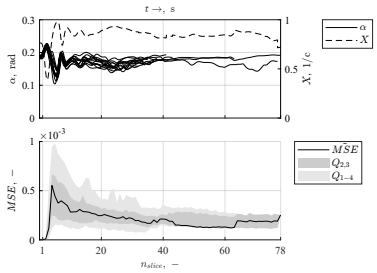

Figure C-73: Metric MSE.

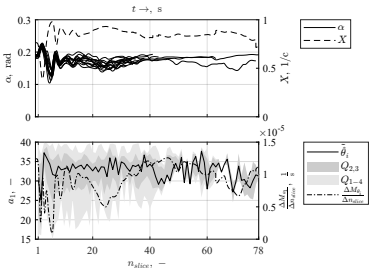

Figure C-74: Parameter a_1.

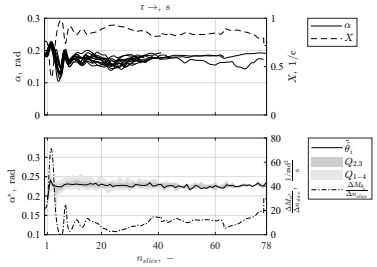

Figure C-75: Parameter α^*.

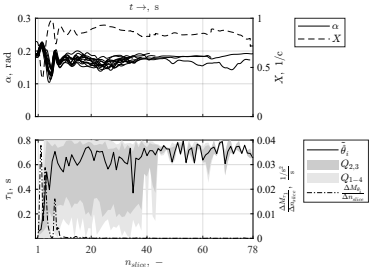

Figure C-76: Parameter τ_1.

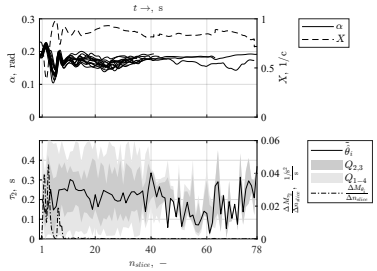

Figure C-77: Parameter τ_2.

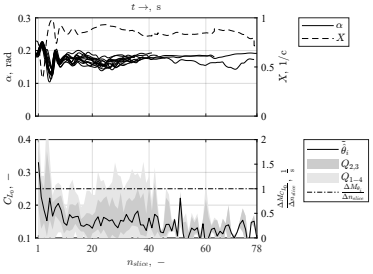

Figure C-78: Parameter C_{L_0}.

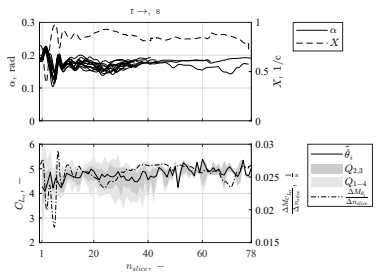

Figure C-79: Parameter C_{L_α}.

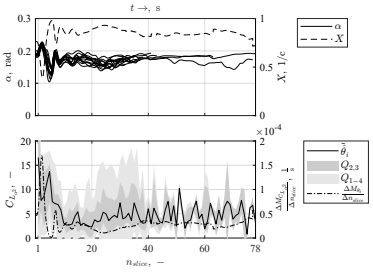

Figure C-80: Parameter $C_{L_{\alpha^2}}$.

C-3 Wiggle Input

C-3-1 Simulation Data

Pre-stall Slicing

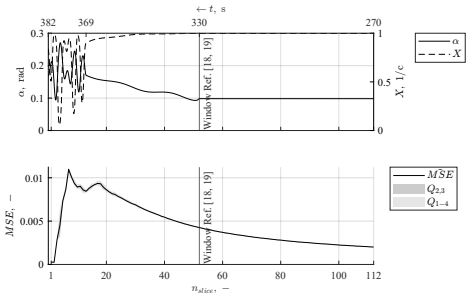

Figure C-81: Metric MSE.

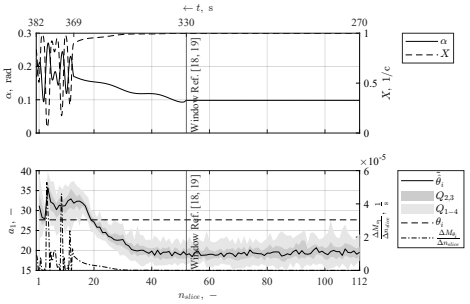

Figure C-82: Parameter a_1.

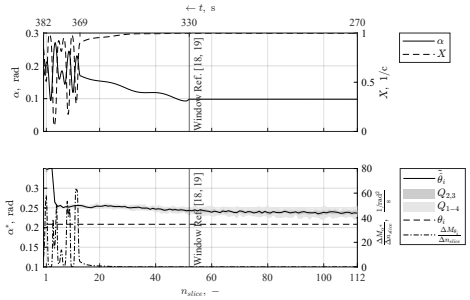

Figure C-83: Parameter α^*.

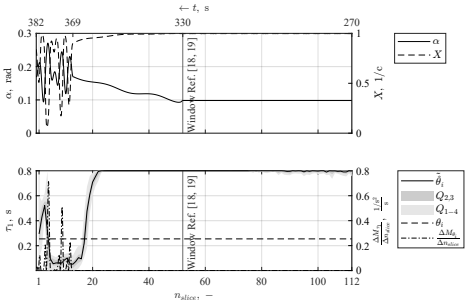

Figure C-84: Parameter τ_1.

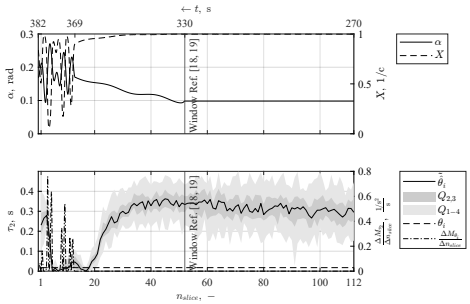

Figure C-85: Parameter τ_2.

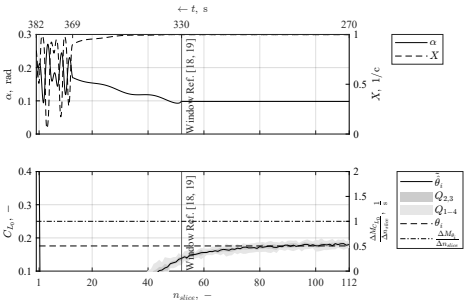

Figure C-86: Parameter C_{L_0}.

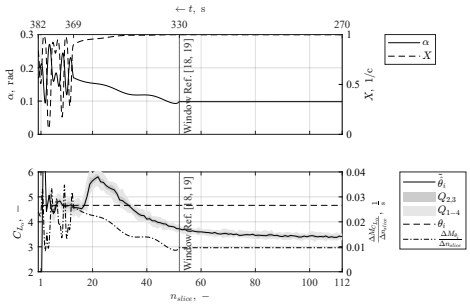

Figure C-87: Parameter C_{L_α}.

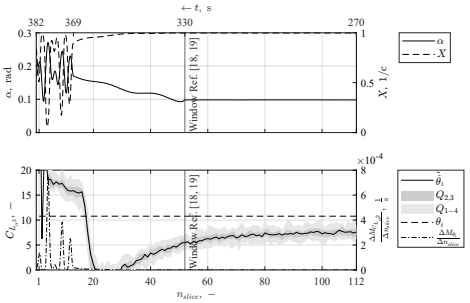

Figure C-88: Parameter $C_{L_{\alpha^2}}$.

Post-stall Slicing

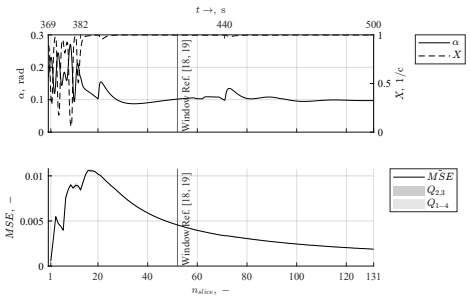

Figure C-89: Metric MSE.

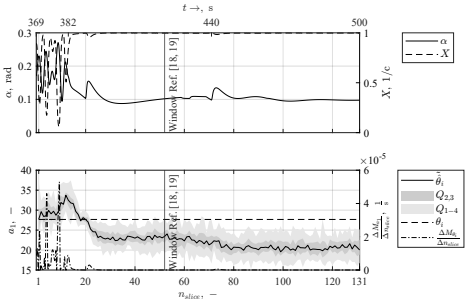

Figure C-90: Parameter a_1.

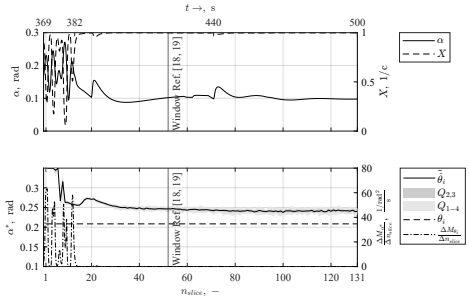

Figure C-91: Parameter α^*.

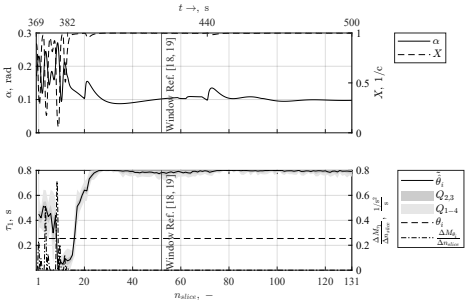

Figure C-92: Parameter τ_1.

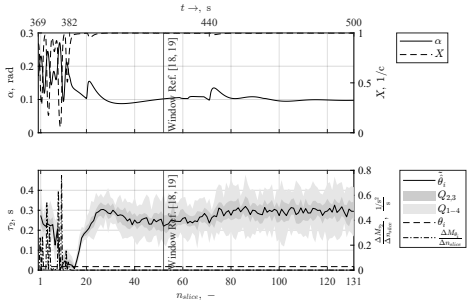

Figure C-93: Parameter τ_2.

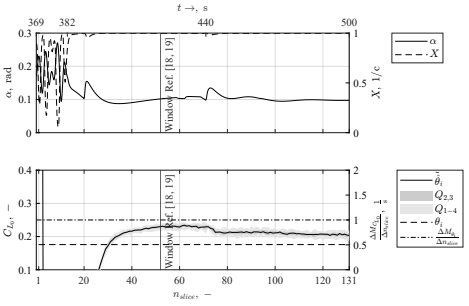

Figure C-94: Parameter C_{L_0}.

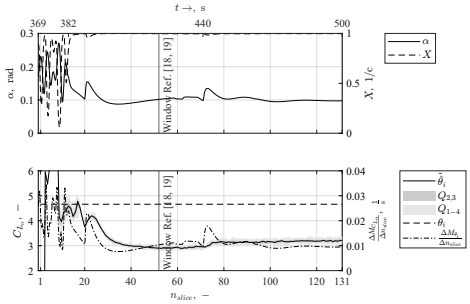

Figure C-95: Parameter C_{L_α}.

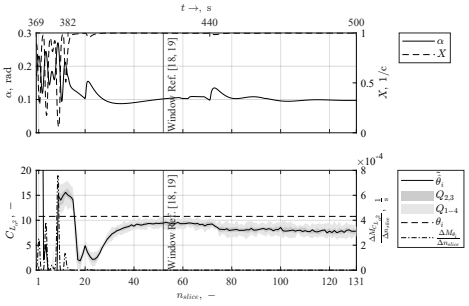

Figure C-96: Parameter $C_{L_{\alpha^2}}$.

Pre-stall and Post-stall Slicing

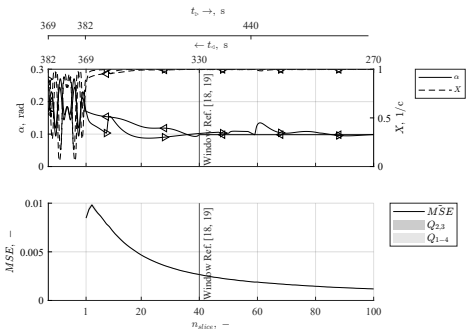

Figure C-97: Metric MSE.

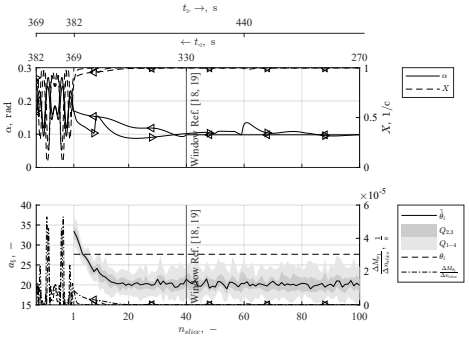

Figure C-98: Parameter a_1.

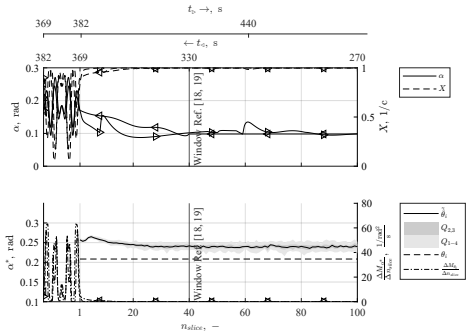

Figure C-99: Parameter α^*.

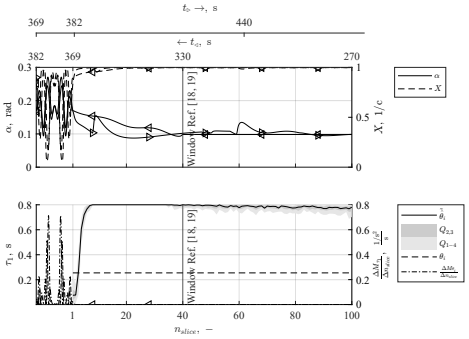

Figure C-100: Parameter τ_1.

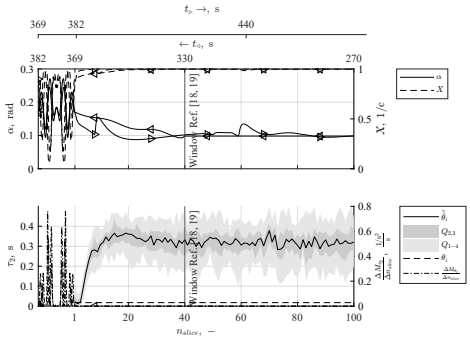

Figure C-101: Parameter τ_2.

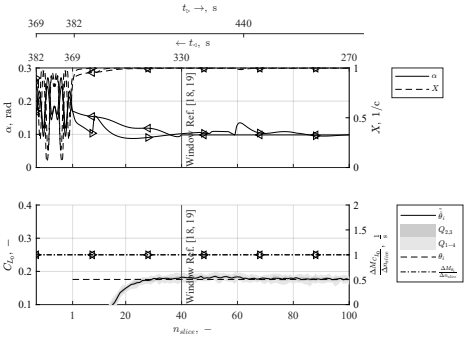

Figure C-102: Parameter C_{L_0}.

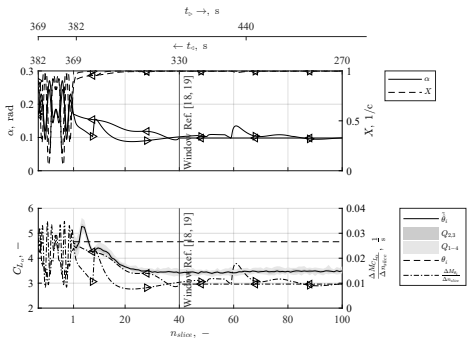

Figure C-103: Parameter C_{L_α}.

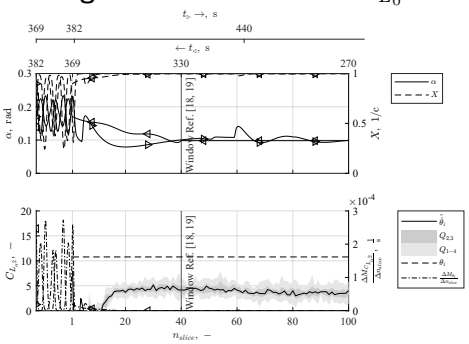

Figure C-104: Parameter $C_{L_{\alpha^2}}$.

C-3-2 Flight Test Data

Pre-stall Slicing

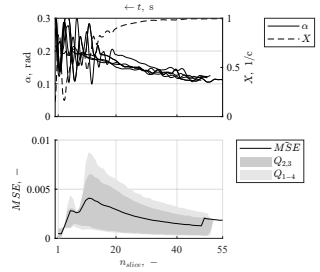

Figure C-105: Metric MSE.

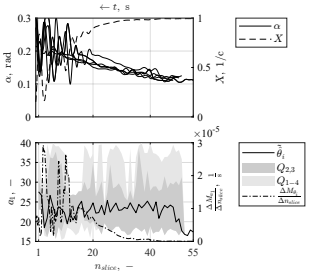

Figure C-106: Parameter a_1.

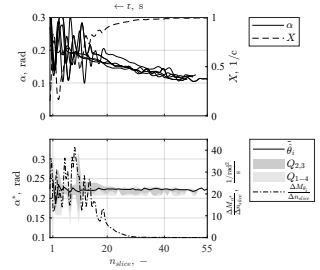

Figure C-107: Parameter α^*.

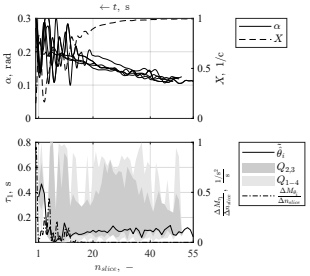

Figure C-108: Parameter τ_1.

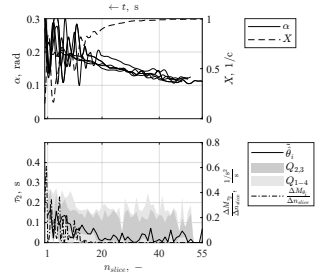

Figure C-109: Parameter τ_2.

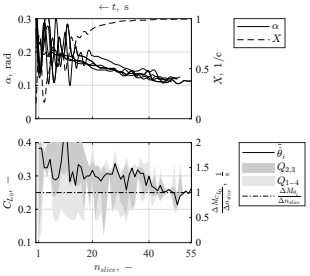

Figure C-110: Parameter C_{L_0}.

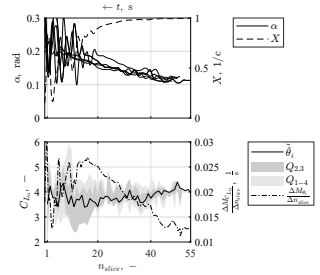

Figure C-111: Parameter C_{L_α}.

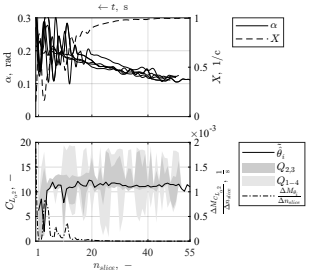

Figure C-112: Parameter $C_{L_{\alpha^2}}$.

Post-stall Slicing

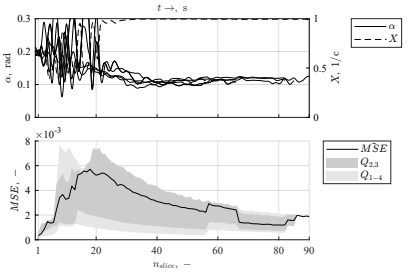

Figure C-113: Metric MSE.

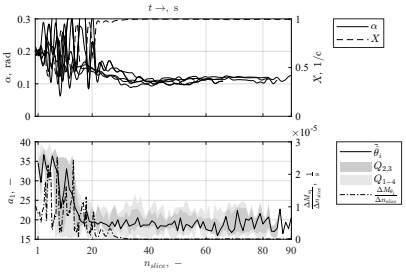

Figure C-114: Parameter a_1.

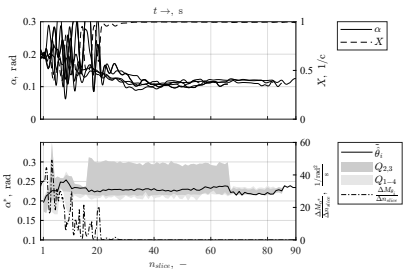

Figure C-115: Parameter α^*.

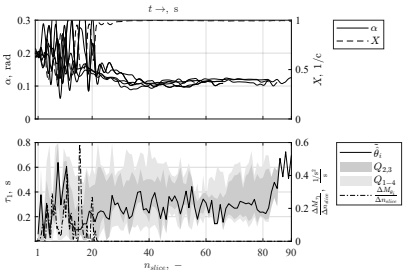

Figure C-116: Parameter τ_1.

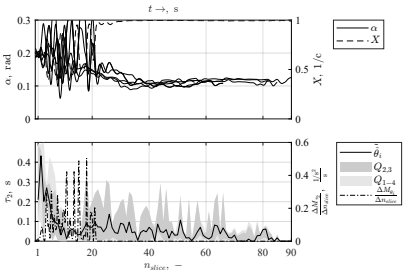

Figure C-117: Parameter τ_2.

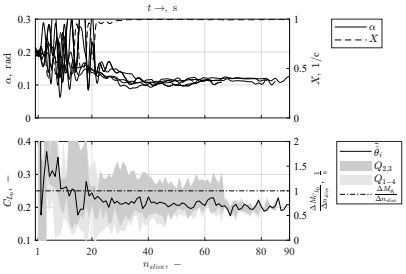

Figure C-118: Parameter C_{L_0}.

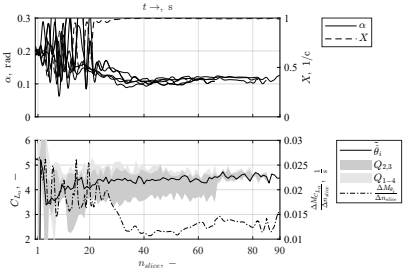

Figure C-119: Parameter C_{L_α}.

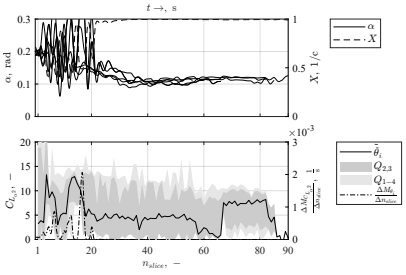

Figure C-120: Parameter $C_{L_{\alpha^2}}$.